Exclusive ρ^0 Meson Cross Section Ratios on Deuterium and Hydrogen Targets

Andrew G.S. Osborne

A Thesis presented for the degree of
Doctor of Philosophy

Nuclear Physics Experimental Research Group
Department of Physics and Astronomy
University of Glasgow
Scotland
June 2006

Exclusive ρ^0 Meson Cross Section Ratios on Deuterium and Hydrogen Targets

Andrew G.S. Osborne

Submitted for the degree of Doctor of Philosophy
June 2006

Abstract

The HERMES experiment is a large forward angle spectrometer located at the HERA accelerator ring at DESY, Hamburg. This thesis presents the analysis of the kinematic dependencies of ρ^0 vector meson production on hydrogen and deuterium targets. The relative gluon and quark contribution to the ρ^0 production amplitude is expected to depend on the kinematical variable x_{Bj}, and by measuring the ratio of ρ^0 electroproduction cross sections on deuterium and hydrogen from HERMES data this dependence is confirmed. This thesis describes the methods used to extract the cross section ratio from the HERMES data taken between the years 1996 and 2000 and compares the results with the theoretical predictions.

Until 2005 the missing mass resolution of the HERMES spectrometer was only sufficient to allow exclusivity at the level of a data sample. The HERMES Recoil Detector, installed in early 2006, is an upgrade which will augment the HERMES spectrometer by establishing exclusivity at the event level and therefore improving the resolution to which various kinematical variables may be reconstructed. Additionally, the Recoil Detector will contribute to the overall background suppression capability of the HERMES spectrometer. These improvements will provide a strong reduction in the statistical uncertainties present in the ρ^0-analysis and other analyses at HERMES. The Recoil Detector critically relies on its track reconstruction software to enable its capability to provide event level exclusive measurements. This tracking code is presented in detail.

Declaration

The work in this thesis is based on research carried out at the Nuclear Physics Experimental Research group, Department of Physics and Astronomy, University of Glasgow, Scotland. No part of this thesis has been submitted elsewhere for any other degree or qualification and it is all my own work unless referenced to the contrary in the text.

Acknowledgements

This thesis would not exist were it not for the people who provided me with help and support during my three and a half years as a Ph.D student. In reality this thesis reflects the efforts of scores of individuals, but this section is devoted to those who were sufficiently kind, patient and available to contribute personally.

First of all, thanks go to Prof. Guenther Rosner for giving me the opportunity to pursue my Ph.D at Glasgow University. Big thanks to my supervisor Ralf Kaiser for his patience and willingness to help with all aspects of my research. Thanks to Bjoern Seitz who, during my tracking studies, was an indispensable second supervisor. Thanks also go to Wolfgang Sommer, Nils Pickert, Bernhard Krauss, Artem Borysenko, Michael Tytgat and Dan Protopopescu for their input into the tracking. Maurice Bouwhuis, Larry Felawka and Markus Ehrenfried generously donated their time to explain to me the intricacies of the software setup at HERMES and for this I owe them my thanks.

Sasha Borissov took on the task of teaching me about ρ^0 analysis at HERMES and I offer him my thanks for all his help during the latter part of my Ph.D. Thanks go to Delia Hasch for her advice and efforts as HERMES analysis coordinator. I would also like to thank Markus Diehl and Wolfgang Kugler, both of whom provided theoretical insights into the analysis and help whenever I needed it. My analysis would not have been as successful without additional input from Boghdan Marianski and Jeroen Dreschler.

I'd like to thank our Glasgow technicians Scott, Tony and Peter, and our administrator Ken for tolerating my frequent stupid questions. Thanks go to my fellow HERMES Glasgow Ph.D students Craig Shearer, Morgan Murray and Gordon Hill for work-related help as well as the drunken hilarity and entertaining nights out. Craig contributed significantly to my early understanding of the HERMES Monte Carlo; my tracking studies would have been much more difficult without his help. Thanks also go to my fellow non-HERMES Glasgow Ph.D students for their help,

friendship and company at lunch or coffee time: Andreas Reiter, Duncan Middleton, Joseph Melone, Stephen McLaughlan, Steven Waddell, Kris Monstad, David Hamilton, Derek Glazier, Joseph "Fasho" Donnelly, Bryan McKinnon, Evie Downie, Neil "Ride" Thompson, Richard Codling, Russell Johnstone and Eilidh McNicoll. All of you helped to make Glasgow University a great place to work. Additional thanks go to my proof-readers, the aforementioned Morgan and my ex-flatmate Ed Hawkes.

Special thanks go to my parents Bill and Esmenia and my brother David for all they have done for me through the years. Finally, greatest thanks of all go to my beloved Paula, without whose love and support I could not have endured the occasional difficult times of my Ph.D studies.

Contents

List of Figures

List of Tables

Chapter 1

Introduction

Our understanding of the substructure of matter has evolved considerably over the last hundred years. Scattering experiments, beginning with those of Geiger, Marsden and Rutherford, have provided invaluable insights into the fundamental building blocks of matter. The incremental improvements in experimental design, coupled with progressively more sophisticated theoretical formalisms have led to our present-day understanding that all matter is constructed from combinations of six quarks and six leptons. The familiar protons and neutrons which comprise most matter are referred to as baryons and contain three quarks. Mesons are those particles containing a combination of a quark and an antiquark. Baryons and mesons are known as hadrons and are bound together by gluons, the gauge bosons of the strong interaction described by quantum chromodynamics (QCD).

The existence of the constituent quarks from which hadrons are composed was first postulated by Gell-Mann and Zweig in 1964. Deep-inelastic scattering (DIS) is characterised by a large momentum and energy transfer between the beam and the target such that the wavelength of the exchanged virtual photon is small enough to resolve nucleon constituents. DIS experiments at SLAC in the late 1960s provided the first evidence of this underlying substructure. The results of subsequent polarised DIS experiments such as EMC and later E143 led to the startling revelation that the quarks carried less than half of the spin of the nucleon. In sharp contrast to the quark spin contribution expected from the Quark-Parton Model ($\Delta\Sigma = 0.57$), the E143 experiment measures this contribution to be $\Delta\Sigma = 0.29 \pm 0.09$ [1]. The remainder of the nucleon spin could be attributed to contributions from the quark

and gluon angular momenta with the expression

$$\frac{1}{2}\hbar = S_z = \frac{1}{2}\Delta\Sigma + \Delta G + \Delta L \tag{1.1}$$

where $\Delta\Sigma = \Delta u + \Delta d + \Delta s$ refers to the sum of the contributions from sea and valence quarks and ΔG and ΔL are the gluon and quark angular momenta respectively. The HERMES experiment (HERa MEasurement of Spin) was designed to study the spin structure of the nucleon by measuring scattering interactions between a polarised lepton beam and a polarised nucleon target. Precise measurements of the spin polarised structure function g_1 have been obtained at HERMES by analysing measurements of double-spin asymmetries in inclusive lepton-nucleon scattering [2]. Spin asymmetries in different semi-inclusive processes can be measured in order to separate the spin contributions from each quark flavour [3].

In addition to enabling spin physics studies, HERMES is capable of measuring various meson production processes. Of specific interest to this thesis is exclusive vector meson production, one of the processes that can be understood in terms of Generalised Parton Distributions (GPDs) [4]. GPDs link several exclusive production processes and through their study may provide the first determination of the quark and gluon angular momentum contributions to the spin of the nucleon. In this thesis the exclusive, diffractive production of ρ^0 vector mesons from positron and electron scattering reactions on hydrogen and deuterium nuclei is studied in the HERMES kinematic region. The ratio of the cross-sections of ρ^0 meson production between hydrogen and deuterium will provide an insight into the relative contribution to the nucleon cross-sections from quarks and gluons.

The HERMES Recoil Detector is the latest planned upgrade to the HERMES experiment. The Recoil Detector is designed to enhance the capabilities of the HERMES spectrometer and expand the physics programme at HERMES, including the provision of an improvement to the resolutions of the kinematical quantities relevant to the study of vector mesons. Its primary aim, however, is to enable the exclusive measurements of scattering interactions at the event level. This capability, in addition to the improved background subtraction and angular acceptance, will greatly increase the statistics available for the study of Deeply Virtual Compton Scattering (DVCS) reactions, which provides the cleanest method with which to explore the spin properties of the nucleon in the context of Generalised Parton Distributions. This thesis will also present the details of the Recoil Detector with emphasis on the offline software used to reconstruct tracks from scattering events.

Chapter 2 will provide the physics theoretical background to the ρ^0 analysis. A selection of ρ^0 production models will be explored, in addition to the reaction kinematics which are common to most analyses at HERMES. The link from exclusive ρ^0 production to Generalised Parton Distributions is also presented. A short section is devoted to the physics motivation behind the Recoil Detector, containing a discussion of DVCS.

Chapter 3 concerns the setup of the HERMES experiment. This chapter contains a brief description of the HERA accelerator and some of its technical specifications, the bulk of the chapter presents the technical details of the HERMES spectrometer itself and its subcomponents. Special interest is paid to the Recoil Detector for which a separate chapter (chapter 4) describing its design and subdetectors is appropriate.

The track reconstruction software for the Recoil Detector is presented in chapter 5. Within are specific details of the track finding and track fitting algorithms used in the reconstruction, both for cosmic ray tracks used in the winter 2005 test experiment, and the curved proton and pion tracks which will be measured in the final setup inside the HERMES spectrometer. The results of the tests of the tracking algorithms are also presented, using Monte Carlo and real data where applicable.

Chapter 6 contains the results of the ρ^0 analysis, and includes details of each step taken in the procedure in order to obtain the final result. The comparison of the ρ^0 production cross-section ratio as seen in the HERMES data and its expected theoretical behaviour is presented.

Chapter 2

Physics of Vector Meson Production

In this chapter the specifics of exclusive, diffractive ρ^0 meson production are detailed. An introduction to the concepts relating to Deep Inelastic Scattering (DIS) precedes a discussion of nucleon structure in which the separate formalisms of a form factor-based approach and one based on parton distribution functions are presented. Next, the characteristics of diffractive interactions, and their relation to classical diffraction in optics are presented. Following the subsequent discussion of the various theoretical models describing vector meson production, the conceptual unification of nucleon form factors and parton distribution functions is presented via the Generalised Parton Distribution formalism. Finally, the physics motivation behind the analysis of ρ^0 production cross-section ratios is explained.

The natural units $\hbar = c = 1$ will be used throughout this work.

2.1 Kinematics

The specifics of the kinematics relevant to the exclusive, diffractive ρ^0 vector meson production analysis share their features with those of deep inelastic lepton-nucleon scattering. Figure 2.1 depicts exclusive vector meson production from electron or positron scattering on a proton target.

The target nucleon is initially at rest in the laboratory frame, p and M denote its four-momentum and mass respectively. The four-momentum of the incoming lepton is denoted as k, that of the outgoing lepton as k'. After the interaction, the final

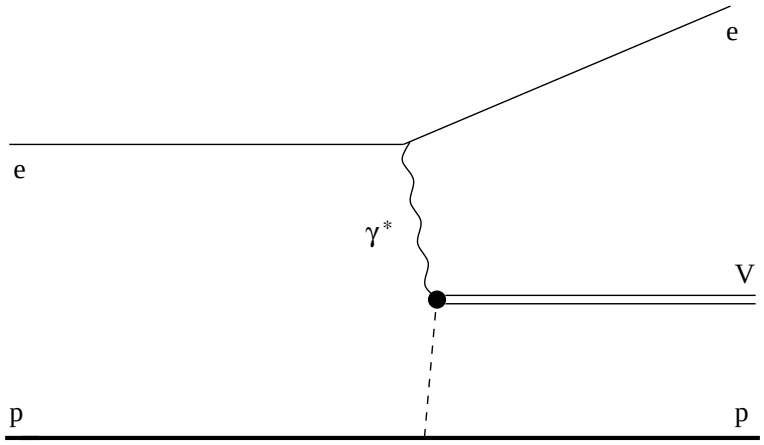

Figure 2.1: Exclusive vector meson electroproduction.

hadronic state has a four-momentum and energy p' and $E_{p'}$ and θ is the scattering angle between the incoming and outgoing lepton momenta.

The interaction proceeds via the exchange of the virtual photon γ^*. Its four-momentum q is given by

$$q = k - k'. \tag{2.1}$$

The scattering kinematics are more usefully expressed as Lorentz-invariant quantities, allowing ready comparison between the fixed-target kinematics of HERMES and other experiments. The invariant quantity Q^2 is also referred to as the photon virtuality and has positive values for a spacelike (virtual) photon. It is given according to

$$Q^2 \equiv -q^2 = -(k - k')^2 \tag{2.2}$$

and in the laboratory frame

$$Q^2 \approx 4EE' sin^2\left(\frac{\theta}{2}\right) \tag{2.3}$$

neglecting the lepton mass as $k \gg m_e$. Here the Bjørken scaling variable x is introduced;

$$x \equiv \frac{Q^2}{2p \cdot q} = \frac{Q^2}{2M\nu}, \tag{2.4}$$

which in DIS is interpreted as the fraction of nucleon momentum carried by the struck quark, in a reference frame where both the lepton and nucleon have very large momenta - in the case of HERMES, the centre of mass system between the lepton and nucleon is such a frame. Here, ν represents the energy transfer, in the laboratory frame, from the beam lepton to the virtual photon, and is given according to

$$\nu \equiv \frac{p \cdot q}{M} \overset{lab}{=} E - E'. \tag{2.5}$$

The Bjørken scaling variable y is given as

$$y = \frac{p \cdot q}{p \cdot k} \overset{lab}{=} \frac{\nu}{E} \tag{2.6}$$

and represents the ratio of virtual photon and incoming lepton energies in the laboratory frame. For the variables x and y, the allowed values are

$$0 < x, y \leq 1. \tag{2.7}$$

The squared centre-of-mass energy of the photon-nucleon system is given by

$$W^2 = (q + p)^2 = M^2 + 2M\nu - Q^2 = M^2 + Q^2 \frac{1 - x}{x}. \tag{2.8}$$

In DIS W^2 also represents the square of the invariant mass of the hadronic final state. For $x = 1$, the last term in equation (2.8) shows that $W = M$ which indicates an elastic scattering event. The variable s denotes the square of the centre of mass energy of the lepton-nucleon system and is given by

$$s \equiv (k + p)^2 \overset{lab}{\approx} M^2 + 2ME. \tag{2.9}$$

In the case of HERMES with a 27.5 GeV beam energy, $\sqrt{s} = 7.2$ GeV. The squared four-momentum transfer to the hadronic vertex is given by

$$t = (q - v)^2 = (p - p')^2, \tag{2.10}$$

where v is the four-momentum of the vector meson. The second term gives, for

exclusive scattering in the laboratory frame,

$$t = 2M(M - E_{p'}) \tag{2.11}$$

which can be rearranged to give an expression for the recoiling target nucleon energy, $E_{p'}$, as a function of t.

2.2 Elastic Scattering

Elastic scattering is characterised by the absorption of the transferred energy and three-momentum by the target nucleon without excitation, and is depicted to leading order in figure 2.2(a). Elastic electron-proton scattering experiments in the 1950s were the first to provide a way to determine the size of the proton [5]. At the photon energies and hence lepton energies required for probing the nucleon effectively, the scattering behaviour diverges from the classical Rutherford formula. The probing leptons are relativistic, produce nuclear recoil and interact via their magnetic moment in addition to their charge. Appropriately, the Rutherford scattering formula is modified to yield the Mott cross-section [6]:

$$\left(\frac{d\sigma}{d\Omega}\right)_{Mott} = \frac{\alpha_{em}^2}{4E^2 \sin^4 \theta/2} \frac{E'}{E} \cos^2 \frac{\theta}{2} \tag{2.12}$$

where α_{em} is the fine structure constant and E', E are as defined in section 2.1. Equation (2.12) only applies, however, to a lepton scattering from a point-like proton with corresponding magnetic moment. The Rosenbluth cross-section for elastic ep scattering is a modification of the Mott formula taking these considerations into account [7];

$$\begin{aligned} \frac{d\sigma}{d\Omega} &= \left(\frac{d\sigma}{d\Omega}\right)_{Mott} \left\{ F_1\left(Q^2\right) \right. \\ &\quad \left. + \tau \left[F_2^2\left(Q^2\right) + 2\left(F_1^2\left(Q^2\right) + F_2^2\left(Q^2\right)\right)^2 \tan^2 \frac{\theta}{2} \right] \right\}, \end{aligned} \tag{2.13}$$

where $\tau = Q^2/4m^2$, m is the mass of the proton, $F_1(Q^2)$ and $F_2(Q^2)$ are the empirically determined Dirac and Pauli electromagnetic form factors respectively. For small lepton energies, in comparison to the nucleon mass, equation 2.13 reduces to

the Mott-Rutherford formula for scattering of an electron by a fixed electrostatic potential [8]. The form factors $F_{1(2)}$ appear in the scattering amplitude as transition current matrix elements sandwiched between nucleon states and represent vector (tensor) transitions between them.

More intuitively, these form factors may be represented by the Sachs electric and magnetic form factors:

$$\begin{aligned} G_E(Q^2) &= F_1(Q^2) - \tau F_2(Q^2), \\ G_M(Q^2) &= F_1(Q^2) + F_2(Q^2) \end{aligned} \tag{2.14}$$

which, in the Breit frame (coincident with the lepton-nucleon centre of mass), are related to nucleon charge and magnetisation densities for a given Q^2. Further, the charge distribution is obtained by taking the Fourier transform of G_E. Additionally, at $Q^2 = 0$, $G_{E(M)}$ gives the proton charge (magnetic) moment while the slopes of the form factors are used in the determination of the mean square proton radius. The observed strong dependence of $G_{E,M}$ on Q^2 provides direct evidence of the extended charge and current distributions of the proton.

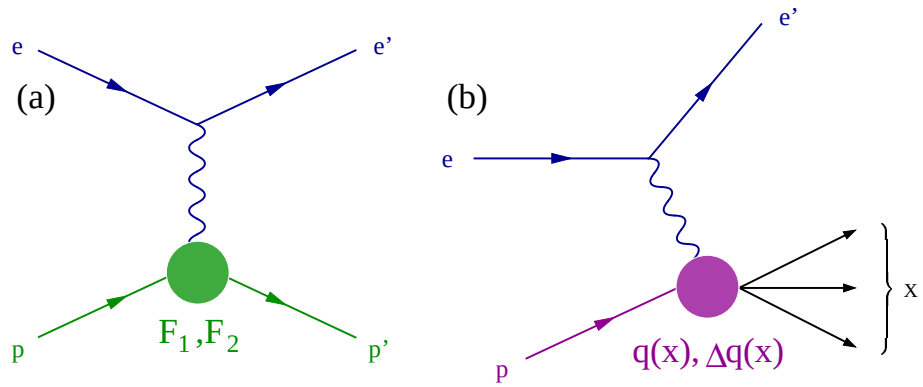

Figure 2.2: Leading order Feynman diagrams for (a) Elastic ep scattering and (b) Deep Inelastic Scattering. Parameterisation of the incalculable hadronic tensor $\mathcal{W}^{\mu\nu}$ is accomplished respectively in terms of form factors $F_{1,2}(Q^2)$ and parton distributions $q(x)$, $\Delta q(x)$ [9].

2.3 Deep-Inelastic Scattering

Increasing the virtuality (Q^2) of the interacting photon in a scattering event improves the resolution to which the target nucleon can be investigated. Inclusive

lepton-nucleon scattering interactions in the Bjørken limit, where Q^2 and ν are much larger than the nucleon mass are useful processes for studying nucleon structure as the momentum and energy transfer become large enough to promote nucleon fragmentation into multihadronic states. In DIS, a high-energy electron or positron scatters on a nucleon as depicted to lowest order in figure 2.2(b).

The single-photon exchange approximation is adequate here as heavy boson exchange associated with weak processes lies outside the HERMES kinematic range (the centre-of-mass energy at HERMES being 7.2 GeV^2). Further, multi-photon exchange processes are suppressed by a factor of α_{em} and can be accounted for through the application of so-called radiative corrections.

The squared amplitude for Deep Inelastic Scattering can be written in terms of the product of the leptonic and hadronic tensors $\mathcal{L}_{\mu\nu}$ and $\mathcal{W}^{\mu\nu}$ [10], corresponding to the photon-lepton and photon-hadron vertices in figure 2.2(b). The cross-section can then be expressed as

$$\frac{d^2\sigma^{ep}}{d\Omega dE'} = \frac{\alpha^2 E'}{Q^4 E}\mathcal{L}_{\mu\nu}\mathcal{W}^{\mu\nu}. \tag{2.15}$$

While the leptonic tensor $\mathcal{L}_{\mu\nu}$ can be exactly calculated in quantum electrodynamics, the hadronic tensor cannot and must be parameterised in terms of empirically obtained structure functions and the hadron momentum p, hadron spin s_h and the virtual photon momentum q. Imposing parity conservation, translation and time reversal invariance, hermicity and current conservation, the hadronic tensor is given by

$$\begin{aligned}\mathcal{W}^{\mu\nu} &= W_1\left(-g_{\mu\nu}+\frac{q_\mu q_\nu}{q^2}\right)+\frac{W_2}{M^2}\left(p_\mu-\frac{p\cdot q}{q^2}q_\mu\right)\left(p_\nu-\frac{p\cdot q}{q^2}q_\nu\right)\\ &\quad +i\epsilon^{\mu\nu\alpha\beta}q^\alpha M S^\beta G_1+i\epsilon^{\mu\nu\alpha\beta}q^\alpha\left[(p\cdot q)S^\beta-(S\cdot q)p^\beta\right]\frac{G_2}{M}\end{aligned} \tag{2.16}$$

where $g_{\mu\nu}$ is the metric tensor, $\epsilon^{\mu\nu\alpha\beta}$ is the totally antisymmetric Levi-Civita tensor and S denotes the polarisation vector of the spin 1/2 target nucleon. The coefficients W_1, W_2, G_1, G_2 are functions of Q^2 and ν and are often expressed in terms of four dimensionless structure functions:

$$\begin{aligned} F_1(x,Q^2) &= MW_1(Q^2,\nu), \\ F_2(x,Q^2) &= \nu W_2(Q^2,\nu), \\ g_1(x,Q^2) &= M^2\nu G_1(Q^2,\nu), \\ g_2(x,Q^2) &= M\nu^2 G_2(Q^2,\nu) \end{aligned} \tag{2.17}$$

where the structure functions $F_{1,2}$ are not to be confused with the form factors introduced in section 2.2 and instead relate to the symmetric part of the hadronic tensor, with the spin-dependent part being described by $g_{1,2}$. The distance scale probed by the virtual photon, which defines the resolution of the scattering process, displays a $1/Q$ dependence arising from the relationship between Q^2 and the wavelength of the virtual photon. For fixed x,

$$ƛ = \frac{\hbar}{|\vec{q}|} = \frac{\hbar}{\sqrt{\nu^2+Q^2}} \overset{Breit}{=} \frac{\hbar}{Q}. \tag{2.18}$$

At low photon energies the electron scatters elastically from the nucleon - this is adequately described by the form factors of section 2.2. The observed cross-sections at higher Q^2, however, are inconsistent with the elastic interpretation. As predicted by Bjørken [11], the structure functions $F_{1,2}$ and $g_{1,2}$ exhibit scaling behaviour in the DIS regime, that is, they are approximately independent of Q^2 at fixed x as they are functions of only x to leading order:

$$\begin{aligned} F_{1,2}(x,Q^2) &\overset{DIS}{\approx} F_{1,2}(x), \\ g_{1,2}(x,Q^2) &\overset{DIS}{\approx} g_{1,2}(x). \end{aligned} \tag{2.19}$$

The observation of this scaling behaviour provides direct evidence that, in the DIS regime, the beam lepton scatters on small point-like constituents within the nucleon.

2.4 The Quark-Parton Model

Feynman's interpretation of DIS data, coupled with the quarks postulated by Gell-Mann and Zweig led to the development of the quark-parton model (QPM). This picture provides an intuitive understanding of the phenomenon of scaling; an ex-

tended object possesses a form factor which introduces a dependence on Q^2. The Q^2 independence observed in DIS implies that the proton must contain point-like objects. In the Bjørken limit where both Q^2 and ν approach ∞ and x remains constant, these constituent partons [12] (later identified as quarks) behave as free particles due to the asymptotic freedom of QCD. The inelastic scattering observed from the interaction between the beam lepton and the target nucleon can, in this limit, be interpreted as elastic scattering between the lepton and the quasi-free quarks within the nucleon. In this picture of DIS, the struck quark leaves the target and fragments independently of the remainder of the nucleon.

In order to obtain the unpolarised DIS cross section, a sum over initial lepton and hadron spin states must be performed to cancel out the anti-symmetric parts of the leptonic and hadronic tensors. Appropriately, equation 2.15 becomes

$$\frac{d^2\sigma}{dxdQ^2} = \frac{4\pi\alpha^2}{Q^4}\left[F_1(x,Q^2)y^2\left(1-\frac{2m_e^2}{Q^2}\right)+\frac{F_2(x,Q^2)}{x}\left(1-y-\frac{Mxy}{2E}\right)\right]. \quad (2.20)$$

The parton model is most simply formulated in an "infinite momentum" frame; for example one in which the nucleon is moving with momentum approaching infinity in the z-direction [7]. The relativistic time dilation results in the laboratory frame observation that during the absorption of the virtual photon, insufficient time elapses for any interaction between nucleon constituents to occur. In the infinite momentum frame the masses and transverse momenta of the quarks may be neglected and so the Bjørken scaling variable x (equation 2.4) can be interpreted as the momentum fraction carried by the struck quark prior to the interaction relative to the total nucleon momentum. Justification for this may be found in [7] and [13].

The structure functions of equation 2.20 can now be written in terms of parton distribution functions (PDFs) $q_f(x,Q^2)$ which represent the probability of finding a quark of flavour f with momentum fraction x inside the nucleon. The relation between structure functions and PDFs may be obtained by comparing equation 2.16, which gives the hadronic tensor in the lepton-nucleon interaction, with an equivalent hadronic tensor in the elastic scattering cross section from quarks in the nucleon:

$$F_1(x,Q^2) = \frac{1}{2}\sum_f e_f^2(q_f^+(x,Q^2)+q_f^-(x,Q^2)), \quad (2.21)$$

$$F_2(x,Q^2) = \sum_f e_f^2 x(q_f^+(x,Q^2)+q_f^-(x,Q^2)), \quad (2.22)$$

$$g_1(x,Q^2) = \frac{1}{2}\sum_f e_f^2(q_f^+(x,Q^2)-q_f^-(x,Q^2)), \quad (2.23)$$

$$g_2(x,Q^2) = 0 \quad (2.24)$$

where $q^{+(-)}$ denotes the probability of finding a quark with spin parallel (anti-parallel) to the nucleon spin. In a more convenient notation, the unpolarised quark distribution function is $q_f = q_f^+ + q_f^-$ and the polarised quark distribution function is $\Delta q_f = q_f^+ - q_f^-$. Recalling the Q^2 independence of nucleon structure functions in the DIS regime, the structure functions may be expressed as

$$F_1(x) = \frac{1}{2}\sum_f e_f^2 q_f(x), \quad (2.25)$$

$$F_2(x) = \sum_f e_f^2 x q_f(x), \quad (2.26)$$

$$g_1(x) = \frac{1}{2}\sum_f e_f^2 \Delta q_f(x), \quad (2.27)$$

$$g_2(x) = 0. \quad (2.28)$$

Combining equations 2.25 and 2.26 yields the famous Callan-Gross relation, the experimental verification of which showed (by imposing helicity conservation) that the partons have $\frac{1}{2}$ spin, as expected of quarks:

$$F_2(x) = 2xF_1(x). \quad (2.29)$$

From this relation, the momentum sum rule is obtained:

$$\sum_f \int x q_f(x) dx = 1. \quad (2.30)$$

The sum rule asserts that the momentum of the nucleon is entirely due to the summed contribution of the individual parton momenta. Experimentally, a weak

scaling violation is observed due to quark interactions mediated by gluons, for which the quark-parton model does not account. In fact, at $Q^2 \sim 2$ GeV^2 the gluons are responsible for 39% of the nucleon momentum [7]. The dynamical structure of nucleons can be probed by further increasing the Q^2 scale; in such regimes processes such as gluon emission, quark-antiquark pair production and gluon splitting contribute strongly to the Q^2 dependence of the PDFs. Figure 2.3 shows the experimentally obtained proton electromagnetic structure function F_2 as a function of Q^2 at increasing x scale.

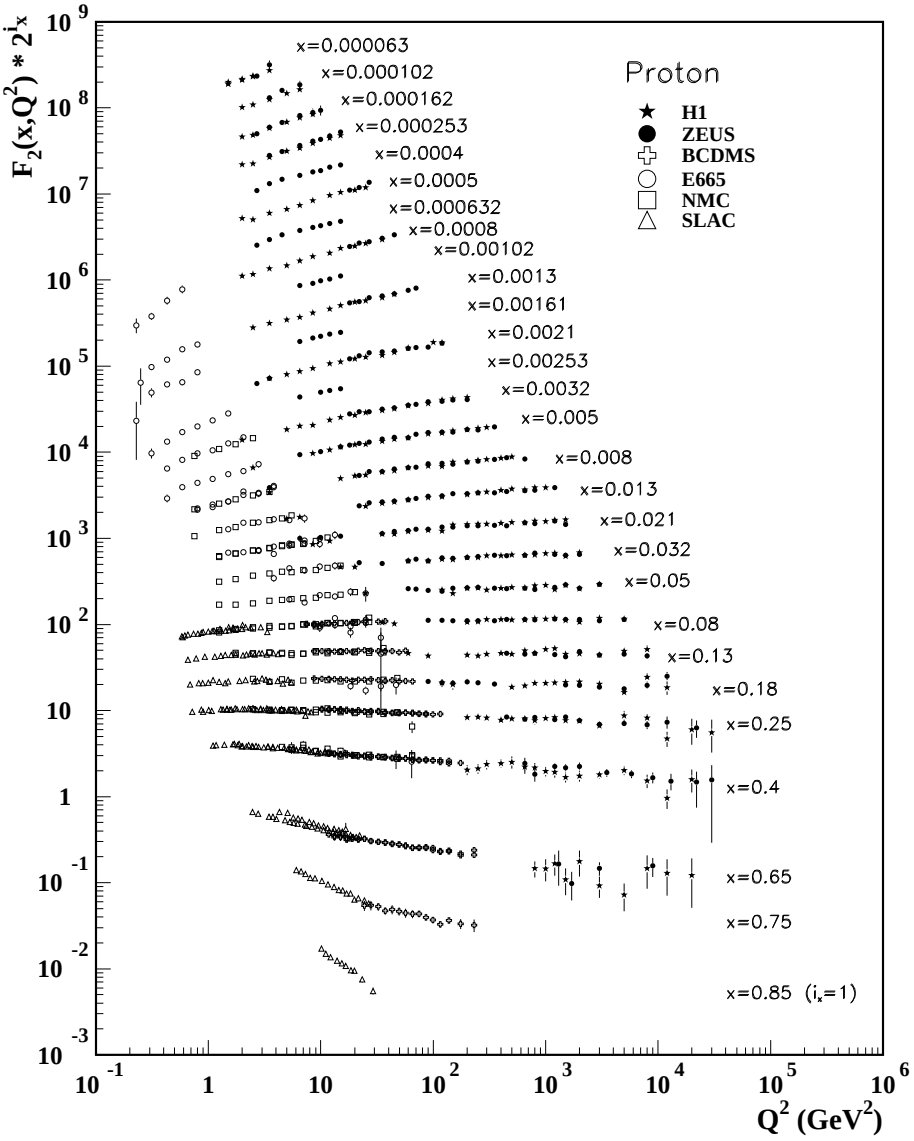

Figure 2.3: Scale dependence of $F_2(x, Q^2)$ [14].

At increasing Q^2 the scaling violation is most pronounced for very low values of x. In this region the increase in resolution allows the observation of $q\bar{q}$ pair production, prompting the increase in F_2. At intermediate values of x the structure function

remains roughly constant over a large Q^2 range, this observation led to the idea of scaling.

The evolution of the PDFs or structure functions are most simply described by the singlet Altarelli-Parisi (or DGLAP) equations, which provide a generalisation of the parton number densities to include gluon distributions [15]. It is possible, from the DGLAP equations, to calculate PDFs at any Q^2 scale where leading-order perturbative QCD applies if the PDF at some value of Q^2 is known.

2.5 Diffraction

High-energy particle scattering interactions display features which share the characteristics of diffractive phenomena in optics, observed when an obstruction is placed in the path of a coherent source of light. Huygens' principle recognises that each point of an advancing wave front is a source of secondary spherical wavelets, and that the advancing wave as a whole may be regarded as the superposition of all secondary waves arising from points already traversed. Wave-particle duality in quantum mechanics allows diffraction in high-energy scattering to be treated similarly; in which case, the overall superposition is represented by the sum of probability amplitudes.

The distinctive shape of optical diffractive minima and maxima is also a feature of diffraction in high energy physics processes. In scattering processes, those reactions during which no internal quantum numbers are exchanged between the beam and target particles are dominated asymptotically by diffraction. As with optics, hadronic diffraction exhibits very steep momentum transfers or angular distributions, and the total cross section increases slowly with energy. Also, the slopes of the angular distributions are observed to increase slowly with energy.

Different classes of diffractive reactions are depicted in figure 2.4. Figure 2.4(a) illustrates elastic scattering, where both particles remain intact after the interaction. Single diffraction is shown in figures 2.4(b) and (c), in this case either the target or beam particle splits into several daughter particles, the sum of whose individual quantum numbers matches those of the parent particle. Figure 2.4(d) depicts those events in which both interacting particles decay into particle jets after the interaction, referred to as double diffraction.

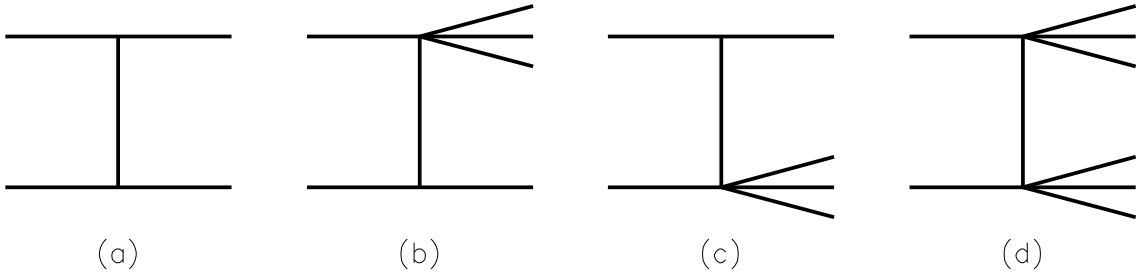

Figure 2.4: Different types of diffraction; (a) elastic scattering, (b) and (c) single diffraction, (d) double diffraction.

2.6 Optical Diffraction

A plane wave incident on a black, totally absorbing disk of well-defined radius R provides the most simple model of diffraction. In this case the angular distribution of the elastic scattering is the Fourier transform of the spatial distribution of the obstacle, in which case the irradiance is given by [16]:

$$\frac{I(\theta)}{I(\theta=0)} = \left(\frac{2J_1(x)}{x}\right)^2 \approx 1 - \frac{R^2}{4}(k\theta^2), \tag{2.31}$$

where the first order Bessel function is denoted by J_1, the wave vector $k = 2\pi/\lambda$ and $x = kR\sin\theta \approx kR\theta$ for small values of θ. The distribution exhibits a peak at the centre of the pattern, at $\theta = 0$, and is symmetrical about the optical axis through the centre of the object. Minima are seen at $|x| = 3.83, 7.02...$, figure 2.5 illustrates optical diffraction.

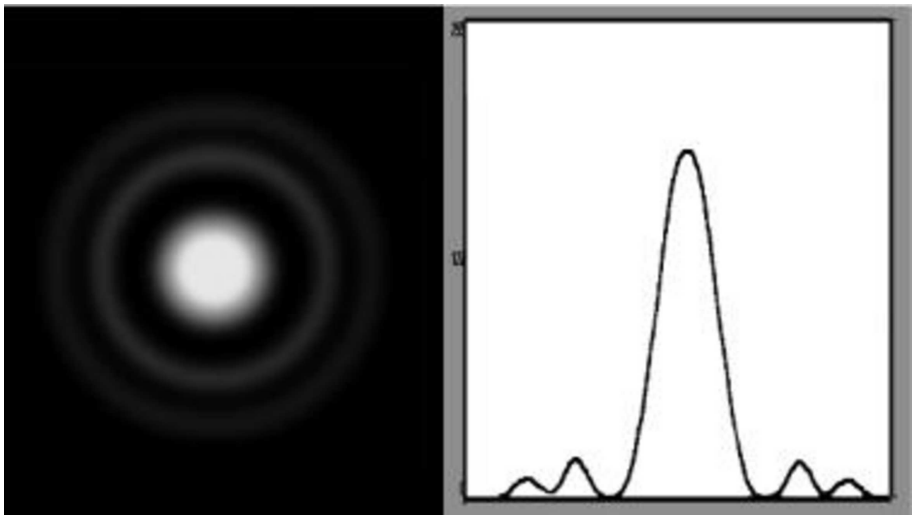

Figure 2.5: Left, diffraction pattern from light incident on black, totally absorbing disk. On the right is the illuminance distribution.

Elastic hadron-hadron scattering exhibits a similar pattern. In the centre of mass frame the squared momentum transfer between the two hadrons is $t = (p_1 - p_1')^2 = (p_2 - p_2')^2$ and can be expressed as $-t = q^2 = \left(2p \sin\frac{\theta}{2}\right)^2$ where p_i are the four-momenta corresponding to either hadron and θ is the scattering angle. The differential cross-section for this process depends primarily on q, and is illustrated in figure 2.6.

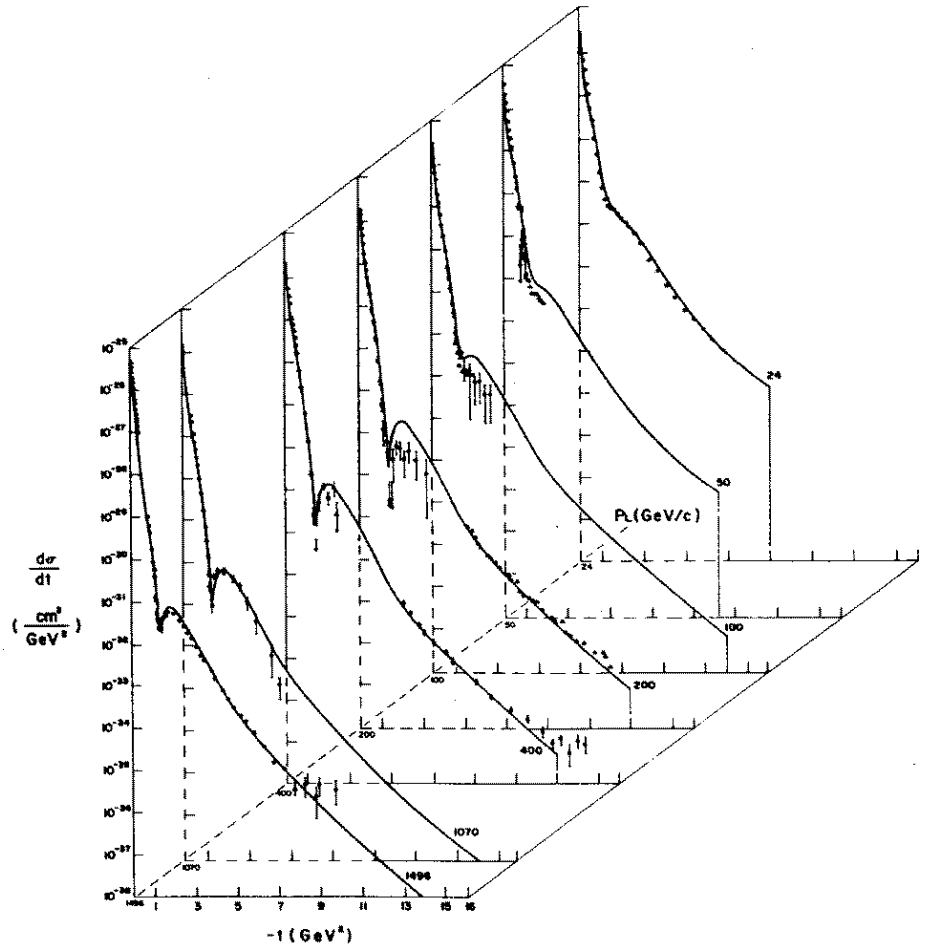

Figure 2.6: Differential elastic pp cross-section for different incident proton momenta [18]. The solid lines represent the expected behaviour from the optical model.

As prescribed in the optical model, the differential cross section can be expressed in terms of the first order Bessel function J_1, independently of the energy of the incident particle [20]:

$$\frac{d\sigma_{el}}{d|t|} = \pi R^4 \left| \frac{J_1(R\sqrt{|t|})}{R\sqrt{|t|}} \right| \tag{2.32}$$

where J_1 has minima at $R\sqrt{|t|} = 3.83, 7.02...$ and R is the nucleon radius. The diffractive forward peak is clearly visible in figure 2.6 at $|t| \leq 1$ GeV^2. At $|t| \to 0$

there is only a weak dependence of the differential cross section on the incident proton energy. The application of equation 2.32 gives a nucleon radius of $R \approx 0.7\,fm$. Figure 2.7 depicts the differential cross section for elastic pp scattering as calculated using equation 2.32. The qualitative features of figure 2.6 are also present in figure 2.7 which demonstrates the applicability of equation 2.32 in this domain. Quantitative predictions using the optical model are less reliable as it fails to predict the ratio of elastic to total cross section and their energy dependence.

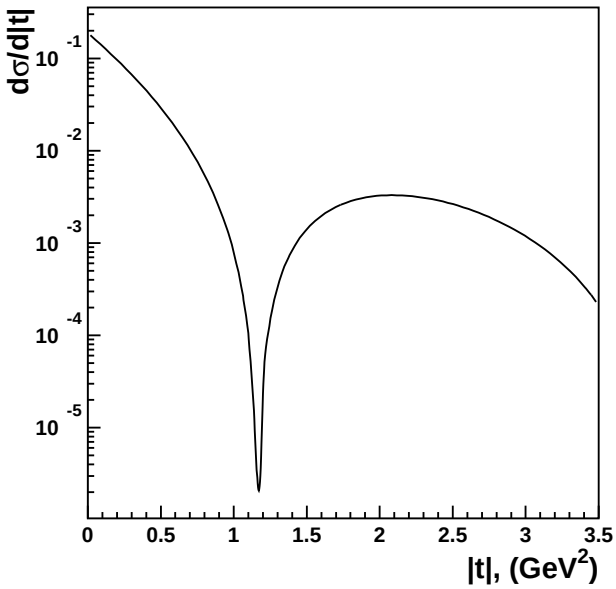

Figure 2.7: Differential cross-section for elastic pp scattering calculated using equation 2.32.

The opaque black disk of the optical model does not provide a reasonable optical description of the nucleon; an improvement can be made by modifying the disk to a "grey" scattering centre with a Gaussian density distribution. The density reflects the probability of a scatter occurring at some distance (radius) from the centre. The appropriate modification to equation 2.32 is given by

$$\frac{d\sigma_{el}}{d|t|} = \left.\frac{d\sigma_{el}}{d|t|}\right|_{|t|=0} e^{-b|t|}. \tag{2.33}$$

The exponential slope given by the b parameter is related to the radius R of the "grey" disk by $b = R^2/4$. At small $|t|$ the slope b can be obtained using straight line fits to the plots of figure 2.6. At high energies b can no longer be interpreted as a measure of the nucleon size, and provides a description of the strong interaction between the two extended hadronic objects. Additionally, b can be interpreted as

the quadratic sum of the Gaussian width of each nucleon:

$$b \propto R_1^2 + R_2^2. \tag{2.34}$$

The diffractive peak at low $|t|$ has been observed in several hadron-hadron scattering reactions. The optical model, however, neglects particle spin and so no dependence of the reaction on hadron spin states is expected. Elastic pp scattering experiments with polarised beams and targets have demonstrated large single and double spin asymmetries, in contrast to the predictions of the optical model.

The optical model is also adequate in its description of electron scattering from heavier nuclei; this bears a stronger resemblance to the experimental situation at HERMES than pp scattering does. Figure 2.8 shows the electron scattering cross sections on calcium-40 and calcium-48 as a function of the scattering angle θ (related to the kinematical variable t) in which the diffractive peak structure is readily seen.

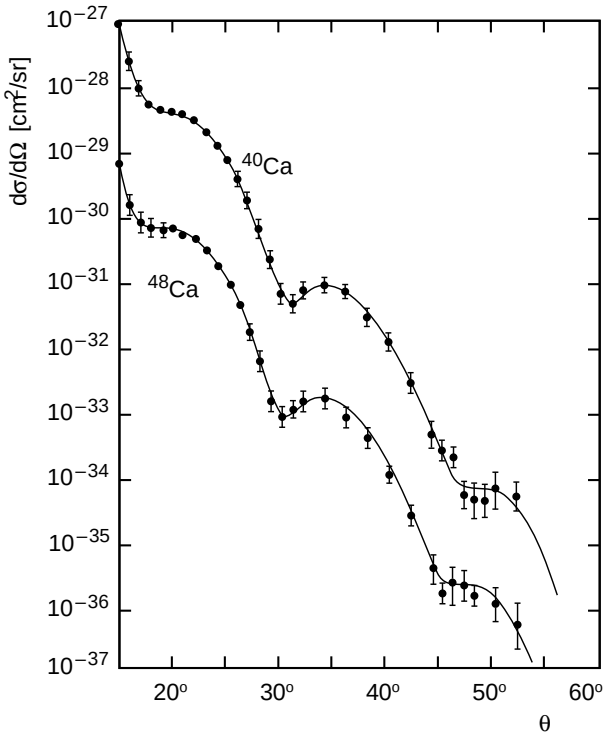

Figure 2.8: Differential elastic $e\,^{48}Ca$ and $e\,^{40}Ca$ cross sections as a function of scattering angle θ [19]. The solid lines represent the expected behaviour from the optical model.

2.7 The Vector Meson Dominance Model

Lepton-hadron interactions are related to the hadron-hadron interactions described in the previous sections through the vector meson dominance model (VMD). The initial description of the photon in quantum electrodynamics was a massless, zero charge pointlike gauge boson which coupled to charged particles. At higher energy scales, however, the photon was observed to fluctuate into electron positron pairs during an interaction with a Coulomb field. Quantum field theory further allows photon fluctuations into more complex virtual particle states such as hadrons, although in this case the reaction is suppressed by a relative factor of $\alpha \sim 1/137$ compared with the bare particle.

Photon-proton interactions observed in scattering experiments in the 1960s showed surprising similarities to the earlier hadron-hadron interactions. Both exhibit similar resonant behaviour at the low and high ends of their respective energy scales, and a similar $|t|$ slope is observed. Also, photon and hadron interactions on composite nuclei exhibit shadowing effects, indicating that the interactions typically occur on the same side of the nucleus as approached by the initial beam particle. These observations could be understood by modelling the photon with a component which interacts purely electromagnetically with the target, and one which takes part in purely hadronic interactions. The physical virtual photon is described by the superposition of a direct coupling bare photon $|\gamma_B>$ with the hadronic state $|\gamma_h>$:

$$|\gamma> \simeq \sqrt{Z_3}|\gamma_B> + \sqrt{\alpha}|\gamma_h> \tag{2.35}$$

where Z_3 assumes proper normalisation of $|\gamma>$ which accounts for the electromagnetic coupling to the target. It is several orders of magnitude smaller than the hadronic coupling and so can be neglected [20]. The hadron states $|\gamma_h>$ must conserve the quantum numbers of the photon: $J^{PC} = 1^{--}$, $Q = B = S = 0$ and so the possible states of $|\gamma_h>$ are constrained to unit spin vector mesons. Indeed, large cross sections for the photoproduction of the light vector mesons ρ^0, ω and ϕ are observed and the vector meson dominance model assumes that the photon only fluctuates into one of these three states (heavier vector mesons such as the J/ψ are included in the so-called generalised vector meson dominance model [21]).

The vector meson dominance model successfully describes vector meson photoproduction. According to its prescription, before interaction with the target nucleon

the photon fluctuates into a virtual vector meson state $q\bar{q}$ for a duration [22]:

$$t_f \approx \frac{2\nu}{Q^2 + M_V^2} \tag{2.36}$$

where M_V is the mass of the vector meson. If t_f is sufficiently long to allow the virtual vector meson to travel a distance much larger than the nucleon radius of about $1\,fm$, the photon fluctuates long before it hits the target and the interaction occurs between the virtual meson and the nucleon. Such a process is depicted in figure 2.9.

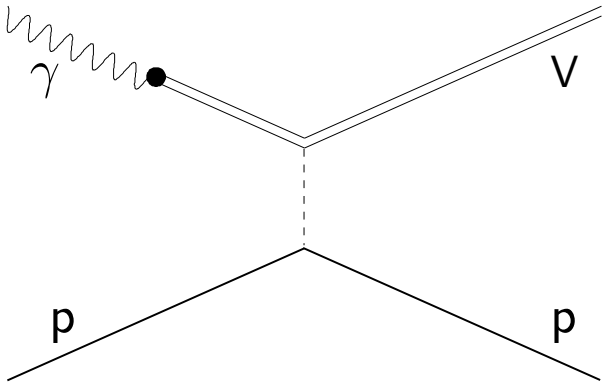

Figure 2.9: Vector meson photoproduction according to the vector meson dominance model. The photon dissociates into a virtual vector meson V which subsequently scatters off a nucleon.

The hadronic term of equation 2.35 can be written as [23]:

$$\sqrt{\alpha}|\gamma_h> = \sum_V \frac{e}{f_V} \left(1 + \frac{Q^2}{M_V^2}\right)^{-1} |V> \tag{2.37}$$

where $|V>$ denotes the vector meson states and f_V denotes the $\gamma \leftrightarrow V$ coupling constant. This is related in the VDM to the vector meson mass M_V and to its leptonic decay width Γ_{ee}^V according to:

$$\frac{4\pi}{f_V^2} = \frac{3\Gamma_{ee}^V}{\alpha^2 M_V}. \tag{2.38}$$

The Q^2 dependence shown in equation 2.37 is entirely contained within the vector meson propagator. The VDM cross sections are given separately for the cases of

transversely and longitudinally polarised photons:

$$\sigma_T^{\gamma^* p}(Q^2, W) = \sum_V \frac{e}{f_V^2} \left(1 + \frac{Q^2}{M_V^2}\right)^{-2} \sigma_T^{Vp}(W) \tag{2.39}$$

$$\sigma_L^{\gamma^* p}(Q^2, W) = \sum_V \frac{e}{f_V^2} \left(1 + \frac{Q^2}{M_V^2}\right)^{-2} \xi_V^2 \frac{Q^2}{M_V^2} \sigma_T^{Vp}(W) \tag{2.40}$$

where σ_T^{Vp} denotes the total cross section for the production of the transversely polarised vector meson. The ξ_V^2 factor is introduced to account for the fact that the longitudinal Vp cross section need not be the same as the transverse one. Appropriately, ξ_V^2 represents the ratio between the two cross sections and according to the VDM it is predicted to be $\mathcal{O}(1)$ [24]. Experimental results on ρ^0 production however, indicate that the ratio is actually lower [25], [26]. Equation (2.40) asserts that the longitudinal cross section vanishes at $Q^2 = 0$, i.e. for real photons.

The vector meson dominance model gives the relation between the total virtual photoproduction and the real photoproduction cross sections:

$$\sigma^{\gamma^* p}(Q^2, W) = \left(1 + \epsilon \xi_V^2 \frac{Q^2}{M_V^2}\right) \left(1 + \frac{Q^2}{M_V^2}\right)^{-2} \sigma^{\gamma p}(W) \tag{2.41}$$

where $\epsilon = \frac{\Gamma_L}{\Gamma_T}$ is the ratio of longitudinal and transverse photon flux. The VDM prediction of the ratio between the longitudinal and transverse photoproduction cross section:

$$R = \frac{\sigma_L}{\sigma_T} = \xi_V^2 \frac{Q^2}{M_V^2} \tag{2.42}$$

is given by taking the ratio of equations 2.39 and 2.40.

2.8 Regge Theory

Regge theory, used in particle physics, shows that it is useful to regard the angular momentum l as a complex variable and relies on the idea of the analytical continuation of the scattering amplitude into the complex angular momentum plane [27]. So-called Regge Poles, the singularities in the scattering amplitudes found in the complex plane, correspond to either bound states or resonances depending on the

angular momentum.

In Regge theory, an incoming particle of momentum p can be regarded as an outgoing antiparticle of momentum $-p$. This is referred to as crossing symmetry and is depicted in figure 2.10.

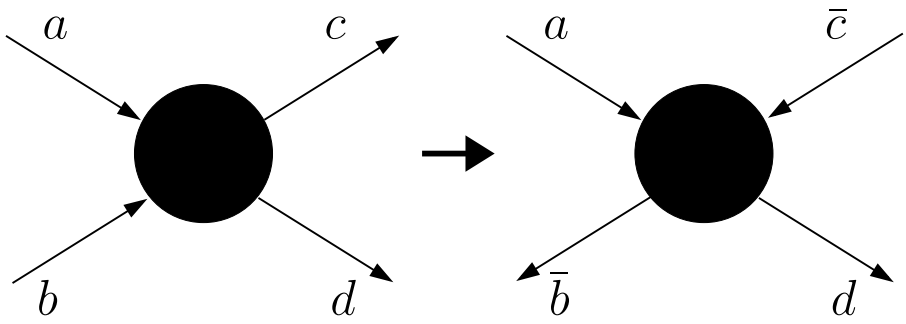

Figure 2.10: The reaction $a + b \to c + d$ and its crossed equivalent $a + \bar{c} \to \bar{b} + d$.

The reaction

$$a(p_a) + b(p_b) \to c(p_c) + d(p_d) \tag{2.43}$$

has a squared centre of mass energy and squared four-momentum transfer

$$\begin{aligned} s &= (p_a + p_b)^2 > 0 \\ t &= (p_a - p_c)^2 < 0 \end{aligned} \tag{2.44}$$

where the scattering angle is related to t. Obtaining the equivalent crossed reaction requires reversing the charge and momenta of a particle on the left and right hand sides; appropriately, the crossed reaction

$$a(p_a) + \bar{c}(-p_c) \to \bar{b}(-p_b) + d(p_d) \tag{2.45}$$

has squared centre of mass energy and squared four-momentum transfer

$$\begin{aligned} s &= (p_a - p_c)^2 > 0 \\ t &= (p_a + p_b)^2 < 0 \end{aligned} \tag{2.46}$$

where again the scattering angle is related to t. The kinematic variables t and s of the first reaction (relation 2.43) correspond to the squared centre of mass and four-momentum transfer respectively of the crossed reaction (relation 2.45). The first reaction is referred to as an s channel reaction, while the second is its t channel counterpart. Despite each reaction taking place in non-overlapping kinematical regions in s and t, both are described by the same amplitude.

Through a representation depicted by the so-called Chew-Frautschi plots, Regge theory introduces the idea of Regge trajectories; those hadronic states possessing the same quantum numbers will form such a straight line trajectory, when the spin of each state is plotted against the square of its mass. Appropriate to the description of a straight line, a Regge trajectory is parameterised as:

$$\alpha(t) = \alpha(0) + \alpha' t \tag{2.47}$$

with $\alpha(0)$ the intercept and α' the slope of the trajectory. Figure 2.11 shows a Chew-Frautschi plot for the reaction $\pi^- p \to \pi^0 n$. The experimentally obtained results of diffractive scattering processes are added to the Chew-Frautschi plot and equation 2.47 is fit to the measured data. The parity transfer in the reaction $\pi^- p \to \pi^0 n$ is positive and is given by $\Delta P = (-1)^J P$ with J and P the angular momentum and parity of the object exchanged in the t-channel. Conservation of the relevant quantum numbers requires the reaction to proceed via ρ, a_2 and ρ_3 exchange, with $J^P = 1^-, 2^+, 3^-$, all of which lie on the Regge trajectory passing through the measured points. This Regge trajectory is almost identical to the ω/f trajectory also shown.

Regge theory gives the total cross section as

$$\sigma_{tot} \propto s^{\alpha(t=0)-1} \tag{2.48}$$

meaning that at high centre of mass energies s, the behaviour of the total cross section is dominated by the highest lying Regge trajectories, corresponding to the ρ/a_2 and ω/f trajectories in figure 2.11. The measurement of their intercepts at $\alpha_{\rho,\omega}(0) \approx 0.5$ requires that the total cross section behaves according to $\sigma_{tot} \propto s^{-\frac{1}{2}}$, conflicting with the observed behaviour of the hadron-proton scattering total cross section at high energy which remains approximately constant with energy and exhibits a slow rise above ~ 10 GeV. A Regge trajectory which reflects this behaviour requires $\alpha(0) \approx 1$, while all known particles have $\alpha(0) < 1$ and the exchanged

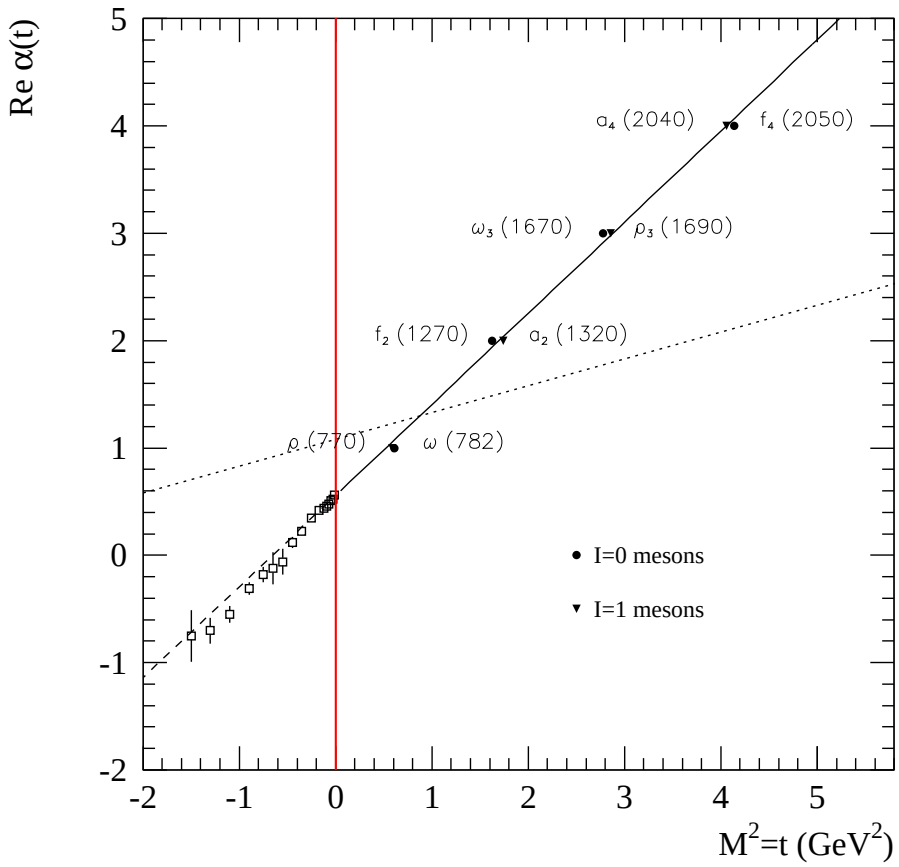

Figure 2.11: Chew-Frautschi plot showing two different Regge trajectories corresponding to natural parity exchange. The solid line is obtained by fitting equation 2.47 to experimentally obtained meson points. The dashed line extending from the solid line is the backwards extrapolation of the fit to $t < 0$, the data points in which region were obtained from $\pi^- p \to \pi^0 n$ scattering data [28]. The dotted line represents the trajectory corresponding to Pomeron exchange.

particle needs to have the quantum numbers of the vacuum. The so-called Pomeron trajectory satisfies these requirements and is parameterised as:

$$\alpha_{\mathbb{P}} = 1 + \epsilon + \alpha'_{\mathbb{P}} t \tag{2.49}$$

where $\alpha_{\mathbb{P}}(0) = 1 + \epsilon$ and $0 < \epsilon \ll 1$. Assuming that vector meson cross sections exhibit the typical behaviour of hadron-hadron cross sections, the intercepts of the Regge and Pomeron trajectories can be described by the sum of two terms:

$$\sigma_{tot} = X s^{\epsilon} + Y s^{-\eta} \tag{2.50}$$

where X and Y are arbitrary normalisations. The exponents ϵ and η refer to Pomeron and Reggeon exchange respectively and can be determined from fits to

experimental data. Appropriately, the first term corresponds to Pomeron exchange while the second term corresponds to the highest lying Regge trajectory. The exponents are assumed to be independent of the interacting hadrons and X and Y depend on the specific process. The values for the exponents, $\epsilon = 0.0808$ and $\eta = 0.4525$ were determined by Donnachie and Landshoff [29] by applying a fit to pp and $p\bar{p}$ data at $\sqrt{s} > 10$ GeV.

2.9 The Donnachie and Landshoff Model

Donnachie and Landshoff obtain the total ρ^0 real photoproduction cross section by combining their Regge type fits of hadron-hadron cross sections with the additive quark model and vector meson dominance model. This was determined to be

$$\sigma_{tot}^{\rho^0 p} = 13.6 s^{0.0808} + 31.8 s^{-0.45}. \tag{2.51}$$

Although this result describes the behaviour of the cross section with energy well, the absolute magnitude is $\sim 15\%$ higher than measured values. The discrepancy arises from the insertion of the $\gamma - V$ coupling constant f_{ρ^0} into the model, which is related to e^+e^- decay. Measurements of vector meson photoproduction show a larger coupling constant, its use with the Donnachie and Landshoff fits in the $9 < W < 18$ GeV kinematic region provides a much better agreement with the data [30].

2.10 The Manayenkov Model

Manayenkov combines a light-cone wavefunction description of the $\gamma^* \to q\bar{q}$ dissociation amplitude and a Reggeon exchange formalism describing the scattering of the meson from the nucleon [43]. The production of the final vector meson state from the scattered $q\bar{q}$ is calculated with the aid of the parton-hadron duality concept.

The model reproduces cross sections with good accuracy at $W > 4$ GeV where Regge theory applies. Predictions of the ratio of longitudinal to transverse production cross section agree reasonably with world data at $Q^2 < 4$ GeV^2, where pQCD loses some of its predictive power. This approach fails, however, at higher Q^2 where pQCD describes the data well.

2.11 Generalised Parton Distributions

The recent introduction of Generalised Parton Distributions (GPDs), often referred to as off-forward or skewed parton distributions, is the result of efforts to unite the form-factor based study of the structure of the nucleon with the usual parton densities. Both formalisms are now known to be limiting cases and moments of GPDs. GPDs have received special attention since Ji's discovery that the second moment of two unpolarised quark GPDs is related to the gauge invariant total quark angular momentum [4]. For the first time, this discovery offers a way to derive the orbital angular momentum carried by quarks in the nucleon.

Inclusive DIS, $ep \to eX$ provides a convenient starting point to introduce some of the concepts associated with GPDs. In the Bjørken limit where both the photon virtuality $Q^2 = -q^2$ and the squared hadronic centre of mass energy $(p+q)^2$ become large at fixed $x_{Bj} = Q^2/(2p \cdot q)$, the reaction amplitude factorises into a hard scattering part, calculable in perturbative QCD, and a parton distribution representing the probability of finding a parton with momentum fraction x.

The meaning of the relationship of GPDs to parton distribution functions is best elucidated using virtual Compton scattering as an example, as depicted in figure 2.12(a). Here, no momentum is transferred between the left and right hand sides of the diagram ($t = 0$). The optical theorem links the imaginary part of the Compton amplitude $\gamma^* p \to \gamma^* p$ to the inclusive $\gamma^* p$ cross section.

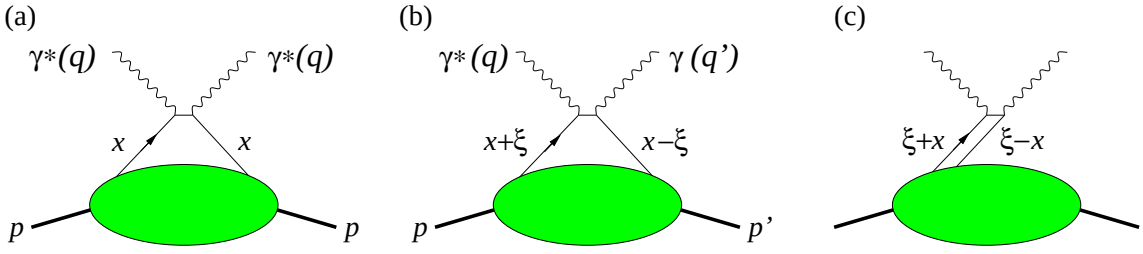

Figure 2.12: (a) The Born level diagram of the forward Compton amplitude, the imaginary part of which gives the DIS cross section. The blob denotes the quark and antiquark distributions in the proton. (b) The Born diagram for deeply virtual Compton scattering in the region $\xi < x < 1$. In this case the blob is described by GPDs. (c) The same in the region $-\xi < x < \xi$. In each case, a second diagram may be obtained by exchanging photon vertices [31].

The factorisation of the dynamics into short (pQCD) and long (PDF, GPD) range components is also applicable in the case where there is a finite momentum transfer to the target for large Q^2. Deeply virtual Compton scattering $ep \to e\gamma p$ (DVCS), depicted in figure 2.12(b), is an example of such a process. DVCS is the exclusive

reaction in which the nucleon absorbs a virtual photon and produces a real photon, leaving the target nucleon intact, and is one method of gaining access to GPDs.

Exclusive meson production, where the outgoing real photon in the DVCS handbag diagrams is replaced with a vector or pseudoscalar meson, is another reaction allowing access to GPDs. Where the meson quantum numbers permit, the gluon GPDs enter at the same order in α_s, the strong coupling constant, as those for quarks. Figure 2.13 illustrates this.

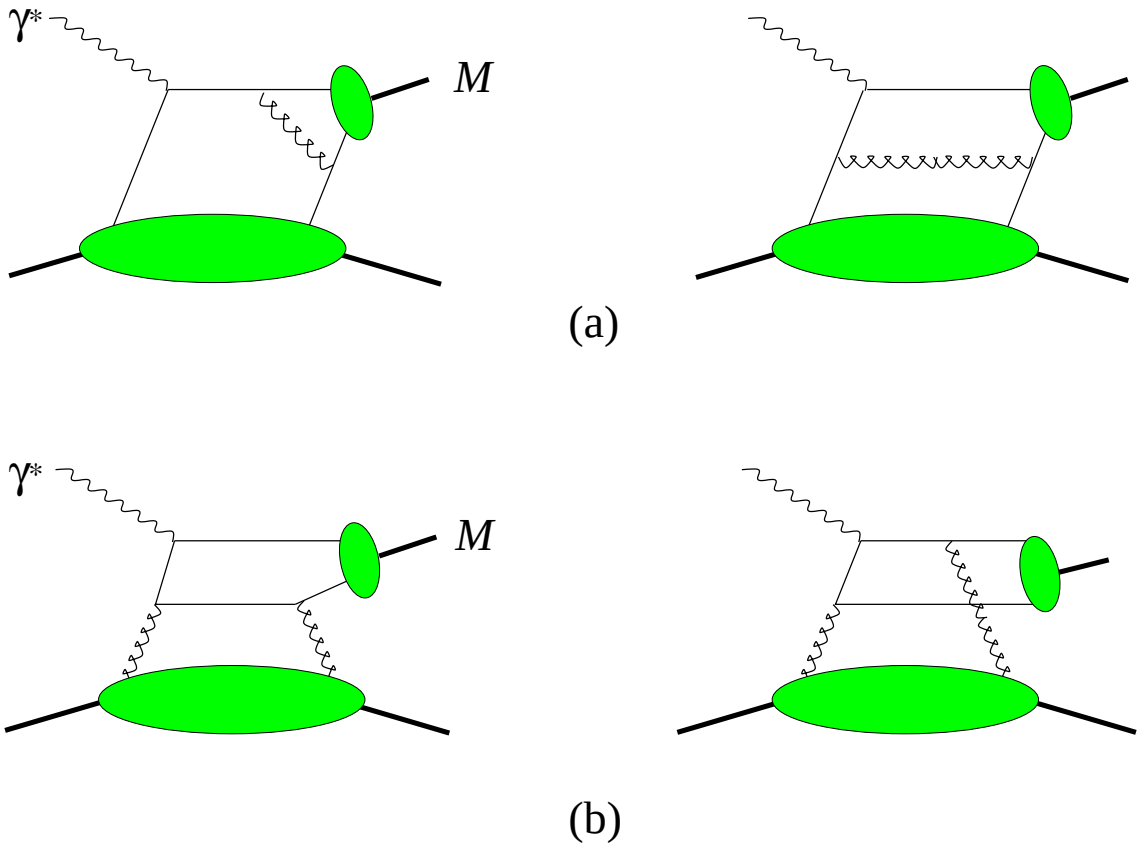

Figure 2.13: Diagrams of hard meson production showing the quark (a) and gluon (b) contributions [31].

The nucleon structure information contained in these handbag diagrams can be parameterised in leading order QCD in terms of the quark chirality conserving GPDs H^q, $\tilde{H}^q$, E^q and $\tilde{E}^q$ for each quark flavour $q = (u, d, s)$. The properties of each GPD are listed in table 2.1. In addition to the variable x, the GPDs depend on the invariant momentum transfer t and the so-called skewedness parameter $\xi = -\Delta^+/2p^+$, which is the light-cone momentum fraction transferred to the target nucleon. This notation was adopted from that used in the formalism of light front dynamics [32] in which a particle with four-momentum $p^\mu = (p^0, p^1, p^2, p^3)$ can be represented in a system with momentum along the p^3 axis approaching ∞, such

that:

$$p^{\pm} = p^0 \pm p^3 = constant. \tag{2.52}$$

This notation is particularly convenient for use with reactions such as DIS as momentum transfers can be represented by simple Lorentz boosts. Additionally, at high nucleon momenta the transverse and longitudinal components are naturally separated.

GPD	Properties	Association
$H^q(x,\xi,t)$	Unpolarised distribution Nucleon helicity conserving Access via DIS	Electromagnetic interaction
$\tilde{H}^q(x,\xi,t)$	Polarised distribution Nucleon helicity conserving Access via DIS	Weak interaction
$E^q(x,\xi,t)$	Unpolarised distribution Nucleon helicity flip No access via DIS	Electromagnetic interaction
$\tilde{E}^q(x,\xi,t)$	Polarised distribution Nucleon helicity flip No access via DIS	Weak interaction

Table 2.1: Properties of the four quark chirality conserving GPDs.

As depicted in figure 2.14, in the forward limit where $t \to 0$, $\xi \to 0$

$$\begin{aligned} H^q(x,0,0) &= q(x) \\ \tilde{H}^q(x,0,0) &= \Delta q(x) \end{aligned} \tag{2.53}$$

the GPDs reduce to the usual quark unpolarised and polarised PDFs. This is not the case for E and $\tilde{E}$ which are inaccessible in DIS since these tensors disappear in the forward limit. For equation 2.53, $-1 \leq x \leq 1$ and negative values of x correspond to antiquark distributions according to:

$$\begin{aligned} q(-x) &= -\bar{q}(x) \\ \Delta q(-x) &= \Delta\bar{q}(x). \end{aligned} \tag{2.54}$$

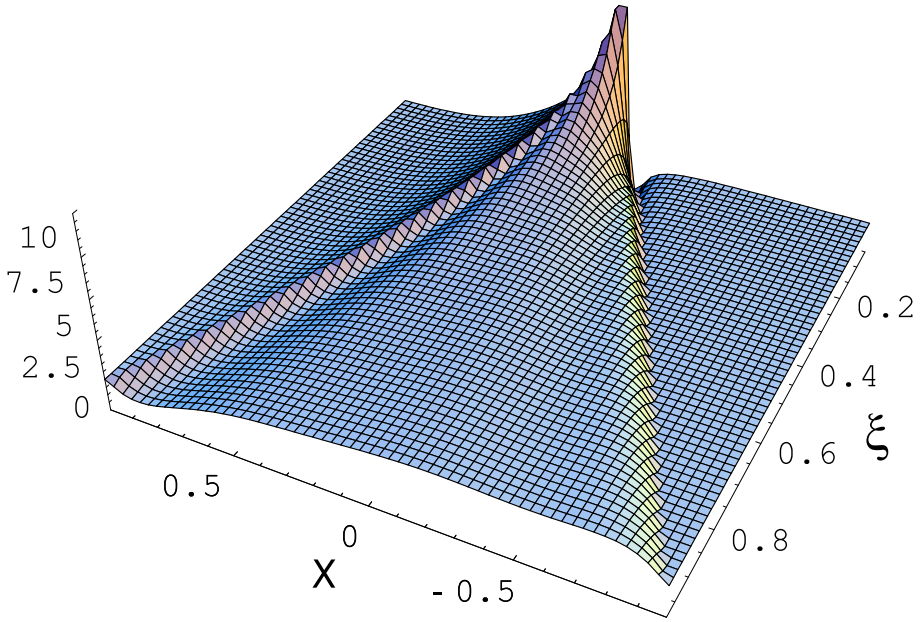

Figure 2.14: The unpolarised up quark GPD $H^u(x,\xi,t=0)$ [33]. At $\xi = 0$ the GPD reduces to the ordinary up quark PDF.

The first moments of the GPDs simplify to the flavour-dependent form factors [4,34]:

$$\begin{aligned}
\int_{-1}^{1} dx H^q(x,\xi,t) &= F_1^q(t) \\
\int_{-1}^{1} dx E^q(x,\xi,t) &= F_2^q(t) \\
\int_{-1}^{1} dx \tilde{H}^q(x,\xi,t) &= g_A^q(t) \\
\int_{-1}^{1} dx \tilde{E}^q(x,\xi,t) &= h_A^q(t)
\end{aligned} \tag{2.55}$$

where $F_1(t)$ and $F_2(t)$ are the Dirac and Pauli form factors and $g_A(t)$ and $h_A(t)$ are the axial vector and pseudoscalar form factors which arise in weak, rather than electromagnetic, currents. The second moments of the unpolarised GPDs at $t = 0$ give:

$$\frac{1}{2}\int_{-1}^{1} dx x \left[H^q(x,\xi,0) + E^q(x,\xi,0)\right] = \frac{1}{2}\Delta\Sigma + L_q = J_q \tag{2.56}$$

where $\frac{1}{2}\Delta\Sigma$ and L_q are the quark spin and orbital angular momentum contribution to the nucleon spin. As the former quantity is also accessed in polarised DIS measurements, the measurement of the sum rule (equation 2.56) leads to the deter-

mination of the quark orbital momentum contribution to the total quark angular momentum. The relation

$$\frac{1}{2} = J_q + J_g \tag{2.57}$$

may subsequently lead to the total gluon angular momentum J_g. As equation 2.56 includes only unpolarised GPDs, the nucleon spin information can, in principle, be accessed without a polarised beam or target via DVCS and exclusive meson production.

2.12 Quark and Gluon Distributions

For the exclusive process $\gamma^* p \rightarrow \rho p$ in the limit of large Q^2 and fixed x_{Bj} and t the longitudinal scattering amplitude factorises into a hard scattering kernel, generalised quark or gluon distributions and the light-cone distribution amplitude of the produced meson [35] as depicted in figure 2.15. Additional factors arise from power-suppressed corrections.

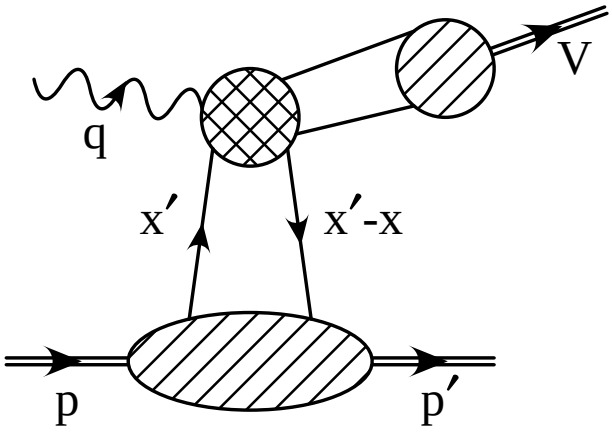

Figure 2.15: Factorisation theorem in exclusive vector meson electroproduction. The rightmost circle represents the meson distribution amplitude, the leftmost circle represents the hard scattering part and the lower blob represents the Generalised Parton Distribution [35].

To leading order in α_s the hard scattering term in the ρ^0 production amplitude from a proton is equal to that from a neutron. The meson distribution amplitude, describing a ρ^0 in both cases, is also equal. The ratio [31, 36] of ρ^0 production amplitudes in scattering from a neutron and a proton target, adopting the light-cone notation given in section 2.11, is:

$$\begin{aligned} \mathcal{A}^{n}_{\rho^0} : \mathcal{A}^{p}_{\rho^0} &= \int_{-1}^{1} \frac{dx}{\xi - x - i\epsilon} \left(\frac{F^{u(+)} + 2F^{d(+)}}{\sqrt{2}} + \frac{9}{4\sqrt{2}} \frac{F^{g}}{x} \right) \\ &: \int_{-1}^{1} \frac{dx}{\xi - x - i\epsilon} \left(\frac{2F^{u(+)} + F^{d(+)}}{\sqrt{2}} + \frac{9}{4\sqrt{2}} \frac{F^{g}}{x} \right) \end{aligned} \tag{2.58}$$

where $F^{q(+)} = F^{q}(x,\xi,t) - F^{q}(-x,\xi,t)$ and $F^{q(g)}$ are related to the quark (gluon) GPDs by:

$$F^{q(g)} = \frac{1}{2P^{+}} \left[H^{q(g)}(x,\xi,t)\bar{u}(p')\gamma^{+}u(p) + E^{q(g)}(x,\xi,t)\bar{u}(p')\frac{i\sigma^{+\alpha}\Delta_{\alpha}}{2m}u(p) \right] \tag{2.59}$$

where $P = \frac{p+p'}{2}$, u and $\bar{u}$ are the nucleon spinor and its complex conjugate, m is the nucleon mass and $\Delta = p' - p$. Equation 2.58 demonstrates that to $\mathcal{O}(\alpha_s)$, the ρ^0 meson production amplitude ratio on neutrons versus protons depends only on the neutron and proton GPDs.

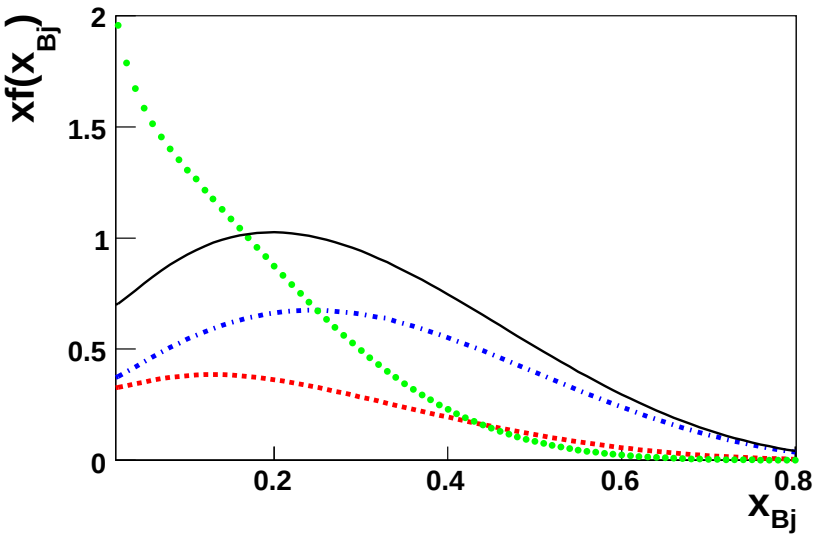

Figure 2.16: Proton PDF as a function of x_{Bj} calculated using MRST2001LO parameterisation at $Q^2 = 1.5$ GeV^2. The solid curve (black) is the total quark PDF $q(x_{Bj})$, the dotted curve (green) is the gluon PDF $g(x_{Bj})$. The alternating dashed and dotted (blue) curve shows the up quark PDF, and the dashed (red) curve shows the down quark PDF.

From the behaviour of the usual quark and gluon densities, it is expected that ρ^0 production is dominated by gluons at very small x_{Bj} and quarks at very large x_{Bj} [37], and it is natural to ask where the transition between those two regimes

takes place. Analyses of Deep Inelastic Scattering have been performed from leading order (LO) to next-to-next-to-leading order (NNLO) by groups such as CTEQ [38], GRV [39], MRST [40] and ALEKHIN [41]. The MRST NLO and NNLO PDFs are based on a 2001 LO analysis for which theoretical calculations of ρ^0 production cross section ratios on deuterium versus hydrogen are available. Using the MRST2001LO parameterisation, the PDF for the proton is shown in figure 2.16. The nucleon PDFs are used as an input to the GPD calculation which is described in reference [42].

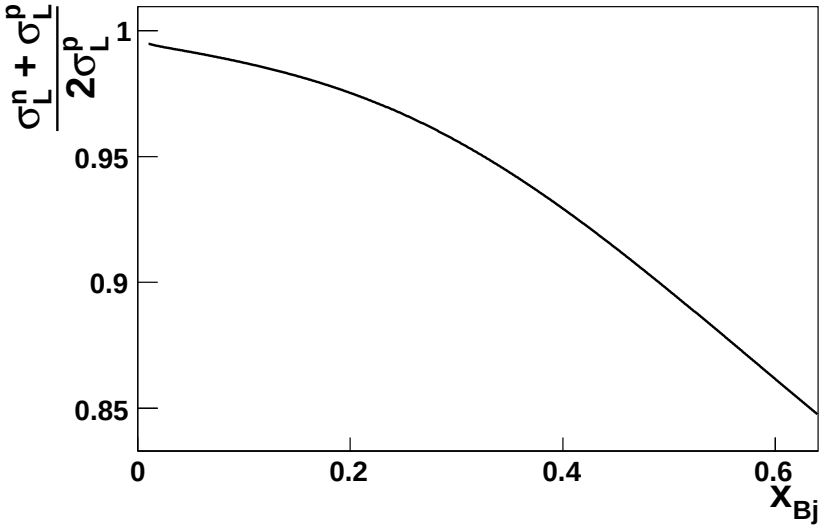

Figure 2.17: Longitudinal cross section ratio of ρ^0 meson production on deuterium versus hydrogen, calculated for $Q^2 > 1.5$ GeV^2 with MRST2001LO parameterisation as input to the GPDs [42].

Previous analyses have indicated that quarks and gluons contribute to the ρ^0 cross section with comparable strength at $x_{Bj} \approx 0.1$ [37]. This is consistent with the point at which $q(x_{Bj}) = g(x_{Bj})$ in figure 2.16. Equation 2.58 suggests that the gluon contribution to the scattering amplitude is the same for protons and neutrons. It is then expected that the ρ^0 production cross section ratio from a deuterium and hydrogen target should be $\simeq 2$ at very low x_{Bj} and fall off at increasing x_{Bj}. The behaviour of the cross section ratio has been predicted using the MRST2001LO parameterisation and is depicted in figure 2.17. This behaviour is reflected in the HERMES experimental data; the results are detailed in section 6.6.5.

2.13 Perturbative QCD Models

While Regge theory describes vector meson production adequately at low $|t|$, the formalism fails for hard processes in the regions of high Q^2 and $|t|$. Perturbative QCD models provide a good description of the data when the hard scale sets in. Section 2.12 introduces the idea of factorising the vector meson production amplitude into perturbative and non-perturbative components.

2.13.1 The Model of Goloskokov and Kroll

Goloskokov and Kroll introduced an approach based on the gluon GPD H^g to describe light vector meson electroproduction at low x_{Bj} [44]. H^g parameterises the response of the proton to the emission and reabsorption of gluons and thus controls the process. The present indeterminability of H^g requires an ansatz based on double distributions to construct the GPD and the electroproduction amplitudes are calculated at $t \approx 0$ then multiplied by an exponential factor dependent on t.

This approach produces results which are consistent with low x_{Bj} data on ρ and ϕ meson electroproduction measured by H1 and ZEUS for $Q^2 > 4$ GeV^2 and promises to enable studies of t dependence of electroproduction, if the t dependence of GPDs can be better understood. This approach must be improved when more detailed cross section data become available.

Chapter 3

The HERMES Experiment

The HERMES (HERa MEasurement of Spin) spectrometer located at the DESY (Deutsches Elektronen SYnchrotron) facility in Hamburg has, since 1995, measured scattering reactions from polarised lepton beams on polarised or unpolarised gas targets of various types. Presented in this chapter is the description of its experimental setup, including external components such as the HERA storage ring and the spin rotators required to achieve longitudinal beam polarisation.

3.1 The HERA Synchrotron

The 6.3 km circumference HERA storage ring is comprised of two separate accelerators 10 to 25 m underground which provide the polarised lepton and proton beams for the three experiments currently operating at DESY; H1, ZEUS and HERMES. HERMES is the only remaining fixed-target experiment and makes use of the lepton beam, which contains either electrons or positrons at 27.5 GeV. The collider experiments H1 and ZEUS also make use of the 920 GeV proton beam orbiting in the opposite direction, which is brought into collision with the lepton beam at interaction points located within the experiments. Despite the original intention for HERA's lepton beam to contain only electrons, the accumulation of positively charged dust along the beam path restricted the electron beam lifetime via Bremsstrahlung losses and thus HERA was operated solely as a positron/proton accelerator during the 1995-1997 period. A vacuum system upgrade in 1998 re-enabled running with electrons and so charge dependent electroweak processes could be studied at the higher energy regions accessible by H1 and ZEUS.

The lepton beam is divided into 189 bunches ordered in three bunch trains and

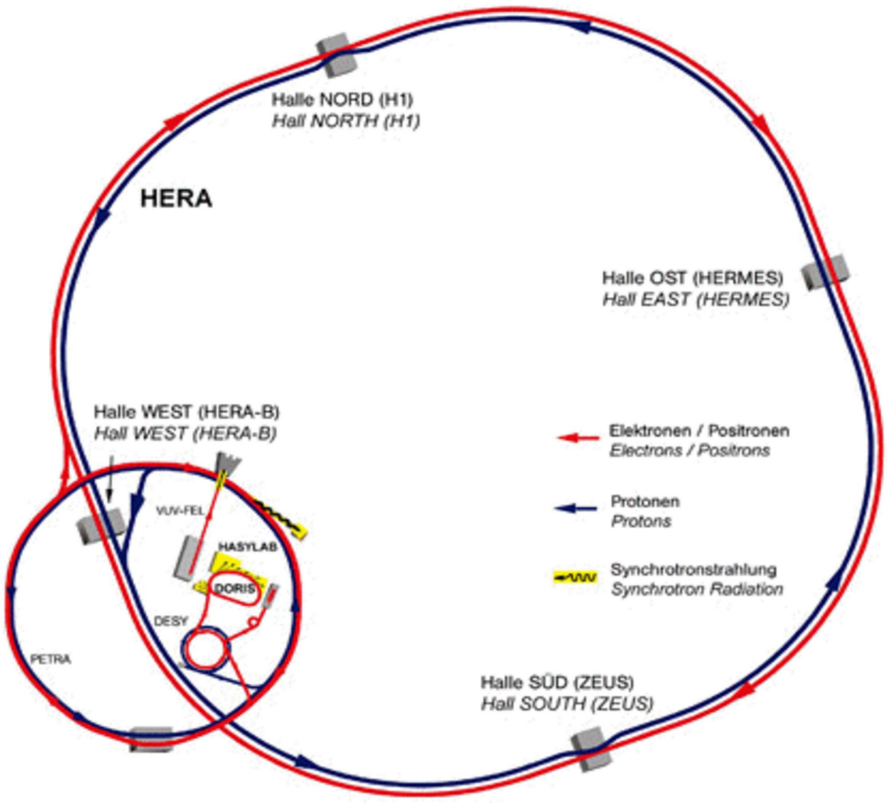

Figure 3.1: The DESY accelerators, also shown is the decommissioned fixed-target experiment HERA-B.

separated by 96 ns, each with a length of 27 ps (8 mm). Every eleventh bunch is known as a pilot bunch and is used to monitor and tune the beam parameters, their bunch timing having been configured to avoid collision with the proton beam. Average beam lifetime is around 10 hours for the lepton beam whereas the proton beam has a lifetime exceeding 2000 hours but is dumped at the end of every fill.

Unpolarised protons and leptons are injected into HERA by the PETRA preaccelerator, which in turn requires beams supplied by the smaller booster rings and linear accelerators (figure 3.1).

Transverse lepton beam polarisation is achieved spontaneously via the Sokolov-Ternov effect [45]; electrons and positrons deflected by the magnets in the storage ring emit synchrotron radiation with a dependence on the lepton's initial spin state. The emission of synchrotron radiation is known to possess an asymmetry in its small spin-flip amplitude, while the emission associated with a spin-flip is strongly suppressed, the effect accumulates over successive orbits and leads to a large overall

polarisation. The polarisation P is defined as

$$P = \frac{N\downarrow - N\uparrow}{N\downarrow + N\uparrow} \tag{3.1}$$

where $N\uparrow$ ($N\downarrow$) denotes the number of leptons with their spins aligned parallel (antiparallel) to the vertical field supplied by the bending magnets. The rise in polarisation has an exponential time dependence in accordance with

$$P(t) = P_{ST} \cdot (1 - e^{-\frac{t}{\tau_{ST}}}) \tag{3.2}$$

where P_{ST} is the asymptotic maximum polarisation value (92%) which corresponds to the asymmetry in the spin-flip amplitude, and the characteristic polarisation rise time is given by

$$\tau_{ST} = P_{ST} \frac{m_e}{\hbar c^2 r_e} \frac{\rho^3}{\gamma^5} \tag{3.3}$$

where ρ is the bending radius in the magnetic field, r_e denotes the classical electron radius and $\gamma = \frac{E}{m_e}$, with the beam energy E and the electron mass m_e. Under ideal conditions and according to equation 3.3 the polarisation rise time at HERA is around 40 minutes. Magnetic field inhomogeneities, stray off-vertical field components and the presence of magnets with configurations besides dipoles, however, give rise to depolarisation effects which impose a limit on the polarisation to values below P_{ST}. Additional contributions to depolarisation arise from spin diffusion [46], interactions between lepton and proton beams and magnet misalignments.

Obtaining the effective polarisation rise time for HERA requires combining depolarisation effects with the Sokolov-Ternov effect. Expressing the result of this combination as a time constant τ_D, the effective maximum asymptotic polarisation P_{max} and effective rise time constant τ are given by

$$P_{max} = P_{ST} \frac{\tau_D}{\tau_{ST} + \tau_D}, \tag{3.4}$$

$$\tau = \tau_{ST} \frac{\tau_D}{\tau_{ST} + \tau_D}. \tag{3.5}$$

Typical beam polarisation at HERA reaches around 60% in $\tau \approx 25$ minutes, values as high as 70% have been measured.

Some of the physics of interest to HERMES requires a longitudinally polarised beam interacting with the target. Longitudinal polarisation is achieved by placing two spin

rotators in front of and behind the spectrometer (figure 3.2).

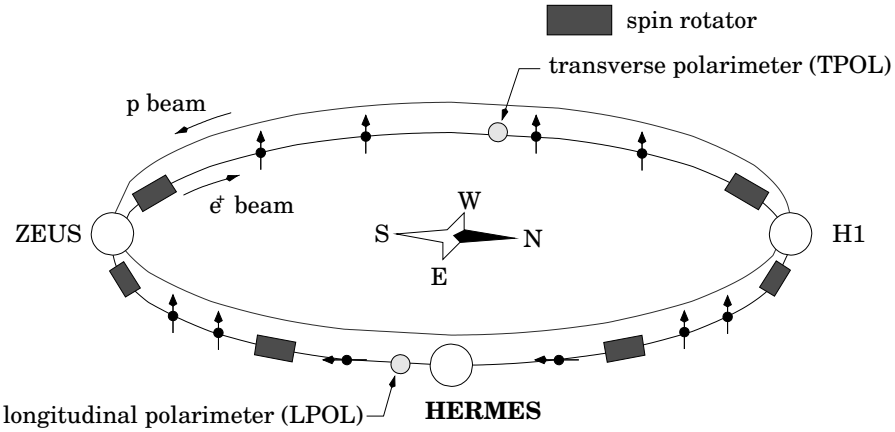

Figure 3.2: The HERA ring showing the positions of the spin rotators with the HERMES spectrometer in between.

The polarisation of the leptons is modified through small successive angular deflections of the beam direction by horizontal and vertical dipole magnets leading to a corresponding rotation about the spin axis. Figure 3.3 illustrates this process.

3.2 The HERMES Target

The HERMES experiment uses an internal gas target which operates in an unpolarised or polarised mode (figure 3.4). Polarised gas is injected into an open-ended storage cell within the beam vacuum. This setup is necessary because rather than operate with a bunch switching system to divert a portion of the beam towards HERMES, the orbit of the HERA lepton beam passes directly through the HERMES spectrometer in the same beam pipe. Thus a low density target must be employed in order to avoid significant losses in beam current.

Also, a polarised gas target enables fast polarisation reversal which reduces systematic uncertainties in the experiment, and ensures a low concentration of spectator nuclei. For polarised operation, the atomic beam source (ABS) separates the spins of dissociated molecular $H2$ with a Stern-Gerlach apparatus and injects the resulting polarised states into the beam vacuum (Figure 3.5). The mix of atomic versus molecular states and target polarisation are monitored by the target gas analyser (TGA) and Breit-Rabi polarimeter (BRP) respectively. To prevent beam-induced depolarisation of the target gas a strong uniform magnetic field over the target region is provided by the target magnet [47]. The ABS is also capable of injecting polarised deuterium into the target cell.

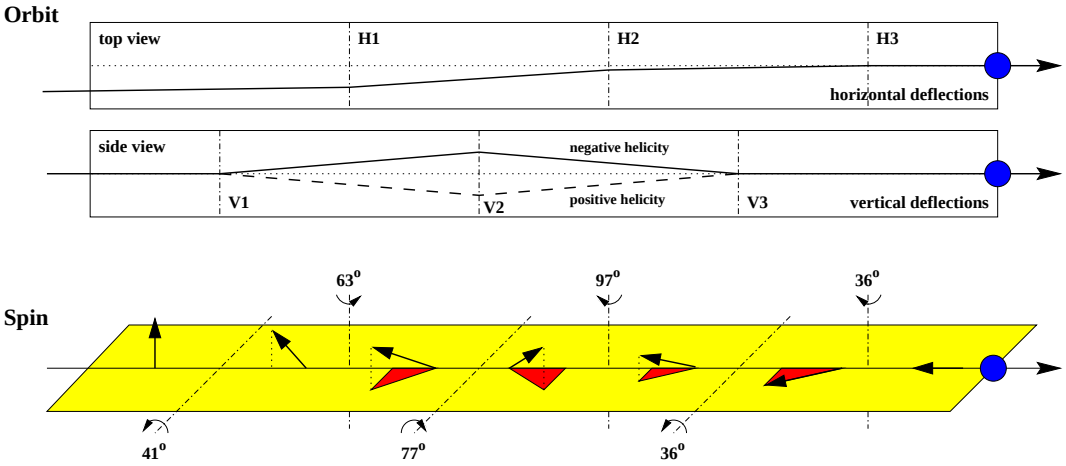

Figure 3.3: Illustration of the principle for rotating spin via sequential beam interactions with horizontal and vertical dipole magnets.

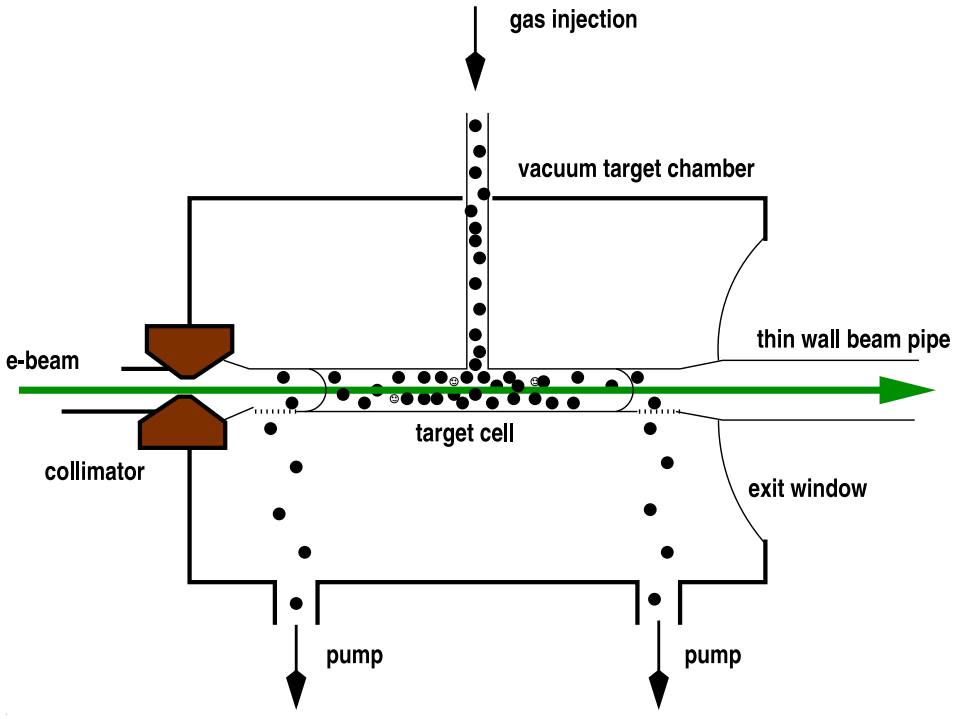

Figure 3.4: HERMES target cell schematic. Vacuum pumps ensure gas is only present within the boundaries of the target cell.

3.2.1 The Unpolarised Gas Feed System (UGFS)

The UGFS injects unpolarised molecular gas in place of the ABS when HERMES is running in the so-called high-density mode. High-density running is enabled during the final hour of each lepton fill after the beam current has dropped from around 30 mA to approximately 10 mA. This mode of operation is due to the requirements from the experiments at HERA running in parallel to HERMES; the beam current must remain above a certain amount in order to allow H1 and ZEUS to operate.

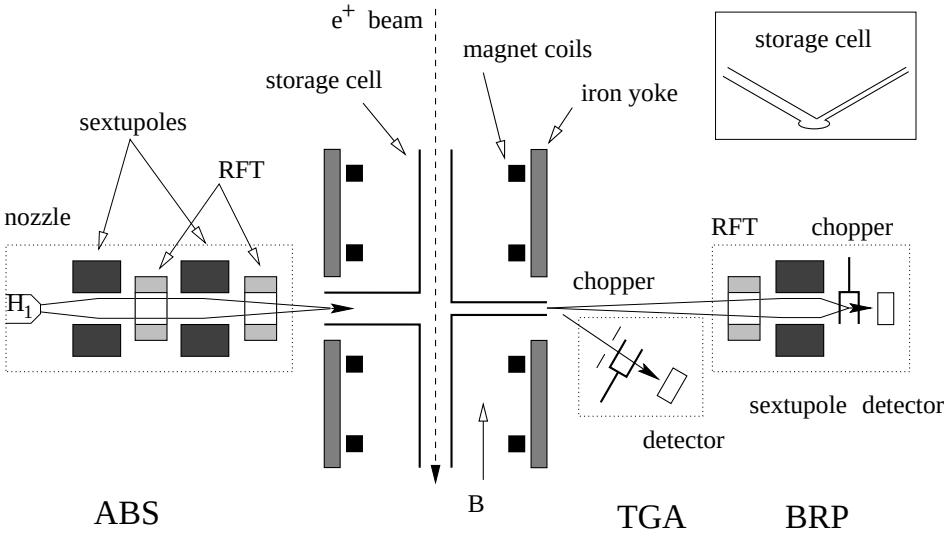

Figure 3.5: Schematic of the HERMES target cell with injection and monitoring apparatus.

The type of gas injected by the UGFS is changed between fills and running periods. The gases used during 2004 were hydrogen, deuterium, helium, nitrogen, krypton, neon and xenon. The density of the injected gases are only limited by the beam lifetime requirements and the HERMES DAQ. This permits the collection of high statistics for analyses of spin-independent processes in a short period of time.

3.3 The HERMES Spectrometer

HERMES makes use of a forward angle spectrometer surrounding the lepton (and proton) beam line to measure leptons and hadrons from scattering reactions, enabling inclusive, semi-inclusive and exclusive analysis of nucleon spin structure. A central horizontal iron plate in the magnet region separates the two symmetric portions of the detector and serves to protect the beam from the magnet's effect. A diagram of the spectrometer is shown in figure 3.6.

The HERMES coordinate system has the z axis pointing along the beam direction, the x axis horizontal and pointing outside the HERA ring and the y axis vertically upwards. Track reconstruction is provided by the spectrometer's front drift chambers (FC), Drift-Vertex Chamber (DVC), back chambers (BC) and proportional chambers (MC) which also help match tracks in the forward and backward regions after deflection by the magnetic field. This deflection is one measure of track momentum, and the magnetic field is supplied by a large spectrometer magnet with 1.3 Tm integrated field strength [48].

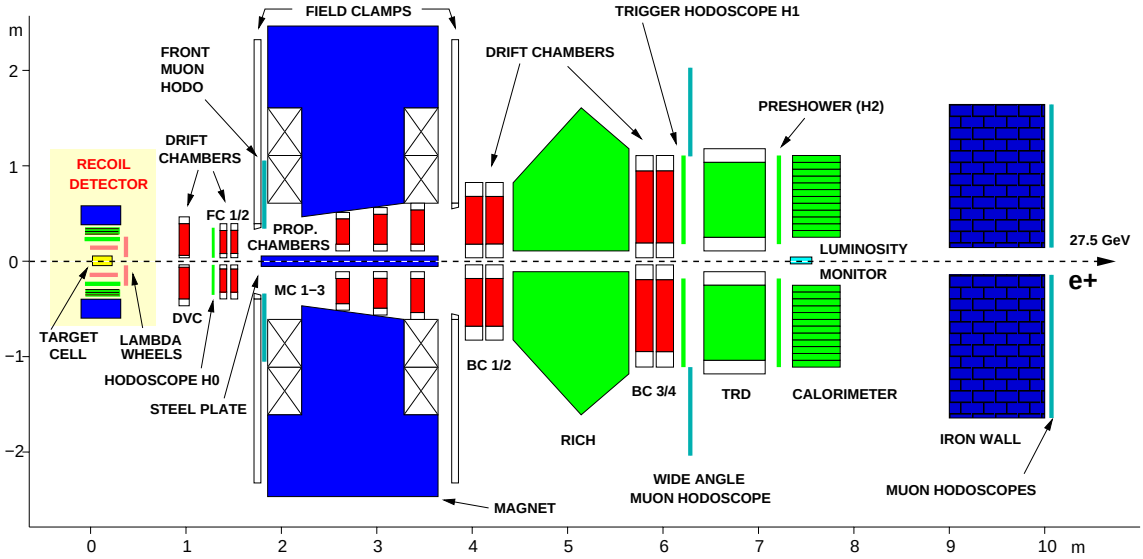

Figure 3.6: Schematic of the HERMES spectrometer, with the Recoil Detector and Lambda Wheel upgrades also shown but not yet used in the present ρ^0 analysis. The PID detectors are shown in light shading (green), the energy deposition measurement instruments are shown in dark shading (blue). Tracking detectors are shown in intermediate shading (red).

The spectrometer also possesses several instruments which provide particle identification (PID). These are the Transition Radiation Detector (TRD) and a threshold Cerenkov counter which in 1998 was replaced by a Ring-Imaging Cerenkov (RICH) detector. The RICH was not used (in its standard mode of operation) in the present ρ^0 analysis, therefore a more detailed description in this chapter will be omitted. Additional PID is provided by the electromagnetic calorimeter (CALO) which also provides an energy measurement for leptons and photons [49], and the H2 hodoscope. Although its primary function is to serve as part of the HERMES trigger system, the H2 hodoscope has a lead curtain placed in front of it which enables its use as a preshower detector.

The standard HERMES trigger for DIS events is provided by a combination of the hodoscopes H0, H1, H2 and the CALO which makes the decision of whether to run the trigger system as a lepton or hadron trigger, depending on the energy deposition. Luminosity is determined by a dedicated monitor (LUMI) which detects Møller and Bhabha scattering events from the beam-target interaction.

3.3.1 Tracking Detectors

The HERMES tracking detectors are categorised according to the regions across which they are split. These are the front, magnet and back regions with the DVC

and FCs at the front region outside the magnetic field, the MCs within the magnet and BCs at its rear. The tracking chambers all possess three wire planes to allow position reconstruction in the x, u and v directions (in their own coordinate systems), enabling resolution of tracking ambiguities arising from coincident track impacts on the detector surfaces. Figure 3.7 illustrates the geometry of the tracking detectors; the x axis points vertically upwards with the u and v components at $\pm 30^\circ$ to the x axis. The restricted horizontal length of the BCs necessitated the geometrically identical construction of the different tracking detectors. This setup has the benefit of permitting the use of fast track reconstruction algorithms [48].

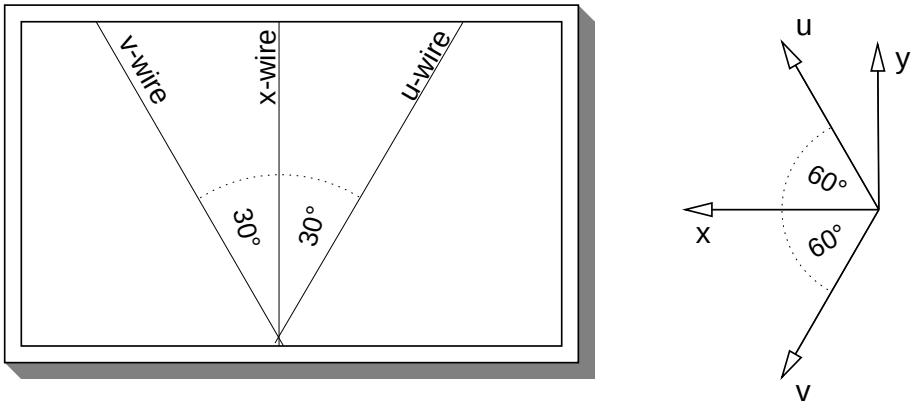

Figure 3.7: Drift chamber wiring scheme and the direction of their projections x, u and v. z points along the beam direction. [50]

All HERMES tracking instruments installed prior to 2002 are two variations on wire chambers which rely on electric field distortion by ionisation [51]; proportional and drift chambers. The HERMES proportional chambers are the MCs and TRD readout chambers and are constructed from arrays of anode wires inside a gaseous medium enclosed by cathode plates. Charged particles traversing the detector ionise the gas and a strong electric field quickly accelerates the resultant electrons towards the anode. The accelerated electrons inelastically collide with other atoms causing further ionisation and subsequent repetitions of this process cause the so-called Townsend Avalanche. Despite the large number of secondary events for each original ion, the chamber is operated such that the number of secondary events is proportional to the number of primary events [52]; this avalanche gives rise to a signal in the anode wire(s) which is read out.

Drift chambers are similar in construction to proportional chambers, the difference being a smaller electric field which is insufficient to create the Townsend Avalanche, and leads to a slower drift of the ions toward the anode. The total electron drift time, in this case, is used to locate the intersection point between the detector and the track. The DVC, FCs and BCs are all drift chambers.

Lambda Wheels

Installed in 2002, the Lambda Wheels (LW) detector system expands the HERMES physics programme by increasing the acceptance of the HERMES spectrometer in the front region, enhancing the reconstruction the tracks from charmed and strange particles such as the Λ^0, Λ_c^+ and J/Ψ [61].

Λ^0 particles decay via the channel $\Lambda^0 \rightarrow p+\pi^-$ (64% branching ratio). The alternate channel is the decay $\Lambda^0 \rightarrow n + \pi^0$. The HERMES standard acceptance is only sufficient to measure the decay proton and scattered beam lepton, at several Λ^0 decay lengths ($c\tau$ = 7.89 cm) downstream from the target. The position of the Lambda Wheel detectors increases acceptance to enable measurement of the pion from the Λ^0 decay [62].

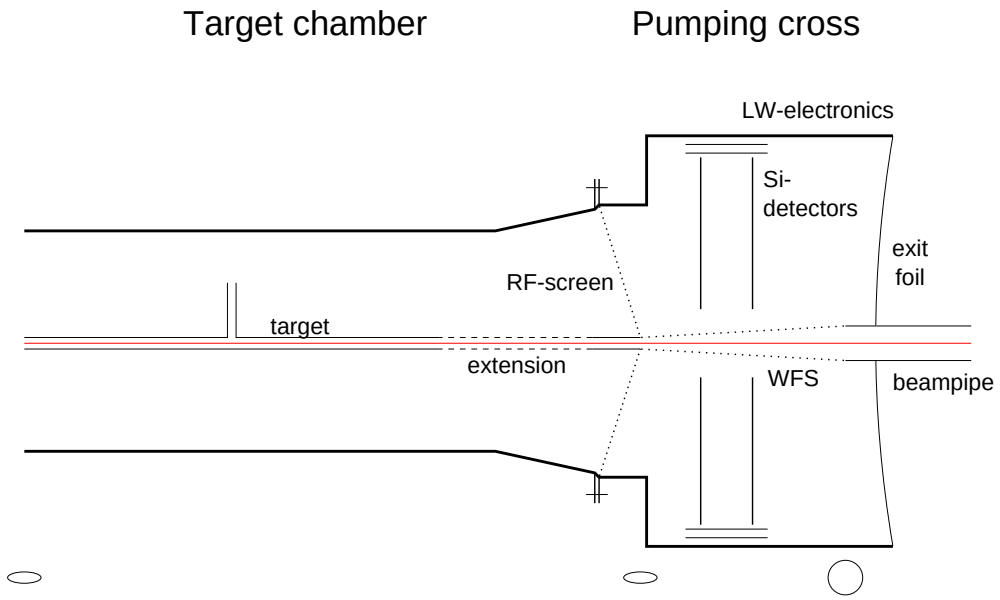

Figure 3.8: Lambda Wheel schematic [62].

Figure 3.8 is a schematic of the region surrounding the target and Lambda Wheels. The detector consists of two wheel shaped silicon planes of diameter 34 cm positioned 45 cm and 50 cm downstream from the target, each divided into 12 identical trapezoidal "paddle"segments (figure 3.9), enabling an 80% acceptance for Λ^0 decay events. Each paddle is a double sided 300 μm thick n-type silicon wafer, with 516 strips on each side oriented parallel to the oblique edges of each paddle, yielding a 93% active surface area.

Charged particles traversing the semiconductor material of the Lambda Wheel detector ionise the material resulting in the formation of electron-hole pairs. An external electric field is applied which causes the positive and negative charges to drift in

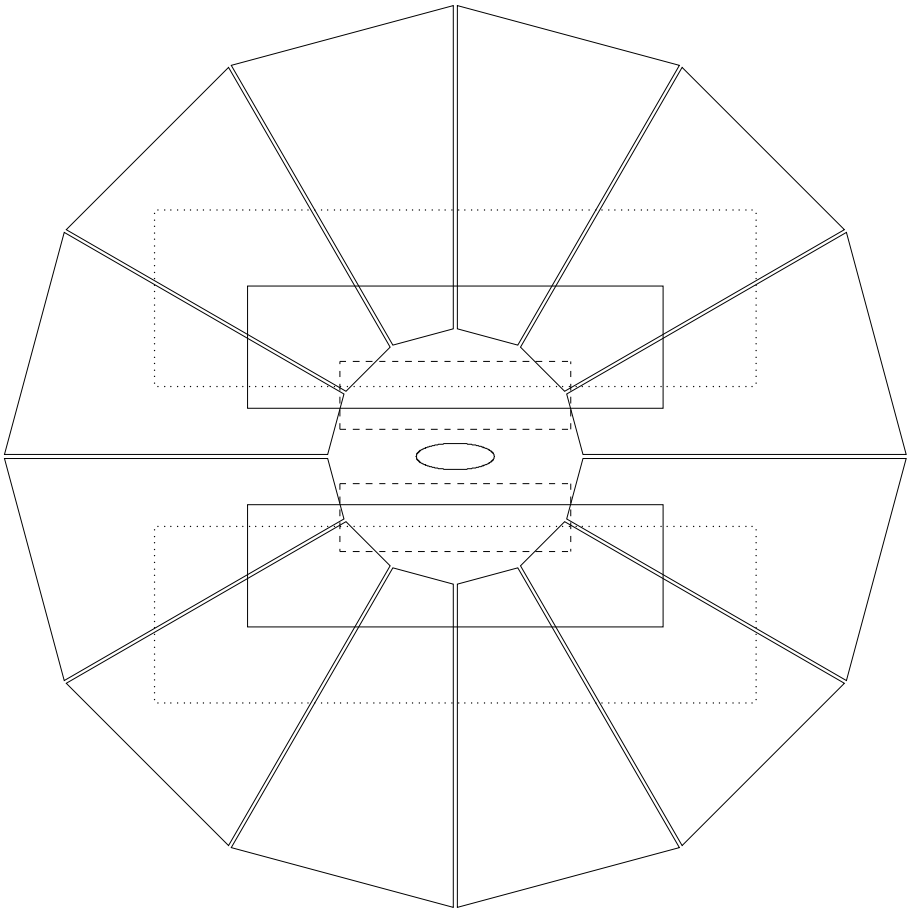

Figure 3.9: Comparison of Lambda Wheel size at $z = 45cm$ with standard HERMES acceptance at $z = 0cm$ (solid box), $z = -20cm$ (dotted box) and $z = 20cm$ (dashed box) [62].

opposite directions to electrodes, whereupon a signal can be read out. In contrast to gas chamber detectors secondary ionisations do not generally occur in a semiconductor; these detectors must possess very specific properties in order to produce a useful signal-to-noise ratio [61].

3.3.2 Particle Identification

The HERMES PID system is capable of discriminating between scattered leptons (electrons/positrons), pions and other hadrons, providing a level of hadronic contamination in the lepton sample below 1% [48]. It consists of several subsystems. Relevant to ρ^0 analysis are the electromagnetic calorimeter, threshold Čerenkov, transition radiation detector and the preshower supplied by the H2 hodoscope. During the years 1998 and 1999 no threshold Čerenkov PID was available as it was replaced by the Ring-Imaging Čerenkov detector. The later productions of 2000 and

productions from subsequent years however, obtained the PID information relevant to the present ρ^0-analysis by relying on the ability of the RICH to operate as a threshold Čerenkov counter simultaneously with its normal operation.

The Electromagnetic Calorimeter and Preshower Detector

The HERMES electromagnetic calorimeter discriminates between hadrons and $e^{\pm}$ by comparing the difference in their ratio of energy deposition to momentum. The construction of the calorimeter is shown in figure 3.10, it is composed of 840 (420 per half) identical lead-glass blocks of length 50cm (18 radiation lengths) and cross-sectional area 81 cm^2 (9×9 cm^2), stacked in two 42×10 arrays [53].

The thickness of the lead-glass blocks allows the calorimeter to fully contain an electromagnetic shower, which is produced by $e^{\pm}$ or photon interactions with the material. In such an interaction, the shower propagates along the material and radiates until the electrons and positrons lose enough energy to preclude further radiation. Subsequent interactions are through atomic ionisation which proceed until the $e^{\pm}$ stops. The ratio of the deposited energy in the calorimeter and prior momentum measurement (with the spectrometer magnet) of the scattered lepton $E_{calo}/p \simeq 1$.

Hadronic showers tend to start further inside the material and cannot, in most cases, be fully contained by the HERMES calorimeter. They are characterised by an inelastic nuclear interaction length λ defined as the mean free path between inelastic collisions and can be considered a rough analogy to the radiation length X_0 in electromagnetic interactions. The λ of a material, however, is typically an order of magnitude larger than its radiation length. Hence, a hadron deposits only a portion of its energy inside the calorimeter and so the ratio $E_{calo}/p < 1$ [54].

The H2 hodoscope is positioned behind a 1.1 cm thick lead plate which provides two additional radiation lengths bringing the total to $20X_0$ for the hodoscope and calorimeter; this helps to contain an electromagnetic shower in its entirety. The lead plate contributes very little, however, to the total nuclear interaction length λ (6.4% λ alone) and so increases the difference between the profiles of each type of shower. Figure 3.11 illustrates the response of the calorimeter and the separation between electromagnetic and hadronic showers.

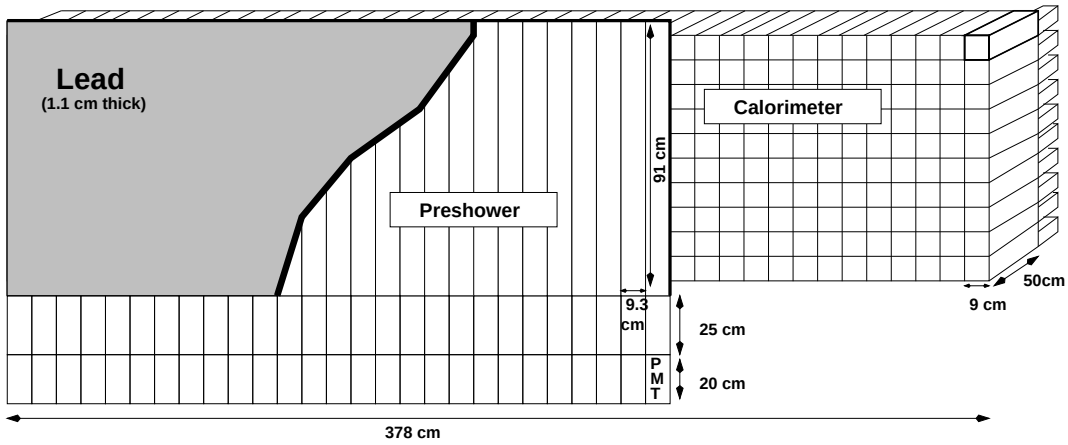

Figure 3.10: H2 hodoscope (preshower) and the calorimeter.

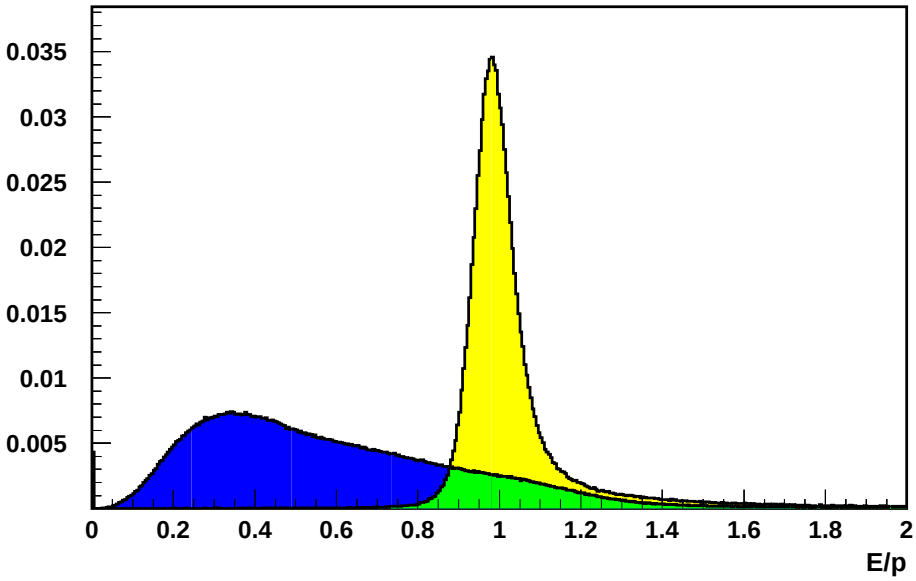

Figure 3.11: Normalised response of the HERMES calorimeter for hadrons (dark shading/blue) and $e^{\pm}$ (light shading/yellow) [54].

The Threshold Čerenkov Counter

The primary function of the HERMES threshold Čerenkov counter is to identify which hadrons are pions, and makes use of the Čerenkov effect to achieve this [48]. A charged particle propagating within a dielectric medium emits so-called *Čerenkov Radiation* when its velocity βc exceeds the phase velocity of light in the medium c/n, where n is the refractive index of the material and c is the speed of light in vacuo [55]. This radiation is emitted at an angle θ given by

$$cos\theta = \frac{c}{nv} = \frac{1}{\beta n} \tag{3.6}$$

$$\theta = arccos(\frac{c}{nv}) = arccos(\frac{1}{\beta n}) \tag{3.7}$$

Equation 3.7 has no real solution for the case where $c/n > v$ and so elucidates the important result that for a given momentum, only particles with sufficiently small mass (high enough β) will radiate. This enables discrimination of particles based on mass thresholds when prior momentum measurement is available [56].

The Čerenkov counter is positioned between the two pairs of BCs and its schematic is shown in figure 3.12. Its radiator box is constructed from a 1.17 m deep aluminium container with entrance and exit windows made from two layers of 100/30 μm mylar/tedlar foils separated by a 1 cm gap filled with continuously flowing nitrogen to avoid atmospheric gas diffusion into the radiator. Emitted Čerenkov light is reflected onto 12.7 cm diameter photomultipliers by two sets of ten spherical mirrors.

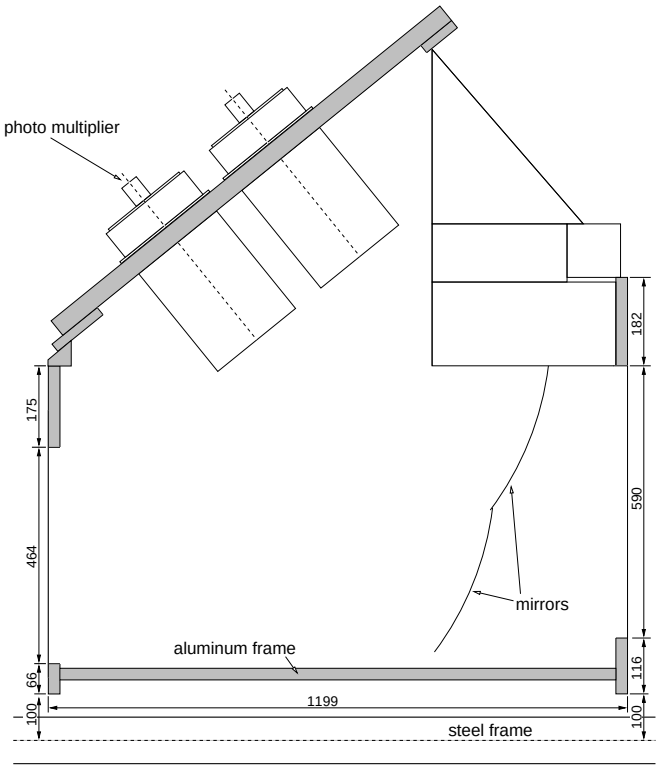

Figure 3.12: Side view of upper Čerenkov counter.

The momentum thresholds for pions, kaons and protons can be tuned by altering the gas mixture inside the Čerenkov counter (the radiator). During the first year of running, a nitrogen radiator was used yielding Čerenkov momentum thresholds of 5.6, 19.8 and 37.6 GeV for pions, kaons and protons respectively. The nitrogen radiator was replaced in 1996 with a 70% nitrogren/30% perfluorobutane mix, lowering corresponding thresholds to 3.8, 13.6 and 25.8 GeV [48]. Figure 3.13 shows

the response of the threshold Čerenkov to hadrons and positrons. Leptonic contamination of the pion sample between the pion and kaon thresholds is suppressed by using the other PID detectors to separate leptons from hadrons.

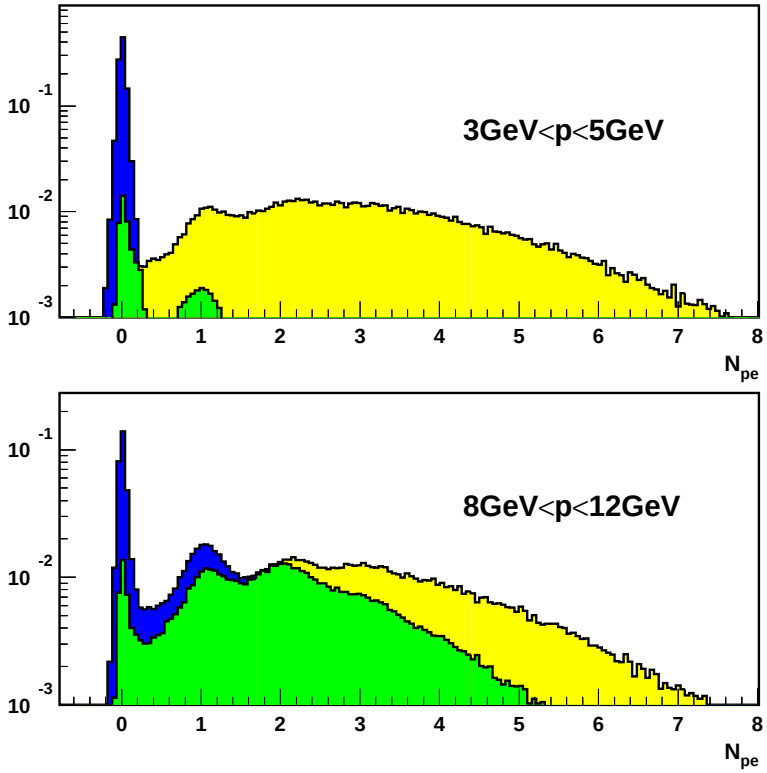

Figure 3.13: Normalised Čerenkov response above and below pion threshold in 1995 for positrons (light shading/yellow) and hadrons (dark shading/blue). Intermediate shading (green) represents overlap region [54].

The Transition Radiation Detector

The HERMES TRD separates hadrons and leptons by comparing the measured signal proportional to the Lorentz factor of a passing particle $\gamma = E/mc^2$ with that which is expected from hadrons and leptons at the HERMES kinematic region. This quantity is accessible by measuring the transition radiation emitted by an ultrarelativistic particle traversing the boundary between two materials with different dielectric constants ϵ. The mean energy of transition radiation is proportional to γ, which at HERMES exceeds 10^4 for leptons and < 200 for hadrons; the response of the TRD is shown in figure 3.14.

The TRD is constructed from six modules above and below the beam, each of which contains a radiator and a Xe/CH_4 filled proportional chamber [48]. The 6.35cm radiator consists of a series (around 300 per radiator) of two-dimensional

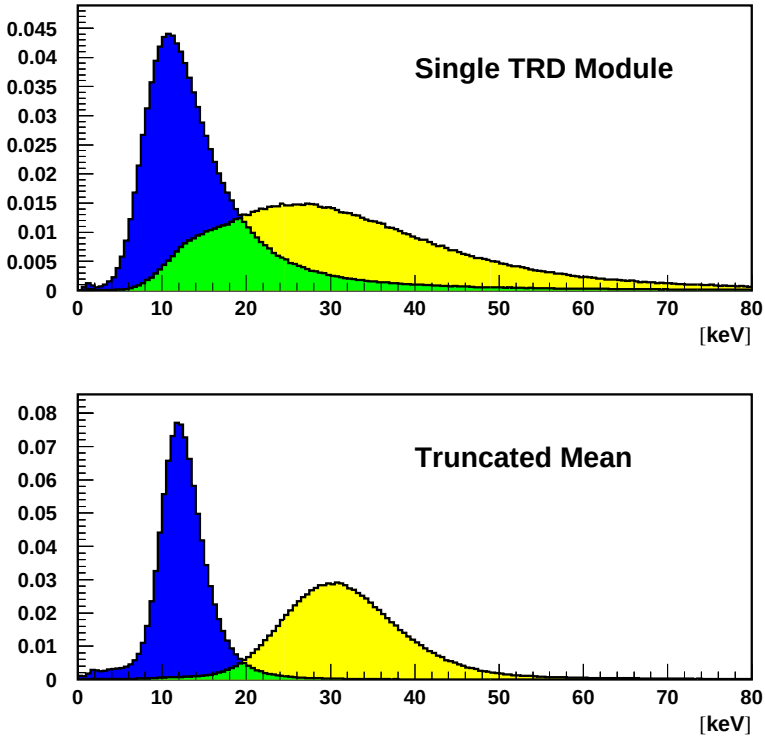

Figure 3.14: Normalised response of the TRD. Dark shading (blue) represents hadrons, light shading (yellow) represents leptons. Intermediate shading (green) is the overlap region [54].

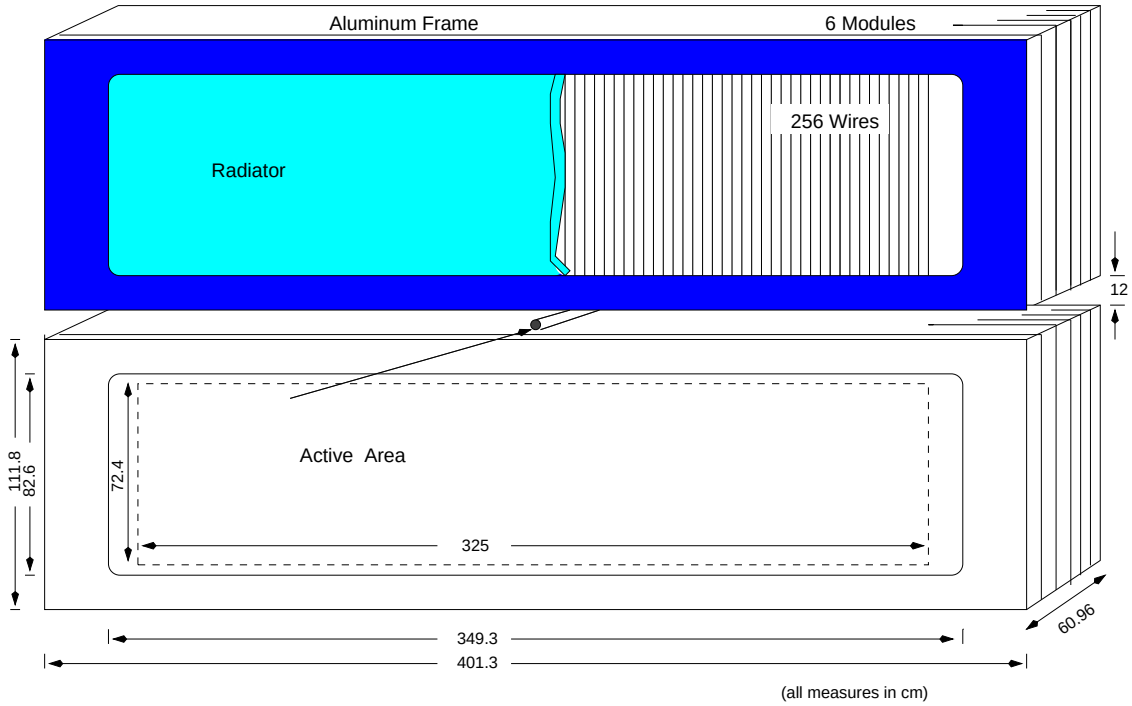

Figure 3.15: TRD schematic.

layers of polyethylene/polypropylene fibre matrices [54]. This differs from earlier foil

radiator design as the large size of the modules (325 × 75 cm^2) made polyethylene foils impractical; it is very difficult to ensure uniform foil separation with such large module dimensions. The 2.54 cm thickness proportional chambers are 256 wire MWPCs, making each module a total of 10.16 cm thick when spacing gaps' thicknesses are added. Figure 3.15 illustrates the construction of the TRD.

3.3.3 The Luminosity Monitor

The HERMES luminosity monitor (LUMI) is constructed from two calorimeter modules placed 7.2 cm downstream from the target cell on either horizontal side of the beam pipe (Figure 3.16).

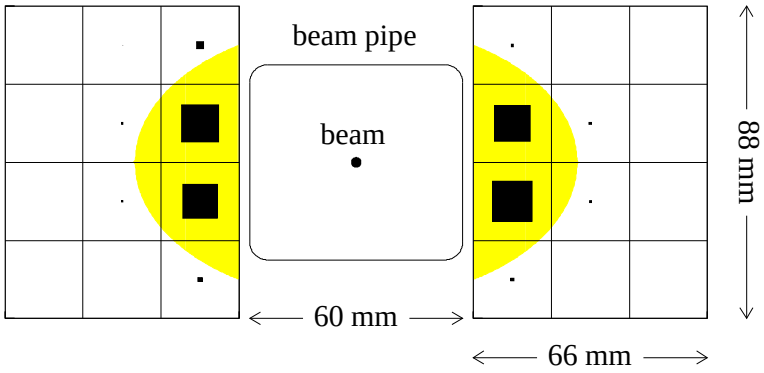

Figure 3.16: HERMES luminosity monitor schematic. Size of boxes within grid illustrates hit frequency per channel, and yellow shaded area shows the beam pipe acceptance [48].

A calorimeter module consists of 12 $NaBi(WO_4)_2$ Čerenkov crystals, each with dimensions 2.2×2.2×20 cm^3. The principle on which the HERMES LUMI operates is the detection of Møller ($e^-e^- \rightarrow e^-e^-$) and Bhabha ($e^+e^- \rightarrow e^+e^-$) scattering events from beam-target interactions, both of which are exactly calculable from Quantum Electrodynamics including radiative corrections. Background is suppressed from Møller and Bhabha events by imposing a requirement of at least 5 GeV deposited energy in each half of the luminosity monitor. Figure 3.17 shows typical LUMI response.

3.3.4 The HERMES Trigger

The trigger system in a high-energy physics experiment instructs the detector components to perform digitisation and readout when an event of interest is detected. Physics triggers required for studies at HERMES correspond to Deep-Inelastic Scattering, photoproduction processes and additional triggers for detector monitoring

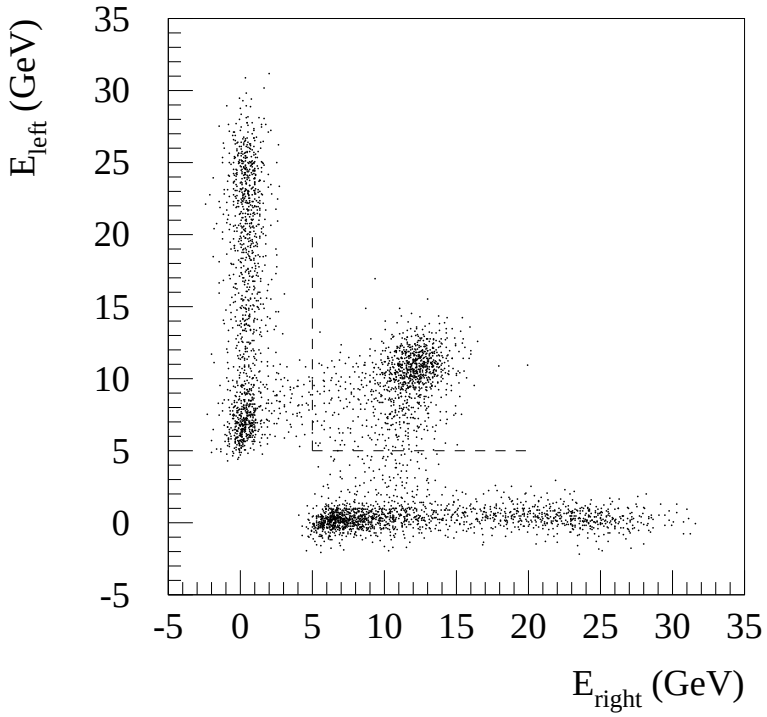

Figure 3.17: LUMI response, with a Bhabha event shown in region above required deposited energy thresholds (dashed line).

and calibration [48].

DIS events are selected by the imposition of three requirements; hits in the hodoscopes (H0, H1, H2), sufficient energy deposition in two adjacent columns in the calorimeter and both prior requirements in coincidence with the accelerator bunch signal provided by the HERA clock. Photoproduction events are those with the scattered lepton missing, and the corresponding trigger detects hadrons from low Q^2 events such as kaons, ρ, D^0, J/ψ mesons and Λ^0 resonances which decay into a pair of charged particles. Such events satisfy trigger requirements when hits in all three hodoscopes and hits in the back chamber BC1 are present in their upper and lower halves, indicating a charged particle track in each half. As with the DIS trigger, a coincidence with the HERA clock is also required.

3.3.5 The Gain Monitoring System

The response of a detector component varies with its age; continuous exposure to radiation is particularly harmful to photomultipliers. Every detector instrument equipped with photomultipliers (hodoscopes, calorimeter, luminosity monitor and Čerenkov counter) contains light sources. The light from a 500 nm dye laser is sent to the photomultipliers and to a reference counter photodiode. The intensity of the

laser light is varied with a rotating wheel containing several attenuation plates, and the response of the photomultipliers is compared with that of the photodiode which has a stable gain. Hence the gain monitoring system can monitor relative changes in gain over time and can also be employed to find dead channels.

3.3.6 Data Acquisition

The HERMES data acquisition (DAQ) system is based on a Fastbus backbone, consisting of 10 front-end crates plus event collector and receiver crates connected to an online workstation cluster via SCSI interfaces. Fastbus masters are provided by CERN Host Interfaces (CHI), the readout performance of which is enhanced by the equipped Struck Fastbus Readout Engines (FRE). An electronics trailer in close proximity to the experiment houses the front-end electronics as well as the event collector crate which is connected, via a Fibre Optical Link (STR330/FOL) to the event receiver crate located in the HERMES counting room. In addition to standard physics event data, monitoring, calibration and slow control information is passed to the event receiver crate via additional VME and CAMAC branches connected to the event collector crate.

During each fill of the storage rings the data are written to 9 GB staging disks in EPIO (Experimental Physics Input Output) format. Between fills, the data are copied to a local tape backup system and to a taping robot at the DESY main site via an FDDI link. The CPU and IO bandwidth of the event distributing workstation, an Alpha 3000X, determined the maximum DAQ thoroughput of 1.5 Mb/s. This corresponds to a 150 Hz event rate on average, which was doubled after 1997 by replacing the 175 MHz 3000X with a 266 MHz 5/266 [48].

3.3.7 HERMES Online Monitoring

During HERMES running, a shift crew has the responsibility of monitoring the status of the experiment. The information needed to perform this task is provided by the HERMES online monitoring system; a set of clients and servers which collect and display relevant information. Additionally, the online monitoring keeps a record of experiment calibration and operational parameters necessary for offline physics analysis.

The data structure of the online monitoring system is based on ADAMO [57], DAD [58] and PinK [59]. ADAMO, an entity relationship model for data handling,

provides the object structures in which to store information. DAD, the Distributed ADAMO Database, complements ADAMO, enabling cross-platform accessibility of ADAMO information via a client-server model. The GUIs employed for displaying the information to the shift crew are specific DAD clients written in PinK which is a Tcl/Tk interface to ADAMO and DAD objects. This system allows continuous monitoring of the spectrometer, DAQ and HERA status by the shift crew at a level of detail such that most problems can be quickly identified. More detailed information is available through context-sensitive help accessible from the GUI.

Chapter 4

The HERMES Recoil Detector

4.1 Introduction

Installed during the final quarter of 2005, the HERMES Recoil Detector is designed to significantly expand the physics programme of the HERMES experiment. The Recoil Detector, currently in its commissioning phase, will enable the measurement of exclusive processes from electron scattering reactions on a per event basis by detecting the recoiling protons which previously had been inaccessible due to the acceptance of the HERMES spectrometer. The present position and momentum resolution of the HERMES spectrometer is insufficient to permit event level exclusive measurements, exclusivity must currently be established with the application of restrictive missing mass cuts to a data sample.

The study of GPDs at HERMES will be greatly aided by the addition of the Recoil Detector, one of whose primary aims is to detect protons from Deeply Virtual Compton Scattering reactions (described in section 2.11). The protons measured by the Recoil Detector may also arise from the competing Bethe-Heitler (BH) process whose final state is identical to DVCS but can be exactly accounted for via quantum electrodynamics. Figure 4.1 illustrates both processes.

Additionally, the Recoil Detector will improve the resolution of the kinematical variable $t = (p' - p)^2$, where p and p' are the four-momenta of the target and recoil protons respectively. The improvement is at a level of around an order of magnitude at low values of t, providing the opportunity to perform studies of t dependence.

Finally, the Recoil Detector will reduce background by rejecting events in which a real photon is accompanied by a Δ resonance production instead of a proton. The

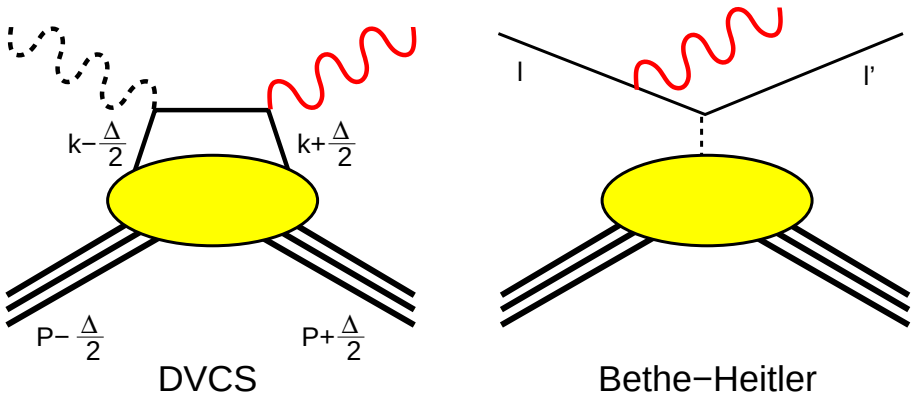

Figure 4.1: Left: Deeply Virtual Compton Scattering, where the proton absorbs a virtual photon and emits a real photon. Right: the Bethe-Heitler process, where a real photon is emitted by the incident lepton due to the interaction with the electric field of the proton.

Δ decays into a nucleon and a pion emitted back-to-back in the rest frame of the Δ, and so these decay products will usually possess a transverse momentum component with respect to the recoil momentum. This is a violation of the coplanarity with the reaction plane defined by the momenta of the virtual and real photons (Figure 4.2). These events can be recognised and rejected, promoting a decrease in the contamination of the sample [65]. The resulting effect is a reduction of the systematic uncertainty associated with Δ contamination to the level of the improved statistical errors expected from unpolarised data taking. The expected effects of this background suppression are shown in table 4.1.

Process	detected	passing p_t-cut and PID	passing total cut
TDR			
BH/DVCS	68%	53%	52%
BH,Δ	47%	13%	8%
Present model			
BH/DVCS	65%	52%	51%
BH,Δ	50%	8%	4%
BH,$M > 1.4$ GeV	44%	2%	1%
inclusive	44%	2%	1%
exclusive π^0	44%	2%	1%

Table 4.1: Effects of exclusivity cuts expected in original Recoil Detector TDR [65] compared with figures obtained with updated Monte Carlo event generator and detector geometry [49].

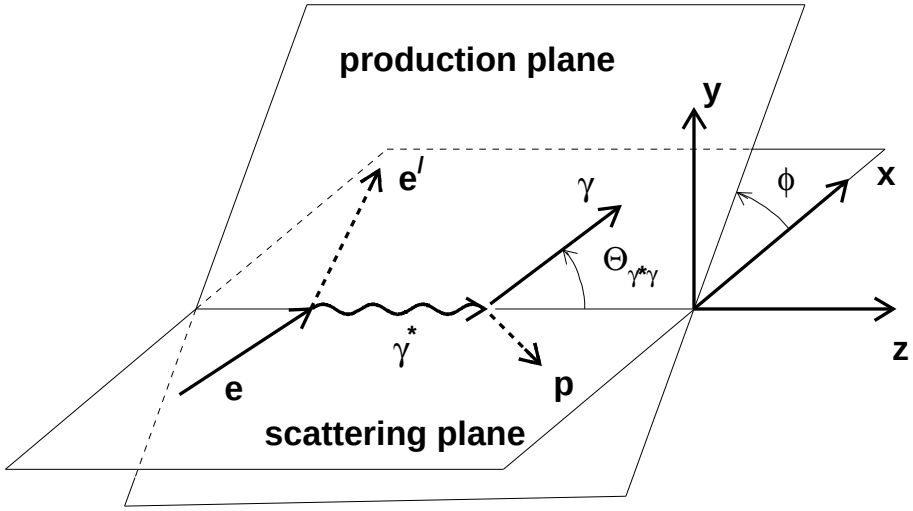

Figure 4.2: Visualisation of the azimuthal angle ϕ between the scattering and the production planes. [65]

4.2 Detector Components

The Recoil Detector contains three active subcomponents: a silicon detector around the target cell within the beam vacuum, a Scintillating Fibre Tracker (SciFi) surrounding the silicon and an outermost photon detector. Enclosing the active detectors is a superconducting solenoidal magnet which provides a 1 Tesla longitudinal field enabling momentum measurement by deflection and contributes to the suppression of background from atomic electrons. A 3 dimensional CAD drawing of the Recoil Detector can be seen in figure 4.3.

4.2.1 The Silicon Detector

The silicon detector measures the energy deposited by recoil particles from exclusive processes such as DVCS passing through its semiconductor material. Momentum is reconstructed via this dE/dx method for "slow" particles ($110 - 500 MeV/c$). In addition, the silicon detector provides up to two space points for determining the bending radius of a charged particle in the magnetic field generated by the Recoil Detector superconducting magnet. Hence, higher momentum particles ($300 - 1200 MeV/c$) can be reconstructed with this geometrical information and appropriate tracking codes. Another major purpose of the silicon detector is to reject background from events with intermediate Δ resonances [51].

Monte Carlo studies [63] have shown that DVCS events, from which the scattered lepton generates a trigger signal in the remainder of the HERMES spectrometer,

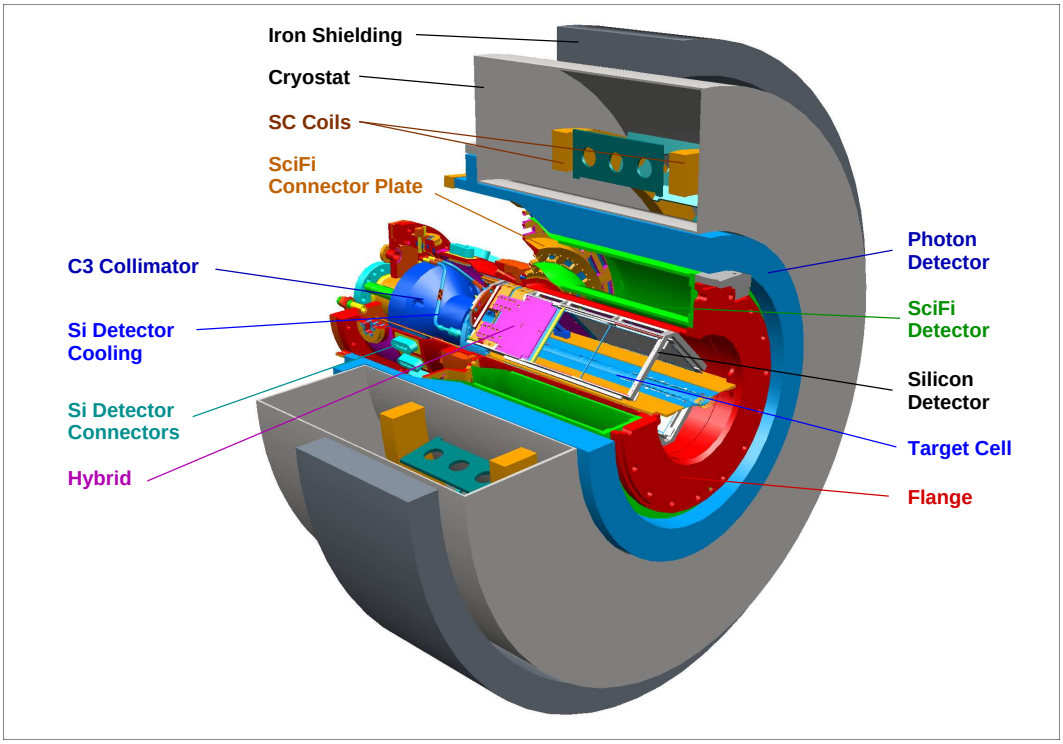

Figure 4.3: CAD drawing of the Recoil Detector.

produce protons with polar angle $10° < \theta < 80°$. The Recoil Detector is designed to cover this region and as much of the 2π azimuthal acceptance as possible, a 4% angular resolution suffices for the silicon detector as momentum reconstruction and particle identification is calculated via energy deposition. This resolution translates to approximately $1mm$ strip pitch when the silicon detector is mounted $50 - 70mm$ perpendicularly from the beam line [65].

The recoil particles are produced with momenta in the range $0.135 - 1.4GeV/c$, which corresponds to an energy range between 9 and $750MeV$. This low energy places a constraint on the amount of material which can be placed between the silicon detector and the interaction point; the detector is mounted within a newly constructed scattering chamber (figure 4.4) inside the HERA vacuum. With this configuration a recoil particle avoids any encounter with thick-walled vacuum vessels hence improving momentum resolution. However, this introduces a requirement that the components of the silicon detector must be vacuum compatible. Usefully, HERMES possesses expertise in operating silicon detectors within the HERA vacuum as both the Silicon Test Counter and Lambda Wheels have been employed in such a situation. The developments of the HERMES NIKHEF group provided the largest contribution to the design of the silicon detector [65].

A practical solution to the problem of time and manpower constraints for the HER-

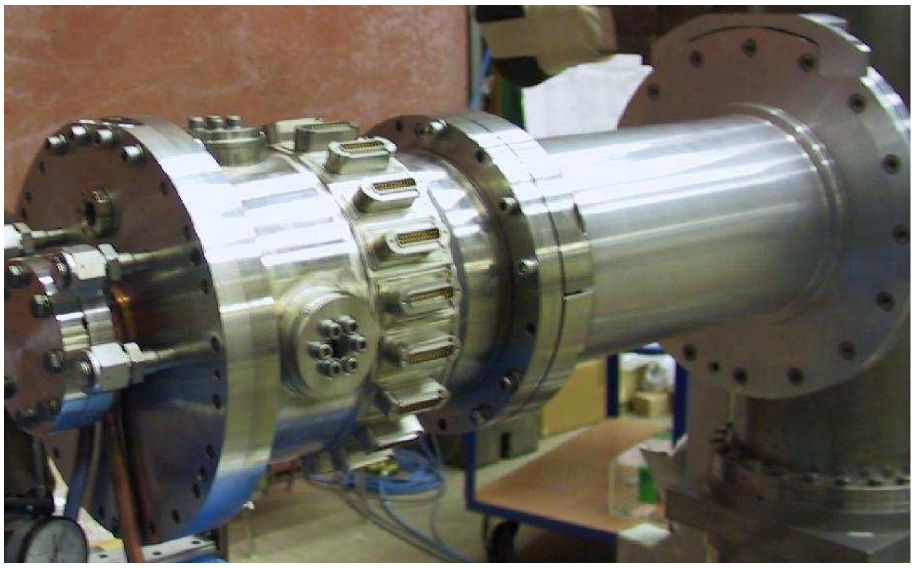

Figure 4.4: Recoil Detector scattering chamber (back) bolted to service chamber (front), set up for use in 2005 test experiment.

MES Recoil Detector project was to rely on tested designs for the silicon microstrip detectors and readout chips. 99×99 mm double-sided 300 μm thick TIGRE detectors manufactured by MICRON Semiconductor are used in the design of the silicon detector as they are the largest ones available. Each side of the TIGRE detector is separated into 128 strips of 758 μm strip pitch, with the strip direction on a side orthogonal to the other.

The silicon detector consists of 16 TIGRE microstrip detectors divided into 4 identical modules mounted in a tilted cuboid shape with square cross-section (figure 4.5). Each module (Figure 4.6) is subdivided into two layers of two TIGRE detectors separated by 15 mm in a staggered configuration with the outer layer positioned slightly downstream from the inner. Present in the upstream end of each module is the detector hybrid, a circuit board containing readout chips and electronics for each TIGRE sensor.

4.2.2 The Scintillating Fibre Tracker

While the silicon detector performs measurements based primarily and most accurately on energy deposition, the scintillating fibre tracker (SciFi or SFT) reconstructs track momentum by measuring the degree of track deflection in the magnetic field supplied by the superconducting magnet. The silicon detector, with its relatively poor angular resolution coupled with the low number and small separation of its planes, is insufficient to perform this task alone. The SciFi provides momentum de-

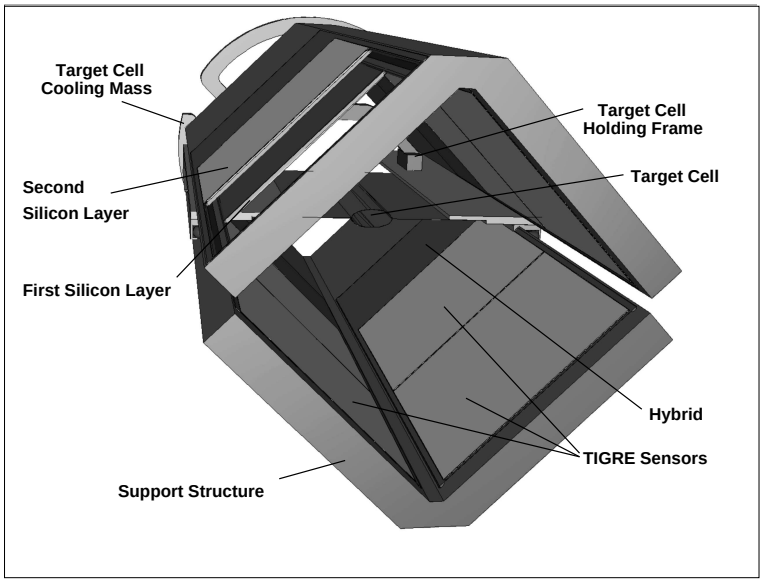

Figure 4.5: Schematic of the silicon detector from downstream end perspective.

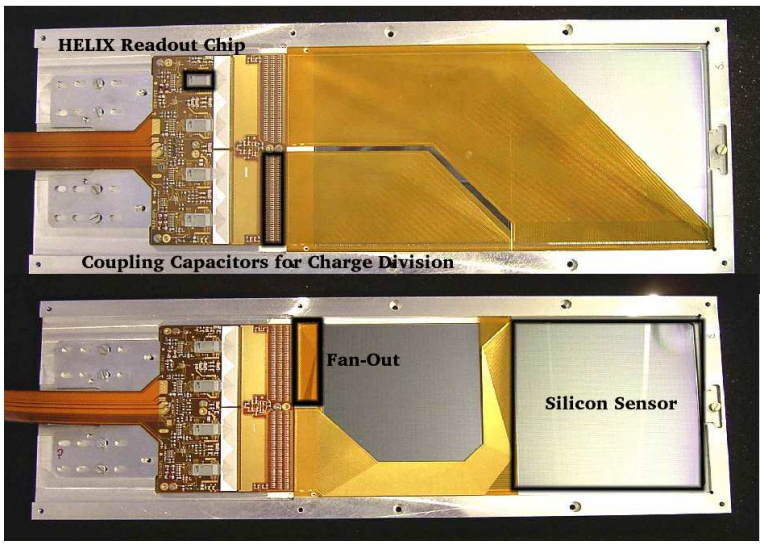

Figure 4.6: Photograph of one layer of a silicon module shown from the top (n side, upper photo) and bottom (p side, lower photo). The inner layer has the n side (top portion) facing the beam line, the outer layer has the n side facing away from the beam line.

termination and particle identification for recoil protons and (charged) pions in the momentum range between 0.3 and 1.4 GeV. It is expected that optimal momentum resolution of the SciFi will be achieved for particle momenta above 0.4 GeV.

Particle identification with the SciFi is achieved by measuring the amount of scintillation light produced by an incident particle traversing the scintillating material. The SciFi is located around the scattering chamber outside the beam vacuum, its angular coverage is 2π around the azimuth and in the polar angle ranges from 90° down to a cutoff determined by the polar angular acceptance of the Lambda Wheels [65].

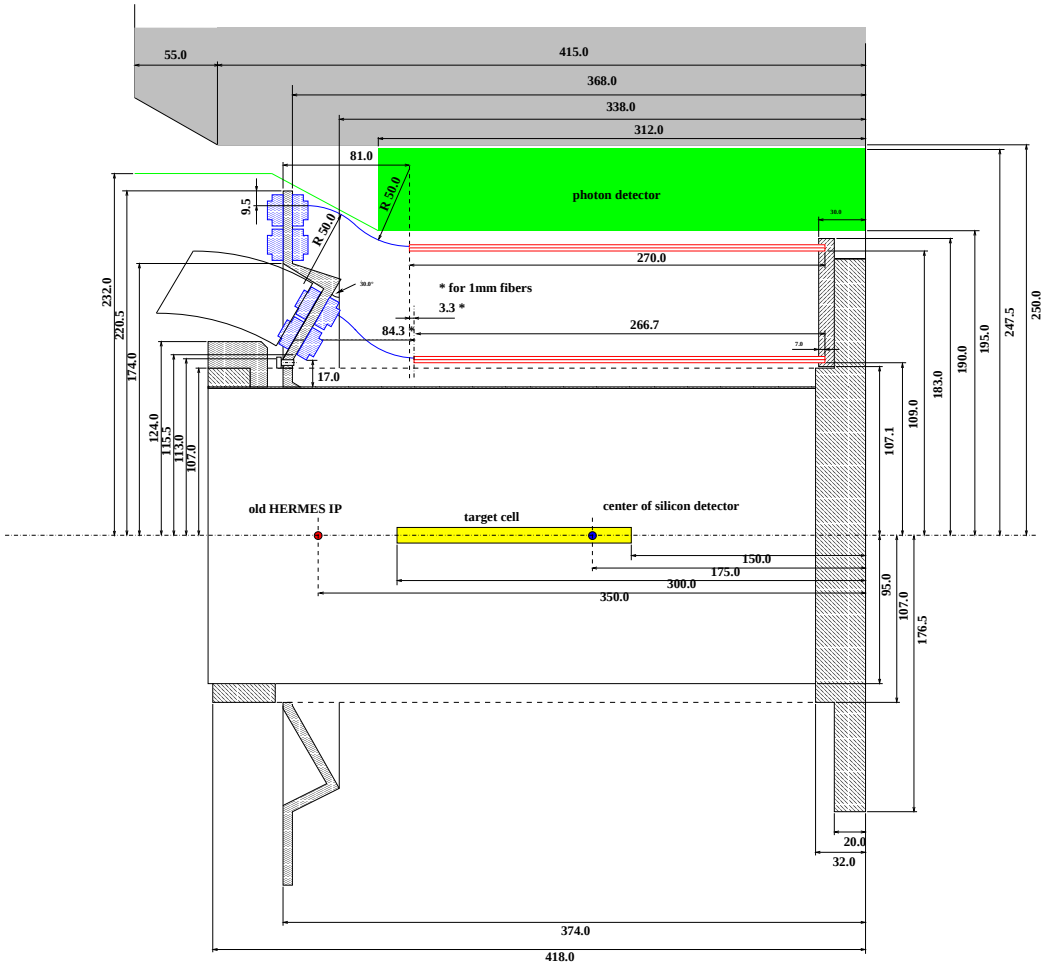

Figure 4.7: Side view of the Recoil Detector with the cross-section of the SciFi barrels and photon detector shown [66]. Part of the magnet's cross section is shown in dark shading (grey), the photon detector is shown in light shading (green). The Sci-Fi barrels are the thin layers (red) below the photon detector.

The scintillating fibre tracker is constructed from two concentric cylindrical modules (barrels) with inner radii of 109 mm (SciFi1) and 183 mm (SciFi2) respectively, each with a thickness of 4 mm and a length of 280 mm. Figure 4.7 illustrates the placement of the SciFi barrels inside the Recoil Detector.

Each barrel consists of two layers of 1 mm diameter scintillating fibres, a parallel layer oriented along the beam direction and a stereo layer at a 10° angle to the parallel layer (figure 4.8). The stereo layer enables, in addition to the transverse momentum and azimuthal ϕ track parameter, measurement of the longitudinal momentum component and polar track angle θ. Each layer is further divided into two sublayers of two fibre rows per sublayer, the upper row being staggered to fit the grooves formed by the spaces between the fibres in the lower row.

The fibres which comprise each barrel are held together with a glue which provides

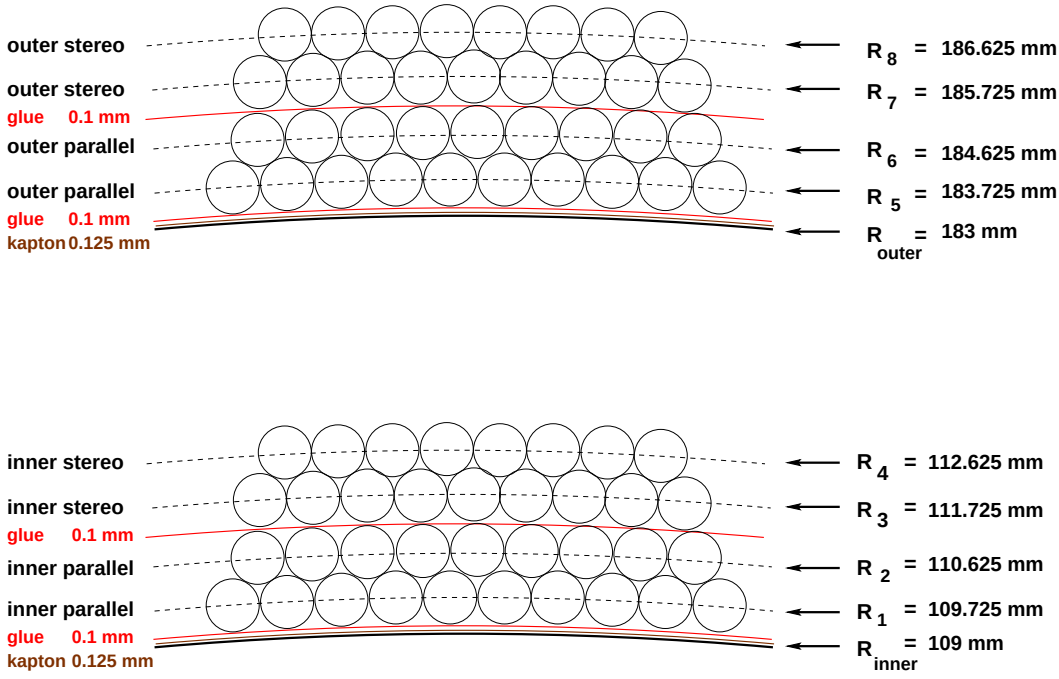

Figure 4.8: Illustration of segments of inner and outer SciFi barrels.

sufficient stiffness for the structure to be able to support itself. The fibres are attached to a supporting ring at either end, at the downstream end the fibre tips are mirrored and polished to prevent light losses and the ring is attached to the flange of the HERMES pumping cross. Upstream the fibres connect with clear light guides via connectors which are attached to an aluminium support ring (figure 4.9). The light guides are fibres which are fabricated from the same material as the scintillating fibres. In this case, however, there is no dopant present to produce scintillation light. The light guides connect to 64 channel Hamamatsu photomultipliers (PMT). A total of 78 PMTs is used to read out the 4992 channels of the SciFi [64].

4.2.3 The Photon Detector

The photon detector improves the capability of the Recoil Detector of suppressing background by rejecting events in which an intermediate Δ-resonance is produced. This is achieved by detecting at least one of the photons into which a neutral pion emitted from a Δ-decay subsequently decays. Direct measurement of π^0 particles becomes possible upon detection of two separate decay photons. Also, the first layer of the photon detector augments the pion/proton separation capability of the SciFi, a pion rejection factor of 10 is expected for momenta up to $800 MeV/c$ [65]. Finally, the photon detector provides a method by which to align the subcomponents of the

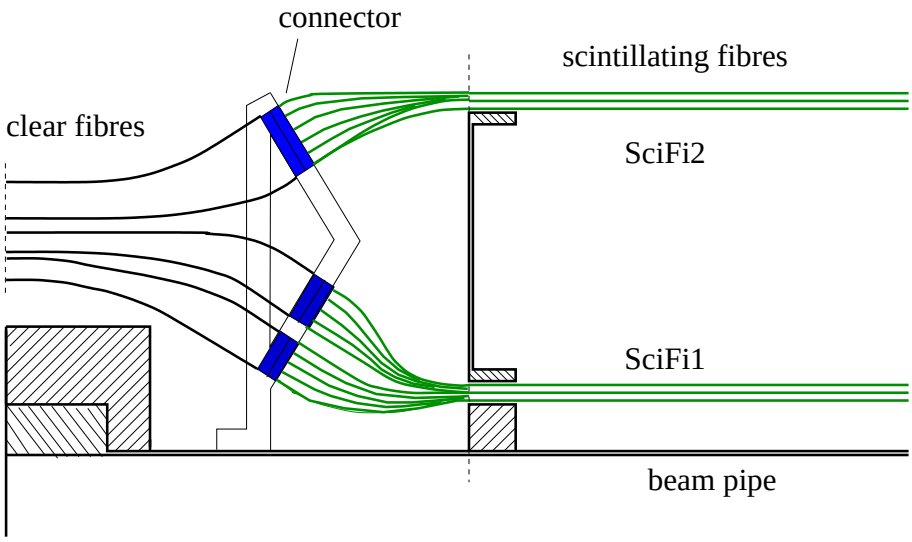

Figure 4.9: Upstream end of the Scintillating Fibre Tracker, not to scale.

Recoil Detector by acting as a trigger for cosmic ray events.

The photon detector is constructed from six layers, alternating between a tungsten converter layer from which incident charged particles produce electromagnetic showers, and a scintillator layer which detects these showers. Figure 4.10 illustrates the geometry of the photon detector, and figure 4.11 is a photograph of the detector taken during its construction. The inner layer is segmented into 60 trapezoidal blocks aligned parallel to the beam axis, the middle and outer layers are segmented into 44, aligned at $+45$ and -45 degrees to the beam. Scintillation light produced by incident photons or cosmic ray particles is collected by two light guide fibres in grooves on the sides of each scintillator block. The light guides are connected to 64 channel Hamamatsu PMTs and the signal is read out via ADCs, the signals from which can be used to perform PID in some cases and distinguish tracks from electromagnetic showers. The photon detector is positioned between the second layer of the scintillating fibre tracker and the recoil magnet, its extent having inner and outer radii of $190mm$ and $250mm$ respectively [67].

The photon detector efficiency is constrained mainly by geometry. It is known that decay photons are often emitted at low polar angles. Photons emitted at 220 mrad will enter the standard HERMES acceptance while up to 400 mrad photons will be detected at all. Despite the 2π azimuthal coverage of the photon detector, its length is restricted to roughly that of the Recoil Detector. Detection probabilities are calculated to lie between 77 and 80% for a single photon, the situation is much worse for a pair of photons from the same vertex and in this case the probability lies between 18 and 20% [49].

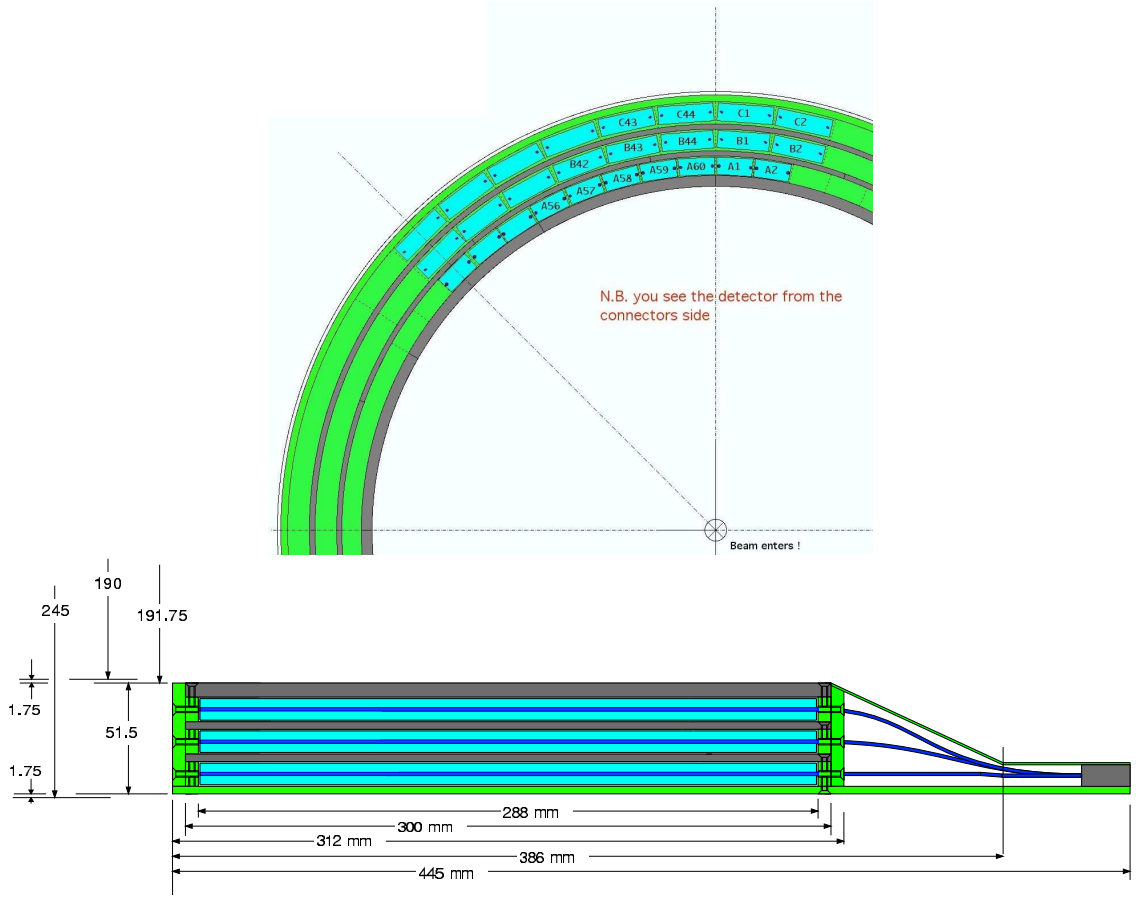

Figure 4.10: Schematics of the photon detector [67]. Upper diagram is shown from upstream perspective with numbering scheme, lower diagram shows longitudinal cross-section. Grey shading represents tungsten preshower layer, blue represents scintillator material.

4.2.4 The Superconducting Magnet

The primary purpose of the Recoil Detector superconducting magnet is to provide a means for the SciFi to measure track momentum by bending charged particle tracks in a 1 Tesla magnetic field. Additionally, the magnet protects the silicon detector from background electrons emitted from Møller scattering events by allowing these electrons to spiral forward in the magnetic field.

The superconducting solenoid design was chosen for a variety of reasons. Most importantly, the restricted space available for the Recoil Detector required the least bulky solution. Also, a 20% or better field homogeneity is required to ensure the momentum resolutions of the silicon and SciFi detectors are smoothly connected. Finally, a 0.7 Tesla field strength near the beam line is adequate to sufficiently reduce Møller background. Knowledge of field inhomogeneity is important for tracking and is discussed in section 5.6.3. The magnet was constructed by the Efremov Institute

Figure 4.11: The photon detector during its assembly. The scintillator strips of the outer layer are visible, as are the wavelength shifting fibres and the connector ring.

in St. Petersburg, it is shown in figure 4.12.

4.2.5 The Target Cell

The Recoil Detector employs a target cell design which is similar to the previous polarised HERMES target. The only mechanical difference is the active length which has been reduced from 40 cm to 15 cm. Its upstream end is positioned $5cm$ downstream from the centre of the old HERMES target. The cell is a thin-walled aluminium tube (50 μm) with an elliptical cross-section of 2.1 cm (0.9 cm) major (minor) axis length, the low momentum cutoff of the silicon detector being determined by the thickness of the cell wall. The main difference between the HERMES target and the new Recoil target which replaces it is that the latter only contains unpolarised gas, which is injected through a small capillary under the cell which runs along the length of the tube. A water-cooled mass is thermally coupled to the upstream end of the cell to counter the heating effect of the HERA accelerator

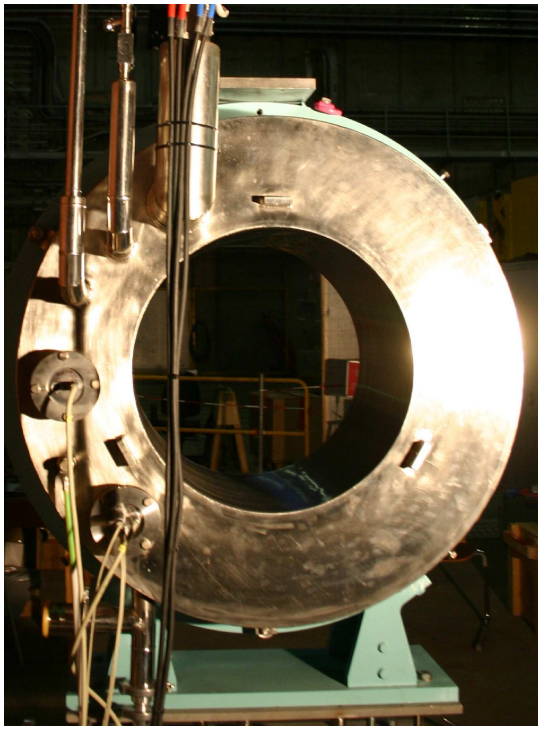

Figure 4.12: Photograph of the Recoil Detector superconducting magnet.

(heating power estimated at 15 Watts) [65]. A photograph of the target can be seen in figure 4.13.

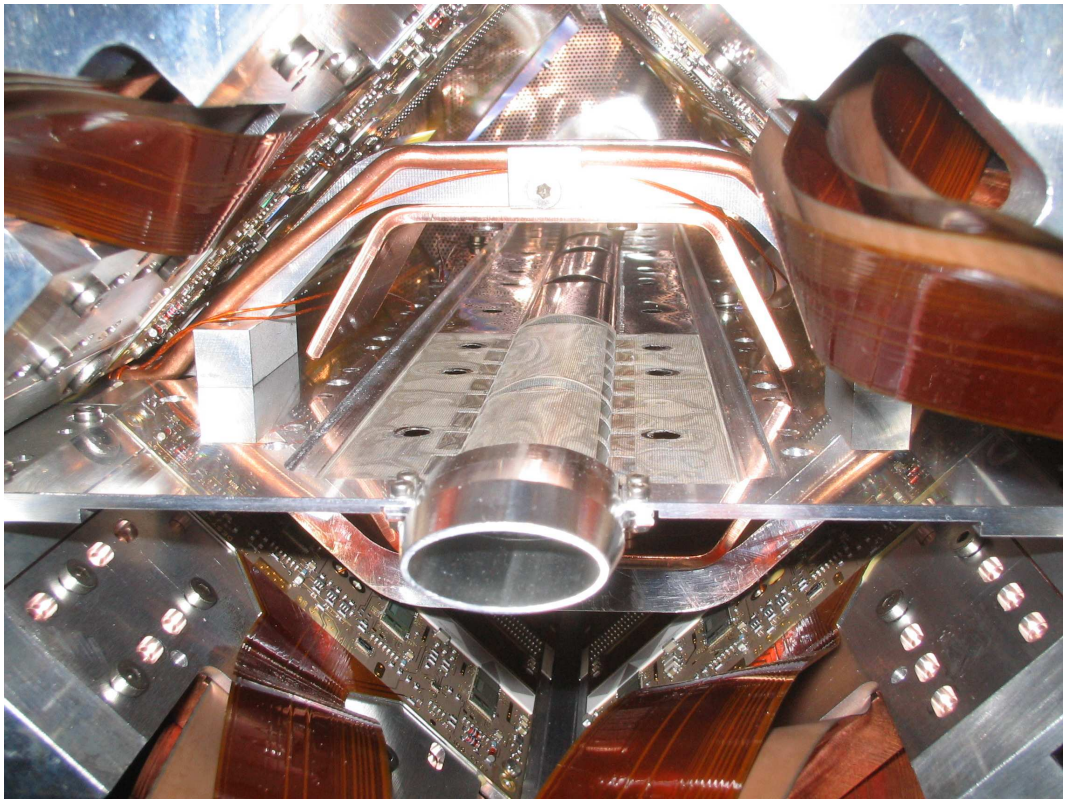

Figure 4.13: Upstream end of the Recoil Detector target. The beam enters the elliptical tube opening into the page.

Chapter 5

Track Reconstruction Algorithms for the HERMES Recoil Detector

In order to fulfil its objectives the HERMES Recoil Detector, described in chapter 4, requires dedicated tracking software in addition to that used by the HERMES spectrometer. Several different approaches to track finding and fitting with the Recoil Detector are proposed in this chapter, and performance results from tests with early Monte Carlo data and test experiment cosmic ray data are presented.

As the distinction can often be subtle, throughout this chapter a "hit" refers to a particle impact on a detector surface which deposits sufficient energy to be measured. Depending on the geometry of the specific detector, a hit may give only limited position information. A "space point" or "point" refers to a particle impact on a detector surface which has been fully reconstructed by combining the hits on that detector, giving a three dimensional position measurement in addition to energy deposition.

5.1 Introduction

5.1.1 Basic Aspects of Tracking

Track reconstruction or tracking in the context of a particle physics experiment refers to sorting position and energy deposition signals from various particle detectors into disjoint subsets enabling the identification of products from particle interactions and the measurement of their corresponding kinematical properties. Generally tracking can be split into the two separate tasks of track finding and the subsequent fitting

to the found track. Exceptions can be found in global methods such as Kalman Filtering [68] where the two tasks are performed simultaneously.

The task of track finding given a set of position measurements is to split this set into subsets such that the following conditions apply:

- Each subset contains measurements which, with some reasonable probability, are caused by the same particle.
- One, possibly empty, subset contains all measurements which cannot be associated with particles with sufficient certainty. These measurements may arise from accidental signals, distorted measurements, ambiguities in the association with tracks, weaknesses of the track model or from deliberately excluded tracks [69].

Subsets of detector signals (hits or space points) must demonstrate a strong similarity to an expected track model, which is a function satisfying the equation of motion of the particle. The problem is essentially one of pattern recognition, which is trivially performed by the human brain even in the presence of noise, discontinuities ("kinks") in the track shape, vertices and overlaps. The large quantities of data produced by modern experiments require tracking software which attempts to perform pattern recognition as effectively as the eye, only enormously faster.

Track fitting is concerned with the estimation of the parameters (such as track curvature and coordinates of intersection with axes) of a given subset of hits (a "track candidate") which have previously been found to match an expected track model. In addition to this, a track fit provides a measurement of the quality of the fit to the track model (via, for example, the familiar χ^2). This requires the consideration of:

- The geometrical configuration of the detector, the resolution of its active subcomponents and its operational specifics (such as magnetic fields).
- A mathematical model which provides a sufficiently accurate approximation of the particle trajectories [69].

Track fitting, in contrast to track finding, is far more effectively performed by a computer than by eye, which is typically only able to fit straight lines to data with any accuracy. Additionally, a preliminary fit to a track candidate complements the

track finding procedure as iterative refinements can be made if the candidate is discovered to yield a poor quality of fit or low fit probability.

Following a successful application of the tracking algorithms, individual tracks are resolved and the remaining hits, which are not associated with any tracks, can be regarded as background.

5.1.2 Requirements for Tracking with the Recoil Detector

The HERMES Recoil Detector presents a challenging environment in which to perform tracking. Due to time constraints, the tracking software, a functioning Monte Carlo code and the detector itself were developed in parallel which left many unknown potential requirements. Consequently, a set of tracking codes were created with differing capabilities which would be employed according to the needs of the final experiment. Some requirements, however, were evident prior to investigations with the Monte Carlo. The tracking code was to be capable of:

- finding tracks in the presence of noise from background and combinatorials arising from multiple track impacts on segmented detector surfaces.
- Performing track fitting in a magnetic field expected to exhibit an inhomogeneity of around 10%.
- Finding tracks with low redundancy. The maximum number of possible detector space points (in 3-space) for the Recoil Detector is 5 including the primary vertex.
- Fast execution speed, generally required of tracking code.

5.2 HERMES Software Organisation

Prior to a detailed discussion of the tracking for the Recoil Detector, this section will provide a description of HERMES software conventions, the structures of which determine the operational constraints on the recoil tracking software.

5.2.1 HERMES Event Structure

The HERMES data production chain consists of several steps invoking many separate pieces of software in order to produce experimental data samples containing sufficiently high-level information for physics analysis. The data production begins with the HERMES DAQ (Data AcQuisition), a set of codes based around an event builder which responds upon receiving a detector trigger signal indicating that an interesting event has been detected by the spectrometer. The DAQ also responds to so-called scaler events which occur every 10 seconds and contain weakly time dependent information such as luminosity and trigger dead time. Trigger and scaler events are recorded by the DAQ as EPIO (Experimental Physics Input-Output) files [70].

In addition to that which is recorded by the DAQ, information regarding hardware parameters which change on a slow time scale is written to ADAMO files by the HERMES slow control. The slow control records measurements such as vacuum pressures, high voltage readings and phototube gains (measured by the Gain Monitoring System) every few minutes. The DAQ and the slow control make up the online portion of the HERMES data production chain, subsequent steps are carried out by offline software; the main production.

A simplified flowchart of the main production is shown in figure 5.1. The HERMES Decoder (HDC) reads the EPIO files created by the DAQ, which contains basic readout information from each subdetector. HDC converts this into calibrated quantities, such as wire hit positions and energy deposition, using the information provided by calibration and geometry servers. HRC (HERMES ReConstruction) reads information piped from HDC and produces tracking and particle identification information for the portion of the spectrometer downstream of the Lambda Wheels. XTC (eXternal Tracking Code) performs tracking for the remainder of the spectrometer, in particular the Lambda Wheels and the Recoil Detector. Finally, the writeDST program synchronises the tracking information from HRC and XTC with the slow control and creates the μDST files which are used in the physics analysis.

The code for performing Recoil Detector tracking is inserted into XTC. This is a natural choice, the position of XTC within the production chain allows additional tracking information to be provided from HRC (for example, the reconstructed primary vertex).

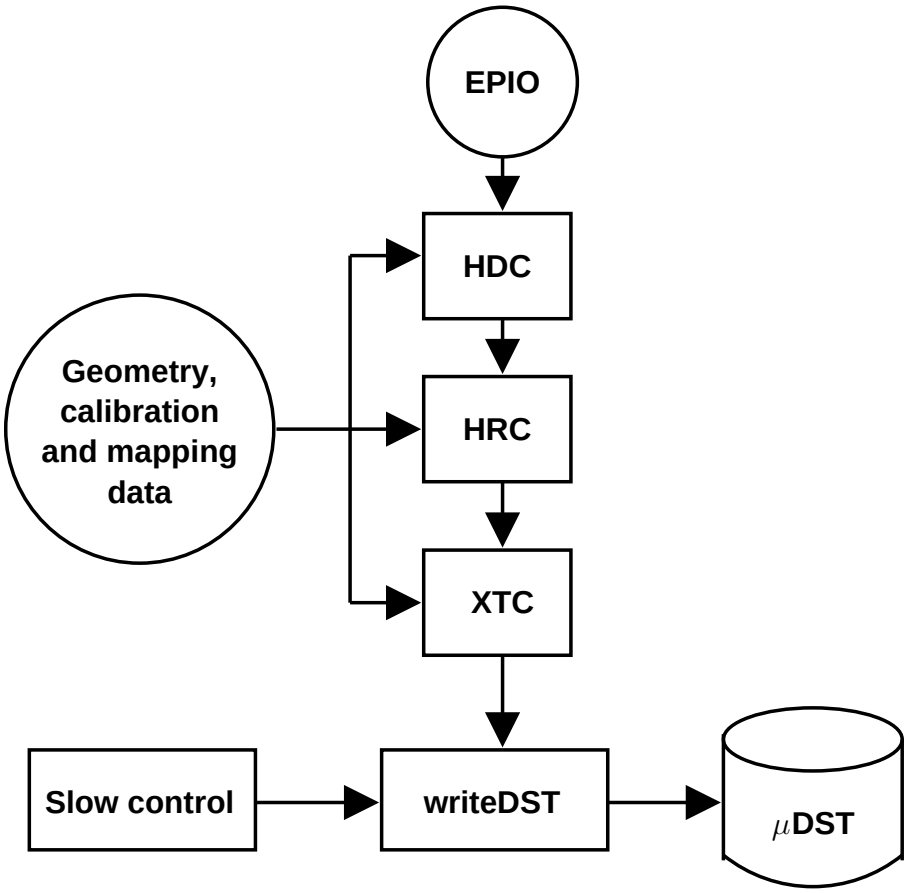

Figure 5.1: Simple illustration of HERMES main production chain.

5.2.2 Monte Carlo

The Monte Carlo setup at HERMES consists of two separate components, the Generator Monte Carlo (GMC) and the HERMES Monte Carlo (HMC). GMC simulates physics events which are tracked through a simulation of the spectrometer by HMC. The resulting file format is such that the Monte Carlo can be used as a substitute for HDC output (and the DAQ which precedes it), a flowchart showing part of the Monte Carlo production chain is shown in figure 5.2.

GMC can be used with various different physics process generators as required. The DVCS/BH generator, for example, produces the Deeply Virtual Compton Scattering and Bethe-Heitler processes which are of interest to the Recoil Detector, and the PYTHIA generator is used in the analysis of ρ^0 cross-sections to obtain estimates for non-exclusive background rates.

HMC uses calls to the GEANT package to propagate the particles generated by GMC through the HERMES spectrometer. A detailed simulation of the spectrometer must be supplied to HMC, this is accomplished by the HDB (HERMES DataBase)

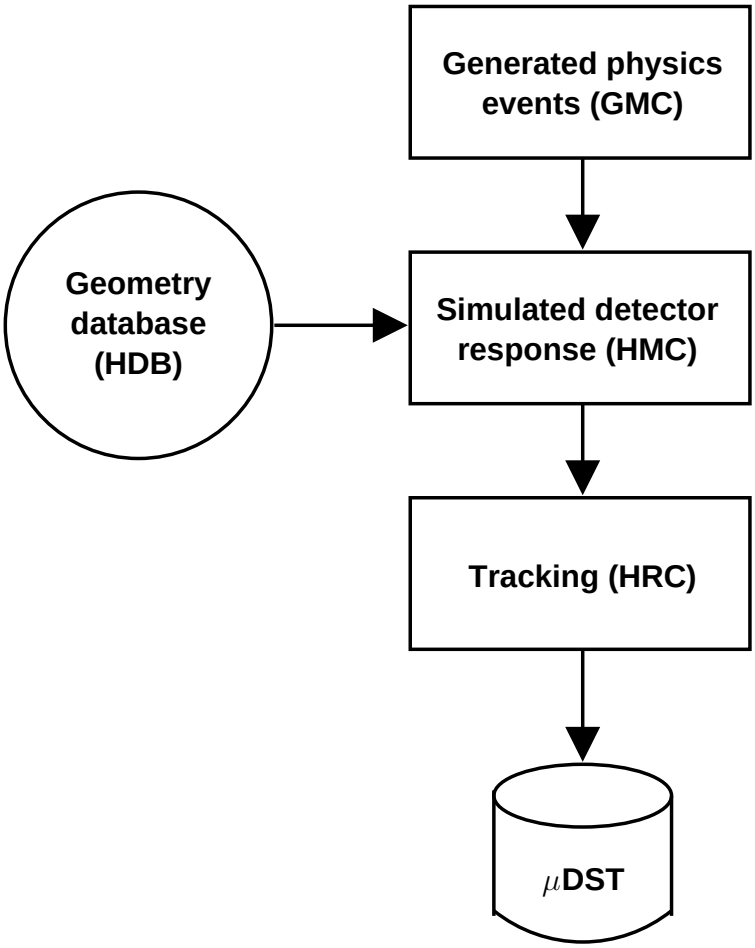

Figure 5.2: Flowchart of HERMES Monte Carlo production chain.

program. A detector simulation must be stored in a geometry file containing the dimensions, material composition and location of every detector component. HDB, taking the geometry file as input performs various consistency checks (e.g. ensuring no component overlaps are present) and creates a new geometry file in the format required by the geometry server. The information stored in the geometry file is also used by HDC, HRC and XTC via the aforementioned geometry, mapping and calibration servers.

5.3 Structure of Recoil Tracking in XTC

In addition to the tracking, XTC contains subroutines which perform tasks such as clustering for the subdetectors, space point reconstruction and interfaces to the ADAMO libraries which provide the database scheme for HERMES. The structure of XTC relevant to recoil tracking is shown in figure 5.3.

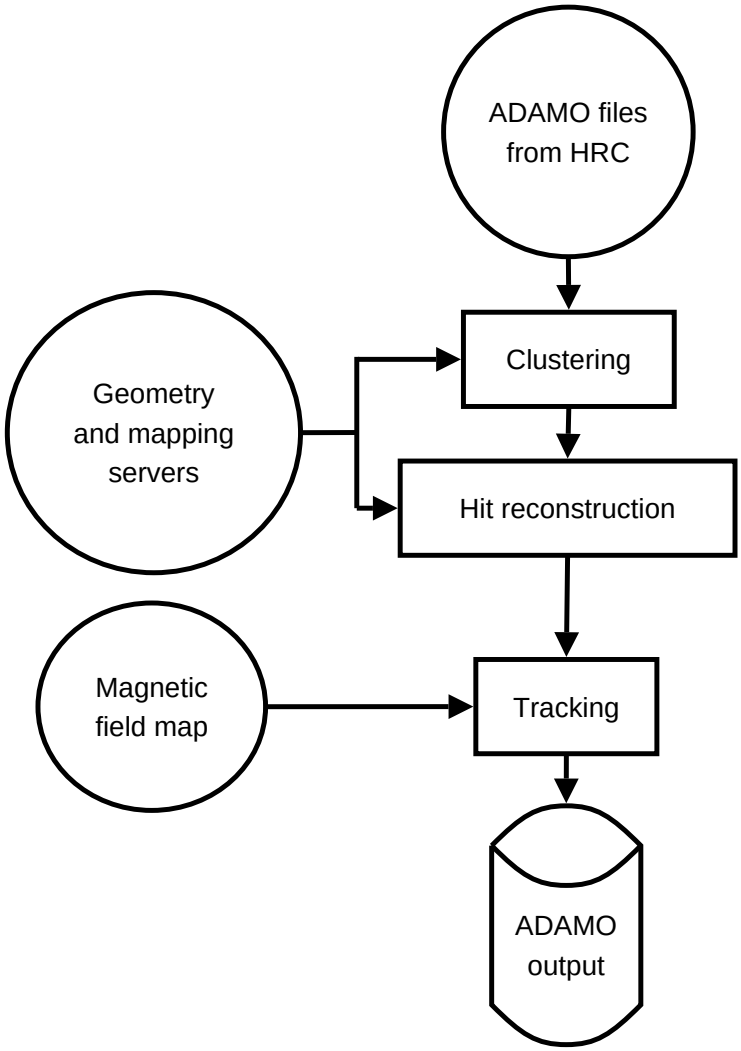

Figure 5.3: High level flowchart of the recoil XTC code.

5.4 Clustering and Space Point Reconstruction

A charged particle which passes through a segmented detector (e.g. a microstrip or fibre detector) generally deposits energy in a region which spans more than one strip or fibre. Clustering refers to a procedure applied to each subdetector (silicon, SciFi, photon detector) in which detector signals from physically adjacent strips or fibres are combined in order to obtain a more accurate estimate of the position (in the coordinate system of the detector plane) where the incident particle struck. A clustering routine also typically uses calibration information to convert the detector signal from ADC pulses into an energy deposition measurement.

Space point reconstruction is the application of a transformation of the calculated position on the detector plane into the coordinate system required by the tracking

algorithm. Additionally, the space point reconstruction code may search for matching hit information, such as clustered hits on either side of a double-sided silicon detector (as performed for the silicon detector).

5.4.1 Silicon Detector

The silicon detector, described in section 4.2.1, consists of 16 square silicon wafers (TIGREs) each with an area of approximately 100 cm^2. A TIGRE has 128 strips on each side, the orientation of the strips on the n and p sides are at a relative angle of 90° with the strips on the p side oriented parallel to the beam axis. A schematic of the numbering scheme and orientation is shown on figure 5.4.

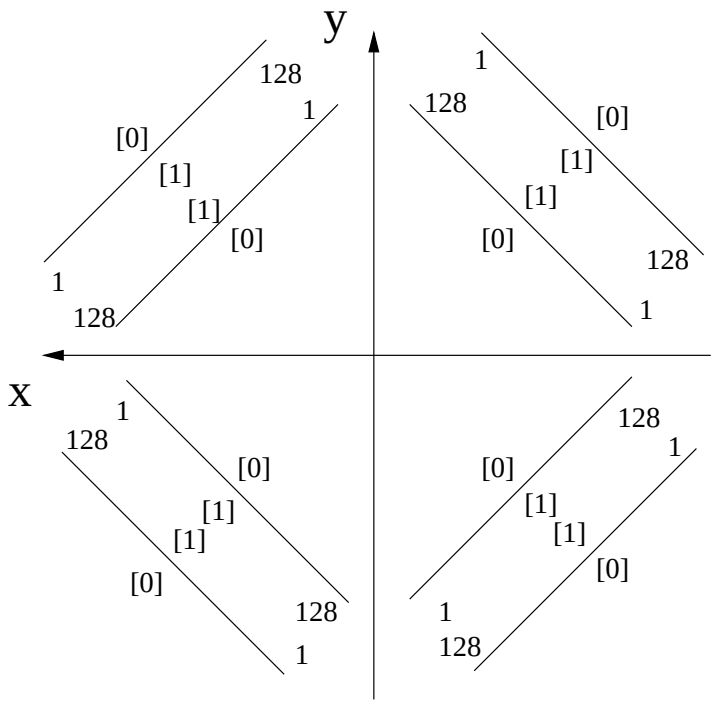

Figure 5.4: Schematic of silicon detector layout from front perspective. [0] denotes the n side of the silicon wafer, [1] denotes the p side. The strip numbering convention for n side is indicated by the numbers 1-128, the convention for the p side is numbered 1-128 with the low end upstream. The beam enters into page at the origin [51].

Clustering for the silicon detector in XTC is performed using a relatively simple algorithm. A search is performed in numerical order on strips 1 to 128 on the n and p sides of each TIGRE. Upon encountering a struck strip, further consecutive struck strips are sought. The procedure stops when no further consecutive strips are encountered, or a maximum of six consecutive strips are found.

The next step in clustering is the calculation of the position where the particle struck. Figure 5.5 illustrates a situation where three particles strike a single TI-

GRE, producing peaks in the ADC spectra as shown. For each individual peak the clustering algorithm calculates a mean value using a "centre-of-mass" approach (figure 5.6).

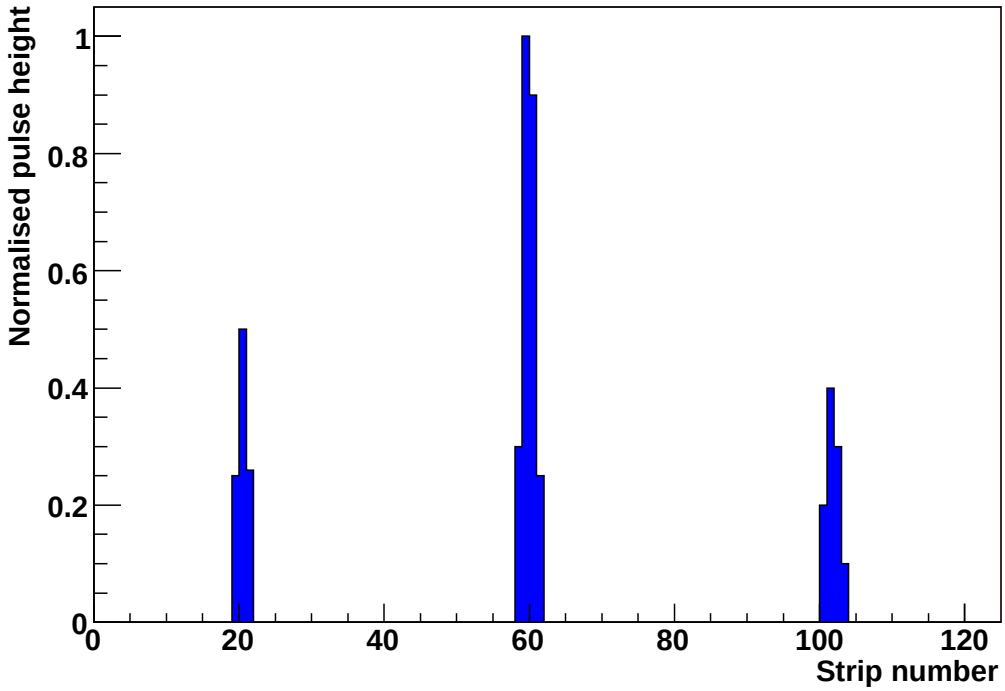

Figure 5.5: Illustration of signals expected from an event with three strikes on a single TIGRE. The pulse height is in arbitrary units for illustrative purposes, and is normalised to 1. Noise has not been included for clarity.

The result of applying the clustering routine to the entire silicon detector is a set of position measurements in the local coordinate system, and the associated pulse value which is the sum of the ADC values from each struck strip across each cluster. In order to produce a position measurement in 3-space, and provide information for momentum reconstruction with energy deposition, it is necessary to use calibration information to convert the summed ADC value into a deposited energy. In this case, the calibration information was provided by test beam studies carried out at the Tandem Accelerator Facility in Erlangen [71].

The energy deposited on a silicon module by a passing charged particle is given by:

$$E_{dep} = \frac{S}{gck} \tag{5.1}$$

where S is the digitised output of the ADC, g is the amplifier gain and c is the conversion factor of the ADC. The calibration factor, k, varies between silicon detector

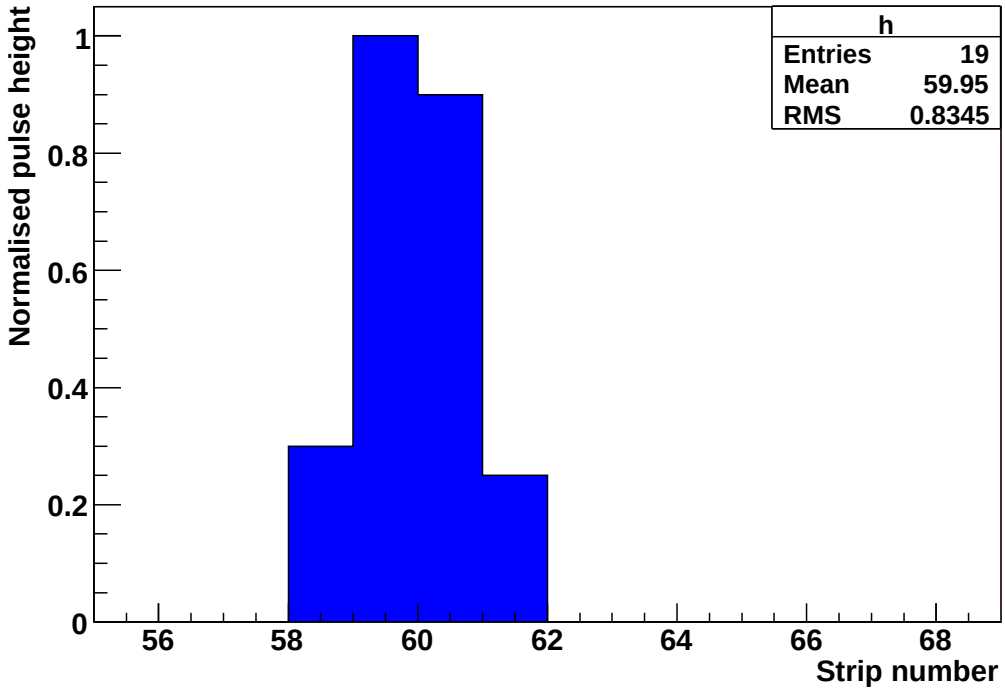

Figure 5.6: Zoom picture of middle peak in figure 5.5. Also shown is the calculated mean value.

modules. In practice, the ADC output is split into a high gain and low gain channel in order to increase the dynamic range of the silicon detector and correspondingly, k has been calculated as k_l and k_h at the Tandem facility for the low and high gain channels respectively. As a single test module was investigated in Erlangen, it is estimated that k should vary by $\pm 20\%$ between detector modules [72]. This variance, while important for measuring energy deposition, does not result in inconsistent space point reconstruction between modules as the ratio $\frac{k_h}{k_l}$ in principle should remain fixed.

Reconstructing space points in 3-space requires a passing charged particle to deposit energy on both sides of a silicon detector wafer. The ADC values on either side of a silicon module are correlated and so can be matched, and a coordinate transformation can be performed using information from the mapping server. In practice, however, this is made more difficult by a variation in detectors' responses. Investigations have shown that, in addition to variations between modules and wafer sides, the ratio of the signals in the n and p sides of a silicon module also vary with strip number as shown in figure 5.7. A calibration server provides XTC with a map of individual strip parameters so that energy depositions on either side are more easily matched. XTC matches two signals on opposing sides of a TIGRE if the corrected

signals match by an amount better than 20%.

5.4.2 Scintillating Fibre Tracker

Performing clustering and space point reconstruction is simpler in the case of the SciFi than the silicon detector. In the absence of correlated energy deposition information from alternate detector layers the clustering relies on a simple search for adjacencies only, calculating the struck position by using the unweighted mean. Matching hits between the stereo and parallel layers of each SciFi barrel relies on searching for clusters of hits which lie physically close to one another. A simple schematic of the SciFi detector is shown in figure 5.8, and table 5.1 lists the properties of each layer.

Layer Name	Orientation	Fibres
SFI1	parallel	659
SFI2	parallel	659
SFI3	stereo	660
SFI4	stereo	660
SFO1	parallel	1098
SFO3	stereo	1090

Table 5.1: List of properties for inner (SFI[1-4]) and outer(SFO[1,3]) SciFi layers.

Both inner and outer SciFi barrels are comprised of four layers, two parallel and two stereo. However, for the outer barrel the decision was made to combine the same-orientation layers, that is, the SFO1 and SFO2 layers were combined, as were the SFO3 and SFO4 layers, thus the numbering scheme is not consecutive.

Clustering for the SciFi begins with the combination of strips in individual layers. Before clusters on the parallel layer are matched with those on the stereo layer, the inner SciFi barrel requires an additional step; the clusters on SFI1 and SFI2, which now have the position value of a single strip, are combined in order to yield a position measurement (in local coordinates) which is the average of the two. Clustering for the parallel layers SFI3 and SFI4 is performed by a similar method to this.

The combination of clustered hits on the parallel and stereo fibre layers can lead to problems with combinatorials. Following the geometry of the stereo layer fibres, at 10° to the beam axis, the path of a single stereo fibre crosses 44 parallel fibres on the inner SciFi barrel and 45 fibres on the outer barrel. The inner and outer parallel layers being comprised of 659 and 1098 fibres around their circumference

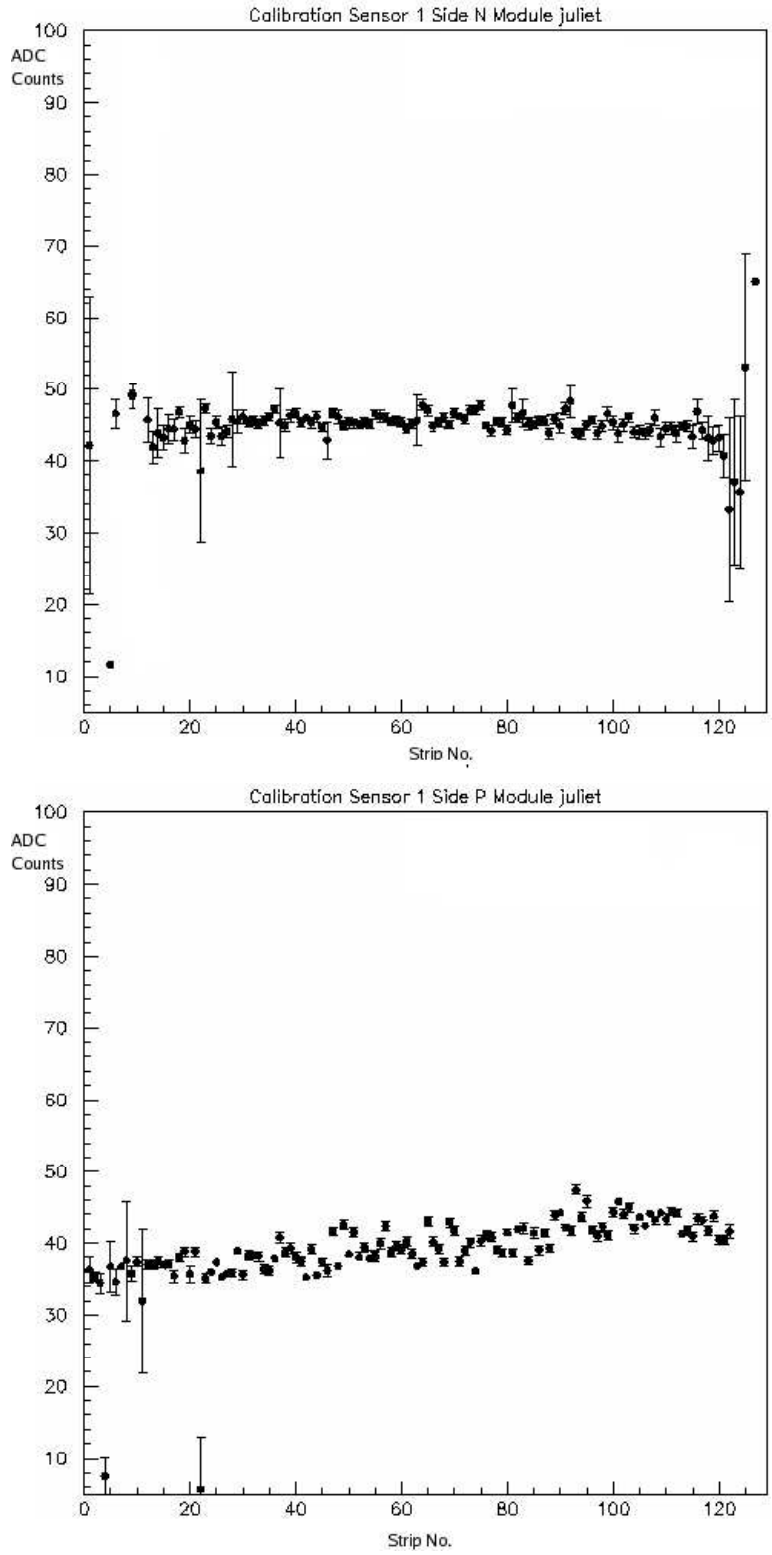

Figure 5.7: Calibration values for one of the silicon sensors versus strip number for n side (top) and p side (bottom). The errors are obtained a from Landau-Gauss convolution fit. Errors larger than $\sim 3\%$ arise from low statistics, increased noise or a defective strip. The data were obtained at the DESY T22 test beam [73].

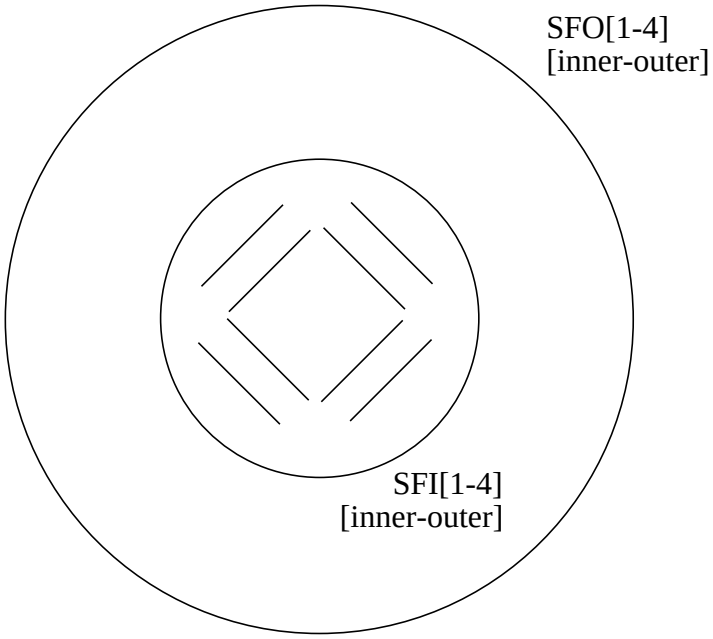

Figure 5.8: Simplified SciFi front cross-section schematic with silicon detector also shown. SF[I0][1-4] refers to the naming and numbering scheme for SciFi inner and outer barrels, layers 1-4 [51].

respectively, the search for a matching stereo layer hit must cover approximately $\pm\frac{\pi}{4.7}$ radians away from the position of the hit in the parallel layer for the inner barrel, and $\pm\frac{\pi}{7.7}$ radians for the outer. Any clusters satisfying this condition are combined and transformed into cylindrical polar coordinates. The components r, ϕ are easily obtained from the known geometry of the SciFi. The z coordinate is obtained according to [74]:

$$z = \frac{R_{SciFi}\Delta\phi}{tan10^{\circ}} \tag{5.2}$$

where R_{SciFi} is the radius of the struck barrel and $\Delta\phi = |\phi_{parallel} - \phi_{stereo}|$.

5.4.3 Photon Detector

The photon detector is described in section 4.2.3. As with the silicon and SciFi detectors, clustering and space point reconstruction for the photon detector is performed in XTC. Unlike the silicon and SciFi, however, the photon detector is not used for the tracking of protons and pions; the tungsten layers which encourage a strong deformation in the track shape and the limited resolution of the scintillator blocks preclude the use of the photon detector as a tracking detector. However, the photon detector provides a trigger for cosmic ray events and a pair of initial space

points from which to begin a search for subsequent cosmic space points on the inner detectors. Figure 5.9 shows the naming scheme for the photon detector, and table 5.2 lists the properties of each layer.

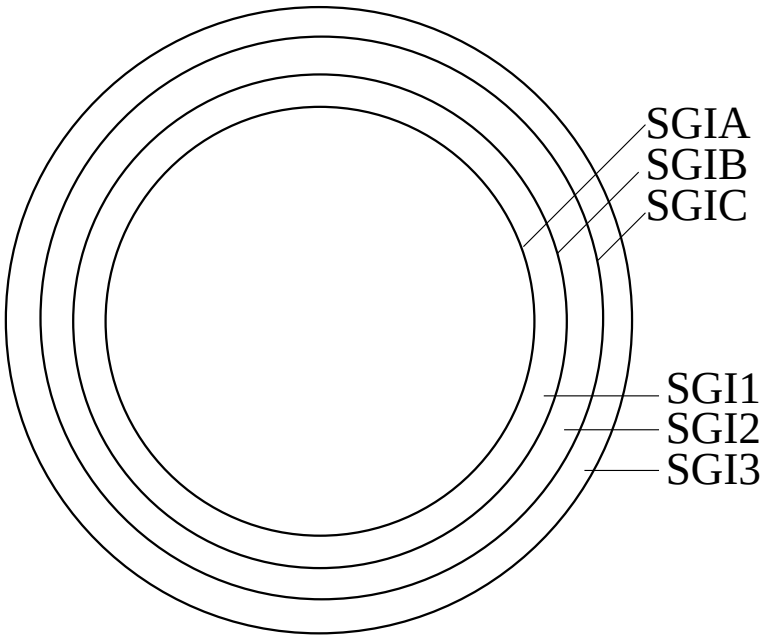

Figure 5.9: Simplified photon detector front cross-section schematic. SGI[A-C] is the Monte Carlo naming convention for the preshower layers, the SGI[1-3] naming convention for the scintillator layers is retained for use with XTC [51].

Layer Name	Orientation	Strips
SGI1	parallel	60
SGI2	stereo $+45°$	44
SGI3	stereo $-45°$	44

Table 5.2: List of properties for SGI[1-3] photon detector layers. The sign convention for stereo layers are; + clockwise, − anticlockwise.

Clustering for the photon detector is performed in each layer separately. Figure 5.10 illustrates an example event in which energies are distributed along several strips, with one instance of two closely spaced tracks creating an overlap of clusters. In this scheme local maxima of energy deposition are sought in groups of consecutive strips. Non-maximal energies in surrounding strips are assigned to the local maximum, in the case of an overlap, the energy measured in the strip which corresponds to the local minimum is split and assigned to the two maxima. The split is computed according to e^{-x}, where x is the mean distance of the energy-maximal strip to the energy-minimal strip in units of strip width [75]. The position where the particle struck is estimated with an energy-weighted mean calculation over the strip cluster.

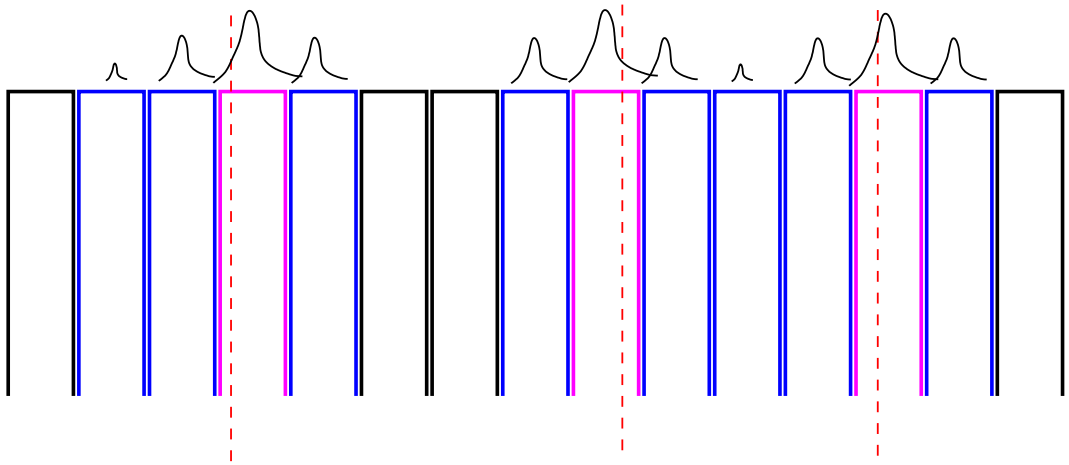

Figure 5.10: Illustration of clustering algorithm for the photon detector. The dashed line shows the energy-weighted calculated mean position. [75]

Space point reconstruction for the photon detector proceeds similarly to that for the ScFi. Some differences, however, arise due to the presence of an additional stereo layer. Additionally, the photon detector measures energy deposition but this is not useful for matching clusters on separate scintillator layers as the preshower layers between them weaken the correlation.

A particle which is measured by all layers will generate a total of 4 space points, one in layers SGI1 and SGI3 and two in SGI2. The two space points in SGI2 are present as the stereo layers above and below it each provide different values of z. The radial thickness of each layer allows the particle to travel further along the tangential surface of the detector, consequently the ϕ and z values drift across the 3 scintillator layers. This is illustrated in figure 5.11.

A position in 3-space can be reconstructed from hits in at least two of the three layers. Matching hits to their partners in the different layers is performed by searching for hits which are separated by a perpendicular distance of less than 5 cm. Prior to this another clustering step is required; in the presence of two space points in the SGI2 layer (as figure 5.11 shows), again, the energy-weighted mean position is calculated. In the instance of multiple crossings between strip clusters such as figure 5.12, the energy of the single cluster is split between the crossings. Ghost crossings between strip clusters as shown in figure 5.13 are treated by removing the points which do not have partners in the remaining layer [75].

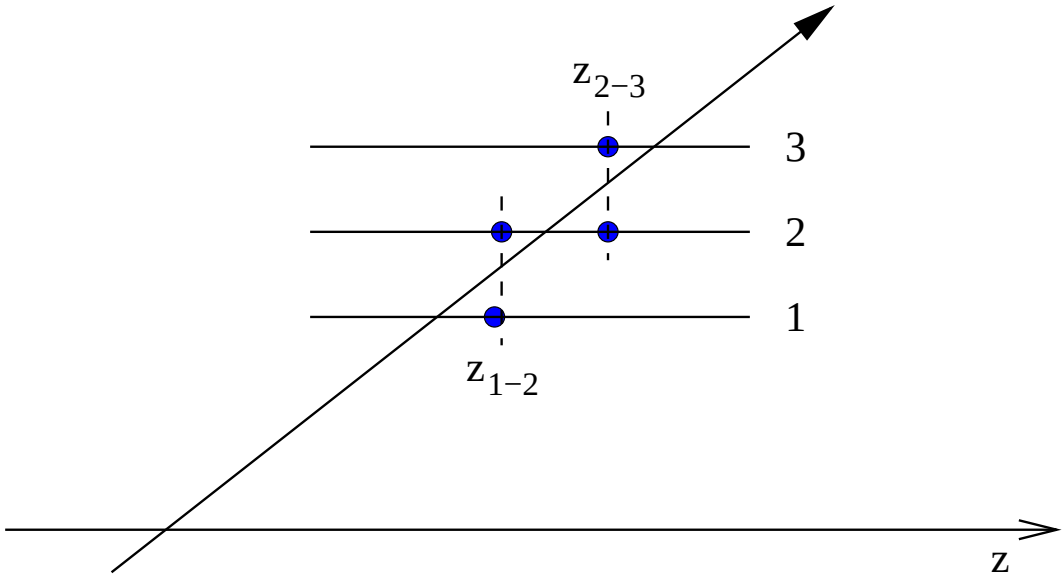

Figure 5.11: A charged particle leaving 4 space points in the photon detector [75].

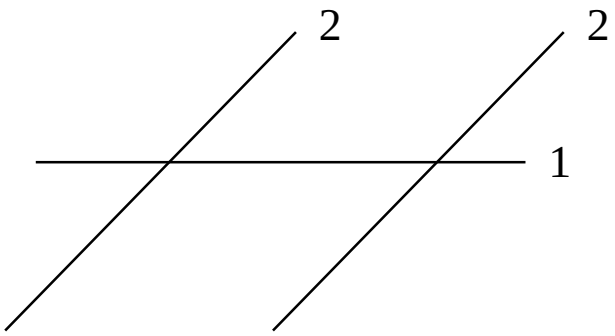

Figure 5.12: Two clusters in layer SGI2 crossing one cluster in layer SGI1. The energy of the cluster on SGI1 is split between the clusters on SGI2 and assigned to each space point [75].

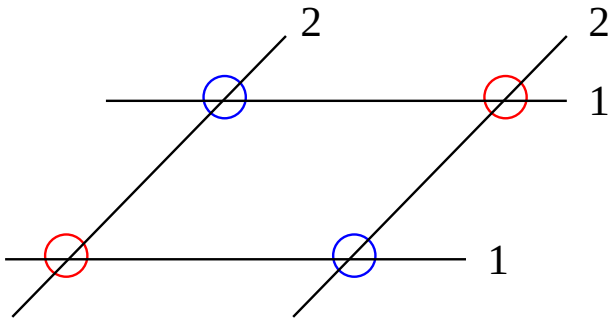

Figure 5.13: Two ghost points created by the crossing of two clusters on each of two photon detector layers [75].

5.4.4 Data Tables

A Monte Carlo or experimental data event sample contains information stored in several tables. In both cases, the tables dataSiliRec, dataSciRec and dataPhotoRec,

shown in tables 5.3, 5.4 and 5.5 respectively, are present. These tables represent the digitised response of each individual subdetector. In the case of Monte Carlo generated events samples, the table values are filled with simulated detector responses to the simulated particle traversing the volume of the detector. In addition, the Monte Carlo event samples contain an additional table, mcHit (table 5.6), which provides the exact parameters of the interaction between the particle and the detector, including the position of the space point in 3 dimensions. Other tables in the Monte Carlo samples which were important for tracking are the mcTrack and mcVert tables, containing exact generated track and vertex parameters respectively. The tests of the tracking were performed by comparing the reconstructed track parameters with the parameters given in the mcTrack table.

dataSiliRec	
ID	Entry number
iStrip	Strip number 1-128/1001-1128
iADCHigh	ADC value, high gain channel
iADCLow	ADC value, low gain channel
rPulsHigh	Energy deposition, high gain channel
rPulsLow	Energy deposition, low gain channel
iCMHigh	Common mode noise high gain channel
iCMLow	Common mode noise low gain channel
dgDETS	Detector component identifier

Table 5.3: ADAMO table for digitised silicon detector. Using the iStrip numbering convention, 1-128 denotes n-side of the TIGRE, 1001-1128 denotes the p-side. This convention is in place to make the best use of disk space.

dataSciRec	
ID	Entry number
iPMT	PMT channel number
iADC	ADC value
rPuls	Energy deposition
dgDETS	Detector component identifier

Table 5.4: ADAMO table for digitised SciFi detector.

5.5 Cosmic Ray Tracking

Besides those emitted during solar flare events, cosmic rays originate from outside the solar system. Primary cosmic rays have a peak in their energy distribution

dataPhotoRec	
ID	Entry number
iPMT	PMT channel number
iADC	ADC value
rPuls	Energy deposition
dgDETS	Detector component identifier

Table 5.5: ADAMO table for digitised photon detector.

mcHit	
ID	Entry number
X	x-coordinate of space point
Y	y-coordinate of space point
Z	z-coordinate of space point
XEnter	x-coordinate at volume entrance
YEnter	y-coordinate at volume entrance
ZEnter	z-coordinate at volume entrance
Module	Module number
TOF	Time of Flight (w.r.t HERA clock) at entrance
E	Energy
rDE	Energy loss
iGType	GEANT particle type
iStak	GEANT stack number
mcTrack	Track associated with space point
mcVert	Vertex associated with space point
dgDETS	Detector component identifier

Table 5.6: ADAMO table listing space points from generated Monte Carlo tracks.

at about $0.3GeV$ and interact with atmospheric particles to produce muons which make up the bulk of cosmic rays detected at sea level. Here the muons' angular distribution is proportional to $cos^2\theta$ at their characteristic energy of $E_\mu = 3GeV$. The muon flux at sea level varies with geographical latitude, typical flux at DESY, Hamburg is 100 events per square metre per second.

Cosmic ray muon events were used to test several characteristics of the Recoil Detector during the test experiment of 2005. Of particular relevance to tracking is the detector alignment. Following the detector installation into the HERMES spectrometer, cosmic ray muons will still be used for such studies.

5.5.1 Monte Carlo - CRAYG Cosmic RAY Generator

Early tracking routines were tested using cosmic ray events tracked by HMC through the simulated HERMES Recoil Detector. This required a custom-written cosmic ray muon event generator, CRAYG [76]. CRAYG generates muons in the energy range $2 < E_\mu < 4GeV$ and with a $cos^2\theta$ distribution, as can be seen in figure 5.14.

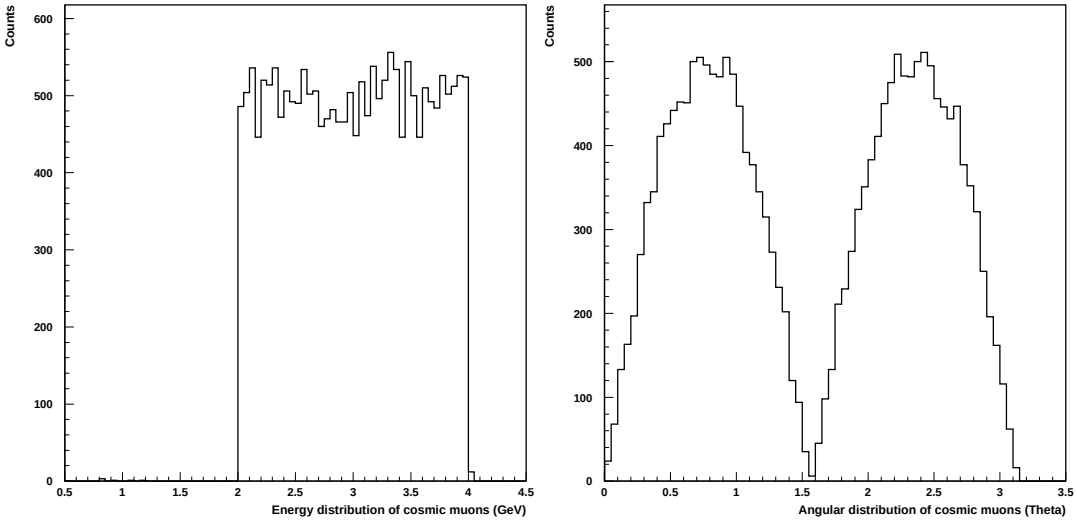

Figure 5.14: Energy (left) and angular (right) distributions of muons generated by CRAYG [76].

CRAYG simulates cosmic ray events by generating a pair of identical muons travelling in opposite directions from a common vertex within the Recoil Detector volume. This enables the most efficient use of processor time; most muons will pass through active detector volumes in this setup, producing the same effect as a single muon from an external vertex. The vertex position is a point selected by a random number generator on a region in the (x, z) plane, as illustrated in figure 5.15.

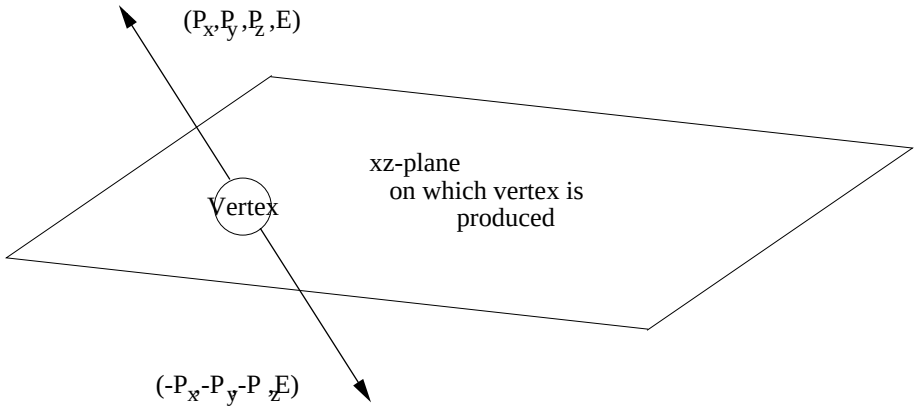

Figure 5.15: CRAYG generated muon pair with vertex constrained to (x, z) plane [76].

CRAYG Monte Carlo samples contain one cosmic event per record, without simulated background.

5.5.2 Track Finding

Track finding for cosmic rays relies on pattern matching to a track prototype given by a parameterised line equation in 3 dimensions. The finding algorithm requires two initial "seed" points, which are provided by the photon detector naturally as it is used as the cosmics trigger. For testing with the Monte Carlo the seed points are provided by a pair of hits on the outer layers of opposing silicon modules as a digitised simulation of the SciFi and photon detectors was unavailable during development of the CRAYG generator. The seed is obtained simply by performing a search over individual detector planes.

A line in 3 dimensions can be written as the parametric equation:

$$\vec{a} = t\vec{b} + \vec{c} \tag{5.3}$$

where $\vec{b}$ can be interpreted as a vector identical (except, not at a fixed point in the coordinate system) to the corresponding line, $\vec{c}$ as an offset vector and $\vec{a}$ as the vector joining a point on the line and the coordinate origin. The t parameter specifies the fraction of the length of $\vec{b}$ to which $\vec{a}$ points, $0 < t < 1$ for points on the line. External collinear points can have $t < 0$ or $t > 1$. This is illustrated in figure 5.16.

The line equation is split into components according to:

$$\begin{aligned} a_x &= tb_x + c_x \\ a_y &= tb_y + c_y \\ a_z &= tb_z + c_z \end{aligned}$$

and the initial parameters $\vec{b}, \vec{c}$ are obtained from the two seed points:

$$\begin{aligned} c_x &= x_1, b_x = x_2 - x_1 \\ c_y &= y_1, b_y = y_2 - y_1 \\ c_z &= z_1, b_z = z_2 - z_1 \end{aligned}$$

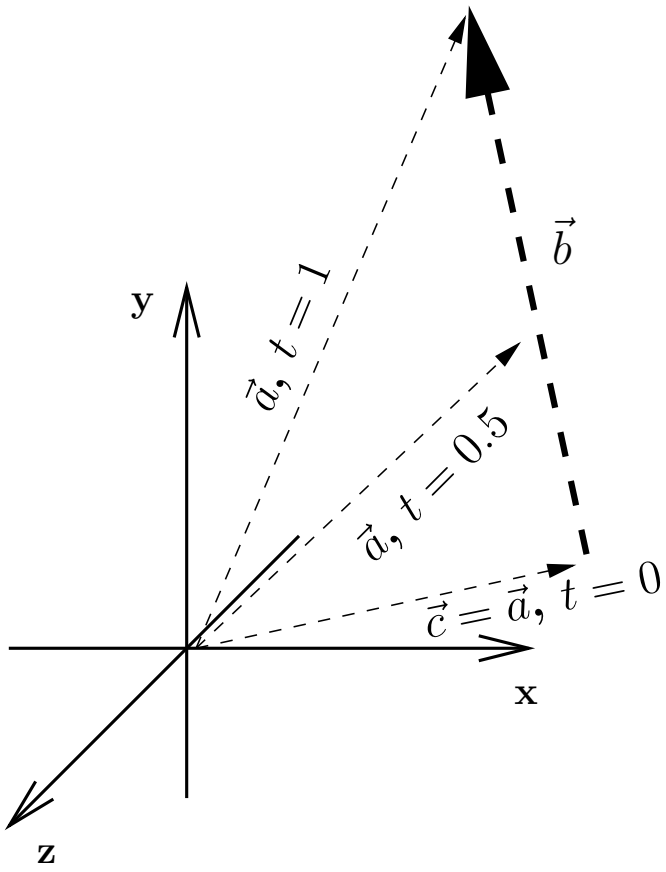

Figure 5.16: A track (strong dashed line) and the vectors which describe it in Cartesian coordinates. At $t = 0$, the pointing vector $\vec{a}$ is equivalent to the offset vector $\vec{c}$.

where $x_{1,2}, y_{1,2}$ refer to the corresponding components of each space point. A space point which is collinear with the line defined by the seed points satisfies the condition that upon replacing $\vec{a}$ in equation 5.3 with its coordinates, the parameter t remains the same for each component of the equation. A track finding algorithm can therefore search through space points and recalculate t for each new set of x, y and z components given by each point. The recalculated values t_x, t_y and t_z must agree to within a threshold defined by the detector resolution and the accuracy of the alignment in order for the space point to be classified as belonging to the track.

Such a parameterisation, however, leads to practical difficulties in applying thresholds. It is difficult to estimate the threshold difference acceptable for the agreement between t_x, t_y, t_z as t can only be considered a track "road width" in parameter space. This idea can be elucidated by considering a point which lies exactly on the x, y projection of the track but is displaced from the corresponding z coordinate of the track at that point. In this case $t_x = t_y$ but t_z will have a different value and so this parameterisation immediately shows which points are not collinear. As this is

still difficult to visualise, the scheme is modified to allow simple tuning of the road width.

Let a line in 3 dimensions be specified by the two points $\vec{p_1} = (x_1, y_1, z_1)$ and $\vec{p_2} = (x_2, y_2, z_2)$. The distance of the point $\vec{p_0} = (x_0, y_0, z_0)$ from the line is given by:

$$d = \frac{|(\vec{p_2} - \vec{p_1}) \times (\vec{p_1} - \vec{p_0})|}{|\vec{p_2} - \vec{p_1}|} \tag{5.4}$$

where terms enclosed in bars denotes the vector norm. The full derivation is presented in appendix A.1. Track finding in this scheme becomes the simple task of comparing the distance between each other space point and the line defined by the initial seed points. Tests of track finding performance are unremarkable as all Monte Carlo samples are organised with a single track per event; obtaining 100% efficiency is trivial due to the possibility of using wide road widths.

5.5.3 Track Fitting

Two different methods of track fitting have been tested with the CRAYG cosmic generator, one of which was also applied to actual data taken during the cosmics recoil test experiment. In this case momentum reconstruction is unimportant as only geometrical information is relevant to alignment. The reconstructed track parameters are the vertex coordinates (y is constrained to zero) and the track angles θ and ϕ, illustrated in figure 5.17.

3 Dimensional Fitting

This approach requires the minimisation (using the MINUIT package from CERN) of an energy function which is defined by the line equation described by the track and its associated points in 3-space. The method uses a least squares fit with errors measured orthogonally to the proposed line rather than measured in components [78]. The energy function is written in terms of a matrix whose smallest eigenvalue corresponds to the energy minimum. The 3-D fitting method is described in appendix A.2.

The fitting routine was tested with 10,000 CRAYG generated Monte Carlo events, with clustering implemented only for the silicon detector as no digitisation routines were available for the SciFi and photon detectors. Space points in the photon detector and SciFi were not used. Figures 5.18 and 5.19 show the difference between the

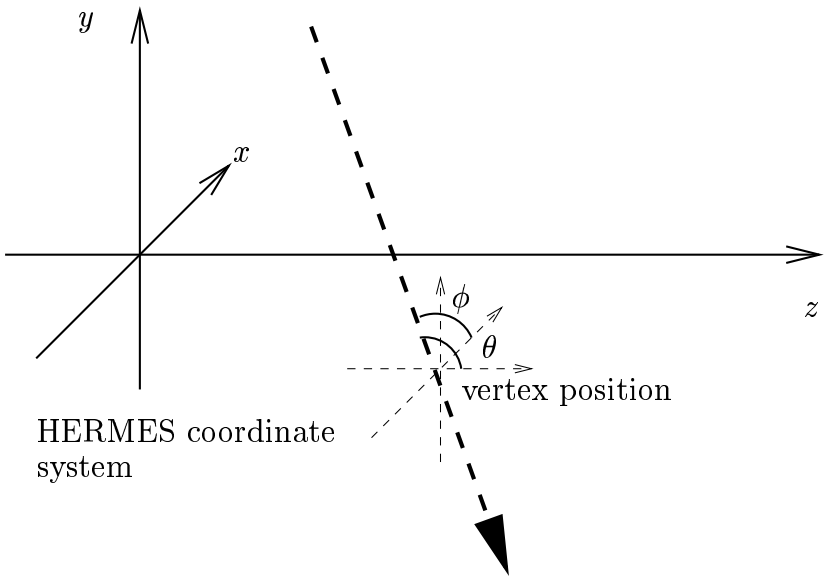

Figure 5.17: A cosmic ray track (strong dashed line) and the angles which define it within the detector coordinate system. Vertex constrained to x, z plane ($y = 0$). ϕ is in fact azimuthal angle defined between x-axis and projection of track on x, y plane, anticlockwise and $0 < \theta < \pi$.

reconstructed and CRAYG generated primary vertices and track angles respectively.

2 Dimensional Fitting

An alternative approach is to combine 2 dimensional fits. A χ^2 fit is performed on the projection of the track on the x, y and the z, y plane. If the fits are successful on the two planes the results are combined and track parameters are subsequently retrieved. The χ^2 fit proceeds according to the method described in reference [79], section 15.3.

In the following notation, z can be substituted for x when the fit is being applied in the z, y plane. The fit to the set of points is performed with errors on both axes. Thus, for the straight line model $y(x) = a + bx$ the merit function is written as:

$$\chi^2(a, b) = \sum_{i=1}^{N} \frac{(y_i - a - bx_i)^2}{\sigma_{yi}^2 + b^2\sigma_{xi}^2} \tag{5.5}$$

where σ_{xi} and σ_{yi} are the errors (standard deviations) of the x and y components of the ith point. The weighted sum of variances in the denominator of equation 5.5 can be understood both as the variance in the direction of the smallest χ^2 between each data point and the line with the slope b, and also as the variance of the linear

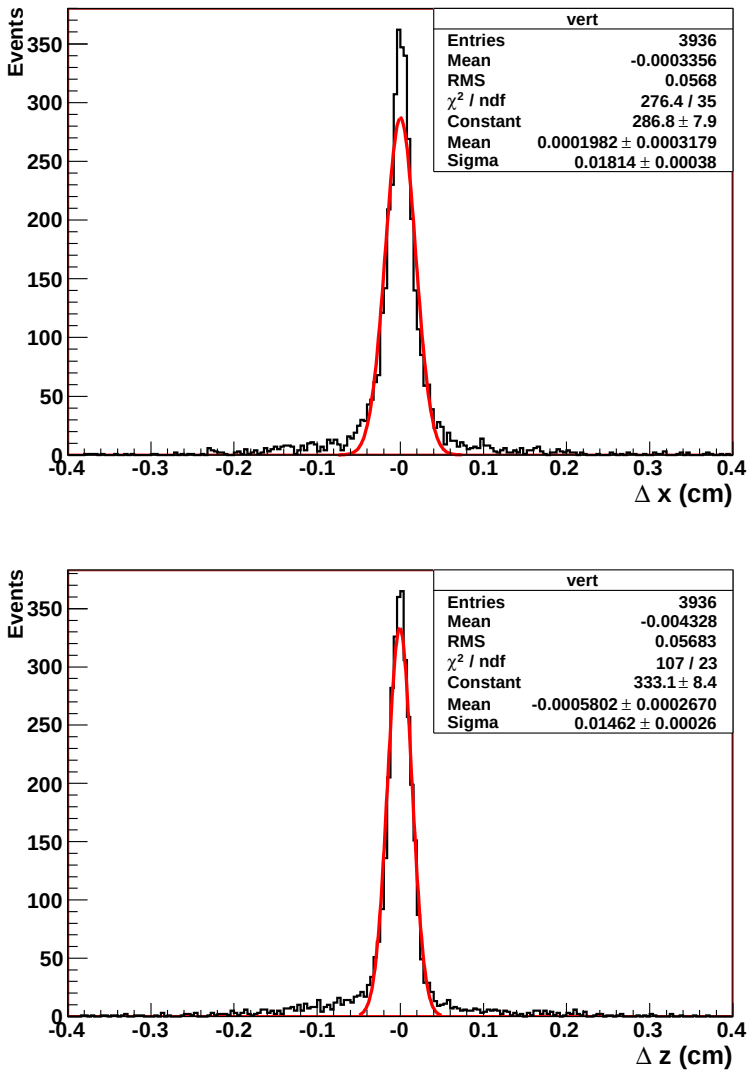

Figure 5.18: Difference in Monte Carlo generated vertex components and those reconstructed by the 3D fitting of cosmic tracks. The y component is not shown as the vertex is constrained to $y = 0$. The red curve shows a Gaussian fit.

combination $y_i - a - bx_i$ of two random variables x_i and y_i,

$$Var(y_i - a - bx_i) = Var(y_i) + b^2 Var(x_i) = \sigma_{yi}^2 + b^2\sigma_{xi}^2 \equiv 1/w_i. \qquad (5.6)$$

The sum of the square of N random variables, each normalised by its variance is thus χ^2 distributed. The task of track fitting in this case requires minimisation of equation 5.5 with respect to a and b. The occurrence of b in the denominator of equation 5.5 however, makes the resulting equation for the slope $\frac{\partial\chi^2}{\partial b}$ nonlinear. The

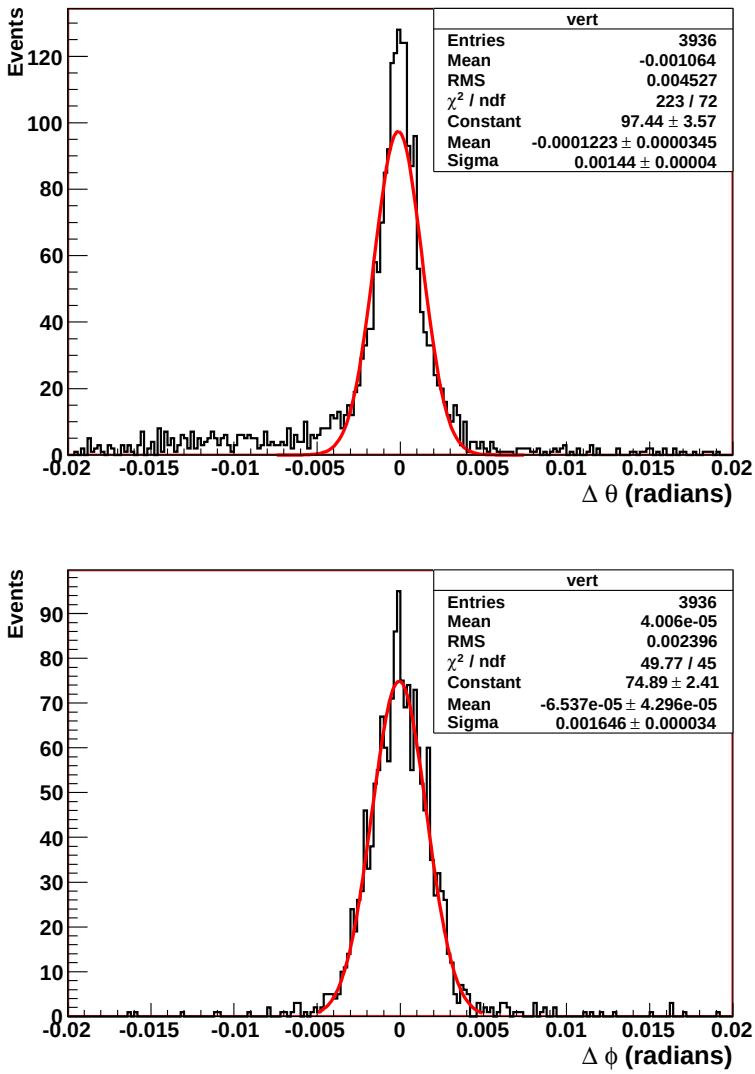

Figure 5.19: Difference in Monte Carlo generated vertex components and those reconstructed by the 3D fitting of cosmic tracks. The red curve shows a Gaussian fit.

corresponding equation for the intercept, $\frac{\partial \chi^2}{\partial a} = 0$, remains linear and yields

$$a = \frac{\sum_i w_i(y_i - bx_i)}{\sum_i w_i} \tag{5.7}$$

where w_i is defined by equation 5.6. The parameters a and b are obtained by minimising a one-dimensional function with respect to b while cross-checking with equation 5.7 at each stage to ensure that the minimum with respect to b is also minimised with respect to a. In this case Brent's method is an appropriate solution for performing the minimisation. This approach applies successive inverse parabolic interpolations until convergence is achieved. Details of Brent's method can be found

in reference [79], section 10.2.

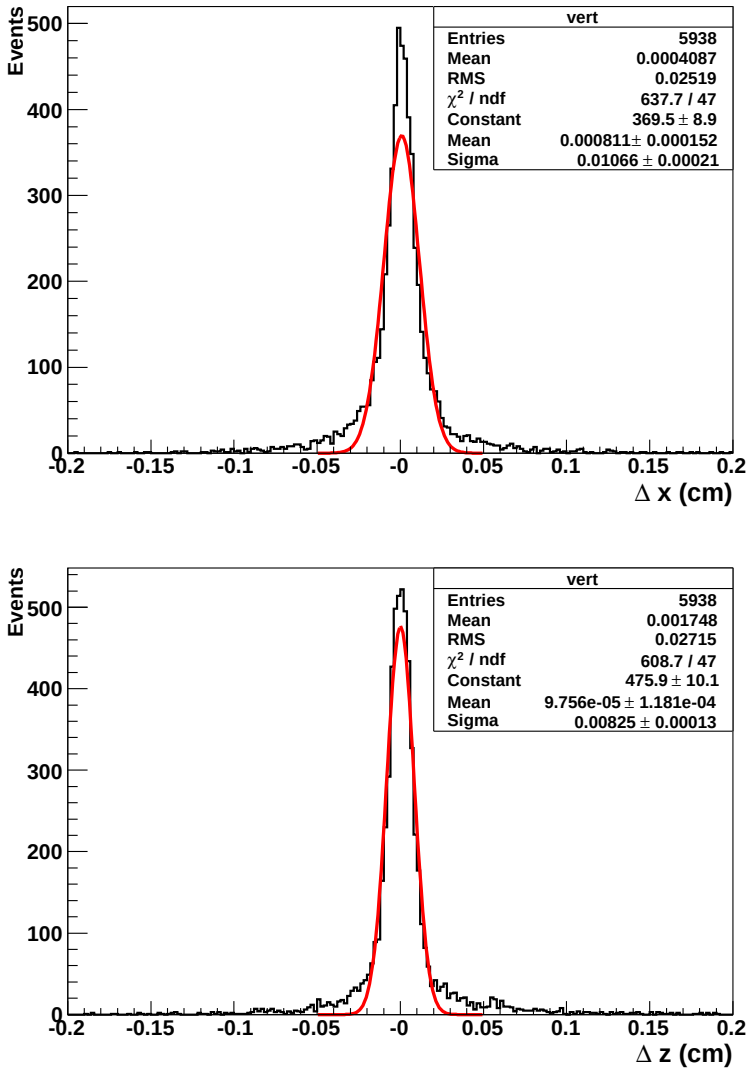

Figure 5.20: Difference in the x (top) and z (bottom) vertex components reconstructed with the 2D fit of cosmic tracks and Monte Carlo generated vertex components. The y component is not shown as the vertex is constrained to $y = 0$. The red curve shows a Gaussian fit.

This procedure was tested using the CRAYG Monte Carlo sample. At this stage, the implementation of the SciFi detector into the Recoil Monte Carlo existed as a set of barrel-shaped detector layers only. Consequently, clustered SciFi hits for tracking were unavailable, but the space point position tracked by the Monte Carlo could be used to test the 2 dimensional fitting routine. Reconstruction plots are shown in figures 5.20 and 5.21.

The 2 dimensional method provided a significantly better reconstruction as the minimisation stage of the 3 dimensional algorithm would frequently terminate at

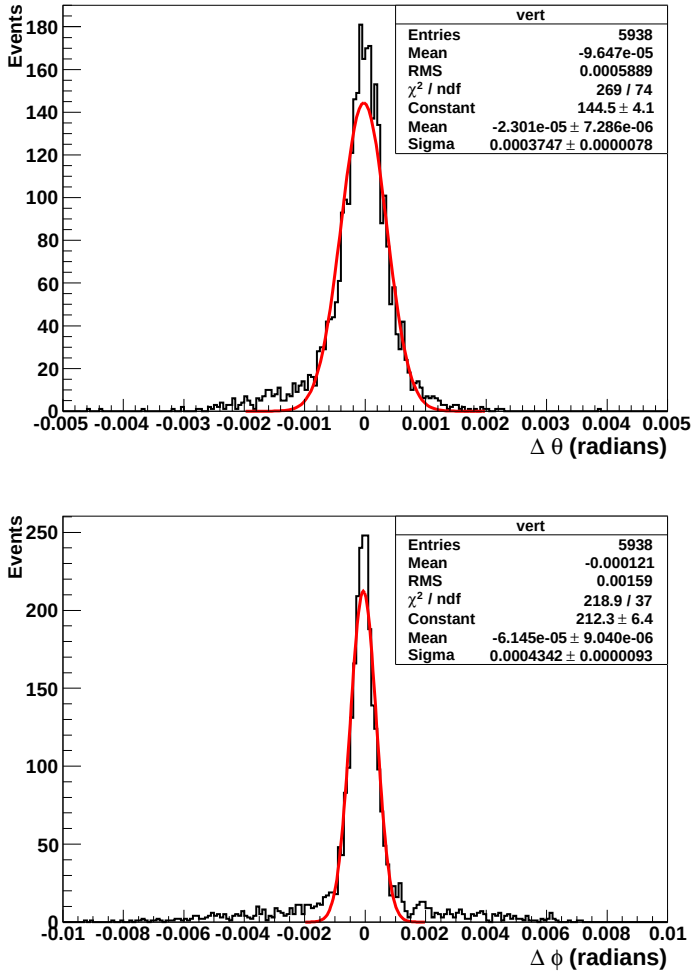

Figure 5.21: Difference in the track angles reconstructed with the 2D fit of cosmic tracks and Monte Carlo generated track angles. The red curve shows a Gaussian fit.

local minima. The absence of abnormally reconstructed tracks, coupled with the improved execution speed over MINUIT, resulted in the decision to use the χ^2 2 dimensional method for cosmics tracking. A typical Monte Carlo reconstructed event is shown in figure 5.22.

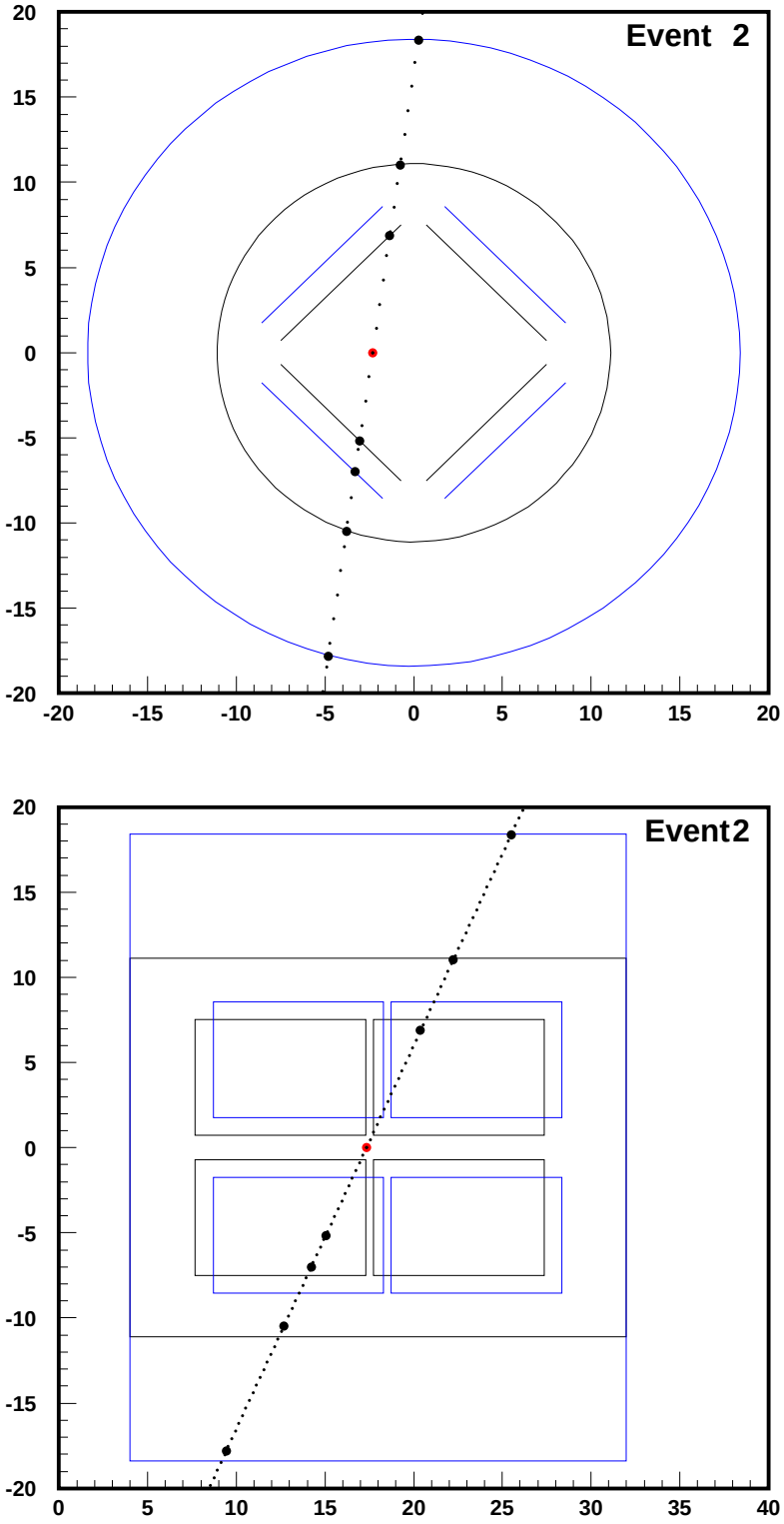

Figure 5.22: A Monte Carlo generated track producing hits in the silicon and SciFi detectors. The red point is the primary vertex, the dotted line shows the reconstructed track. The top diagram shows the x, y plane with the beam entering into page. The bottom diagram is the z, y plane with the beam entering from the left.

5.5.4 The Cosmic Ray Test Experiment

The cosmic ray test experiment, conducted between April and September of 2005, aimed to collect cosmic ray data in order to study the separate subsystems of the Recoil Detector. Usefully, the test experiment also helped to improve the understanding of the mechanical setup of the Recoil Detector and provided HERMES the ability to anticipate some of the problems likely to arise during its installation into the spectrometer.

The entire Recoil Detector (including magnet) was set up in the East HERA Hall outside the interlock region. The detector was operated continuously in several data taking modes, save for regular short periods when the detector modules needed to be switched off to prevent damage (e.g. when ramping the magnet up and down), or when other maintenance was being carried out. In total, 6610 runs were taken during the operating period of the test experiment.

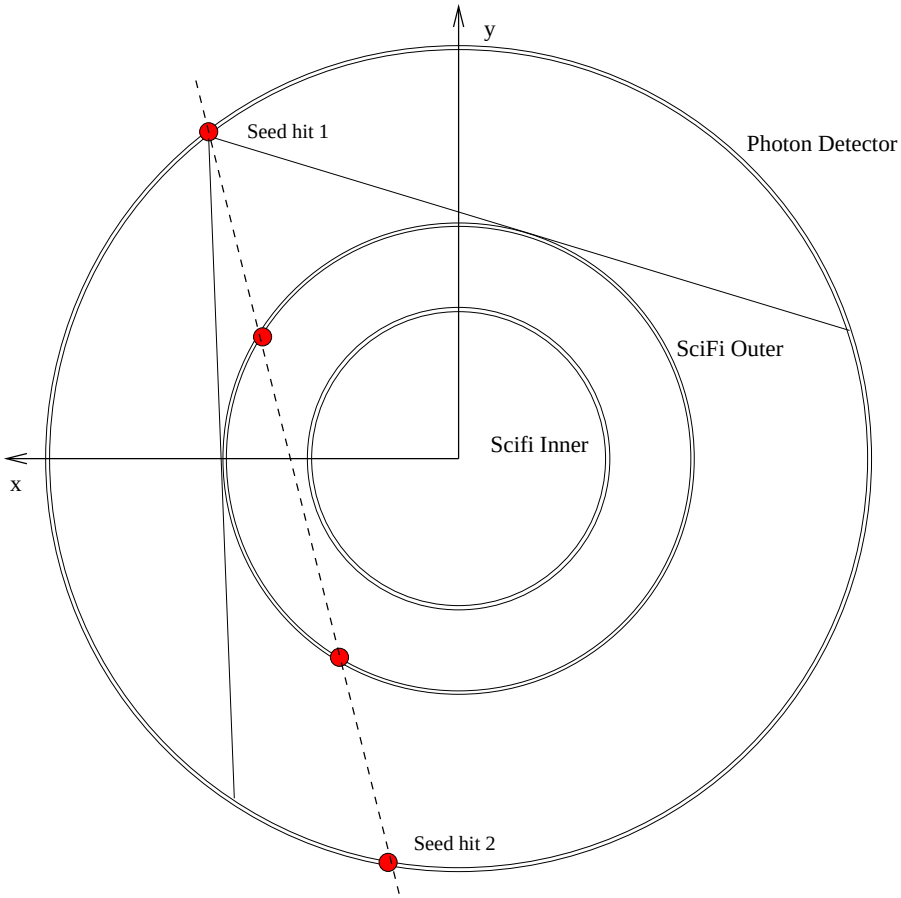

Figure 5.23: Illustration of the region to which the search for a second seed space point is constrained in a typical cosmic event. Dashed line shows path of track, red circles are points left by the track. Search region is defined by opening angle between the photon detector and the SciFi, and the first found seed point.

The parameters for track finding in the test experiment were modified slightly. Firstly, a restriction was placed on the seed search through the photon detector. With its use as a cosmics trigger, an initial seed of two points was only selected when their angular separation was such that the track must have passed through the outer SciFi barrel (figure 5.23).

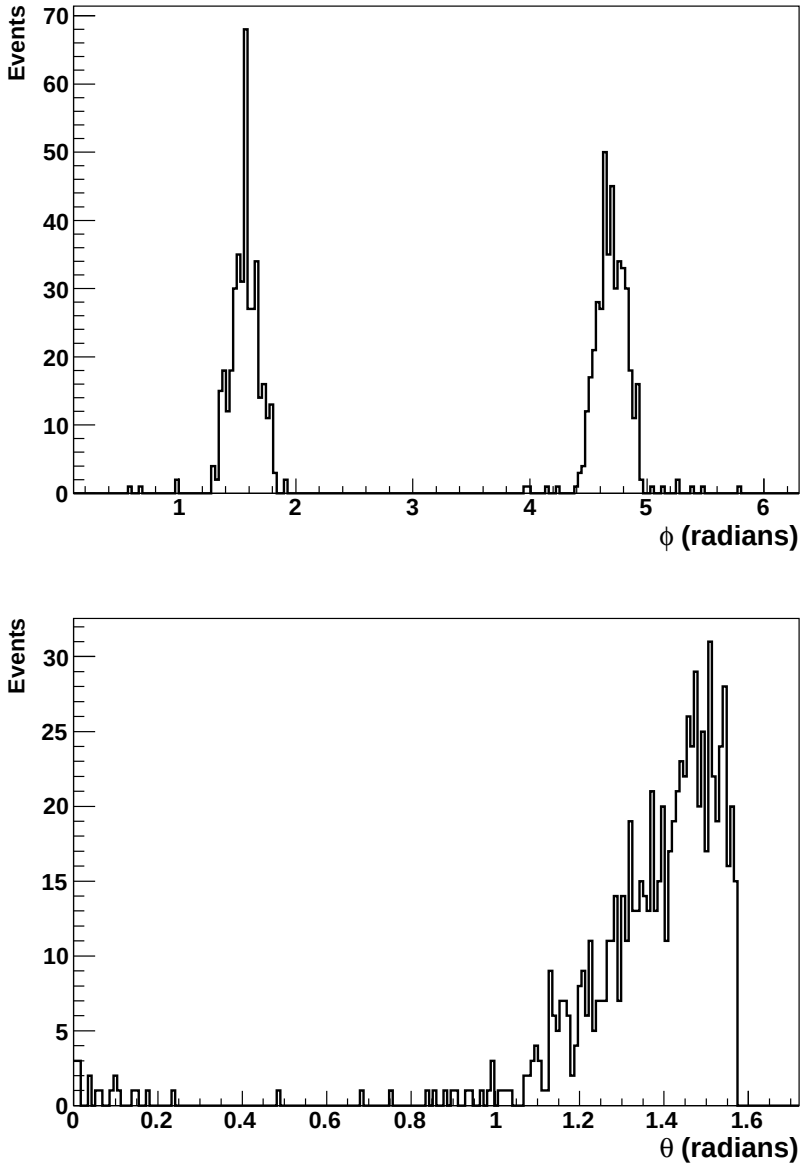

Figure 5.24: ϕ (upper) and θ (lower) distributions for a single cosmics data taking run with the test setup.

This constraint resulted in a ϕ distribution of reconstructed tracks with strong peaks at $\pi/2$ and $3\pi/2$ and few counts elsewhere. This is shown in figure 5.24. The double peak feature is seen as a track originating from above the recoil detector is, with this setup, indistinguishable from a track originating below it.

The θ distribution (figure 5.24) has a different profile to the CRAYG generated cosmics shown in figure 5.14. The convention for measuring θ in the CRAYG generator is different to that in the track reconstruction; the tracking code measures track parameters using the standard convention in cylindrical polar coordinates in which $0 \leq \theta \leq \pi$, whereas in CRAYG $0 \leq \theta \leq 2\pi$ in order to separate the two muons generated back-to-back.

It is expected that the θ distribution should be symmetric around $\pi/2$, something which is not observed. The behaviour seen in figure 5.24 is due to the indistinguishability of a straight track at angles $\phi = \phi, \theta = \pi/2 - \theta'$ and one at angles $\phi = \phi + \pi, \theta = \pi/2 + \theta'$. A typical tracked cosmic ray can be seen in figure 5.25, which also demonstrates the space point reconstruction for the SciFi and photon detectors.

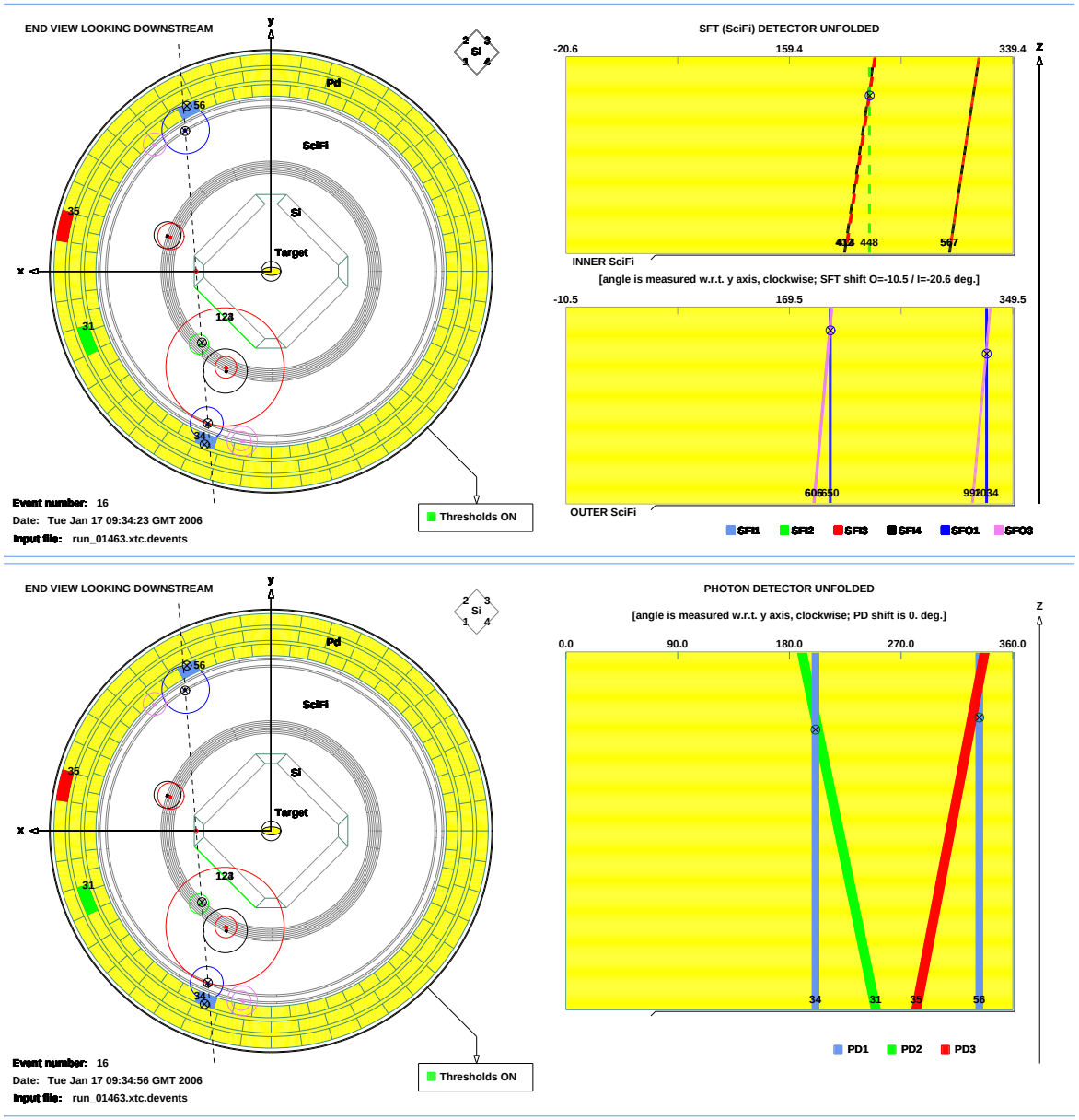

Figure 5.25: Event display [80] screen captures for an event with a single cosmic ray track. Front cross section on the left, unrolled SciFi detector (upper) and photon detector (lower) on the right. Hits on the photon detector are shown as coloured blocks, hits on the SciFi are shown as encircled dots. The circle diameter shows the relative signal size in the SciFi. Reconstructed space points on the right hand diagrams are shown as encircled crosses, the dashed lines depict struck stereo layer fibres. Diagrams are not to scale.

5.6 Proton and Pion Tracking in the Magnetic Field

As discussed in chapter 4, the primary functions of the Recoil Detector are, firstly, to enable event-level exclusivity by detecting the recoiling proton from the beam-

target interaction and secondly, to enhance background suppression by detecting pions emitted from Δ decays. In both cases the particles are emitted close to the beam, all proton and pion tracking (referred to as curved tracking) described in this section is performed with this constraint as an assumption.

The curved tracking has been tested with Monte Carlo event samples only. The HERMES Recoil Detector Monte Carlo developed during the development of the CRAYG generator has been employed for this purpose.

5.6.1 Recoil Detector Acceptance

The momentum and θ acceptance of the recoil detector are depicted in figure 5.26. The ϕ acceptance is taken to be 2π due to the coverage of the scintillating fibre tracker. In practice, however, this value is reduced for the purposes of curved track finding as at least one space point in the silicon detector is required for such a track to be found. Small gaps in ϕ are present in the acceptance of the silicon detector.

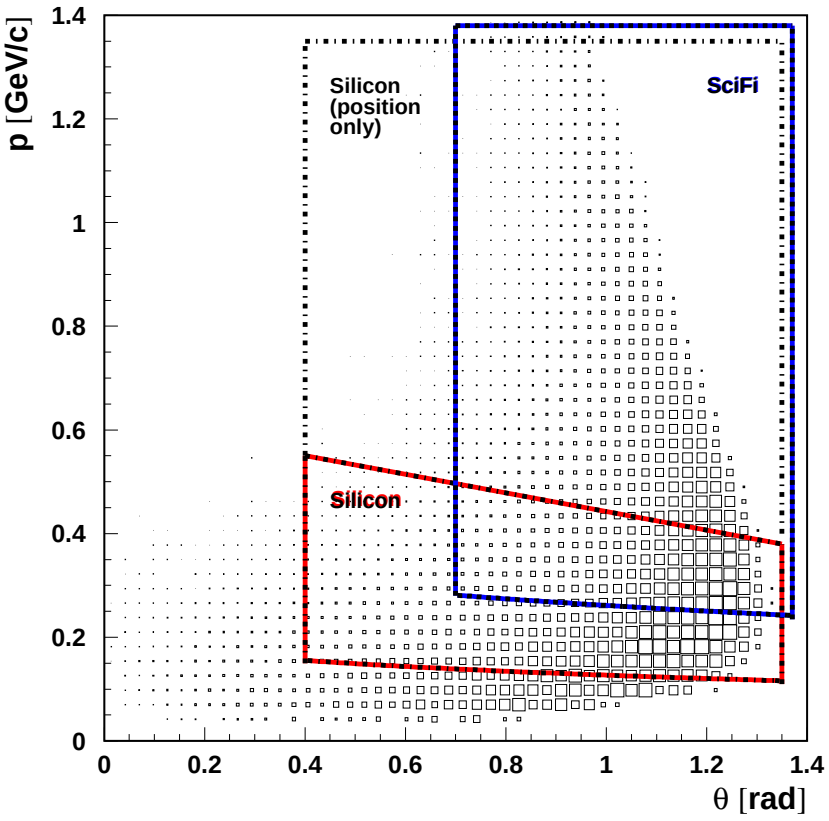

Figure 5.26: Recoil detector acceptance in p and θ. [65]

5.6.2 Monte Carlo

The curved tracking was tested with events produced by two generators. Firstly, the gmc_ dvcs generator simply reproduces the final-state particle tracks originating from a DVCS event: a positron, photon and proton in the case of HERMES, with angular and kinematical distributions to match those empirically determined. No background accompanies each event; all additional tracks in such an event originate from an interaction between the particles generated at the primary vertex and the material of the detector. The momentum and angular distributions of the generated DVCS protons are shown in figure 5.27.

The gmc_dvcs generator provides a useful means to test the track fitting routines. Naturally, gmc_dvcs samples were also useful during tests of the track finding code.

The track finding routine was initially tested with Monte Carlo events generated by the PYTHIA program which can be used to generate high-energy physics events from interactions between two incoming particles. PYTHIA provides an accurate representation of event properties in a wide range of reactions, with emphasis on those in which the strong interaction plays a role and so multihadronic final states are produced [81]. In the case of HERMES, PYTHIA simulates positron-proton interactions resulting in samples containing tracks from a variety of processes, of which only a subset are useful for studies of tracking performance. The momentum and angular distributions of π^- and π^+ events in a PYTHIA sample are shown in figure 5.28.

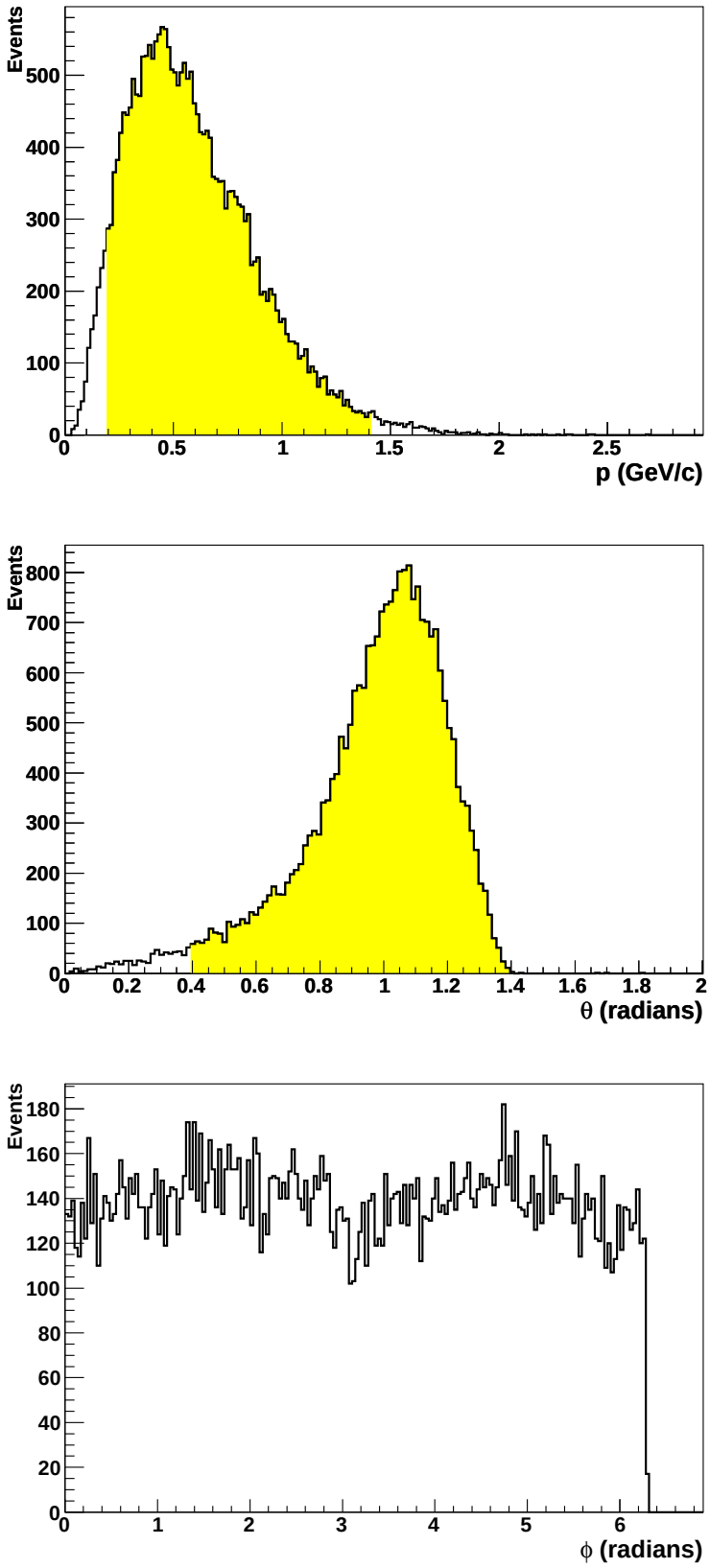

Figure 5.27: Momentum and angular distributions for a sample of gmc_dvcs generated protons. The shaded regions show the recoil detector acceptance.

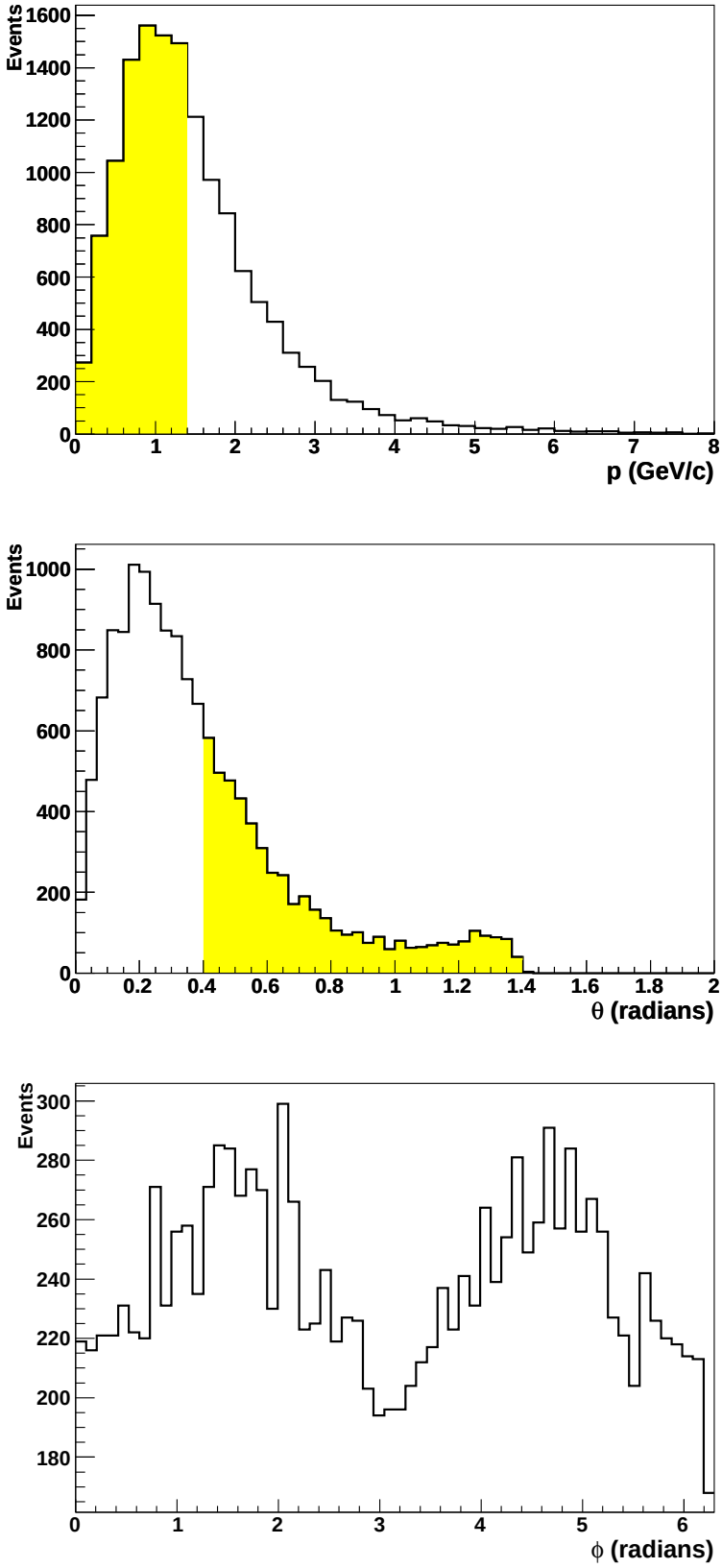

Figure 5.28: Momentum and angular distributions for a sample of PYTHIA generated π^- and π^+ particles. The shaded region in the upper plot shows the approximate upper limit of DVCS/Bethe-Heitler proton momentum at the HERMES kinematical region, and in the middle plot shows the Recoil Detector Acceptance.

The PYTHIA samples used to test recoil tracking did not contain proton tracks inside the acceptance of the Recoil Detector. Restrictive cuts on the Recoil Detector acceptance led to a large proportion of the statistics accumulated with PYTHIA being rejected. Figure 5.29 illustrates the track multiplicity in one PYTHIA event sample.

All events in which track multiplicity ≥ 1 in figure 5.29 are within the geometrical acceptance of the Recoil Detector. Tracks outside the momentum acceptance are included as the idealised space point reconstruction provided by HMC enables track finding with XTC. Most tracks in the sample belong to charged pions, occasionally a μ^- or positron track is within the Recoil Detector acceptance (and in this case will be tracked by XTC) but these events contribute only a small amount to the overall multiplicity. The PYTHIA event samples test the ability of the track finding routine alone to recognise the track shape.

A further test of the track finder was performed using the gmc_dvcs generator. Although gmc_dvcs generates a DVCS event per record, with a single proton track, a sample of 25,000 DVCS tracks could be combined in such a way that the resulting sample contained 5,000 five-track events. The samples of events with 1 to 5 tracks provided a fairer study of the effectiveness of the track finder as the track multiplicity increased; the overall distribution of track parameters would be identical in each case.

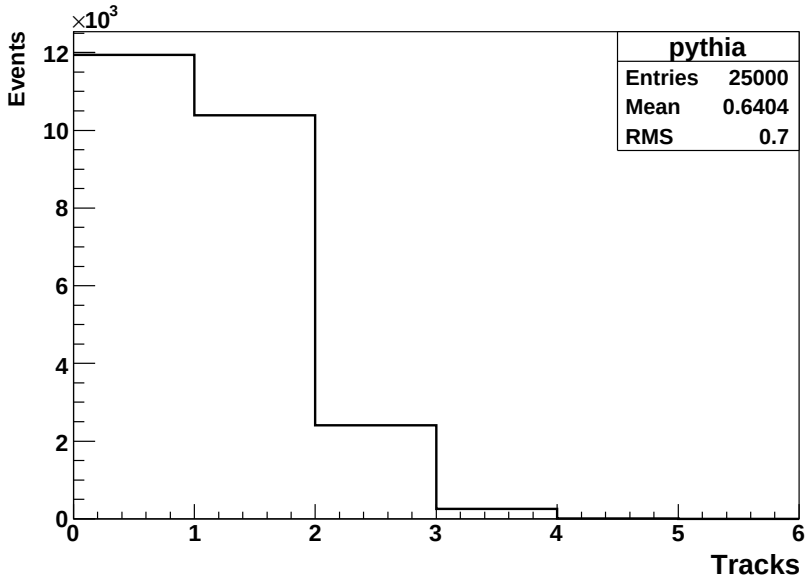

Figure 5.29: Tracks in a typical PYTHIA sample satisfying the requirement that the sum of the space points measured by the silicon and SciFi is ≥ 3.

5.6.3 Magnetic Field

The Recoil Detector superconducting magnet generates a ~ 1 Tesla magnetic field in which charged particles are deflected. The SciFi detector expands the capability of the Recoil Detector to reconstruct particle momenta by providing space points in addition to those provided by the silicon detector and so measures the curvature of the particle tracks in the magnetic field.

The momentum of a charged particle travelling in a homogeneous, longitudinal magnetic field is proportional to its (constant) radius of curvature. The Recoil Detector superconducting magnet produces an inhomogeneous field, however, so tracking routines must be modified in order to reconstruct particle momenta more accurately. For this purpose a magnetic field map is required.

Prior to the construction of the magnet, a field map was calculated by the Efremov Institute, from this an input file for XTC was created. The calculated map describes a rotationally symmetric solenoidal magnetic field which spans the entire z and r range of the HERMES spectrometer at a resolution of 2 cm in both coordinates. This resolution was judged to be insufficient as the magnetic field only affects charged particle tracking for the Recoil Detector up to the radius of the outer SciFi (~ 18.3 cm). The calculated field map is interpolated with a 2-dimensional cubic spline function in order to obtain a field map with 1 cm resolution. This is shown in figure 5.30.

A comparison with a measured magnetic field map was unavailable until October 2004. Figure 5.31 shows a comparison between the calculated and measured magnetic fields. As the field was measured to 1 cm resolution, no subsequent interpolation is required.

The interpolated calculated magnetic field compares well with the measured results as can be seen in figure 5.31, all tests of the curved tracking in an inhomogeneous field use the interpolated field map.

5.6.4 Track Finding

The track finding routine for proton and pion tracks in the magnetic field proceeds similarly to the cosmics track finding described in section 5.5.2. In this case the track prototype is given by a parameterised helix equation in 3 dimensions. The curved track finding algorithm requires as input the complete "pool" of space points on all surfaces of the silicon and SciFi detectors, and selects any three points (satisfying

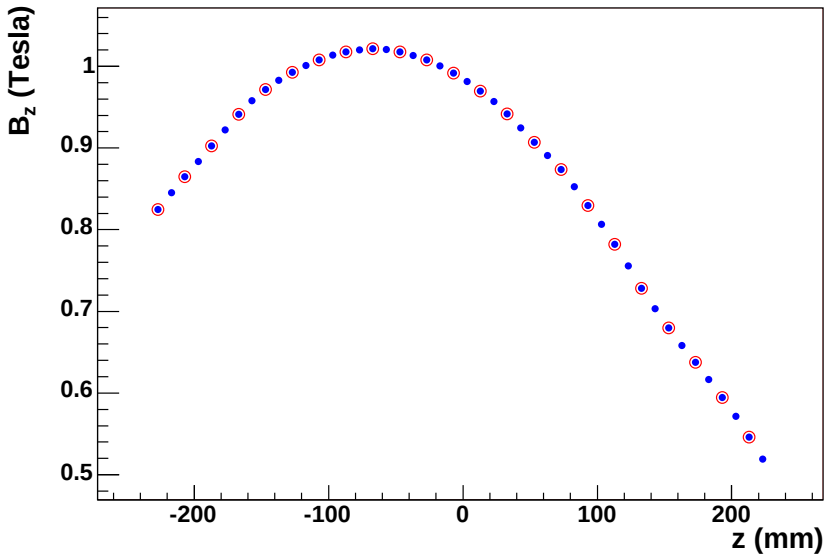

Figure 5.30: Calculated magnetic field component B_z (red circles) and result of interpolation (blue dots). The magnetic field is depicted at $r = 0$ cm, the diagram covers the entire z-length of the Recoil Detector.

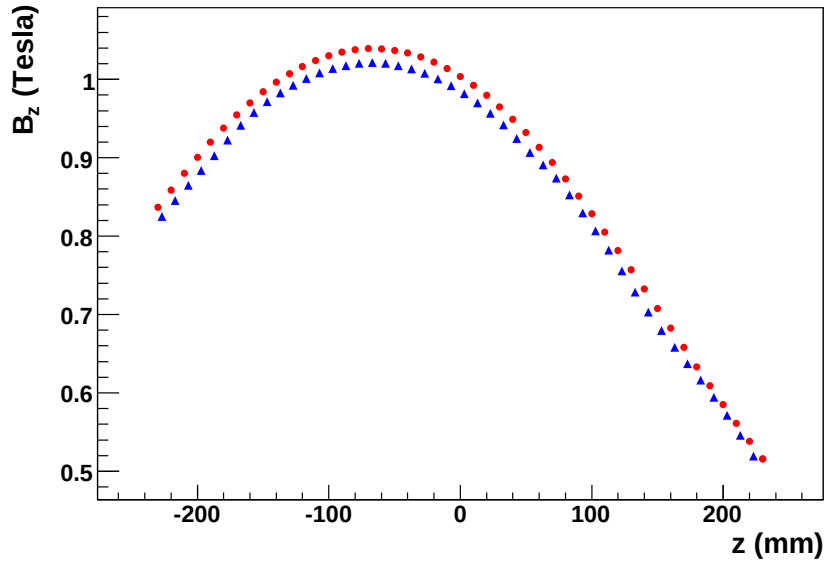

Figure 5.31: Measured (red circles) and interpolated calculated (blue triangles) magnetic field component B_z inside Recoil Detector, at $r = 0$ cm [82].

certain cuts) to form a track seed which defines the helix.

One of the three seed points may be provided by the primary vertex which is reconstructed by HRC. In the absence of the primary vertex, the three points must lie in separate detector layers. In both cases the set must possess a maximum angular separation defined by the curvature produced by particles at the lower momentum

cutoff for the Recoil Detector. At $\sim$ 110 MeV, this cutoff translates to a maximum bending angle of 0.785 radians inside the Recoil Detector. Figure 5.32 illustrates the search region defined by the track seed.

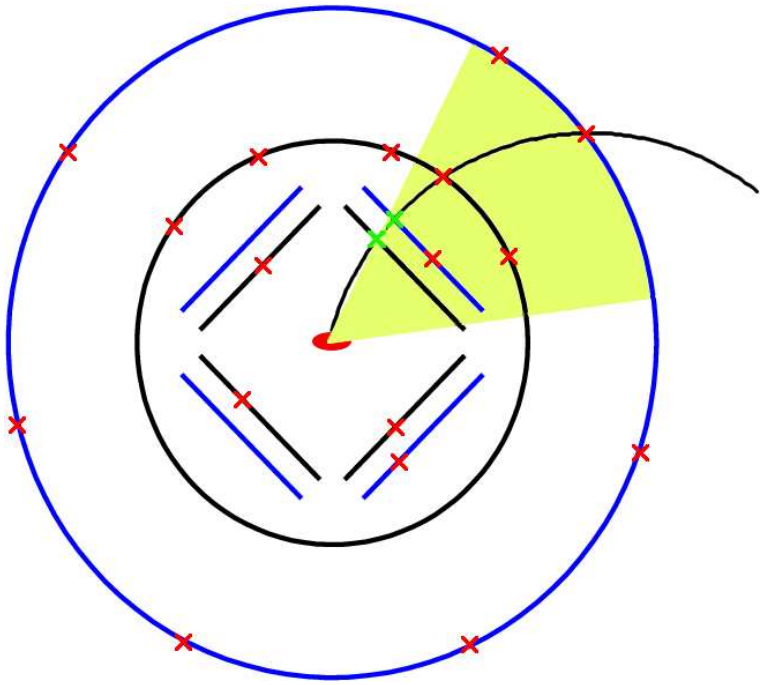

Figure 5.32: Illustration of angle cut applied for track finding. Opening angle of circle section (shaded region) defined by the primary vertex (central oval) and two seed space points (green crosses) in this case in the silicon detector. This cut is also applied in the opposite ϕ direction when searching for tracks from negatively charged particles.

This approach improves the speed at which tracks can be found, as space points outside the region defined by the cut are not tested for compatibility with the helical track model. In principle the opening angle should also provide for the angular deviations from a helix caused by multiple scattering inside the detector materials, however, this is not included as multiple scattering has not been accurately modelled for the Recoil Detector and the track deflection in the magnetic field is expected to be the dominant effect.

A point lying on a helix satisfies the following set of equations:

$$x = rcos(\phi) + x^0$$
$$y = rsin(\phi) + y^0$$
$$z = c\phi + z^0$$

where r is the helix radius, c is a constant which is related to the loop separation (the gradient of z with respect to ϕ) and x^0, y^0, z^0 are the coordinates of the origin of the helix in an external coordinate system. Varying the parameter ϕ selects individual points along the curve formed by the helix such that at $\phi = 0$, the coordinates $x = r + x^0, y = y^0$ and $z = z^0$. For any space point in the detector $\vec{a}^{\,i}$,

$$\vec{a}^{\,i} = \begin{bmatrix} x^i \\ y^i \\ z^i \end{bmatrix} \equiv \begin{bmatrix} r^i \\ \phi^i \\ z^i \end{bmatrix} \tag{5.8}$$

the vector $\vec{a} = \begin{bmatrix} x \\ y \\ z \end{bmatrix}$ is calculated according to the original helix equations

$$\begin{aligned} x &= rcos(\phi^i) + x^0 \\ y &= rsin(\phi^i) + y^0 \\ z &= c\phi^i + z^0 \end{aligned}$$

such that the difference $|\vec{a} - \vec{a^i}|$ gives the distance from the point to the helix. Applying a threshold on this distance establishes a track road around the helix, space points lying inside which are marked as belonging to the track defined by the 3 seed points.

Figure 5.33 demonstrates the efficiency of the track finder when reconstructing tracks from PYTHIA. Efficiency remains high for up to four particles in the Recoil Detector acceptance. Figure 5.29, however, shows strongly reduced statistics at multiplicity = 3 (256 events have three tracks), stronger still at multiplicity = 4 (10 events have four tracks), thus the large statistical uncertainty precludes any strong conclusions about the effectiveness of the track finder in this region.

Figure 5.34, on the other hand, shows the efficiency of the track finder for DVCS proton tracks. Efficiency is high for multiplicities up to five tracks although the initial drop in efficiency in going from one to two tracks is greater than expected considering the very high efficiency for a single track. This can be explained due to the occasional contamination of a found track by space points which belong to a separate track. A track is regarded as "found" if, and only if, all space points belonging to the track are correctly recognised. Extra points are occasionally found

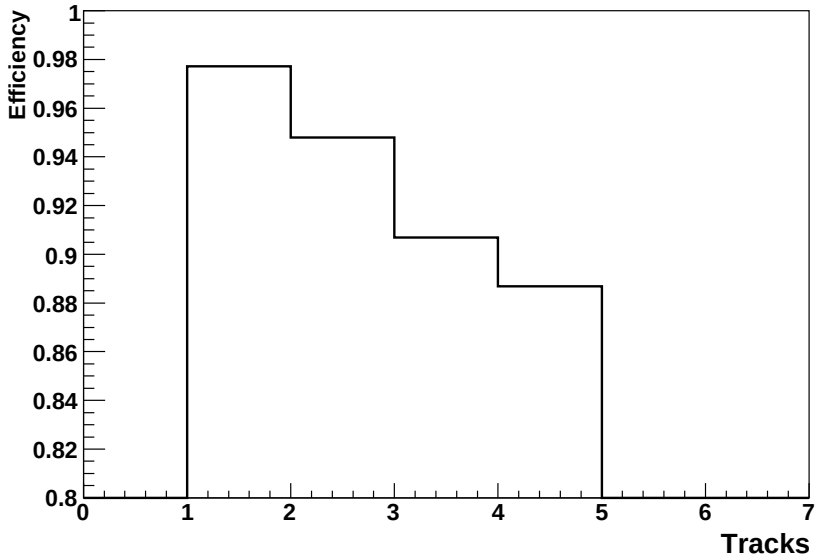

Figure 5.33: Efficiency of track finder with increasing track multiplicity. Event sample used was generated with the PYTHIA program.

when attempting to resolve two closely spaced tracks; the threshold distance between the track candidate and a space point is fairly large (1.1 cm) in order to accommodate the expected deviation from the helical shape due to scattering and magnetic field inhomogeneity. This feature is not present in figure 5.33, since in the case of the PYTHIA sample almost all two-track events come from extremely fast decays which naturally produce daughter particles back-to-back near the primary vertex. Consequently the tracks are more likely to exhibit wide angular separation. Appropriately, the steeper descent in figure 5.33 is seen at the boundary between the two and three track bins where an additional decay may produce a track which lies close to one of the tracks originating from the first decay. The difference in track finding efficiency between the gmc_dvcs sample and the PYTHIA sample is less than 2%, as figures 5.33 and 5.34 show. This is due to the very different event kinematics between the generated samples.

In the case of either the PYTHIA or the gmc_dvcs event sample, these tests calculate efficiency by only considering those tracks which are in the acceptance of the Recoil Detector, originate from the primary vertex and leave sufficient space points (≥ 3) in the subdetector volumes. Additionally, no background space points are present during the track finding procedure.

In contrast to the pure proton sample of gmc_dvcs, the PYTHIA sample includes tracks from particles with positive and negative charge. π^- particles, for example, are abundant in the PYTHIA sample, making track misidentification more likely

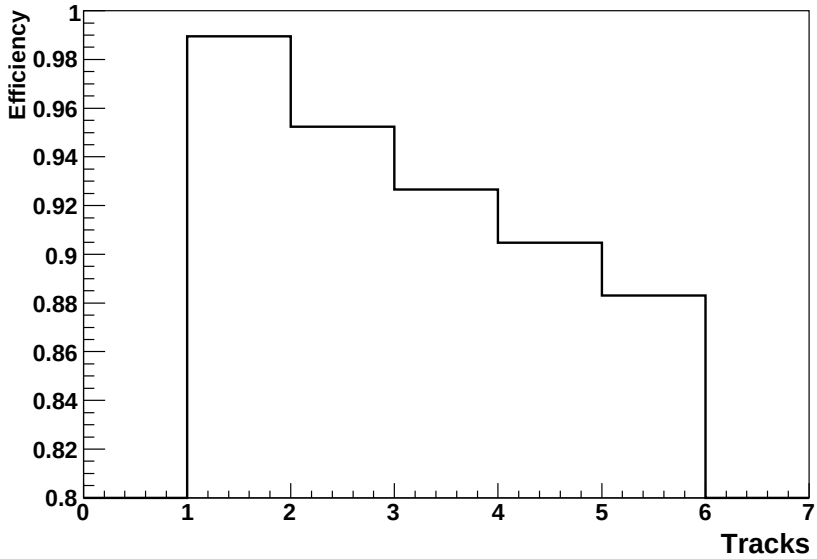

Figure 5.34: Efficiency of track finder with increasing track multiplicity. The event sample in this case was obtained using the gmc_dvcs generator.

due to the more common instance of shared hits between tracks. Unfortunately this is difficult to check as applying a charge cut on the PYTHIA sample results in a severe reduction in the statistics, and roughly zero occupation in the bins for which the multiplicity is greater than two.

The performance of the track finding algorithm may also be sensitive to the angular distribution of the generated tracks. The θ distribution of the gmc_dvcs events peaks at around $\theta = 1.1$ (figure 5.27), corresponding to large transverse and small longitudinal momentum components. The opposite is the case for PYTHIA events, the θ peak being at around $\theta = 0.25$ (figure 5.28). The acceptance of the recoil detector begins at $\theta = 0.4$ and the bulk of the PYTHIA statistics remain at these comparatively low angles. A low transverse momentum component will promote the distortion of the track shape from the expected helix because the inhomogeneous field will affect the path of the particle more strongly. Consequently, these distorted tracks may not be recognised by the track finder.

The gmc_dvcs sample had the additional advantage of high statistics at all values of track multiplicity. Imposing the cuts on the PYTHIA sample which would be necessary in order to allow a fair comparison between generators would result in extremely low statistics at low multiplicity, and almost none at all at high multiplicity. Further studies of the track finding performance are required before the algorithm may be used reliably.

5.6.5 Track Fitting

Track fitting for protons and pions with the Recoil Detector is concerned with reconstructing particle momenta in addition to track angles and vertex coordinates. Here the momentum is reconstructed by measuring the energy deposited by the track in the silicon detector, or calculating the track curvature in the magnetic field. The method of choice depends on the track momentum since below ~ 0.5 GeV the silicon detector provides a better reconstruction resolution. The silicon detector is incapable of making accurate measurements at higher momenta due to those particles "punching through" the detector layers, in which case the track curvature is measured.

Track Fitting in the Inhomogeneous Magnetic Field

Conventionally a track fitting algorithm may reconstruct the track parameters by minimising the χ^2 obtained by comparing a guess of the track shape, given by the equation of motion of the particle in the magnetic field, with the space points belonging to the track. Due to the inhomogeneous nature of the magnetic field in the Recoil Detector, however, the track shape deviates from the usual form of a helix with constant radius and the guesses must be modified accordingly.

Whereas ordinarily a track may be described by a helix, in an inhomogeneous magnetic field the track follows a smooth spiral (with a varying radius) which in this case may be described by a set of parameters (the so-called state vector) propagated by numerical integration through the magnetic field [83]. In the case of the Recoil Detector, the geometry favoured a formalism modified from that given in [83] where tracking was performed for a detector with parallel planes in the z-direction. Here a cylindrical polar representation derived from [84] is adequate.

After propagation is performed, the resulting guess of the track parameters is obtained and the χ^2 is minimised according to a Newton-Raphson iteration method. The procedure is graphically depicted in figure 5.35.

Parameterised appropriately, the state of the particle when it is at step n corre-

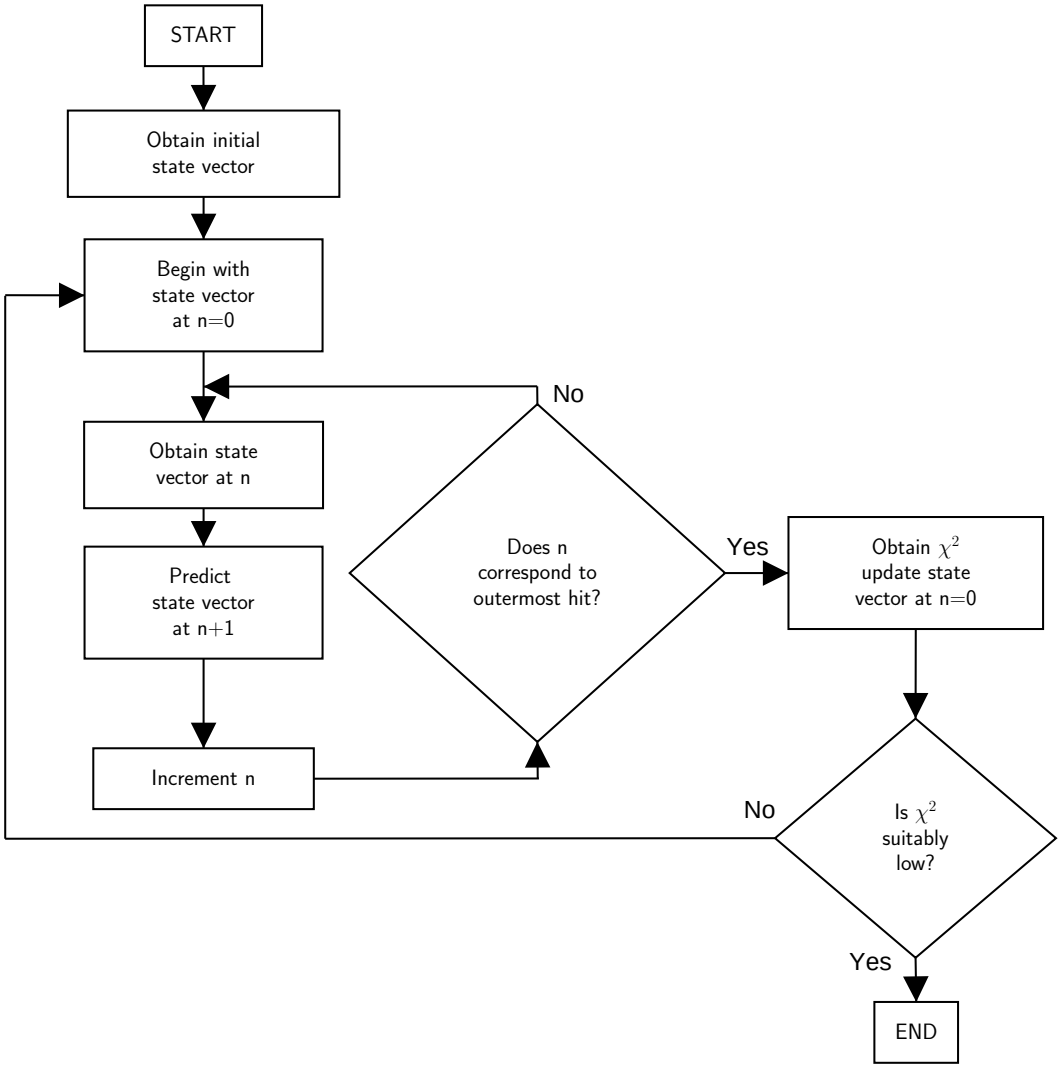

Figure 5.35: Flowchart for track fitting procedure in XTC.

sponding to a distance r from the z axis on its path is given by its state vector;

$$\vec{v}_n = \begin{bmatrix} \phi_n \\ \phi'_n \\ z_n \\ z'_n \\ \lambda \end{bmatrix} \tag{5.9}$$

where primed coordinates denote their first derivative with respect to r. The parameter λ is proportional to the inverse momentum of the particle and remains constant during the propagation from the vertex to the outermost detector. The state vector at $n = 0$ contains the usual track parameters which are iterated following a successful propagation. At the beginning of the procedure, however, a first guess of $\vec{v}_0$ is

required and is supplied by regarding the track as a straight line between the space points closest to and furthest from the beam axis which belong to the track. The first guess of the momentum is therefore infinitely large and $\lambda = 0$.

The state vector is updated as n is incremented (corresponding to an increased radius). In XTC the step length is 1 mm requiring around 180 increments in n between the beam axis and the outer SciFi layer. As the momentum given by $\lambda_n = \lambda_0$ remains fixed, the track direction is changed according to the particle momentum and the magnetic field strength at the position given by the parameters ϕ_n and r corresponding to step n. The equations of motion for a particle in a magnetic field are derived from

$$\frac{d\vec{p}}{dt} = q\vec{v} \times \vec{B}(\vec{r}) \tag{5.10}$$

if energy loss is neglected. In cylindrical polar coordinates,

$$\frac{d^2\phi}{dr^2} = \phi'' = -\frac{2\phi'}{r} - r\phi'^3 + \frac{qQ}{pr}(z'B_r + r\phi' z' B_\phi - [1 + r^2\phi'^2]B_z) \tag{5.11}$$

and

$$\frac{d^2z}{dr^2} = z'' = -r\phi'^2 z' + \frac{qQ}{p}(-r\phi' B_r + [1 + z'^2]B_\phi - r\phi' z' B_z) \tag{5.12}$$

where $B_\phi = 0$ as the Recoil magnet is solenoidal, double primes denote a second derivative with respect to r and

$$\begin{aligned} Q &= \sqrt{[1 + r^2\phi'^2 + z'^2]} \\ \frac{q}{p} &= \lambda \end{aligned}$$

as given by Bugge and Myrheim in reference [84]. Propagating the state vector from the first to the last space point is accomplished by estimating the parameters of $\vec{v}_{n+1}$ when $\vec{v}_n$ is given. Estimates are calculated using equations 5.11 and 5.12 and improved by expanding them in the leading terms of a Taylor series.

Starting with ϕ'' and z'' as given by equations 5.11 and 5.12, at any value of n the first derivatives of ϕ_n and z_n are available from either the previous step (for $n \geq 1$) or from the values given to $\vec{v}_0$ at initialisation time. At $n = 0$ all components of $\vec{v}_0$

and their second derivatives are known to maximum precision. For $n > 0$ estimates are calculated according to:

$$\begin{aligned} h &= r_{n+1} - r_n && (5.13)\\ \phi_{n+1} &= \phi_n + h\phi'_n + \frac{1}{2}h^2\phi''_n && (5.14)\\ \phi'_{n+1} &= \phi'_n + h\phi''_n && (5.15)\\ z_{n+1} &= z_n + hz'_n + \frac{1}{2}h^2 z''_n && (5.16)\\ z'_{n+1} &= z'_n + hz''_n. && (5.17) \end{aligned}$$

From these, new values of ϕ''_{n+1} and z''_{n+1} are obtained by substituting the results into equations 5.11 and 5.12. With the first two terms of a Taylor series better estimates of ϕ, z and their derivatives are calculated;

$$\begin{aligned} \phi_{n+1} &= \phi_n + h\phi'_n + h^2(2\phi''_n + \phi''_{n+1})/6 && (5.18)\\ \phi'_{n+1} &= \phi'_n + h(\phi''_n + \phi''_{n+1})/2 && (5.19)\\ z_{n+1} &= z_n + hz'_n + h^2(2z''_n + z''_{n+1})/6 && (5.20)\\ z'_{n+1} &= z'_n + h(z''_n + z''_{n+1})/2. && (5.21) \end{aligned}$$

Again the improved estimates of ϕ''_{n+1} and z''_{n+1} are obtained as before by substitution into equations 5.11 and 5.12.

The Newton-Raphson minimisation method requires knowledge of the partial derivatives of $\vec{v}_{n+1}$ with respect to $\vec{v}_n$. The derivatives are conveniently given by the components of a 5×5 matrix:

$$\mathbf{M}^{n+1,n} = \frac{\partial \vec{v}_{n+1}}{\partial \vec{v}_n} = \begin{bmatrix} \frac{\partial \phi_{n+1}}{\partial \phi_n} & \frac{\partial \phi_{n+1}}{\partial \phi'_n} & \frac{\partial \phi_{n+1}}{\partial z_n} & \frac{\partial \phi_{n+1}}{\partial z'_n} & \frac{\partial \phi_{n+1}}{\partial \lambda} \\ \frac{\partial \phi'_{n+1}}{\partial \phi_n} & \frac{\partial \phi'_{n+1}}{\partial \phi'_n} & \frac{\partial \phi'_{n+1}}{\partial z_n} & \frac{\partial \phi'_{n+1}}{\partial z'_n} & \frac{\partial \phi'_{n+1}}{\partial \lambda} \\ \frac{\partial z_{n+1}}{\partial \phi_n} & \frac{\partial z_{n+1}}{\partial \phi'_n} & \frac{\partial z_{n+1}}{\partial z_n} & \frac{\partial z_{n+1}}{\partial z'_n} & \frac{\partial z_{n+1}}{\partial \lambda} \\ \frac{\partial z'_{n+1}}{\partial \phi_n} & \frac{\partial z'_{n+1}}{\partial \phi'_n} & \frac{\partial z'_{n+1}}{\partial z_n} & \frac{\partial z'_{n+1}}{\partial z'_n} & \frac{\partial z'_{n+1}}{\partial \lambda} \\ \frac{\partial \lambda}{\partial \phi_n} & \frac{\partial \lambda}{\partial \phi'_n} & \frac{\partial \lambda}{\partial z_n} & \frac{\partial \lambda}{\partial z'_n} & \frac{\partial \lambda}{\partial \lambda} \end{bmatrix} \qquad (5.22)$$

where the matrix entries explicitly calculated for this thesis are given in appendix

A.3. Of particular importance is the matrix $\mathbf{M}^{n,0}$ where

$$\mathbf{M}^{n,0} = \mathbf{M}^{n,n-1}\mathbf{M}^{n-1,n-2}...\mathbf{M}^{1,0}. \tag{5.23}$$

Following successful track propagation through all detector layers, the initial state vector $\vec{v}_0$ is updated according to Newton's method:

$$\vec{v}_0^{N+1} = \vec{v}_0^{N} - \mathbf{G}^{-1}g \tag{5.24}$$

where the superscript on $\vec{v}$ now denotes the iteration and the subscript denotes the stage of propagation. $\mathbf{G}$ is a 5×5 matrix given by

$$\mathbf{G}_{\alpha\beta} = 2\sum_{j}^{points} \frac{\mathbf{M}_{0\alpha}^{j,0}\mathbf{M}_{0\beta}^{j,0}}{\sigma_\phi^2} + \frac{\mathbf{M}_{2\alpha}^{j,0}\mathbf{M}_{2\beta}^{j,0}}{\sigma_z^2} \tag{5.25}$$

where σ_ϕ and σ_z are the errors associated with the measurements of space point positions, and g is a 5 component vector given by

$$g_\alpha = -2\sum_{j}^{points} A_j\mathbf{M}_{0\alpha}^{j,0} + B_j\mathbf{M}_{2\alpha}^{j,0} \tag{5.26}$$

and

$$A_j = \frac{\phi_j^m - \phi_j}{\sigma_\phi^2} \tag{5.27}$$

$$B_j = \frac{z_j^m - z_j}{\sigma_z^2} \tag{5.28}$$

where the superscripted ϕ_j^m and z_j^m indicate measured rather than estimated coordinates. The subscript j in the unsuperscripted ϕ_j and z_j refers to the values of ϕ_n and z_n closest to the corresponding measured coordinates.

The iteration proceeds until $\frac{\chi_N^2 - \chi_{N-1}^2}{\chi_{N-1}^2}$ is sufficiently small or a maximum of 6 iterations is reached. Typically the algorithm requires 3 iterations until convergence is achieved. The covariance matrix is available from the fit as $2\mathbf{G}^{-1}$.

Homogeneous Circle Fitting

While the inhomogeneous fitting procedure accommodates the magnetic field inhomogeneity, the shape of high-momentum tracks in the recoil detector due to the magnetic field is not greatly different from the case where the magnetic field is uniform. Consequently the reconstruction of the track momenta is simpler and the circle approximation in the xy plane is adequate in this region. This method has the advantage of a very fast execution speed, around 2 ms per track whereas the inhomogeneous fit requires around 11 ms.

The fitting algorithm in this case is similar to the inhomogeneous algorithm, the primary difference being a lack of a propagation stage. Again, χ^2 is minimised using the Newton-Raphson iteration method, with the state vector now describing a circle in the xy plane. The z-component of the momentum is simply obtained by measuring the θ track angle.

In principle this method could be easily extended to a helical fit in 3 dimensions by modifying the state vector to represent a helix instead of a circle. Such a modification may yield a momentum resolution on par with the inhomogeneous fit (for high track momenta), and maintain the high execution speed. A full description of this method can be found in reference [85].

Homogeneous Helix Fitting

A simple test of a hypothetical helix fitting algorithm can be performed with the existing inhomogeneous algorithm simply by setting the magnetic field map values to a constant, as in this limit the inhomogeneous algorithm reduces to a helix fit. This number may be obtained by taking the average of the field strength over the recoil detector volume, and optimisations can be subsequently applied depending on the observed performance of the reconstruction. In this case, the B_z component of the magnetic field was set to a constant 1 Tesla, and the remaining components were set to zero, as would be the case for a perfect solenoidal field.

In practice, this approach is not considered for use with the Recoil Detector. The method predictably provides a poorer reconstruction than the inhomogeneous method, and no performance gain is experienced when a constant magnetic field is used with a procedure which propagates a track through the field in small steps.

Momentum Resolution

The gmc_dvcs generated events are the most suitable for testing the fitting algorithm, its easily identifiable final state protons possessing momenta in the range appropriate to the Recoil Detector acceptance. Additionally, the gmc_dvcs generator was used to produce estimates of the expected momentum resolution of the Recoil Detector during its early design stages. All results shown use ideal space point reconstruction (exact position measurements) as Monte Carlo samples with digitised SciFi information was unavailable. This is the case for the TDR reconstruction as well as the XTC reconstruction (where the separate codes are compared). Figure 5.36 shows the preliminary results of momentum resolution.

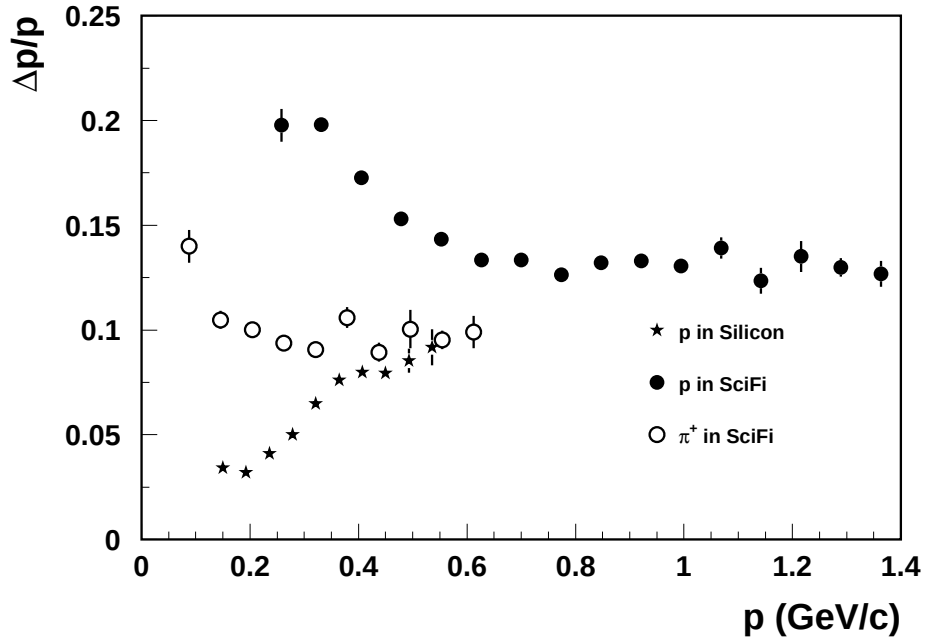

Figure 5.36: Momentum resolution in several momentum bins calculated for Recoil Detector Technical Design Report [65]. Filled circles show the reconstruction from bending in the magnetic field, the open circles (stars) show the reconstruction of π^+ (proton) tracks using the dE/dx method with the silicon only.

In this case the track momenta were reconstructed by measuring the radius of the circle formed by projecting the track shape onto the x, y plane. The longitudinal momentum component can be calculated from the transverse component and the track θ angle. The fit was performed with the assumption of a homogeneous magnetic field. The momentum resolutions presented in the Technical Design Report were calculated by taking the difference between the reconstructed and Monte Carlo generated momenta (p and p_{mc} respectively) over increasing momentum (p_{mc})bins in Recoil Detector acceptance, and dividing by p_{mc}. The inhomogeneous tracking algorithm was tested in the same way and this is shown in figure 5.37.

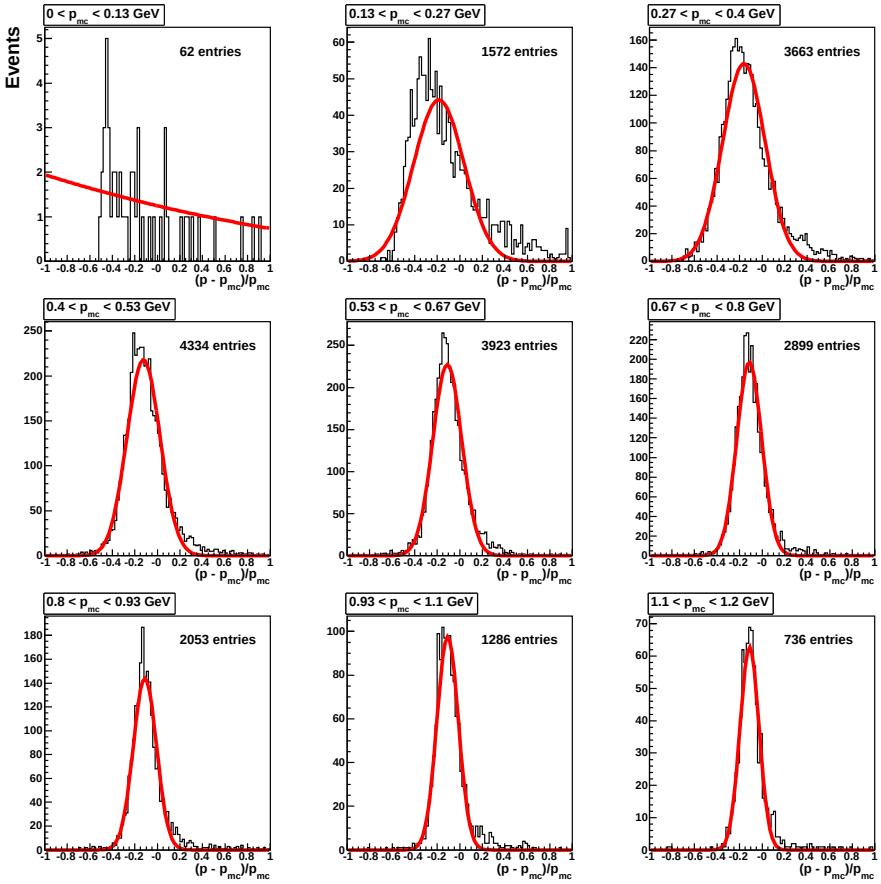

Figure 5.37: Momentum resolution over 9 equidistant momentum bins represented as a proportion of Monte Carlo momentum.

In order to investigate the momentum resolution of the reconstruction, the σ of the Gaussian fit in each momentum bin of figure 5.37 (and its error) is plotted against the mean p_{mc}, as shown in figure 5.38. The momentum resolution for the inhomogeneous fit ranges from ~ 0.22 to ~ 0.19 below ~ 350 MeV. From this up to 1.2 GeV the resolution provided by the inhomogeneous fit is an improvement over that predicted in the TDR. The lack of improvement at lower momenta arises from the difficulty of reconstructing curved tracks in an inhomogeneous magnetic field. The TDR reconstruction does not accommodate field inhomogeneity, but during the generation of the Monte Carlo gmc_dvcs events for testing the TDR reconstruction the simulation of the magnetic field was homogeneous; at that time an inhomogeneous field map was unavailable. In both cases the reconstruction suffers at lower momenta as multiple scattering distorts the track shape. Fortunately this is around the upper threshold at which momentum reconstruction via energy deposition in the silicon detector is enabled.

A similar situation is seen when the homogeneous circle fit algorithm is employed.

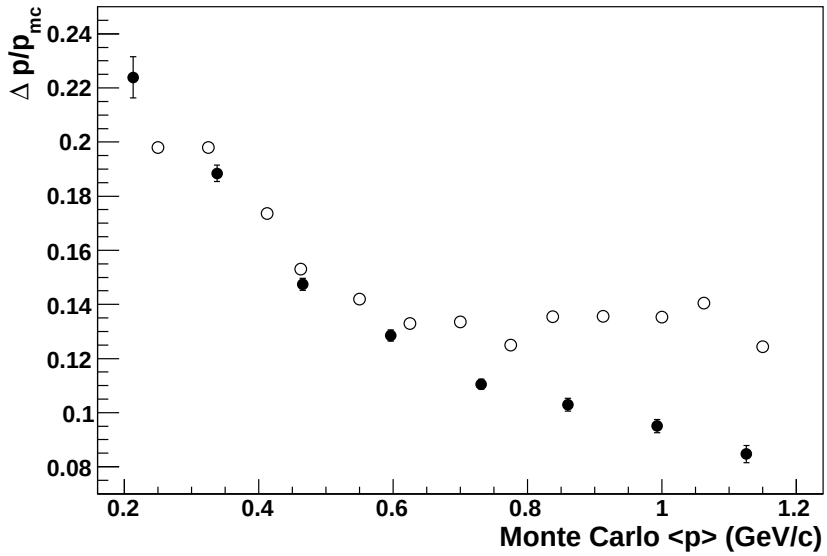

Figure 5.38: Momentum resolution in several momentum bins. Filled circles are results calculated with the inhomogeneous fitting routine, unfilled circles are the TDR results for comparison.

Figure 5.39 shows its performance compared with the TDR results. The performance is much better above around 500 MeV, although the errors in each bin are somewhat larger than those obtained from the inhomogeneous fit (figure 5.38). The poorer performance can trivially be attributed to the homogeneous approximation, but the resolution also suffers from the simple reconstruction of the z-gradient of the track. A comparison of the homogeneous and inhomogeneous algorithms can be seen in figure 5.47.

The performance of the homogeneous helix approach is shown in figure 5.40. The loss in momentum resolution is not as pronounced as that exhibited by the homogeneous circle fit, but clearly the homogeneous approximation remains the most significant source of uncertainty. Its comparison with the circle fit can be seen in figure 5.47, in this case the trade-off between resolution and the expected execution speed of such an algorithm (following subsequent optimisation and removal of the particle propagation routine) may be acceptable.

It can be seen in figure 5.37 that the mean value of the difference between reconstructed and Monte Carlo momentum (Δp) drifts away from the expected value of zero, towards the negative direction, at low momentum. At lower momenta this may be a side-effect of the difference in the discretisation of the magnetic field between the Monte Carlo sample and XTC. The path of the particles simulated by the HMC Monte Carlo program is calculated using a magnetic field map of 2 cm resolution.

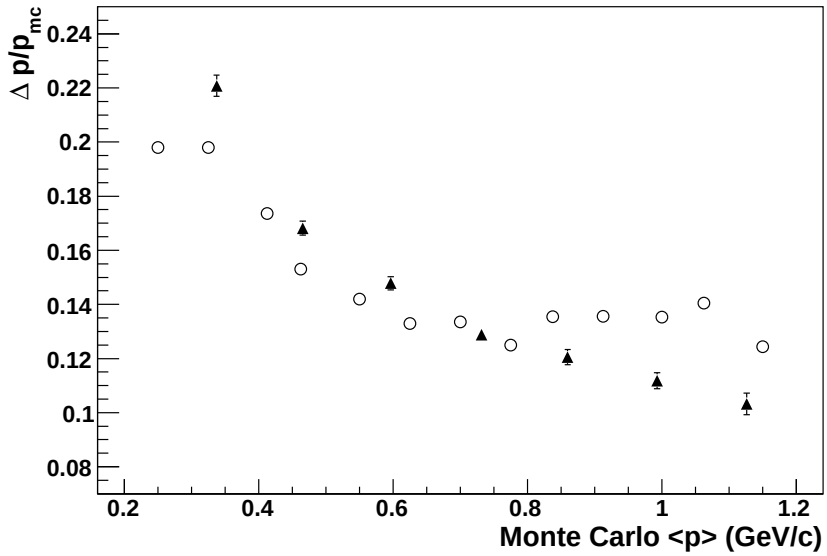

Figure 5.39: Momentum resolution in several momentum bins. The filled triangles are the results calculated with the homogeneous circle fitting routine, unfilled circles are TDR results for comparison.

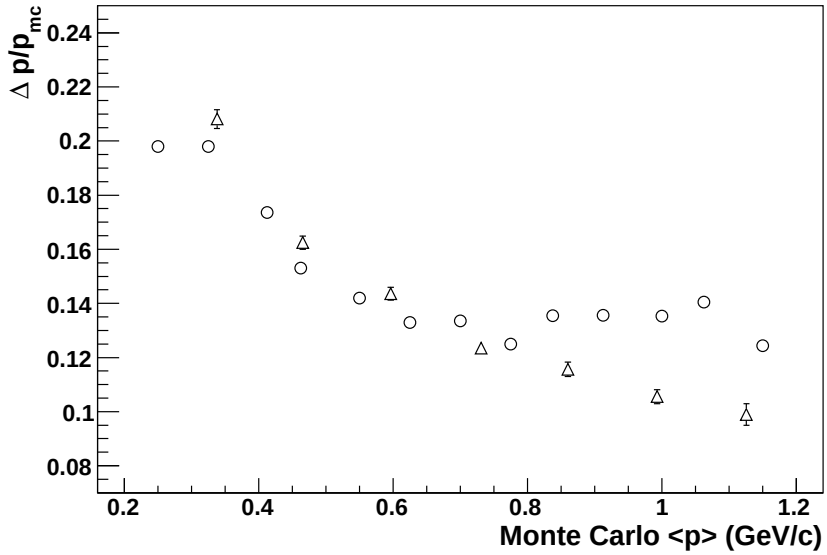

Figure 5.40: Momentum resolution in several momentum bins. The unfilled triangles are the results calculated with the homogeneous helix fitting routine, unfilled circles are TDR results for comparison.

XTC, on the other hand, calculates particle momenta by measuring the degree of bending in an interpolated magnetic field of 1 cm resolution. Due to weakening of the magnetic field as r increases, the track bending radius will increase as the particle proceeds along its path. The integrated field strength of the 1 cm resolution field map will, due to the binning, be smaller than that of the 2 cm field map. The field

map in XTC is consequently weaker than that in HMC; the stronger bending produced by HMC in the stronger magnetic field will be measured in XTC as a strong bend in a weaker magnetic field, therefore the reconstructed momentum will tend to be lower than the momentum given by the gmc_dvcs generator. Low momentum tracks will naturally experience a stronger deflection and so are more sensitive to this difference in the magnetic field maps.

Energy loss also introduces a negative bias in the mean value of Δp. As HMC tracks the particle through detector layers, the energy loss through successive interactions with the material results in a progressive loss in track momentum and hence reduces the effective bending radius. Again, low momentum tracks are most strongly affected, and XTC does not account for the effect of these interactions.

At higher momenta these effects are strongly reduced, and a positive bias is observed. This effect may be present due to the limited detector radius. As track momentum increases, its shape bears a stronger resemblance to a straight line which, in the magnetic field, corresponds to either a neutral particle or a charged particle with momentum approaching infinity. As the outer scintillating fibre barrel is only at a distance of $\sim$ 20 cm from the vertex the measured deviation in such cases is small and begins to approach the uncertainty in each position measurement. In this situation a fitted track shape exhibiting only a slight bend may yield a low enough χ^2 to be accepted, resulting in a positive value of $\Delta p = p - p_{mc}$; the difference between the Monte Carlo and reconstructed momenta.

It is crucial to correct this behaviour in the tracking code in order to ensure the reconstructed momenta are accurate. These effects may be accounted for by investigating the correlation between the values Δp and p. Figure 5.41 depicts this relationship in nine equidistant momentum bins. The tendency for the mean to gradually move from a negative to a positive value can be readily seen. In figure 5.42, the mean value of the Gaussian fit in each momentum bin of figure 5.41 is plotted against p. The horizontal errors are the p bin widths and the vertical errors are obtained from the error on the Gaussian mean. A third-order polynomial function describes the relationship extremely well, and this function can be used with each individual reconstructed momentum value to determine how large a correction must be applied after the reconstruction. Figures 5.41 and 5.42 only reflect the Δp vs p behaviour exhibited in the inhomogeneous reconstruction but an identical method may be used to correct the other fitting algorithms.

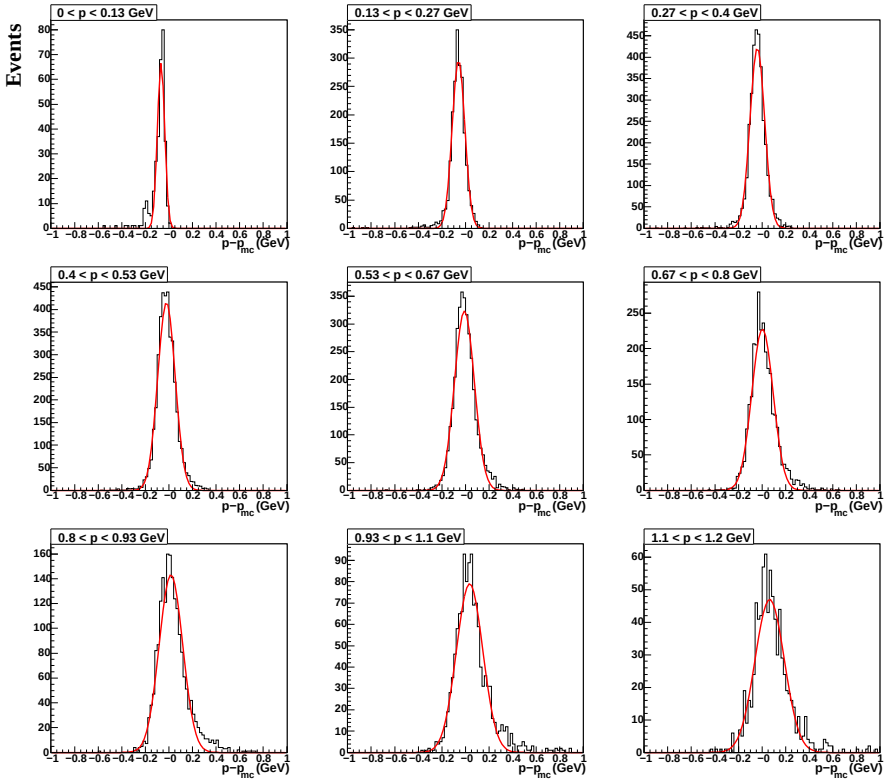

Figure 5.41: Δp in 9 momentum bins. The mean of the distribution gradually moves from a negative to a positive value as momentum increases.

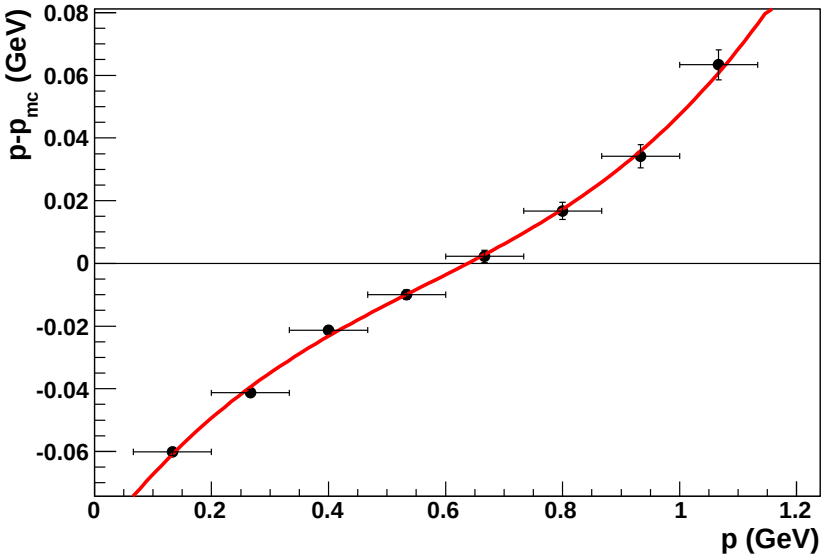

Figure 5.42: Correlation between Δp and p, using the inhomogeneous fit method. A third-order polynomial function adequately describes the relationship.

t Resolution

The kinematic variable t is given by $t = (p' - p)^2$ where p' and p are the four-momenta of the target and recoil protons respectively. One of the goals of the recoil detector is to improve the resolution to which t is reconstructed at low momenta, consequently the t resolution for the inhomogeneous fit is also calculated. Figure 5.43 shows the expected resolution to which t is reconstructed by the Recoil Detector calculated for the TDR, with the measured t resolution of the remaining HERMES spectrometer for comparison.

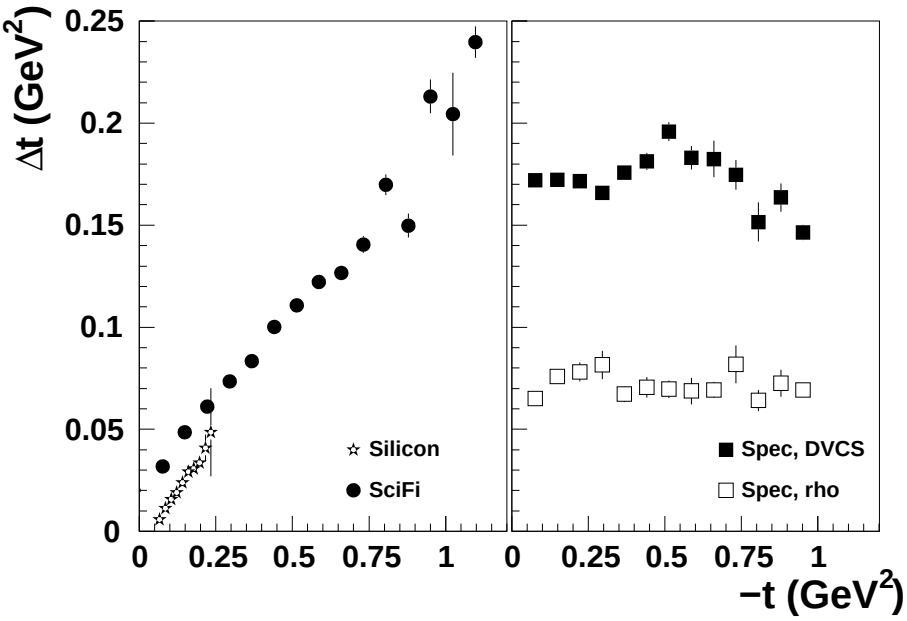

Figure 5.43: Expected t resolution for the Recoil Detector (left) and measured t resolution for the HERMES spectrometer (right). Filled circles show the resolution obtained using the preliminary reconstruction described as before (see section 5.6.5).

Below $\sim 1 GeV^2/c^2$ the resolution obtained with the Recoil Detector is better than that obtained with the spectrometer alone, approximately an order of magnitude improvement is seen at low values of t. The inhomogeneous fitting procedure provides a t resolution as shown in figure 5.44.

Figure 5.44 shows the σ value of the Gaussian fit performed on each bin in t, versus the average value of $-t$ in that bin. The procedure is similar to that in the case of figure 5.38, the difference being the resolution is quoted absolutely in the case of t. The fits to the bins in t are shown in figure 5.45.

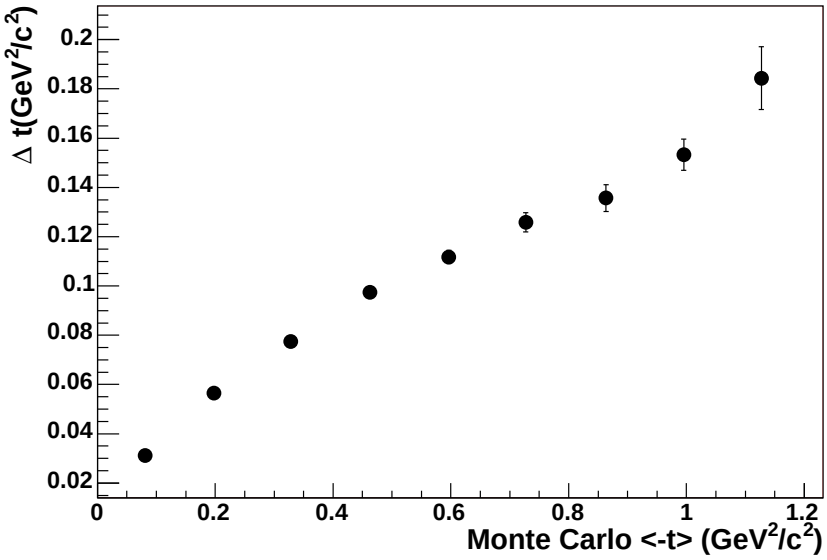

Figure 5.44: $\Delta t = t - t_{mc}$ plotted against $-t_{mc}$, obtained using the inhomogeneous fitting algorithm.

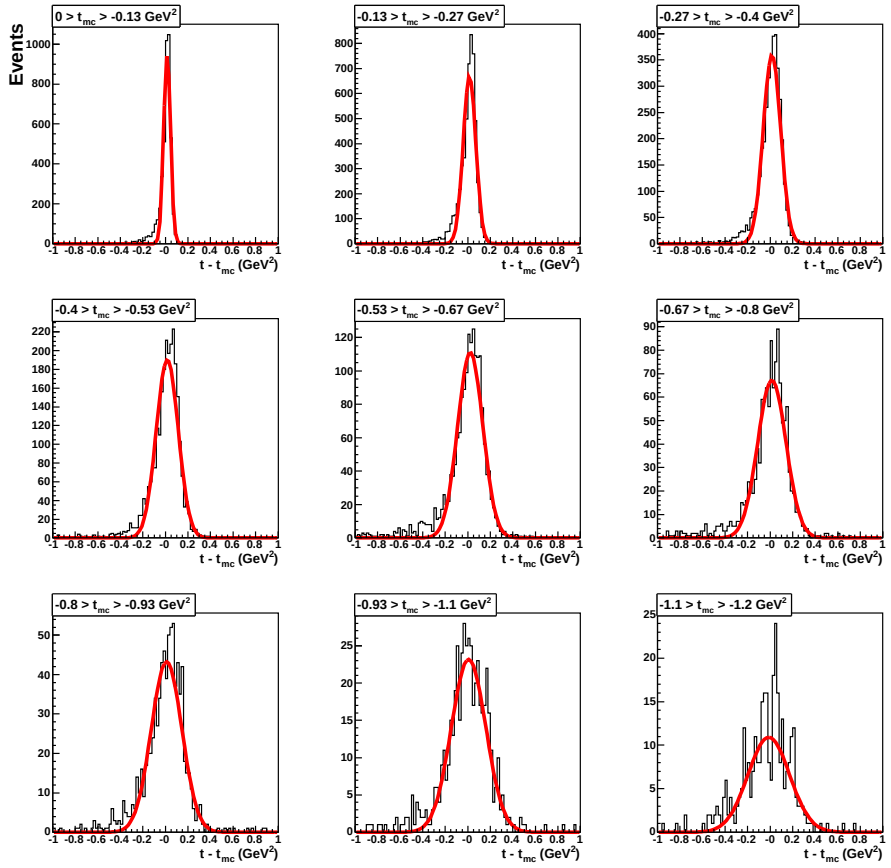

Figure 5.45: Gaussian fits to 9 equidistant bins in t.

5.6.6 Momentum Reconstruction with the Silicon Detector

With the addition of digitisation for the silicon detector in the Recoil Detector Monte Carlo, momentum reconstruction via energy deposition is enabled for protons in the momentum range $\sim 100 - 500 MeV/c$. In XTC this is referred to as the "slow" momentum reconstruction and is implemented in a configuration where the algorithms may either complement or replace the inhomogeneous reconstruction at low momenta. The implementation of the slow tracking in XTC is based on an earlier piece of software [63], [76], [88] which provided only this method of reconstruction. Consequently, the slow reconstruction may use either the straight line track finder, in the case of a track without reconstructed space points in the SciFi, or the curved track finder otherwise. In the latter case the inhomogeneous fit provides a useful cross-check of the reconstructed momentum.

The momentum of a particle which deposits energy in the silicon detector is given by $p = p(E_{corr}, \alpha)$, where

$$E_{corr} = E cos(0.79\alpha) \tag{5.29}$$

and represents the corrected energy deposition, where E is the uncorrected energy deposition and α is the angle the track makes with the vector normal to the plane of the silicon detector. E is calculated with the calibrated ADC response of each silicon detector multiplied by a constant. The corrected E_{corr} has such an α dependence as the particle passes through a greater amount of material at shallow angles to the plane of the silicon detector. The 0.79 factor is an empirically determined constant which corrects for the incremental loss in energy as the particle traverses the volume of the detector layer. Its derivation can be found in references [86] and [87]. The momentum is reconstructed using a look-up table generated with 300,000 Monte Carlo events [88] which provides values of p from given E_{corr} and α values. When space points which are members of the same track are present on both the inner and outer silicon layers, both energy depositions are obtained and an unweighted average is calculated for the reconstructed momentum.

Figure 5.46 shows a comparison between the expected performance of the silicon detector in the TDR and the momentum resolution obtained using the silicon energy deposition code [88] implementation in XTC. The XTC results present an improvement by approximately a factor of two over the expectations of the TDR at higher momenta.

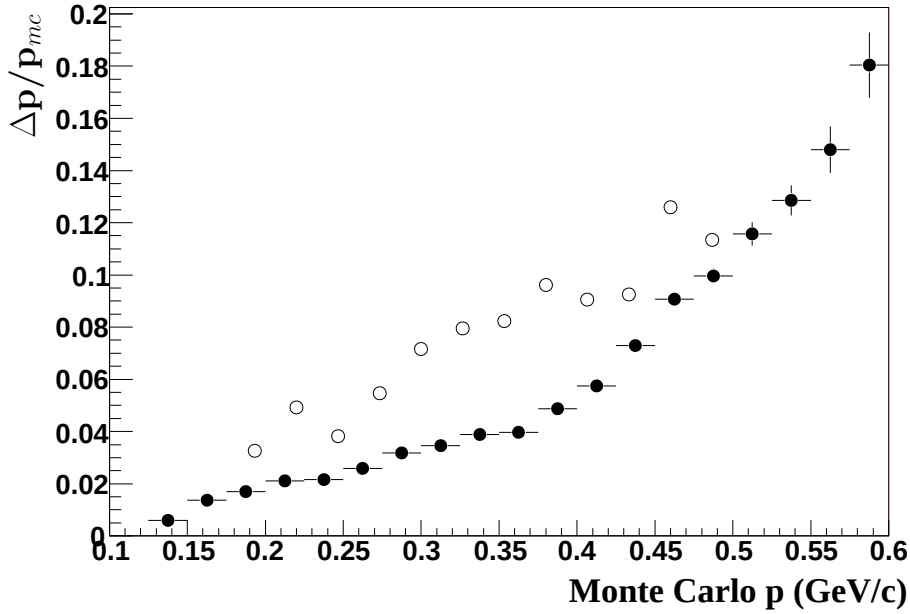

Figure 5.46: TDR momentum resolution in the silicon (unfilled circles) compared with results obtained using updated code in XTC (filled circles) [88].

An overall comparison between tracking in the TDR and XTC can be seen in figure 5.47. The reduction in resolution of the long tracking methods at low momenta is compensated by the enabling of the dE/dx reconstruction in the silicon.

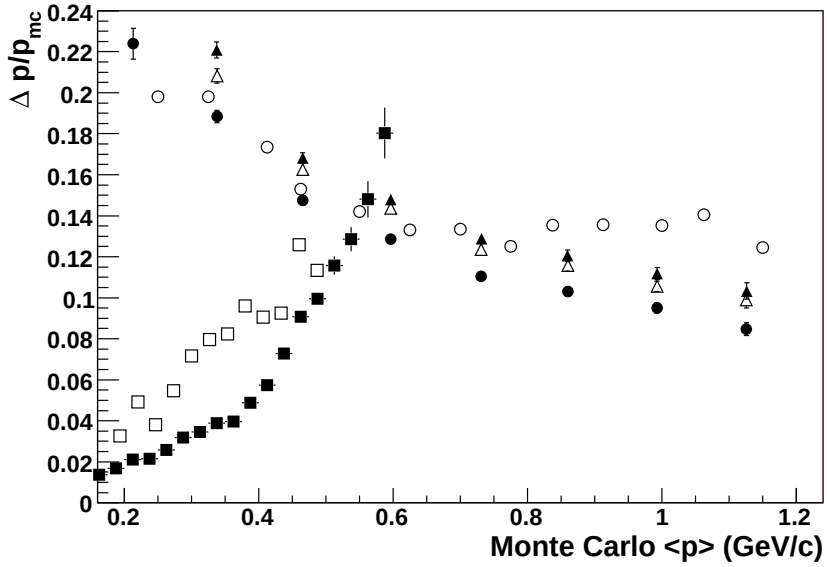

Figure 5.47: Momentum resolution obtained with long tracking and silicon in TDR (unfilled circles and squares respectively) compared with the inhomogeneous tracking (filled circles), homogeneous circle tracking (filled triangles), homogeneous helix tracking (unfilled triangles) and silicon tracking in XTC (filled squares).

Chapter 6

Results of the ρ^0-Analysis

Presented in this chapter are the results obtained from the analysis of cross section ratios of ρ^0 vector meson production from deuterium and hydrogen targets. Prior to this a full description of the methods used to extract the results from HERMES data is presented, including data quality requirements, kinematic cuts and background subtraction. The final result is a comparison of the x_{Bj}-dependency of the ρ^0 electroproduction cross section ratio on deuterium versus hydrogen, seen in the data, with the theoretical expectation. The latter is based on the calculated parton distribution functions parameterised according to MRST2001LO, described in section 2.12.

6.1 Data Quality

The reliability of the data produced during the running of the HERMES experiment is heavily dependent on the performance of each subcomponent of the HERMES spectrometer and on the quality of the beam provided by the HERA accelerator. Data samples containing recorded events during a period of subsystem malfunction or instability are discarded during the analysis; only samples satisfying specific performance criteria remain.

The HERMES data selection occurs at the level of fills, runs and bursts. Generally the shift crew are responsible for identifying problems during each fill and recording fill-level and run-level data quality information in the experiment logbook. Each data production is further scrutinised and a "run-list" is produced containing all run numbers which pass the selection criteria at this level. Because different analyses may not require full functionality of certain detector components, a final data

selection must be applied at burst level where slow control information is available. Table 6.1 lists the data quality cuts used in the ρ^0-analysis. The cuts were derived from the Spin Density Matrix Element analysis [89] which were in turn derived from the HERMES inclusive g_1 analysis [90].

bit	Quantity	Criterion	96	97	98	99	2000
2	Live Time	$50 \leq \tau_{live} < 100\%$	♦	♦	♦	♦	♦
		$0 < \tau_{r21} \leq 100\%$	♦	♦	♦	♦	♦
		$95 \leq \tau_{Art} \leq 100\%$	♦	♦	♦	♦	♦
3	Burst Length	$0 < t_{burst} \leq 11s$	♦	♦	♦	♦	♦
4	Beam Current	$8 \leq I_e \leq 50mA$	♦	♦	♦	♦	♦
6	First Burst	reject first burst in run	♦	♦	♦	♦	♦
7	Last Burst	reject last burst in run	♦	♦	♦	♦	♦
8	μDST Problems	reject bad timing burst records	♦	♦	♦	♦	♦
9	Logbook data quality	reject bad logbook bursts	♦	♦	♦	♦	♦
10 11	Two state mode unpolarised	polarised,unpolarised	♦	♦	♦	♦	♦
17	GMS - Calorimeter data quality	check for dead calorimeter blocks	♦	♦	♦	♦	♦
18	GMS - H2 and luminosity monitor	check for zero bad blocks	♦	♦	♦	♦	♦
19	TRD data quality	reject bad TRD bursts	♦	♦	♦	♦	♦
20	High Voltage trips	reject FC and BC trips	♦	♦	♦	♦	♦
22	RICH High Voltage trips	reject RICH HV trips			♦	♦	♦
25	Čerenkov data quality	reject bad Čerenkov bursts	♦	♦			
22	RICH data quality	reject bad RICH bursts			♦	♦	♦
28	Beam Polarisation Fit	regular polarimeter update	♦	♦	♦	♦	♦

Table 6.1: The 1996 - 2000 data quality cuts.

6.1.1 Data Acquisition

As all HERMES data quality relies on the properly functioning DAQ system, the application of cuts specific to the DAQ at burst level is appropriate here. Data quality bits 2 3, 6 and 7 refer to data selection criteria which apply to the DAQ. Upon receiving a trigger signal the DAQ begins the procedure to read out information from the subdetectors. If, during the time period in which readout is occurring an event

generates a subsequent trigger, this event cannot be read out as the DAQ is busy. This fraction of time, referred to as the dead time, can be alternatively expressed as the DAQ live time and is estimated from the fraction of accepted to generated trigger events in a burst:

$$\tau_{live} = \frac{T_{acc}}{T_{gen}}. \tag{6.1}$$

The selection criterion for τ_{live} is shown in table 6.1. Additional quantities in this category are τ_{21} and τArt. At HERMES the main physics trigger is generated from coincident signals in the H0 and H1 hodoscopes, the H2 preshower and the electromagnetic calorimeter. This is referred to as trigger 21, τ_{21} being the associated quantity. The artificial live time τ_{Art} was calculated from a correction factor applied to the total live time in order to account for missing events in the data stream.

At the beginning and end of each run the DAQ must perform miscellaneous initialisation and clean-up tasks. In order to remove events obtained during this time the first and last bursts in each run are rejected. In addition, bursts which exhibit timing problems are removed by imposing a burst length requirement as given by data quality bit 3.

6.1.2 Tracking

Physics analysis at HERMES requires accurate reconstruction of particle tracks, provided by the various tracking detectors in the spectrometer and the Hermes Reconstruction Code (HRC). HRC reconstructs tracks with a recursive pattern matching approach using so-called *tree lines* which are the resultant combinations of tracking chamber hits in each of the three wire directions (U,X,V).

The pattern recognition algorithm compares hit patterns recorded by the tracking detectors with those in a database which stores patterns belonging to all possible tracks. The storage of such tracks, 126 million in total [50], precludes any comparison using a linear search due to the prohibitive CPU time which would be required using this approach. The comparison is thus performed recursively using a *tree search*, shown in figure 6.1, which performs comparisons at successively increasing resolution.

The measured hit patterns are compared with a low-resolution pattern in the database. The resolution is subsequently doubled and the child patterns from those parent pat-

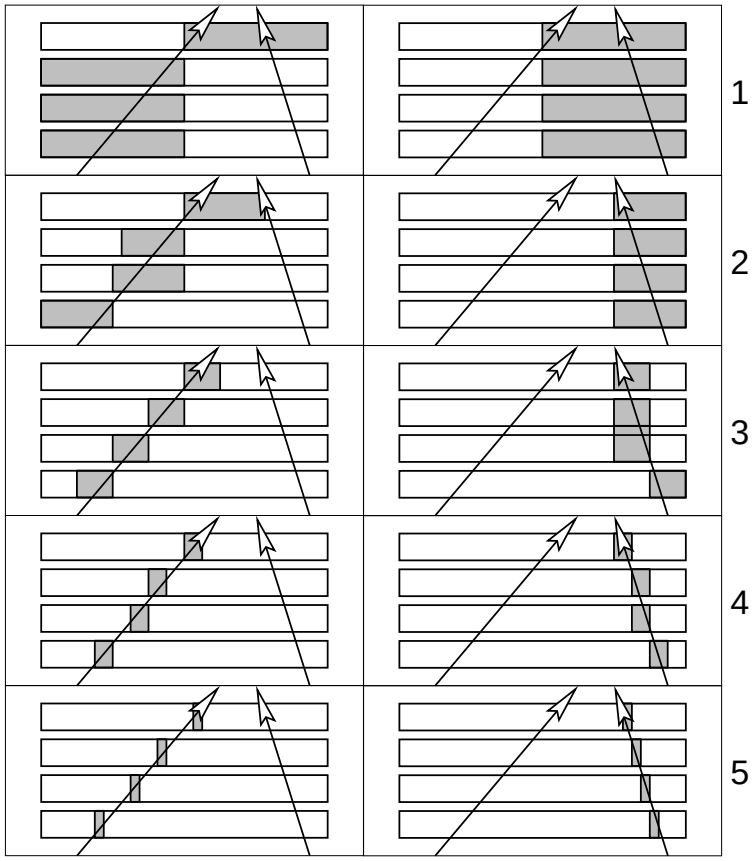

Figure 6.1: Illustration of the tree search algorithm. The procedure begins with a low-resolution comparison (top), successive increases in resolution reduces the number of search candidates at each level.

terns which matched the track in the previous step are searched for a match with the track. The procedure continues until the track is matched with patterns at a resolution which corresponds to that of the tracking detectors.

Momentum reconstruction is performed using a look-up table generated using a large amount of Monte Carlo generated particles tracked through the simulation of the spectrometer and its magnetic field map. This technique yields a momentum resolution better than $\frac{\Delta p}{p} = 0.5\%$ and an angular resolution better than 1 mrad.

Tracking Detectors

The reliability of the reconstructed track parameters used in the ρ^0 analysis depends on the performance of the tracking detectors which must be monitored. Data quality bit 20 corresponds to a high voltage trip in the front and back tracking chambers, which occurs when a drift chamber draws a current exceeding a certain limit. This is usually caused by high background or by radiation produced as a side-effect of

unstable beam conditions. In order to avoid permanent damage to the drift chamber wires, the high voltage is switched off upon such an occurrence. Following a trip and subsequent reactivation of the affected detector, the tracking plane experiences a temporary reduction in efficiency. Consequently, bursts during which a high voltage trip occurs are rejected.

6.1.3 Trigger and PID Detectors

The trigger efficiency and particle identification are affected by the performance of the H1 hodoscope, the preshower H2 and the electromagnetic calorimeter. The PID is also affected by the Čerenkov detector during 1996/7 (and the RICH which replaced it after 1998) and the transition radiation detector. Performance information for the preshower and calorimeter is provided by the Gain Monitoring System (GMS) on a run-by-run basis, the development of faults in a GMS module or a serious degradation can be determined from a comparison of the average gain of the module with its nominal value [90]. Bursts recorded during periods when the GMS contained so-called bad blocks are rejected. As with the tracking detectors the bursts in which high-voltage trips in the RICH are present are also rejected. Additionally, in order to ensure reliable PID the performance and stability of the TRD and Čerenkov/RICH is monitored.

6.2 Event Selection

Following the application of the data quality cuts, the remainder is a reliable sample of tracks originating from several different scattering processes, many of which are studied at HERMES. A further set of cuts must be applied in order to select the events of interest to the particular analysis. The data sample used for the ρ^0-analysis was obtained from the runs taken during the years 1996, 1997, 1998, 1999 and 2000, when the target operated with polarised and unpolarised hydrogen and deuterium. No distinction was made between unpolarised and polarised samples of the same gas type as the ρ^0 analysis is insensitive to beam or target polarisation. The data taken between the years 2001 and 2004 were omitted from this analysis as the contribution to the statistics (around 3,000 events in total) was comparatively small compared to over 10,000 events in the 1996-2000 sample. Also, due to earlier analyses, the 1996-2000 data sample is much better understood.

The ρ^0 has a short lifetime characteristic for a particle which decays via the strong

interaction. The decay width of the ρ^0 is 150.3±1.6 MeV [91] which corresponds, via the relation $\tau = \hbar/\Gamma$, to an expected lifetime of 4.4×10^{-24} seconds. Approximating the distance travelled by the ρ^0 before it decays as $c\tau$ yields $1.3fm$ which corresponds to the scale of a nucleon. The ρ^0 decays via the channel $\rho^0 \rightarrow \pi^+\pi^-$ with a 100% branching ratio. The analysis results were obtained by measuring the scattered lepton and decay pions from the ρ^0 decay. The recoil proton trajectory lay outside the HERMES spectrometer acceptance during the relevant data taking years, the HERMES Recoil Detector upgrade (see chapter 4) installed in late 2005 will provide the increased acceptance required to measure recoil proton tracks for future analyses.

6.2.1 Track Selection

The reconstruction of scattering events in which a ρ^0 is produced relies on the identification of three particle tracks; a π^+, π^- and the scattered beam lepton. The primary method of identification is to study the responses of the HERMES PID detectors which provide particle identification to a very high accuracy; the uncertainty introduced due to particle misidentification can be regarded as negligible. The level of contamination expected in a lepton sample is below 1% (see section 3.3.2).

HERMES PID quantities are calculated with a probability based analysis using a Bayesian algorithm [96]. This method seeks to calculate the probability $P(H_i|E,p)$ that a track seen in a particular detector corresponds to either a lepton or a hadron given a measured track momentum p and energy deposition E in the chosen detector. According to Bayes' theorem, this idea may be expressed as:

$$P(H_i|E,p) = \frac{P(H_i|p)P(E|H_i,p)}{P(E|p)} \tag{6.2}$$

where H_i represents the hypothesis that the track is left by a particle of type i which can be a hadron or a lepton. The quantity $P(H_i|p)$ is the prior probability that a track with momentum p is of type i and $P(E|H_i,p)$ represents the probability for a particle of type i to deposit an energy E in the detector. In the denominator of equation 6.2, $P(E|p)$ gives the probability that a particle with momentum p will deposit an energy E in the detector, and is given by:

$$P(E|p) = \sum_{j=l,h} P(H_j|p)P(E|H_j,p) \tag{6.3}$$

giving

$$P(H_i|E,p) = \frac{P(H_i|p)P(E|H_i,p)}{\sum_{j=l,h} P(H_j|p)P(E|H_j,p)}. \tag{6.4}$$

At HERMES, the parent distributions $P(E|H_j,p)$ are obtained from real data by imposing cuts on the remaining PID detectors (i.e. those detectors other than the one being considered) and assuming that their responses to a particular particle type are uncorrelated. Using a simplified notation, the distribution $P(E|H_j,p) = \mathcal{L}^j$. The prior probabilities $P(H_j|p)$ are equivalent to the flux factors ϕ^j of particle j. The flux factors are calculated in terms of their ratio, $\Phi = \frac{\phi^h}{\phi^l}$ which represents the number of incident hadrons divided by the number of incident leptons. In practice this quantity is a function of momentum p and polar angle θ and is obtained using an iterative procedure. The initial value $\Phi_0(p,\theta)$ is set to 1, this value in addition to the parent distributions are applied to the data set and the total number of lepton and hadron tracks are obtained. $\Phi_1(p,\theta)$ is taken to be the ratio of the number of identified lepton and hadron tracks and is used in the next iterative step. The iteration proceeds until convergence is reached.

For a particular detector, the positron probability is given by

$$\mathcal{P}^e = \frac{\mathcal{L}^e}{\Phi\mathcal{L}^h + \mathcal{L}^e} \tag{6.5}$$

which is easily seen by expanding the sum in equation 6.4 and substituting the parent distributions $\mathcal{L}$ and flux factors ϕ accordingly. From the logarithm of the ratio of probabilities a PID quantity can be created:

$$PID = log_{10}\left(\frac{\mathcal{P}^e}{\mathcal{P}^h}\right) = log_{10}\left(\frac{\mathcal{L}^e}{\Phi\mathcal{L}^h}\right) = log_{10}\left(\frac{\mathcal{L}^e}{\mathcal{L}^h}\right) - log_{10}\Phi. \tag{6.6}$$

In this scheme a $PID > 0$ indicates a greater likelihood that the particle is a positron, $PID < 0$ indicates that the particle is more likely to be a hadron and $PID = 0$ indicates either particle is equally likely. Neglecting the flux ratio Φ results in a shift of $log_{10}\Phi$, and so Φ can be neglected when it is not a strong function of p and θ.

The calculated PID quantities relevant to ρ^0 analysis are known as PID3 and PID5; these labels have developed historically. PID3 is given by the responses of the

electromagnetic calorimeter, H2 preshower and Čerenkov:

$$PID3 = PID_{cal} + PID_{pre} + PID_{cer} = log_{10}\left(\frac{\mathcal{L}_e^{cal}\mathcal{L}_e^{pre}\mathcal{L}_e^{cer}}{\mathcal{L}_h^{cal}\mathcal{L}_h^{pre}\mathcal{L}_h^{cer}}\right). \tag{6.7}$$

The quantity PID5 is computed using responses from the six modules of the transition radiation detector (TRD) only and is given by

$$PID5 = PID_{TRD} = log_{10}\left(\frac{\prod_{m=1}^{6}\mathcal{L}_e^{TRD,m}}{\prod_{m=1}^{6}\mathcal{L}_h^{TRD,m}}\right). \tag{6.8}$$

The quantity $PID3 + PID5$ is used for the separation of positrons and pions in the ρ^0 analysis. Its distribution in a sample of data is shown in figure 6.2.

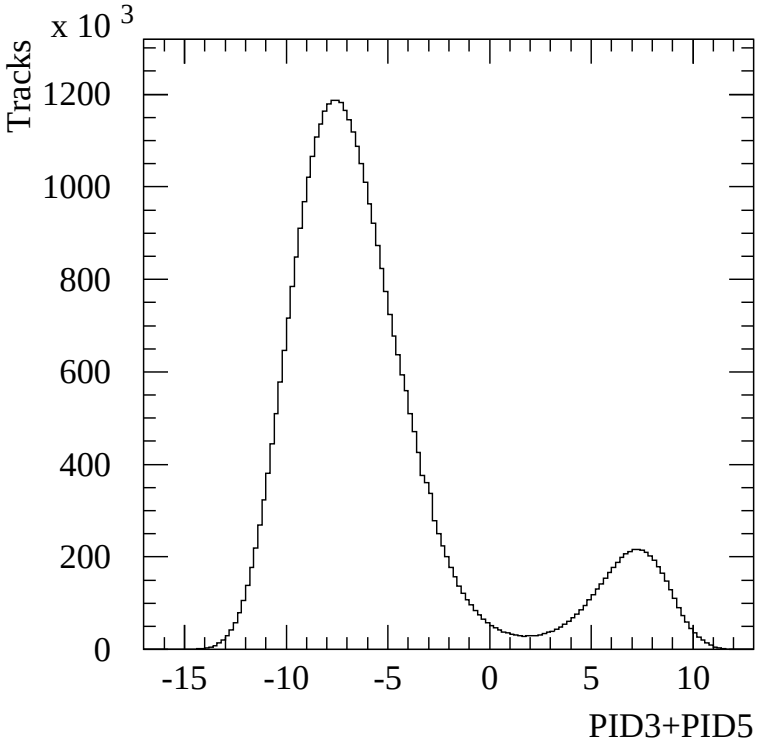

Figure 6.2: $PID3 + PID5$ distribution in the 1996/97 data [51]. This figure shows the distribution without the inclusion of the flux term, and so is shifted by an approximate $PID3 + PID5$ value of 1.

The PID cut used in the ρ^0 analysis required $PID3 + PID5 > 1$ for leptons and $PID3 + PID5 \leq 1$ for hadrons. The statistics in this region are relatively low, any contamination to either the hadron or lepton sample is minimal. In addition, several other track-level cuts were used to further minimise systematic errors. Table 6.2 contains a list of relevant cuts.

PID Cuts	
e^+ selection	$PID3 + PID5 > 1$
π^+/π^- selection	$PID3 + PID5 \leq 1$
Fiducial Cuts	
Horizontal front clamp	$\|x\| < 31$ cm
vertical lower limit (septum plate)	$\|y\| > 7$ cm
Rear vertical clamp	$\|y\| < 54$ cm
Back clamp check	$\|x\| \leq 100$ cm,$\|y\| \leq 54$ cm
Calorimeter check	$\|x\| \leq 175$ cm
	$30cm \leq \|y\| \leq 108$ cm
Vertex Cuts	
Z vertex check	$\|z_{vert}\| < 20$ cm
Beam line distance	$\|D_{vert}\| < 0.75$ cm

Table 6.2: PID and geometrical cuts on reconstructed tracks.

Fiducial cuts were imposed on the tracks at certain positions in the spectrometer in order to reject events where tracks are scattered from dense spectrometer materials. The front magnetic field clamp cuts ensure reconstructed tracks lie within the acceptance defined by the apertures of the clamps, and the magnet septum plate separating the top and bottom halves of the spectrometer is avoided by imposing the vertical cut.

A cut is also made on the calorimeter position, ensuring that the track is entirely contained within in order to allow the positron to deposit all its energy. This cut enables the removal of tracks near the edges of the spectrometer where positron identification efficiency is reduced.

The HERMES target is 40 cm long and has a triangular density profile centred at $z = 0$. At $z = \pm 20$ cm it is therefore reasonable to expect that there is no gas remaining in the target cell, and so the Z vertex cut excludes tracks with a reconstructed Z vertex outside the target cell. The transverse target size is given by the D vertex parameter and the cut is justified with the equivalent reasoning for the Z vertex cut.

6.3 Kinematic Cuts

The ρ^0 vector meson is produced in the reaction $e^+p \rightarrow e^+\rho^0 p \rightarrow e^+p\pi^+\pi^-$. Prior to the installation of the Recoil Detector, the HERMES spectrometer detects only the

pion pair and the scattered positron from the interaction, Pion pairs coming from a ρ^0 decay are selected through the application of a set of kinematic cuts. In this section, each described cut is applied successively; all kinematic plots keep preceding cuts.

6.3.1 ρ^0-Event Selection

The first cut which is performed selects those events in which only three tracks are present in the spectrometer; the aforementioned positron and pion pair. A peak in the invariant mass distribution of the pion pairs indicates the presence of ρ^0 mesons in the sample. This quantity is simply calculated by combining the four-momentum of each pion as given by:

$$M_{2\pi} = \sqrt{(p_{\pi^+} + p_{\pi^-})} \tag{6.9}$$

where p_{π^+} and p_{π^-} are the four-momenta of the hadron pair calculated with the assumption that both are pions. The invariant mass distribution of the two pion system is shown in figure 6.3.

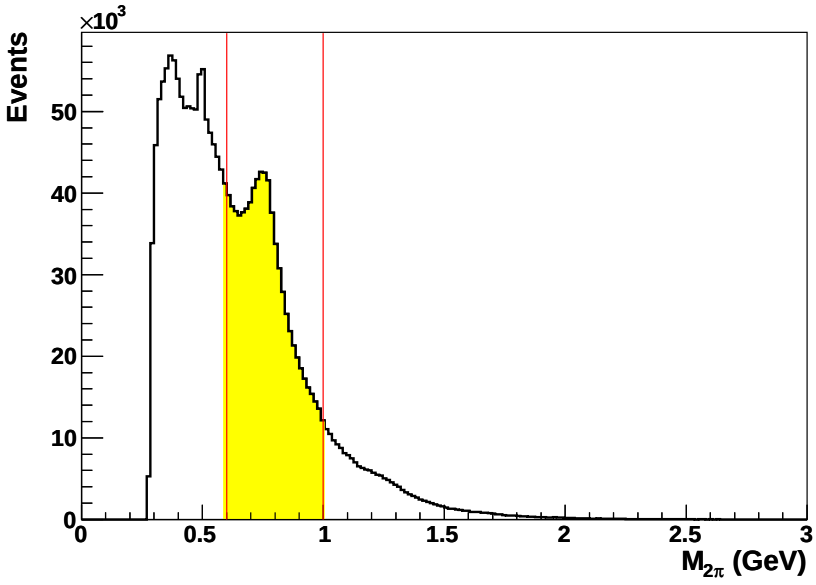

Figure 6.3: Invariant mass distribution calculated from hadron pair with prior hypothesis that hadrons are pions. Vertical lines indicate lower and upper cut on ρ^0 mass, $0.6 < M_{2\pi} < 1GeV/c^2$.

Figure 6.3 shows the ρ^0 peak at around 770 MeV as expected. The next lowest peak corresponds to K^0_S production, K^0_S mesons possess a mass of 497.672 ± 0.031

MeV and also decay into an oppositely charged pion pair with a branching ratio of $68.95 \pm 0.14\%$ [91]. The bulk of the distribution consists of products from processes other than ρ^0 production and is rejected according to the invariant mass cut $0.6 < M_{2\pi} < 1$ GeV. A more comprehensive background subtraction procedure is described in section 6.5

6.3.2 Selection of Exclusive, Diffractive Events

As the analysis concerns only the production of exclusive ρ^0 events a method is required to remove those non-exclusive events when some of the reaction products are produced in a direction lying outside the detector acceptance. As non-exclusive events may exhibit the same event topology as exclusive events, the quantity ΔE was introduced and is given by:

$$\Delta E = \frac{M_x^2 - M_{targ}^2}{2M_{targ}} = \nu - E_v + \frac{t}{2M_{targ}} \tag{6.10}$$

where $M_x^2 = p'^2$ is the invariant mass squared of the recoiling baryonic system and, in semi-inclusive $A(e, e'V)$ is given by:

$$M_x = \sqrt{(p + q - p_v)^2}. \tag{6.11}$$

Here ΔE can be regarded as a measure of exclusivity as for exclusive events, $M_x = M_{targ}$ meaning the target remained intact after the interaction. For non-exclusive events ΔE will therefore be greater than zero. In calculating ΔE for the ρ^0 analysis the target mass M_{targ} was taken to be equal to the proton mass M_p. While this is expected in the case of scattering from hydrogen, the target mass changes when deuterium gas is used in the target cell. In the latter, the scattering reactions can be either coherent (where the positrons scatter from the nucleus) or incoherent (where scattering occurs on individual nucleons). For incoherent scattering the expected target mass should be equivalent to the deuteron mass, but the limited spectrometer resolution makes distinction between coherent and incoherent processes impossible and so M_x was fixed to M_p. The ΔE distribution can be seen in figure 6.4.

The majority of events lie in the non-exclusive region of the graph and the application of the cut at $\Delta E < 0.6$ GeV rejects the events outside the exclusive peak. In practice some negative values of ΔE are obtained due to the limited experimental resolution, a lower cut of $\Delta E > -1 GeV/c^2$ reduces the systematic error by rejecting any events

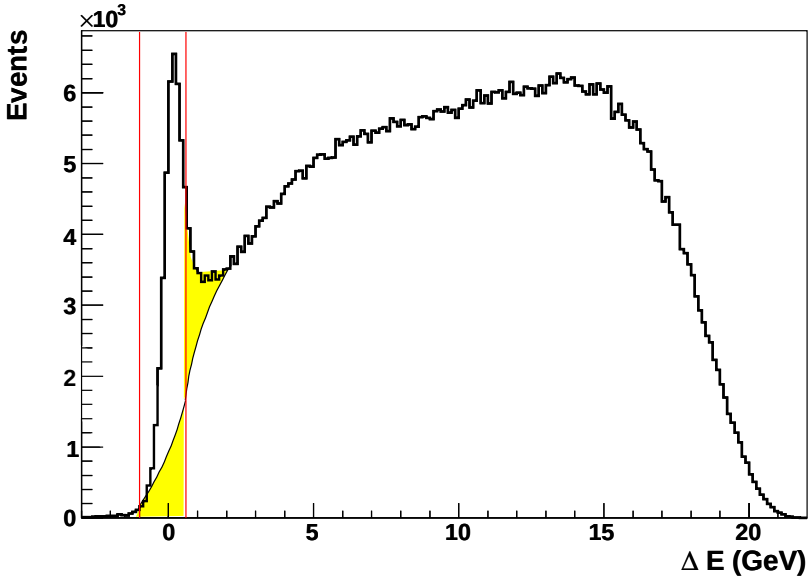

Figure 6.4: ΔE distribution inside ρ^0 mass window. The vertical line indicates the ΔE upper limit for exclusive events, $\Delta E < 0.6$ GeV.

below this for which the resolution of the spectrometer is poor and may arise from large errors on the reconstructed track momenta.

Diffractive processes are selected through the application of a cut on t', defined as

$$t' = t - t_0 \tag{6.12}$$

where t_0 is the maximum value of t permitted by the reaction kinematics and can be interpreted as the longitudinal component of the momentum transfer. Diffractive processes have a greater contribution at small values of t where t_0 is small and so $t \simeq t'$ in this region. The t' distribution is shown in figure 6.5. Early analyses of HERMES data have shown that non-exclusive background is present at $-t' > 0.4$ GeV^2 at a strength comparable with the exclusive signal [92]. The $-t' < 0.4$ GeV^2 cut satisfies the requirement that $-t'$ should be small to select diffractive events, and serves as an additional exclusivity cut.

6.3.3 Rejection of ϕ-Mesons

The use of a prior assumption that the two hadrons which accompany the scattered positrons are pions leads to the possibility of a small contamination of the ρ^0-sample due to the misidentification of the hadrons in the spectrometer. The capability of the threshold Čerenkov to discriminate between hadron types is limited in the

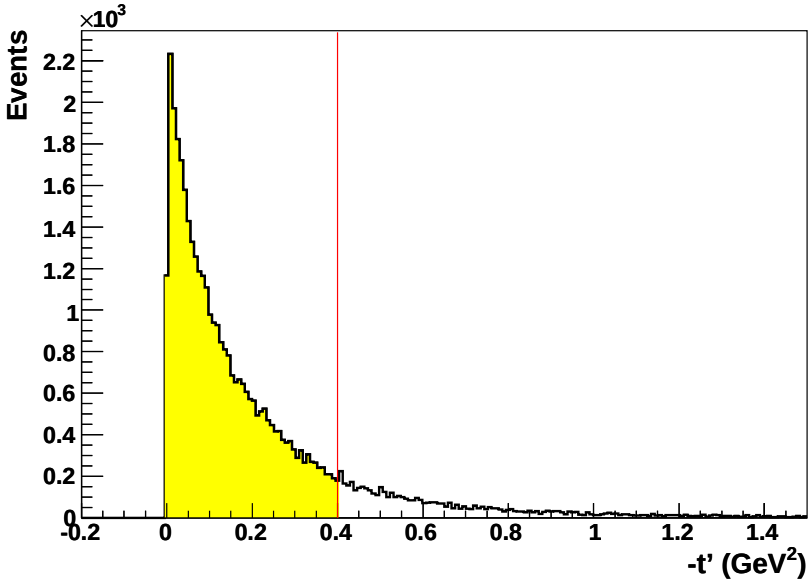

Figure 6.5: The t' distribution inside the window defined by the ρ^0 mass and exclusivity cuts. Events are accepted as diffractive for $-t' < 0.4$ GeV^2 (vertical line).

momentum region of interest to the ρ^0-analysis and so the production of ϕ-mesons and protons contributes to the background. A ϕ-meson has a mass of 1019.456 MeV and decays into a K^-K^+ pair with a $49.1 \pm 0.6\,\%$ branching ratio [91]. Other modes of decay include $\phi \to K^0_L K^0_L$ $(34.0 \pm 0.5\,\%)$ and $\phi \to \rho\pi + \pi^+\pi^-\pi^0$ $(15.4 \pm 0.5\,\%)$, with a small fraction ($< 3\,\%$ in each case) of ϕ-mesons decaying to $\eta\gamma$, $\pi^0\gamma$ or e^+e^-. The $K^\pm$ has a mass of 493.677 MeV and so the ϕ contamination in the ρ^0 sample can be minimised by recalculating the mass of the detected hadron pair with the hypothesis that both are kaons:

$$M_{2K} = \sqrt{p_{K^+} + p_{K^-}} \tag{6.13}$$

where $p_{K^\pm}$ refers to the four-momenta of each kaon. The invariant mass distribution calculated using equation 6.13 is shown in figure 6.6.

The correlation between the reconstructed ϕ and ρ^0 invariant masses is shown in figure 6.7.

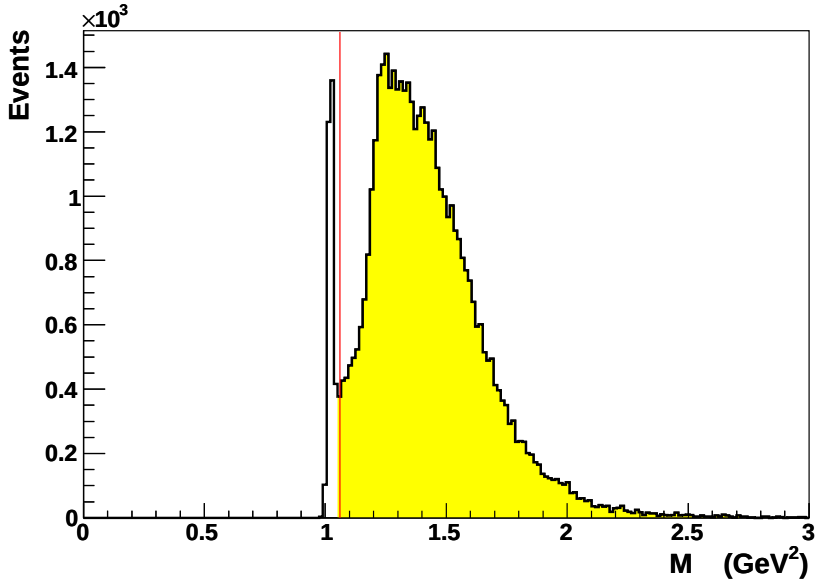

Figure 6.6: Invariant mass distribution calculated for each hadron pair assuming that hadrons are charged kaons. The distribution is within the windows defined by the previous invariant mass and exclusive, diffractive cuts. The vertical line indicates the upper limit on the ϕ mass, $M_{2K} < 1.06$ GeV.

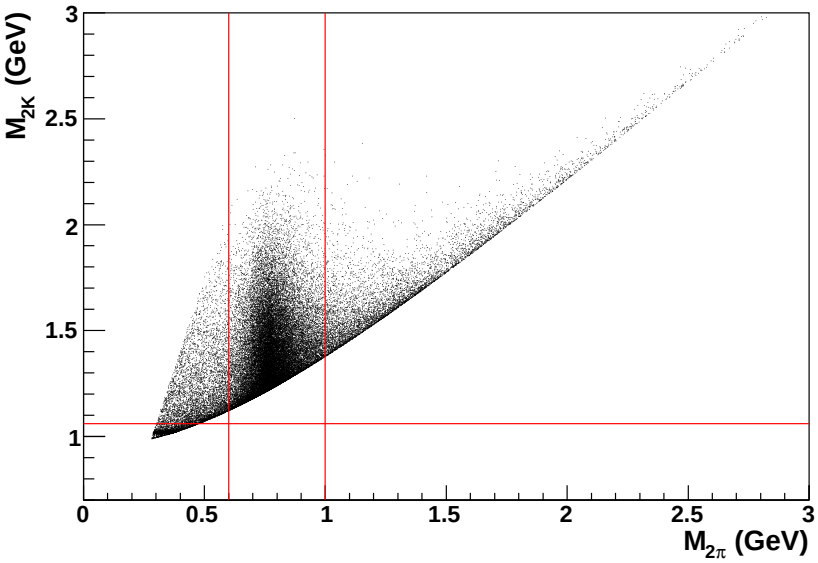

Figure 6.7: Scatter plot of reconstructed ϕ-versus ρ^0-mass. The ρ^0 mass window is defined between the vertical lines. The plot shows that there are no events inside the ρ^0 mass window below the horizontal line defined by the M_{2K} cut. Consequently, there is no ϕ-meson contamination in the ρ^0 sample.

6.3.4 ρ^0-Invariant Mass

The resulting invariant mass distribution of the ρ^0 sample after the application of preceding cuts is shown in figure 6.8. A non-relativistic Breit-Wigner function;

$$\frac{dN}{dM_{2\pi}} = \frac{1}{4}\frac{\Gamma_\rho}{(M_\rho - M_{2\pi}^2) + \Gamma_\rho^2} \tag{6.14}$$

where M_ρ and Γ_ρ denote the mass and width of the ρ^0, is fit to the ρ^0-peak. The results obtained from the fit and those from the Particle Data Group [14] are shown in table 6.3.4.

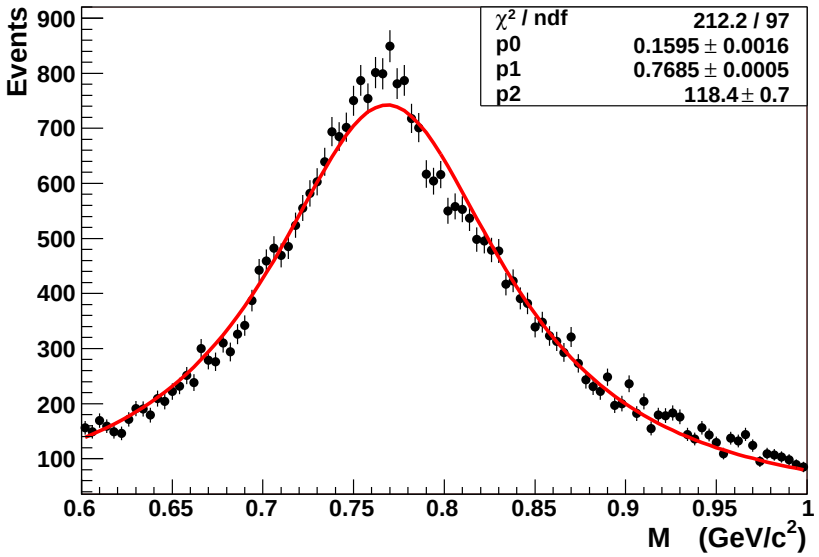

Figure 6.8: Non-relativistic Breit-Wigner fit on the 2-pion invariant mass spectrum for an exclusive, diffractive ρ^0 event candidate sample.

Source	Mass (MeV)	Full Width (MeV)
PDG	775.8 ± 0.5	150.3 ± 1.6
BW fit	768.5 ± 0.5	159.5 ± 1.6

Table 6.3: Mass and full width of the ρ^0-meson obtained from the Breit-Wigner fit and PDG [14]. The PDG values are obtained by aggregating the measurements contributed by various experiments.

The parameters obtained from the fit and PDG are in reasonable agreement. The ρ^0 invariant mass spectrum to which the Breit-Wigner function is fitted has not been corrected for background, but previous analyses indicate that this contribution to the difference is very small [60]. A background subtraction would likely increase the

mass value as the background is expected to exhibit a negative linear dependence on the reconstructed mass. The errors on the fit parameters quoted in table 6.3.4 are not comparable to those errors quoted by the PDG, as they reflect only the uncertainties in the fit and systematic contributions to error have not been accounted for.

6.3.5 Incoherence Cut

The angular distribution of diffractive interactions shows that such processes are dominated by scattering at forward angles. The kinematical variable $t' = t - t_0$ (where t_0 is the maximum kinematically allowed value of t) is related to the scattering angle as $-t'$ is approximately equal to p_t^2 which is the square of the transverse momentum of the ρ^0 with respect to the direction of the virtual photon momentum. The variable $-t'$ is small for diffractive scattering at forward angles and in this region the cross-section has an exponentially decreasing dependence on $-t'$:

$$\frac{d\sigma}{d|t'|} \propto e^{-b|t'|} \tag{6.15}$$

where the parameter b gives the exponential slope. This slope parameter is related to the size of the interacting particles and so the $-t'$ distribution can be studied in order to select only those events in which the target is an individual nucleon.

The analysis of the ρ^0 cross-section ratios is concerned with the investigation of the relative gluon and quark contributions to the vector meson electroproduction amplitude. An incoherent process is one in which the beam lepton scatters from an individual nucleon within a nucleus. In order to make a valid comparison between the entirely coherent scattering process on the free protons in a hydrogen target and the scattering process on bound nucleons in deuterium, the analysis must reject events in which the beam positron scatters from the deuteron as a whole. In this scheme the interactions with the deuterium target can then be considered as scattering from free nucleons.

Due to the coherent and incoherent modes of scattering, two contributions to the momentum transfer in exclusive, diffractive ρ^0 production on deuterium are present. The contributions, arising from the b parameter (equation 6.15) due to the difference in the radii between a nucleon and the deuteron, are manifest as differing exponential slopes in the $-t'$ distribution. Thus, in order to isolate the incoherent scattering, the deuterium data are fit to a shape giving the sum of incoherent and coherent

contributions [93]:

$$b_N e^{b_N t'} + f_A b_A e^{b_A t'} \tag{6.16}$$

where f_A is the ratio of coherent to incoherent total events, $e^{b_N t'}$ ($e^{b_A t'}$) represents the product of the ρ^0 and the struck nucleon (nucleus) elastic form factors squared, and b_N (b_A) is the incoherent slope parameter for each nucleon (nucleus) [94]. Figure 6.9 shows the double exponential behaviour and the transition from a strong coherent contribution (P1 slope) to a dominant incoherent one (P3 slope) at around 0.05 GeV^2.

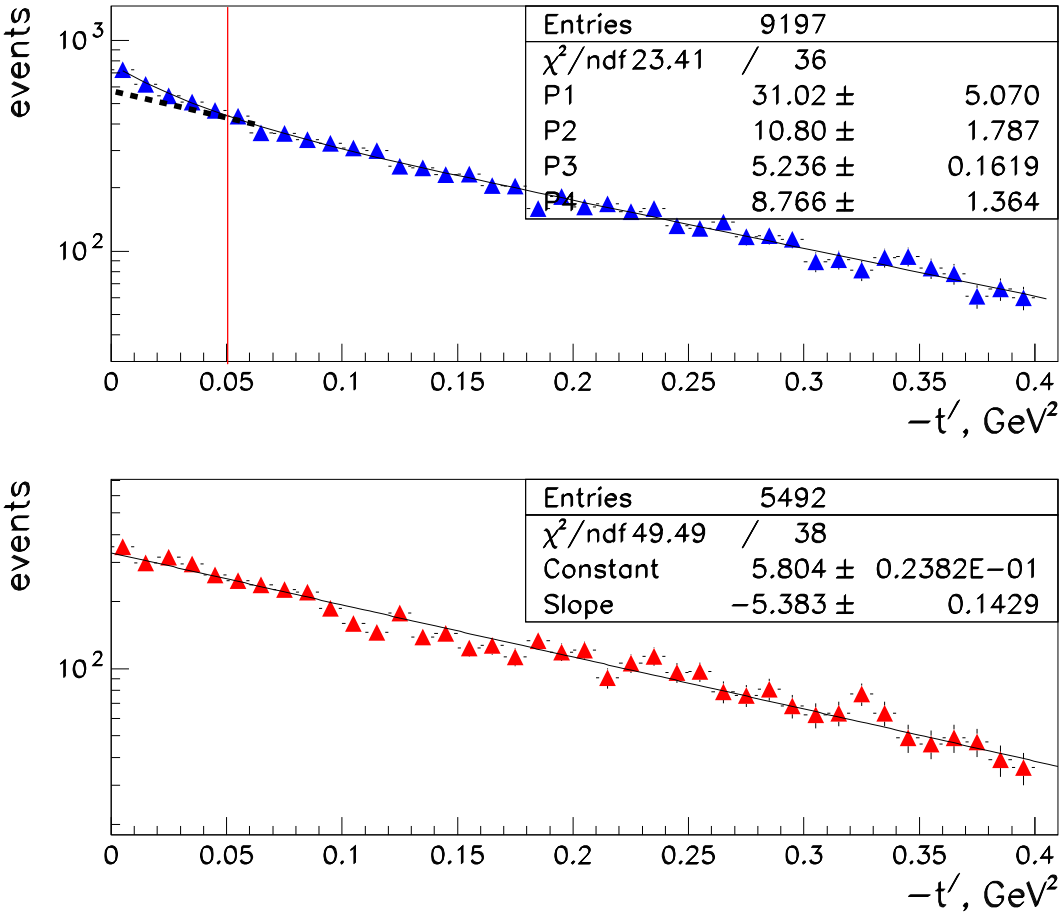

Figure 6.9: Double exponential coherent and incoherent slopes on deuterium (upper) and coherent slope on hydrogen (lower). The thick dashed line on the upper plot shows the continuation of the incoherent slope.

The coherent contribution to the incoherent sample after the $-t'$ cut is estimated to be 2%. This estimate is based upon the results of the exponential fits to the deuterium $-t'$ distribution. The coherent background as a proportion of the total sample for the region between $-t' = 0$ and $-t' = t_c$ where t_c is the upper limit is

given by

$$C_{bg} = \frac{1 - e^{P_1 t_c}}{P_2(1 - e^{P_3 t_c}) + (1 - e^{P_1 t_c})} \tag{6.17}$$

where the parameters P_n correspond to the exponential fit parameters. The application of the $-t' > 0.05 GeV^2$ cut removes the region with the greatest coherent contribution which, according to equation 6.17, is estimated to be $\sim 24\%$ for $0 < -t' < 0.05 GeV^2$.

6.3.6 Statistical Cross-Checks

The exclusive, diffractive ρ^0 events sought for the analysis in this thesis were extracted from the μDST files using software based on the C/C++ programming languages, ADAMO functions and ROOT [98] libraries. In addition, ROOT was used to create the graphical depictions of the analysis results in the thesis. For a cross-check, a completely separate set of extraction and physics codes based on the C programming language were developed by another author [95]. In this case the results were depicted using the PAW [99] analysis framework. Throughout this section the terms ROOT and PAW will be used to distinguish between the separate approaches.

Statistical agreement between analysis codes is desirable as a cross check immediately shows if one or both codes contains mistakes. The distributions of the kinematic quantities Q^2, x_{Bj} are compared for the two target gas types in figure 6.10.

It is readily seen that the kinematic distributions show excellent agreement between the different analysis codes. In addition it is useful to compare the total number of reconstructed ρ^0 events following the kinematic cuts. This is shown in table 6.3.6. The discrepancy in the statistics for both gas types is less than 1% and is also smaller than the statistical error $\sqrt{N}$, and arises from slight differences in the PID cuts used during the selection of 3 track events between ROOT and PAW codes. The PAW code has a greater tolerance for 3 track events when the hadron and lepton PID all lie slightly beyond the hadron or lepton PID threshold. In such an event, if all the values are very close together, the track with the highest PID value is accepted as a lepton track.

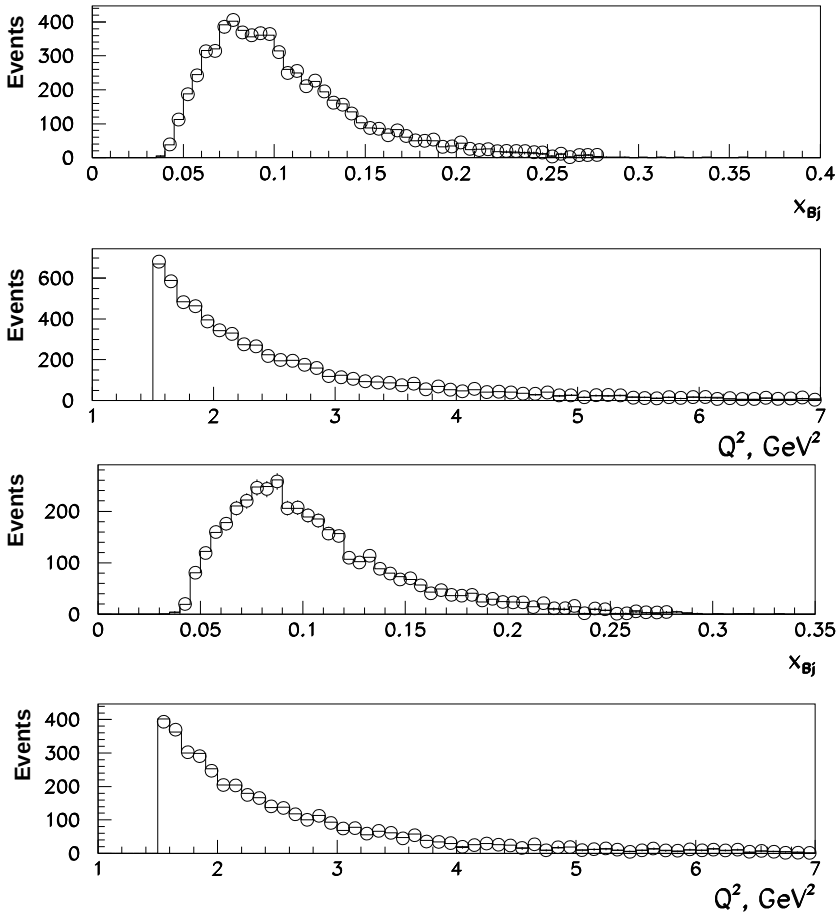

Figure 6.10: Comparison of kinematic distributions between ROOT code (circles) and PAW code (dashes) for deuterium (upper two) and hydrogen (lower two).

Gas Type	ROOT code	PAW code	Discrepancy	Statistical Error
Deuterium	6311	6330	19	79.7
Hydrogen	3964	3965	1	62.9

Table 6.4: Total numbers of exclusive, diffractive ρ^0 mesons in the 1996-2000 data sample for $1.5 < Q^2 < 7GeV^2$ and $0 < x_{Bj} < 0.25$.

6.4 Detector Resolution

The ρ^0 analysis discussed in this chapter will present the x_{Bj} dependence of the ratio of ρ^0 electroproduction cross-sections on deuterium versus hydrogen using a variety of representations. The main result shows the ratio in bins of the kinematical quantities x_{Bj} and Q^2, thus a study of the spectrometer resolution in the respective quantities is appropriate. Additionally, limited statistics in kinematical bins necessitate a binning scheme which adequately reduces statistical error across the distributions in order to allow a convincing fit to be performed.

In principle the minimum bin width in a kinematical quantity should be limited to the detector resolution; the resolution in x_{Bj} and Q^2 was examined in order to produce a reasonable binning scheme. The resolution of the HERMES spectrometer varies with x_{Bj} and Q^2 and so was investigated in four equidistant bins in $0 < x_{Bj} < 0.25$ and $1.5 < Q^2 < 7$ GeV^2. The resolution was calculated by comparing the difference between the kinematic quantities generated by Monte Carlo and the corresponding reconstructed quantities. Figures 6.11 and 6.12 show the Q^2 and x_{Bj} resolutions respectively.

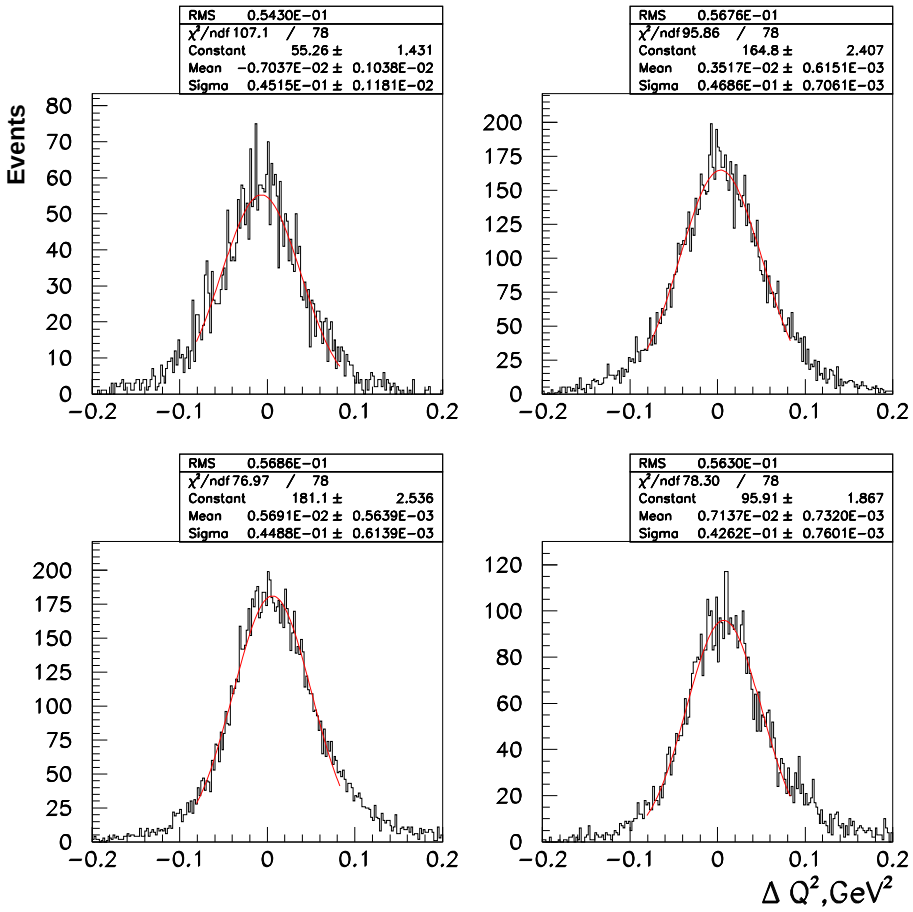

Figure 6.11: Difference between Monte Carlo Q^2 and reconstructed Q^2 for $1.5 < Q^2 < 7$ GeV^2. The resolution is given by the σ of the fit.

The plots suggest that a tentative binning scheme of 12×12 in $Q^2 \times x_{Bj}$ is sufficiently coarse; the σ values inside the kinematical bins of figures 6.11 and 6.12 with the widest distributions are smaller than the bin widths which would be given by a 12×12 scheme in the usual kinematical range. Specifically, the binning scheme would provide bins of width 0.46 GeV^2 in Q^2 and 0.028 in x_{Bj}, both of which are considerably wider than the resolutions of 0.048 GeV^2 in Q^2 and 0.01 in x_{Bj}.

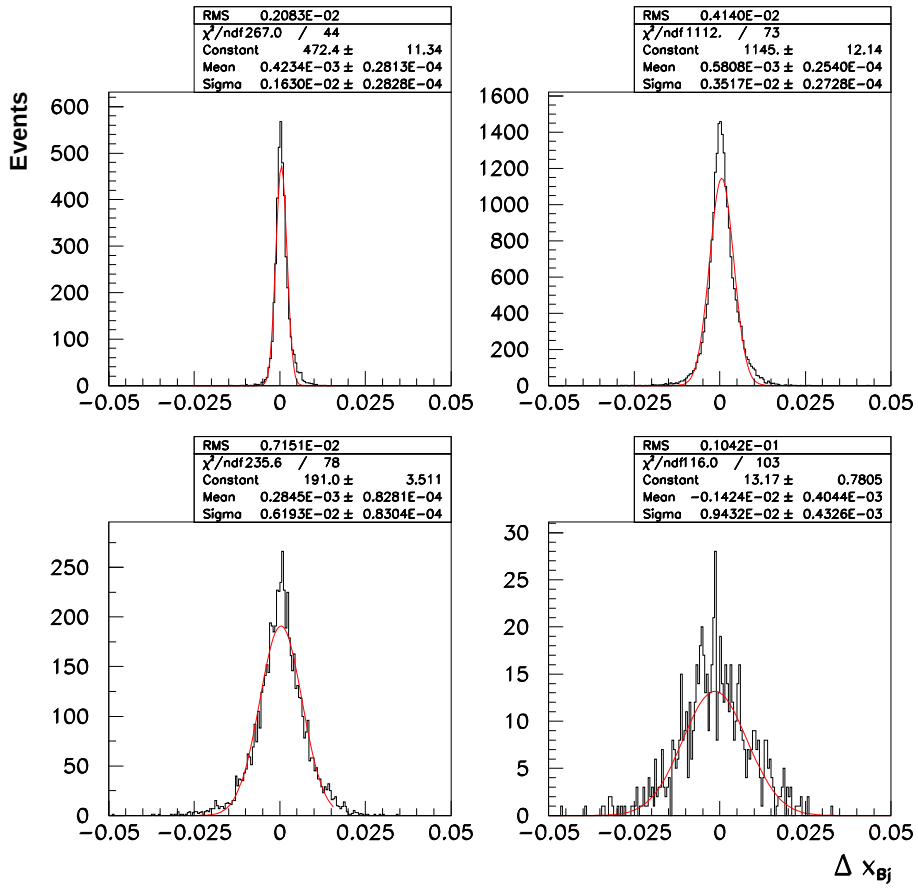

Figure 6.12: Difference between Monte Carlo x_{Bj} and reconstructed x_{Bj} for $0 < x_{Bj} < 0.25$. The resolution given by the σ of the fit.

6.5 Background Subtraction

While the cut $-1 < \Delta E = \frac{M_x^2 - M_{targ}^2}{2M_{targ}} < 0.6$ GeV serves to select only exclusive events in the ρ^0 sample, the spectrometer resolution in ΔE is insufficient to fully suppress non-exclusive background from deep-inelastic scattering fragmentation processes (figure 6.4). An additional method is required to account for the background contamination in the ρ^0 sample, and in this case the HERMES Monte Carlo provides a useful method.

The background subtraction, calculated using a set of ROOT-based analysis codes [98], proceeds according to the methods detailed in [60, 100, 101, 102, 103, 104] and is similar to the background subtraction presented in [89]. Specifically, in order to estimate the proportion of background in the ρ^0 data, a Monte Carlo sample of deep-inelastic scattering (DIS) events was created with the PYTHIA [81] generator. The generated sample contained hadrons originating from fragmentation processes but did not, however, include exclusive, diffractive events. The sample was tracked

through the simulation of the detector using the GEANT-based HERMES Monte Carlo (HMC, see section 5.2.2) using the same cuts which were applied to the ρ^0 sample in the 1996-2000 data.

The amount of the DIS background present in the data could be estimated by comparing the ΔE distribution of the two samples. The exclusivity cut in the data sample is given by $-1 < \Delta E < 0.6$ GeV. The amount of DIS background present in the data sample is therefore given by the number of DIS events present in the Monte Carlo sample inside the window defined by the ΔE cut.

Figure 6.13 shows the ΔE distribution in the data and generated Monte Carlo sample for deuterium. The Monte Carlo distribution shown was obtained by combining the individual samples generated with a proton target and a hypothetical neutron target. A similar distribution is seen using a hydrogen target, and this is shown in figure 6.14.

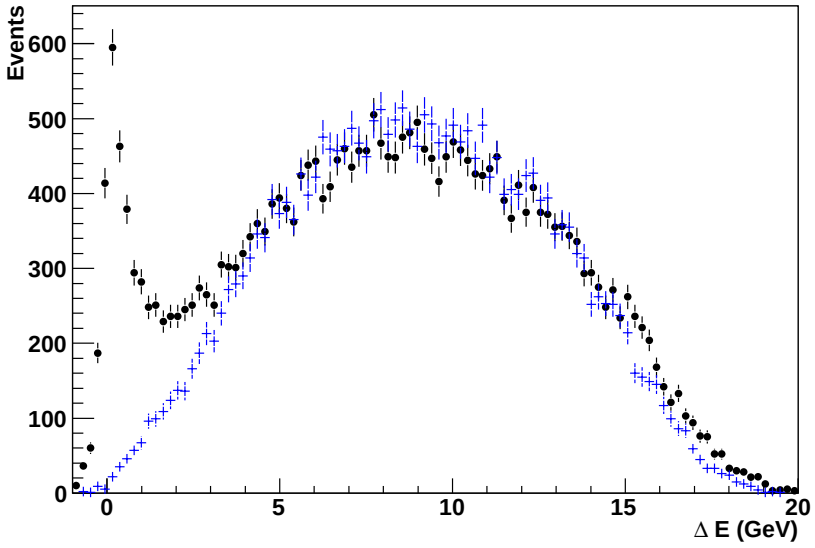

Figure 6.13: ΔE distribution in 1996-2000 data (black circles) and Monte Carlo (blue crosses) for $0.025 < x_{Bj} < 0.08$ using a deuterium target.

The amount of DIS events generated by the Monte Carlo and the DIS background outside the ΔE cut in the data differ, however, due to the impracticality of generating a Monte Carlo sample with matching statistics. In order to obtain a realistic estimate of DIS background inside the exclusive peak it is necessary to normalise the Monte Carlo DIS sample to the data.

The normalisation applied to the Monte Carlo data ensures that a realistic amount of events are present beneath the exclusive peak defined by the ΔE cut as seen in

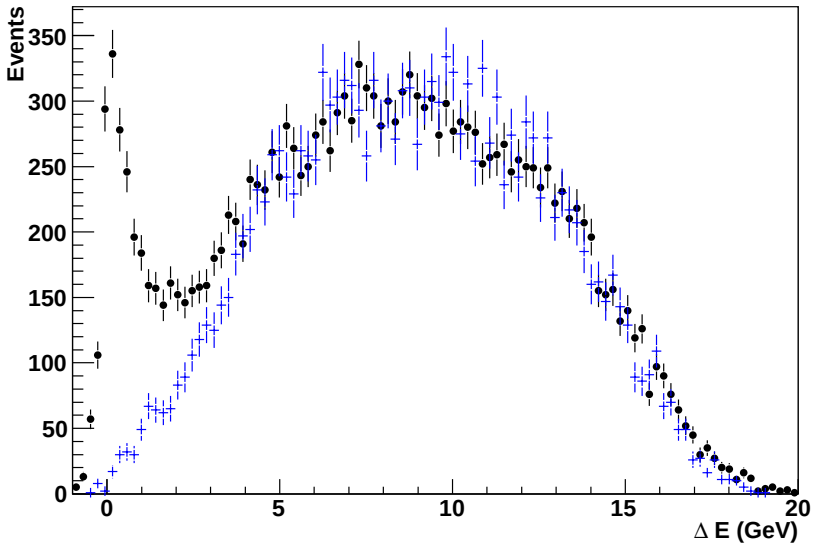

Figure 6.14: ΔE distribution in 1996-2000 data (black circles) and Monte Carlo (blue crosses) for $0.025 < x_{Bj} < 0.08$ using a hydrogen target.

the data. In figures 6.13 and 6.14, each bin of the Monte Carlo distribution was multiplied by a constant $c_{Bg} = I_{data}/I_{mc}$, where I_{mc} (I_{data}) is the integral of the ΔE distribution between the limits 4 and 20 GeV in the Monte Carlo (1996-2000 data). The DIS background inside the exclusive cut can be estimated by performing a subsequent similar integration between the limits defined by the ΔE cut.

Due to the kinematic dependency of the DIS background, a Monte Carlo study in several x_{Bj} bins was required. The background study was performed in six variable-width bins across the range $0.025 < x_{Bj} < 0.25$. The complete set of plots are presented in Appendix B. The resultant calculated contributions to background are shown in table 6.5.

x_{Bj} bin	DIS Background hydrogen (%)	DIS Background deuterium (%)
$0.025 < x_{Bj} < 0.08$	6.7	5.5
$0.08 < x_{Bj} < 0.102$	7.68	7.7
$0.102 < x_{Bj} < 0.124$	14.2	12.6
$0.124 < x_{Bj} < 0.168$	23.5	16.4
$0.168 < x_{Bj} < 0.19$	30.2	23.3
$0.19 < x_{Bj} < 0.25$	30.2	26.5

Table 6.5: DIS background as a percentage of total events over x_{Bj} bins for hydrogen and deuterium, calculated using integration method.

6.6 Calculating ρ^0 Production Cross-Sections

6.6.1 Luminosity

In this ρ^0 analysis the cross-section ratios are calculated according to

$$R = \frac{N^D}{N^H}\frac{L^H}{L^D} \tag{6.18}$$

Where $N^{D(H)}$ and $L^{D(H)}$ are the absolute number of exclusive, diffractive ρ^0 events and integrated luminosity for deuterium (hydrogen) respectively. The integrated luminosities reflect the total number of runs taken with the corresponding gas type in addition to the target gas densities and beam flux. Equation 6.18 provides a method of calculating the cross-section ratio in such a way that the result is independent of experimental conditions.

The integrated luminosities $L^{D(H)}$ are calculated by summing the luminosities measured during all bursts which satisfy data quality cuts. The luminosity measurement is provided by the HERMES luminosity monitor (LUMI, see section 3.3.3) which detects Møller and Bhabha scattering events from the beam-target interaction. Thus the LUMI only provides a measure of the target gas density in terms of the number of atomic electrons present in the target cell. For a given mass density of gas, the target operating with deuterium will result in a LUMI measurement which is half of that when the target cell operates with hydrogen despite both gas samples possessing the same amount of nucleons. In practice, therefore, the L^D quantity is twice the integrated luminosity as counted from good quality μDST bursts in the deuterium data sample. This approach allows the cross-section ratio to be expressed as

$$R = \frac{\sigma_{incoh}(p) + \sigma_{incoh}(n)}{2\sigma_{incoh}(p)} = \frac{1}{2} + \frac{1}{2}\frac{\sigma_{incoh}(n)}{\sigma_{incoh}(p)}. \tag{6.19}$$

6.6.2 Systematic Uncertainties

The contribution to errors in the calculated ratio of ρ^0 production from systematic and statistical effects varies with the kinematic region. Although low statistics near the limits of Q^2 and x_{Bj} provide the greatest contribution in such regions, past analyses reveal the presence of non-negligible systematic effects over the entire kinematic range, the largest of which being the uncertainty in the integrated luminosities on

hydrogen and deuterium. This uncertainty was previously determined to be ∼3% for the data samples with each target gas type [105]. The greatest contribution to this uncertainty is that on the luminosity monitor acceptance which cancels in the ratio; $\simeq 4\%$ is therefore the maximal value for this uncertainty.

Additional sources contribute to the systematic uncertainty. After calculation of the ratio of cross-sections, however, only a negligible remainder is present.

- A small uncertainty is introduced from the non-exclusive background subtraction. Previous HERMES analyses [93] have asserted this uncertainty to be 3%.
- Reconstruction and time efficiencies of the HERMES spectrometer contribute 2% to the systematic uncertainty [106, 107].
- A previous HERMES analysis [107] asserts that the error associated with radiative corrections is less than 2%.
- The double-diffractive contribution to the incoherent ρ^0 production cross section is $< 2\%$ [108, 109].

Ratios of cross-sections have been extensively studied in previous HERMES analyses. The evaluation of systematic errors shows that the overall uncertainty is strongly dominated by statistical errors.

6.6.3 Q^2-and x_{Bj}-Correlation

The results of the x_{Bj} dependence of the ρ^0 production cross-section ratios can be presented in two ways: the dependence can be studied over all Q^2 or in individual Q^2 bins. The former has the advantage in that statistics are preserved over x_{Bj} kinematical bins, but the possibility exists that a correlation between x_{Bj} and Q^2 requires a more restrictive binning scheme in Q^2 which has the effect of reducing the statistics in the x_{Bj} bins. The reliability of the results depends on the amount by which the two kinematical quantities are correlated. Taking ratios against one variable at a fixed value of the other helps to minimise the effect of some possible correlation, the degree of correlation may be calculated by investigating the Q^2, x_{Bj} distribution in two-dimensions.

The procedure for studying the correlation requires the Q^2, x_{Bj} distribution to be plotted following the application of all previous kinematical cuts and background

subtraction. A quadratic polynomial function

$$R(Q^2, x_{Bj}) = A + BQ^2 + Cx_{Bj} + DQ^2 x_{Bj} \tag{6.20}$$

giving the ratio of ρ^0 production cross sections (see equation 6.19) was fit to the measured data. Higher order polynomial fits resulted in extremely large errors on the higher order term coefficients. In this procedure, the χ^2 is minimised with respect to the parameters A, B, C, D. As equation 6.20 shows, the fit parameter D, associated with the $Q^2 x_{Bj}$ term gives the correlation. The fit results are shown in figure 6.15.

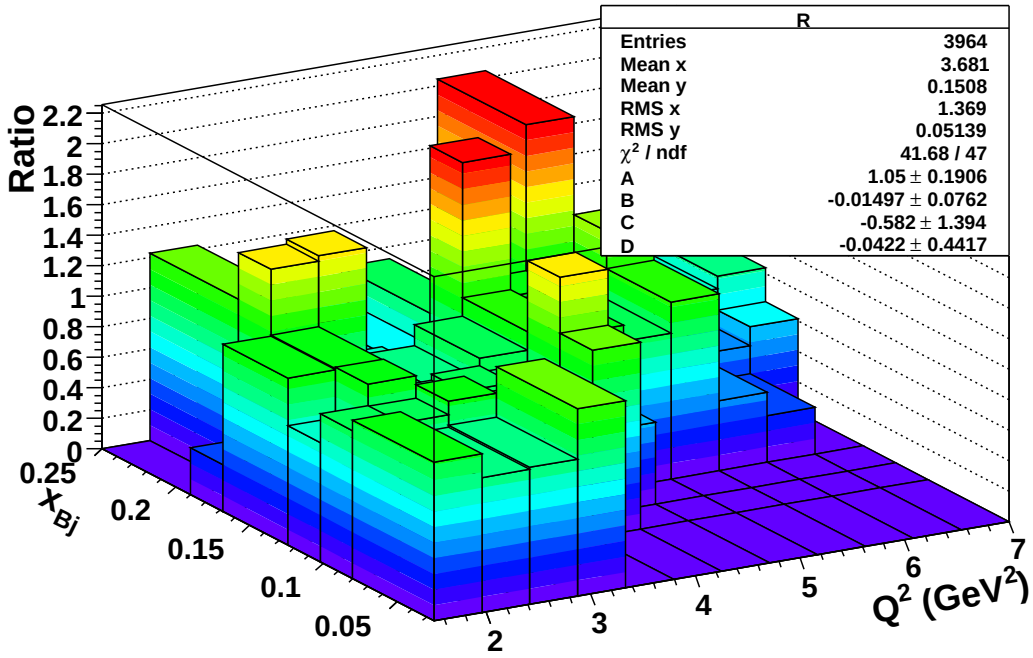

Figure 6.15: Quadratic polynomial fit to measured 2 dimensional Q^2, x_{Bj} background-subtracted distribution. The plane of best fit and the error bars are not shown for clarity.

The parameter D is consistent with zero, however, the limited statistics lead to a very large error associated with the correlation. Thus, in addition to a ρ^0 production ratio dependence study over all Q^2, a more rigorous study over individual Q^2 bins is useful.

6.6.4 Q^2 Dependence

It is expected, from the behaviour of the quark and gluon PDFs, that the cross section ratio for ρ^0-electroproduction on deuterium versus hydrogen should not depend on Q^2 for fixed x_{Bj}. In order to test whether this hypothesis is reflected by the data, it was necessary to investigate the x_{Bj} dependence of the cross-section ratio in separate bins of Q^2.

The cross-section ratio versus x_{Bj} is calculated in 12 bins of Q^2 in the range $1.5 < Q^2 < 7$ GeV^2, each bin having a corresponding width of 0.458 GeV^2. The x_{Bj} distribution in each Q^2 bin is further split into 6 variable-width bins. This binning scheme was chosen in order to reduce statistical error by combining bins with low occupancy. A linear fit to the measured ratio was performed in each Q^2 bin. The low statistics restricted the useful fit functions to those of low order and a linear fit provides a simple indication of the trend of the ratio to either increase or decrease with x_{Bj}. Figure 6.16 shows the cross-section ratios in increasing bins of Q^2.

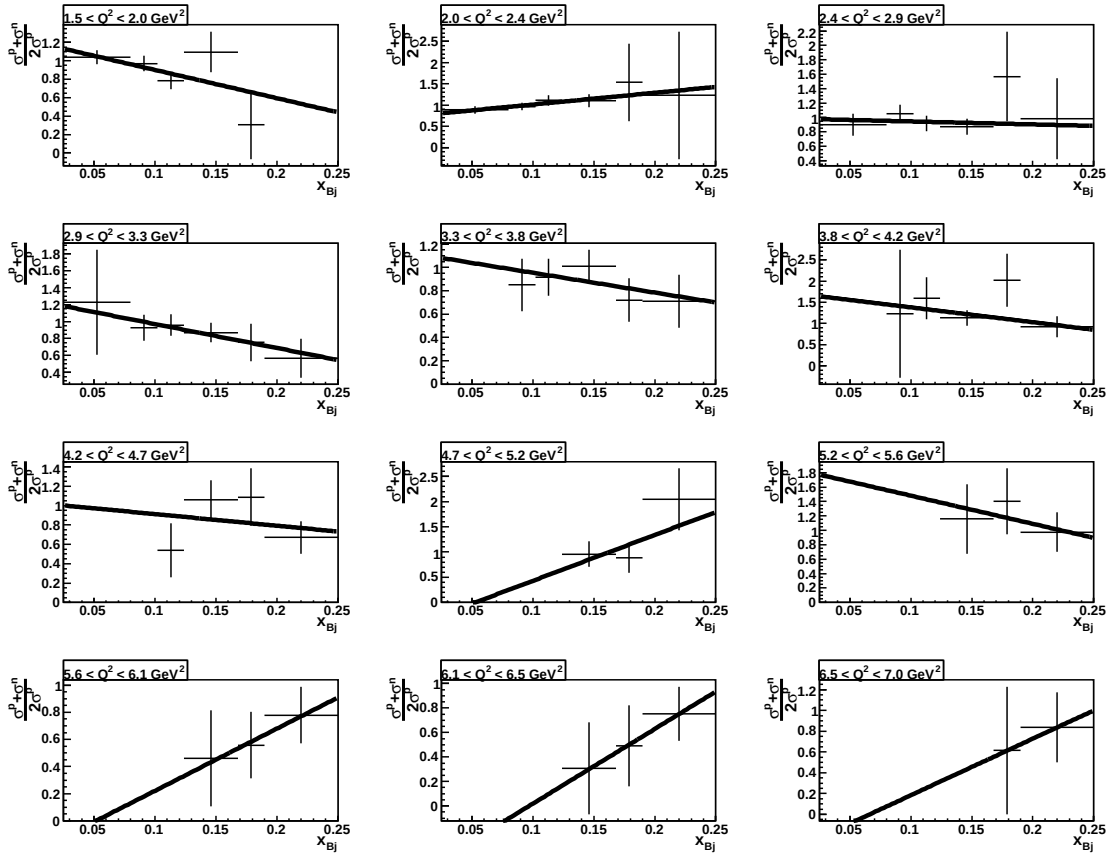

Figure 6.16: Linear fits to x_{Bj} distribution of ρ^0 production cross-section ratio in 12 equidistant bins of increasing Q^2 in the range $1.5 < Q^2 < 7$ GeV^2.

One result of the linear fit performed in each Q^2 bin, the intercept parameter, gives

the cross-section ratio at $x_{Bj} = 0$. The intercept is shown as a function of the mean Q^2 of the distribution inside the corresponding bin in figure 6.17.

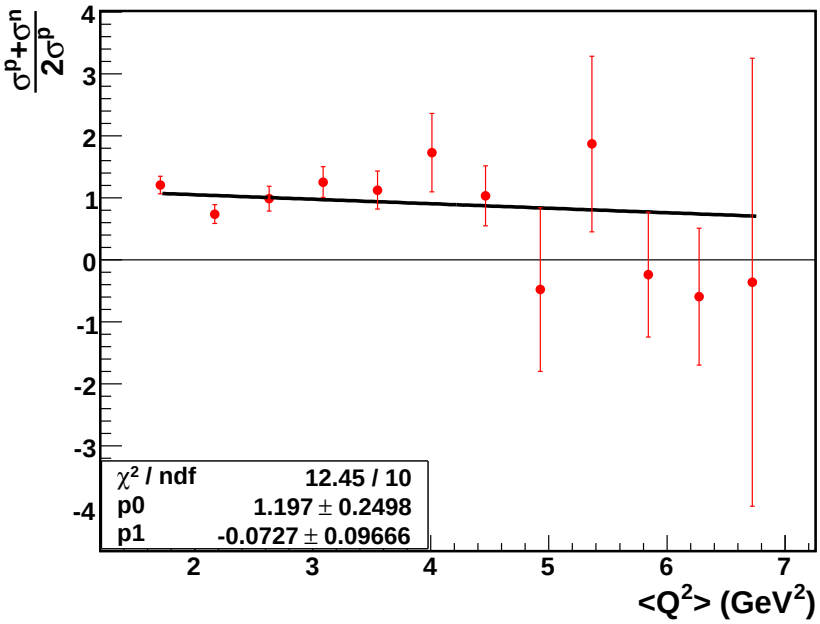

Figure 6.17: Intercept parameter from linear fits to the Q^2 bins, corresponds to ρ^0 production cross-section at $x_{Bj} = 0$.

The hypothesis that the ratio should be independent of Q^2 is tested by fitting a straight line to the data distribution. The $\chi^2 \simeq 1$ value as shown demonstrates that this model describes the data well. The Q^2 dependence, obtained from the gradient parameter p1 of the fit is consistent with zero within experimental error.

Presented in this way, however, the dependence is only valid for low values of x_{Bj} which correspond to ρ^0 production from gluon interactions. In order to test the Q^2 dependence over all x_{Bj} it is necessary to modify the procedure as used for creating figure 6.16. As before, the cross-section ratio versus x_{Bj} was calculated in 12 Q^2 bins, however a constant rather than linear fit was performed. The constant fit parameter in this case gives the average cross-section ratio over the x_{Bj} range in each Q^2 bin, figure 6.18 shows the average ratio as a function of mean Q^2.

The linear fit to the measured mean cross-section ratios displays a slight downward trend. This result, however, must be interpreted with care as figure 6.16 shows that as the x_{Bj} distribution is calculated at increasing Q^2, a corresponding increase in the lower x_{Bj} cutoff value is introduced, having the effect of artificially lowering the cross-section ratio.

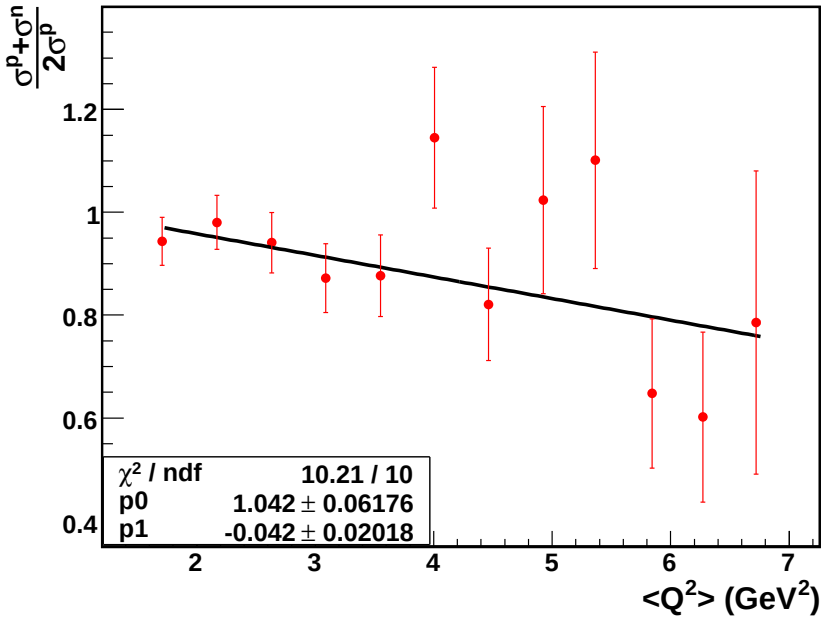

Figure 6.18: Fit parameter from constant fits to the Q^2 bins, corresponds to ρ^0 production cross-section at $\langle x_{Bj} \rangle$ in each Q^2 bin.

6.6.5 x_{Bj} Dependence

The region in which the quark contribution to the ρ^0 production amplitude becomes significant can be investigated by measuring the x_{Bj} dependence of the ρ^0 production cross-section ratio. As was determined in section 6.6.4, the ratio has no measurable dependence on Q^2 and so it is appropriate to explore the cross-section ratio over the entire $1.5 < Q^2 < 7$ GeV^2 kinematic range.

The x_{Bj} dependence of the ρ^0 production cross-section ratio was studied using a similar approach to that described in section 6.6.4. The cross-section ratio as a function of Q^2 is calculated in 6 variable-width bins of x_{Bj} in the range $0.025 < x_{Bj} < 0.25$. No data is present below the lower x_{Bj} limit. The Q^2 distribution in each x_{Bj} bin is divided into 12 equidistant bins. As there was no Q^2 dependence present for fixed x_{Bj} a constant fit was applied to the distribution in each x_{Bj} bin as shown in figure 6.19.

In this approach the result is presented as the mean cross section ratio over all Q^2 in each x_{Bj} kinematical bin. An important quantity in this case is the mean Q^2 value as the Q^2 distribution is skewed according to its corresponding x_{Bj} limits within each bin. The Q^2 distributions are shown in figure 6.20. In this case the Q^2 distribution in the deuterium sample was used to calculate the mean as the statistics in the hydrogen sample are lower. The mean values observed in the hydrogen sample

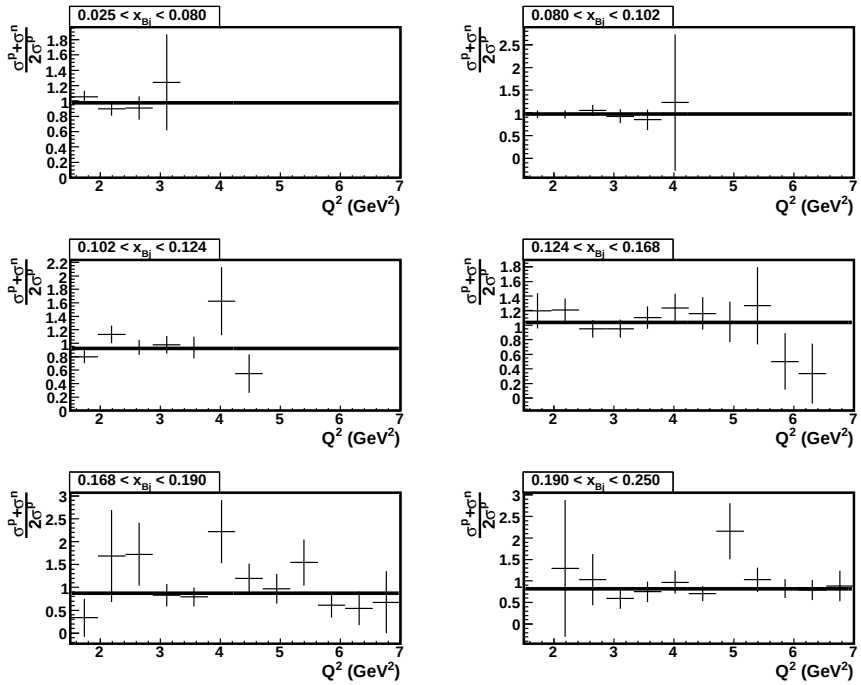

Figure 6.19: Constant fits to Q^2 distribution of ρ^0 production cross-section ratio in 6 variable-width bins of increasing x_{Bj} in the range $0.025 < x_{Bj} < 0.25$.

are consistent with those in the deuterium sample to an accuracy better than 1%, thus this approach would not introduce more than a negligible amount of systematic error.

Figure 6.21 shows the ratio of ρ^0 electroproduction cross sections on deuterium versus hydrogen according to equation 6.19, plotted as a function of mean x_{Bj} and for $1.5 < Q^2 < 7$ GeV^2.

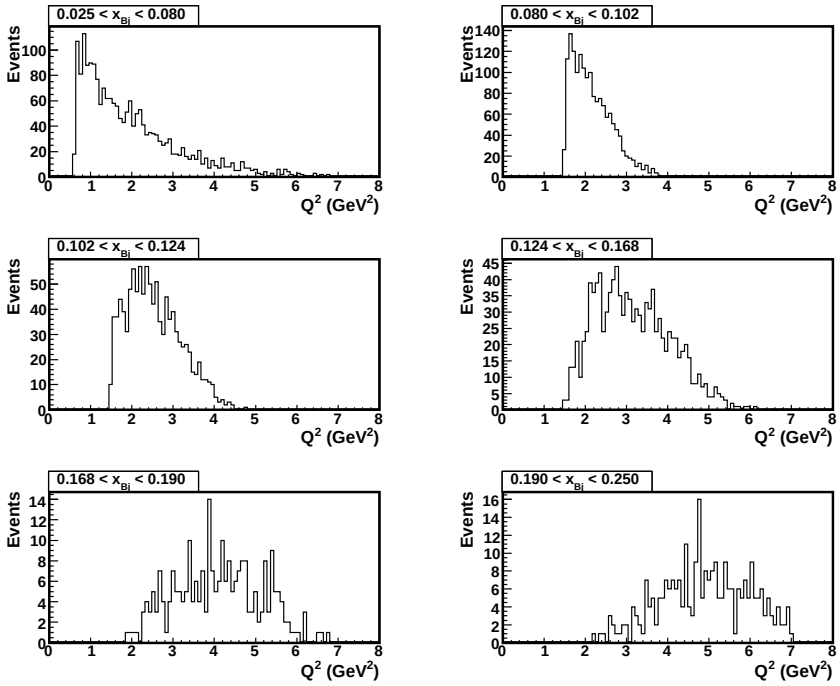

Figure 6.20: Q^2 distributions in 6 variable-width bins of increasing x_{Bj} in the range $0.025 < x_{Bj} < 0.25$.

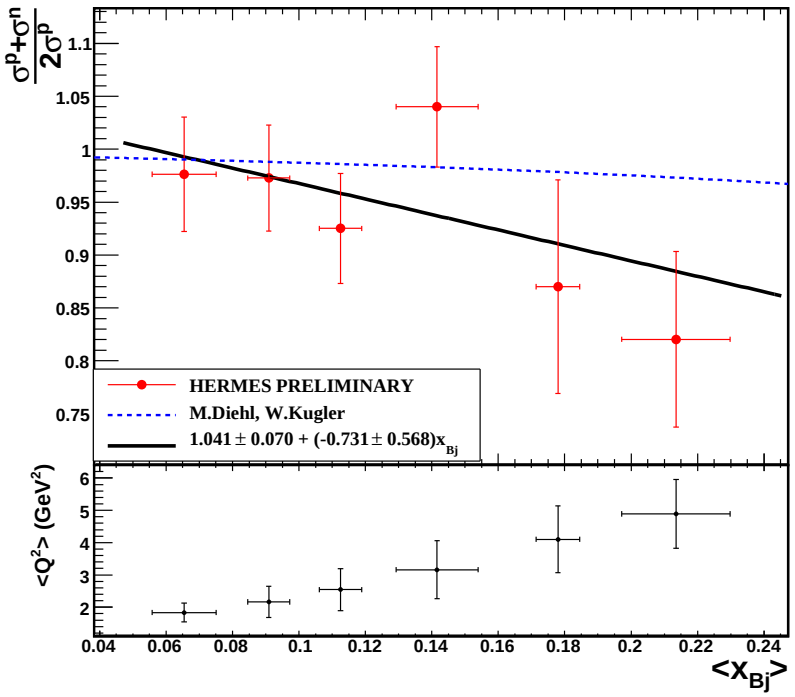

Figure 6.21: Ratio of ρ^0 electroproduction cross sections on deuterium versus hydrogen (upper plot) for $1.5 < Q^2 < 7$ GeV^2. Corresponding mean Q^2 values are indicated on the lower plot. The dashed (blue) curve is the calculated ratio using the MRST2001LO parameterisation (section 2.12) [42]. The solid line is the linear fit to the data. The bottom plot shows the mean Q^2 value in each x_{Bj} bin.

6.7 Projected Results for 2005-2007

During 2005 the HERMES experiment accumulated around half as much data with hydrogen and deuterium targets as in the 1996-2000 period. It is expected that the high density unpolarised target used with the Recoil Detector will yield a substantial amount of additional ρ^0 events. Although the 2005 data have not been fully checked, table 6.6 shows the approximate contribution to the total sample which the 2005 data and the high density target running with the Recoil Detector in 2006-2007 will provide.

Period	DIS Statistics hydrogen (Millions)	DIS Statistics deuterium (Millions)	ρ^0 Events hydrogen	ρ^0 Events deuterium
1996-2000	12.669	17.143	3964	6311
2005	6.3	7.2	1966	2650
2006-2007	33	7.2	10296	2650
Total	51.969	31.543	16226	11611

Table 6.6: DIS and ρ^0 event statistics during different running periods. The 2006-2007 estimates of the ρ^0 statistics are based on the past rates of 312 ρ^0s per million DIS for hydrogen, and 368 ρ^0s per million DIS for deuterium. The DIS statistics for the 2006-2007 period were obtained by estimating the effect of the increased target gas density when running with the Recoil Detector [110].

The effect of the additional statistics to the ρ^0-analysis is illustrated in figure 6.22. Although the effect on the overall ratio and its kinematic dependence can only be speculated on, the statistical uncertainty in each x_{Bj} bin will be reduced. The corresponding error bars will therefore become smaller, as will the errors on the linear fit.

The reduction in the size of the error bars is small at low x_{Bj} but larger at the higher region. This error reduction remains smaller than expected as the size of the error bars are dominated by the errors on the fits performed on the data in each x_{Bj} bin (figure 6.23). In turn, the error on these fits depend on, in addition to the statistical uncertainty of each data point, their spread. Increasing the statistics in such a manner will reduce the statistical uncertainty of each data point of figure 6.23, but may have a lesser effect on their distribution around the mean. Nonetheless, the fit uncertainties in figure 6.22 are considerably smaller than those in the fit to the current data in figure 6.21. Hence, a continuation of this analysis to the extended data set would be profitable once the data become available.

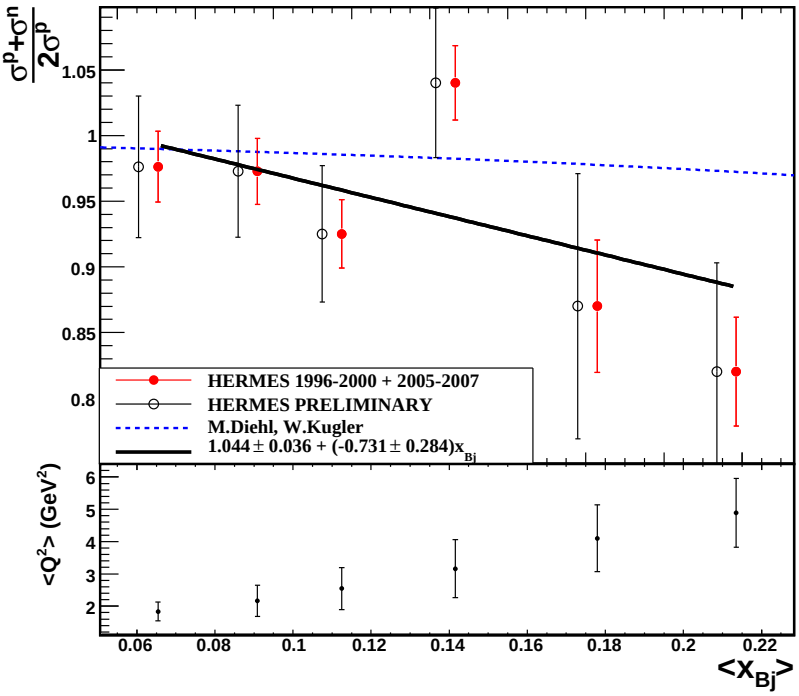

Figure 6.22: Effect of additional ρ^0 statistics from the 2005 data sample and Recoil Detector in 2006-2007 on the x_{Bj} dependency of the cross-section ratio. The fit is in this case performed on the new data points. The current data points, kept for comparison, are shifted in x_{Bj} by +0.005 for clarity.

6.8 Conclusions

This analysis compared theoretical expectations of kinematical dependencies of ρ^0-electroproduction cross section ratios on deuterium versus hydrogen with data gathered by HERMES between 1996 and 2000. The cross-check between the new ROOT based analysis code and the old PAW based one on which it is based shows excellent agreement both in statistics and in the comparison of kinematical distributions.

The theoretical prediction of the ratio, calculated with the MRST2001LO parameterisation, is applicable in the region $Q^2 > 1.5$ GeV^2. Below this threshold, the MRST2001LO parameterisation is unable to make predictions. Thus, the main result shown in figure 6.21 uses this lower limit as a cutoff. The slope seen in the data is steeper than the theoretical prediction. However as the plot shows, the error in the slope is large compared to the slope itself. Crucially, the slope is negative, indicating a gradual transition from a gluon to a quark main contribution to the scattering amplitude.

The result is, as expected, sensitive to the binning scheme used, particularly the

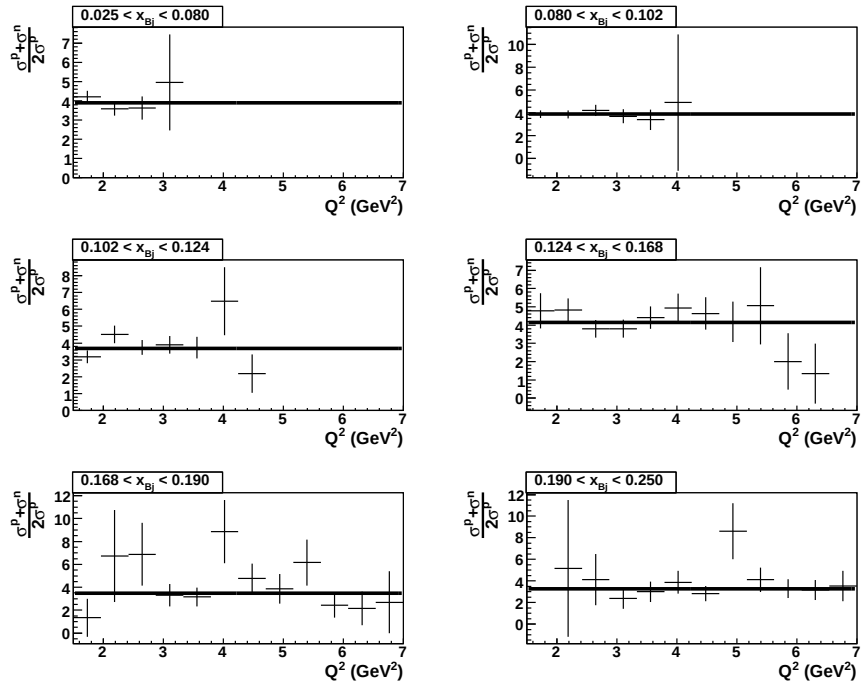

Figure 6.23: Effect of additional ρ^0 statistics from the 2005 data sample and Recoil Detector in 2006-2007 on the Q^2 distribution in separate x_{Bj} bins.

bin configuration at high x_{Bj}. In this region the statistics are low and so slight modifications to bin widths and centres affect the slope significantly, although the error on the slope remains approximately similar. The highest statistics are at low x_{Bj} which corresponds to low Q^2. Some preliminary investigations of the cross section ratio were undertaken at $1.0 < Q^2 < 7$ GeV^2 and $0.8 < Q^2 < 7$ GeV^2; the mean Q^2 values in the low x_{Bj} bins did not drift significantly below the theoretical 1.5 GeV^2 cutoff, this and the fact that DIS should exhibit Bjørken scaling means that these preliminary studies are conceptually reliable. However, due to the lack of statistics at high Q^2, the error on the slope of the ratio was not significantly reduced.

The SDME analysis carried out with the 1996-2000 data set gave, with the set of cuts specific to that analysis, a total of approximately 32,000 hydrogen and deuterium events [89]. Applying similar cuts to the 2001-2004 data yielded approximately 3000 additional events, from this it can be expected that adding the extra three years to this analysis would yield (with its more restrictive cuts compared with the SDME analysis) only around 1000 additional events. Although the addition of the 2005 data would increase the available statistics for the ρ^0 analysis by around 50%, at the end of the period during which this work was undertaken the 2005 data set was incomplete and its quality had not been determined. There are plans to incorporate the 2005 data to the 1996-2000 set in order to improve the analysis once the data

have been fully checked.

The unavailability of theoretical predictions of the ρ^0-production ratio based on parameterisations other than MRST2001LO limits the reliability of comparisons between theory and what is observed experimentally. Although the theoretical PDFs at leading order are similar to those at next-to-next-to leading order, MRST2001LO and MRST2001NNLO may yield very different cross section ratios. The analysis may be further improved by taking those results into consideration, as well as those from parameterisations such as CTEQ, GRV and ALEKHIN. The cross section ratio extracted from the HERMES data in this analysis indirectly introduces constraints on future theoretical GPD predictions, and will serve as a useful cross check once they are made available. It is readily seen that the leading-order approximation does not describe the data sufficiently well.

It must be noted that this analysis compares the total cross section ratio measured in HERMES data with the theoretical longitudinal cross section ratio. It is expected, however, that $\frac{\sigma_L}{\sigma_T}$, the ratio of ρ^0 longitudinal and transverse cross sections should be the same for hydrogen and deuterium targets. In fact, this is confirmed in the HERMES 1996-2000 data [51].

The Recoil Detector is expected to improve the analysis of the ρ^0-electroproduction ratio. The improved resolution in t will allow a refinement of the diffractive cuts while the exclusivity cut (ΔE) may be removed leading to greater statistics. Furthermore the establishment of event level exclusivity will provide a superior degree of DIS background suppression.

The Recoil Detector will collect data during the years 2006 and 2007, after which a continuation of this analysis with the additional statistics is likely to improve our understanding of the behaviour of quark and gluon distributions in the nucleon.

Appendix A

Tracking

A.1 Point-Line Distance in 3 Dimensions

A line in 3 dimensions is defined by two points $\vec{p_1} = (x_1, y_1, z_1)$ and $\vec{p_2} = (x_2, y_2, z_2)$. Let the point whose distance from the line is sought be given by $\vec{p_0} = (x_0, y_0, z_0)$. A vector along the line is given by [77]:

$$\vec{v} = \begin{bmatrix} x_1 + (x_2 - x_1)t \\ y_1 + (y_2 - y_1)t \\ z_1 + (z_2 - z_1)t \end{bmatrix}. \tag{A.1.1}$$

The squared distance between a point on the line with parameter t and the point $\vec{p_0}$ is then

$$\begin{aligned} d^2 &= [(x_1 - x_0) + (x_2 - x_1)t]^2 + [(y_1 - y_0) \\ &\quad +(y_2 - y_1)t]^2 + [(z_1 - z_0) + (z_2 - z_1)t]^2. \end{aligned} \tag{A.1.2}$$

The distance is minimised by setting the derivative of equation A.1.2 with respect to t to zero and solving for t to obtain

$$t = -\frac{(\vec{p_1} - \vec{p_0}) \cdot (\vec{p_2} - \vec{p_1})}{|\vec{p_2} - \vec{p_1}|^2}, \tag{A.1.3}$$

where $\cdot$ and vertical bars denote the scalar product and the vector norm respectively. Substituting equation A.1.3 into equation A.1.2 yields

$$\begin{aligned} d^2 &= (x_1 - x_0)^2 + (y_1 - y_0)^2 + (z_1 - z_0)^2 + 2t[(x_2 - x_1) \\ &\quad (x_1 - x_0) + (y_2 - y_1)(y_1 - y_0) + (z_2 - z_1)(z_1 - z_0)] \\ &\quad t^2[(x_2 - x_1)^2 + (y_2 - y_1)^2 + (z_2 - z_1)^2] \end{aligned} \tag{A.1.4}$$

which can be written as

$$|\vec{p_1} - \vec{p_0}|^2 - 2\frac{[(\vec{p_1} - \vec{p_0}) \cdot (\vec{p_2} - \vec{p_1})]^2}{|\vec{p_2} - \vec{p_1}|^2} + \frac{[(\vec{p_1} - \vec{p_0}) \cdot (\vec{p_2} - \vec{p_1})]^2}{|\vec{p_2} - \vec{p_1}|^2} \tag{A.1.5}$$

and simplified to

$$\frac{|\vec{p_1} - \vec{p_0}|^2 |\vec{p_2} - \vec{p_1}|^2 - [(\vec{p_1} - \vec{p_0}) \cdot (\vec{p_2} - \vec{p_1})]^2}{|\vec{p_2} - \vec{p_1}|^2}. \tag{A.1.6}$$

Using the vector quadruple product $(\vec{A} \times \vec{B})^2 = \vec{A}^2\vec{B}^2 - (\vec{A} \cdot \vec{B})^2$ where $\times$ denotes the vector cross product, and taking the square root,

$$d = \frac{|(\vec{p_2} - \vec{p_1}) \times (\vec{p_1} - \vec{p_0})|}{|\vec{p_2} - \vec{p_1}|}. \tag{A.1.7}$$

A.2 3 Dimensional Line Fitting

The 3-D fitting method proceeds according to the prescription of D. Eberly. The approach is detailed in reference [78] and is reproduced here.

As in equation 5.3, let the line be $\vec{a} = t\vec{b} + \vec{c}$. $\vec{X_i}$ is then the set of vectors describing the sample points to which the line must be fitted:

$$\vec{X_i} = \vec{c} + b_i\vec{b} + p_i\vec{b_i^{\perp}} \tag{A.2.8}$$

where $b_i = \vec{b} \cdot (\vec{X_i} - \vec{c})$ and $\vec{b_i^{\perp}}$ is a unit vector perpendicular to $\vec{b}$. The coefficient p_i is thus the perpendicular distance between the point i and the proposed line. $\vec{Y_i} = \vec{X_i} - \vec{c}$ is defined as the vector joining point i with the previously defined offset vector. The vector

$$\vec{Y_i} - b_i\vec{b} = p_i\vec{b_i^{\perp}}. \tag{A.2.9}$$

joins $\vec{X}_i$ to its projection onto the line, its squared length is $p_i^2 = (\vec{Y}_i - b_i\vec{b})^2$. The energy function which must be minimised represents the sum of squared perpendicular distances p_i to the proposed line; $E(\vec{c},\vec{b}) = \sum_{i=1}^{m} p_i^2$. This function can be written in terms of a matrix $M(c)$ by substituting an expression for p_i^2:

$$E(\vec{c},\vec{b}) = \sum_{i=1}^{m}(\vec{Y}_i^t[I - \vec{b}\vec{b}^t]\vec{Y}_i). \tag{A.2.10}$$

The $\vec{b}$ vectors are then moved outside the sum:

$$E(\vec{c},\vec{b}) = \vec{b}^t\left(\sum_{i=1}^{m}[(\vec{Y}_i\cdot\vec{Y}_i)I - \vec{Y}_i\vec{Y}_i^t]\right)\vec{b} = \vec{b}^t M(c)\vec{b}. \tag{A.2.11}$$

Given $\vec{c}$, the matrix $M(c)$ is determined by equation A.2.11. In 3 dimensions if $\vec{c} = (c_x, c_y, c_z)$, $M(c)$ is given by

$$M(c) = \delta I - S$$

where I is the 3×3 identity matrix, S is given by

$$S = \begin{bmatrix} \sum_{i=1}^{m}(x_i-c_x)^2 & \sum_{i=1}^{m}(x_i-c_x)(y_i-c_y) & \sum_{i=1}^{m}(x_i-c_x)(z_i-c_z) \\ \sum_{i=1}^{m}(x_i-c_x)(y_i-c_y) & \sum_{i=1}^{m}(y_i-c_y)^2 & \sum_{i=1}^{m}(y_i-c_y)(z_i-c_z) \\ \sum_{i=1}^{m}(x_i-c_x)(z_i-c_z) & \sum_{i=1}^{m}(y_i-c_y)(z_i-c_z) & \sum_{i=1}^{m}(z_i-c_z)^2 \end{bmatrix}$$

and

$$\delta = \sum_{i=1}^{m}(x_i-c_x)^2 + \sum_{i=1}^{m}(y_i-c_y)^2 + \sum_{i=1}^{m}(z_i-c_z)^2.$$

$\vec{b}^t M(c)\vec{b}$ has a minimum corresponding to the smallest eigenvalue of $M(c)$, which in the case of cosmics track fitting is solved using the Jacobi method (the details of which can be found in reference [79] section 11.1) and MINUIT. The vector describing the track, $\vec{b}$, is given by the eigenvector corresponding to the smallest eigenvalue.

A.3 Inhomogeneous Fitting Matrix Entries

Equation 5.22 in section 5.6.5 is given by

$$\mathbf{M}^{n+1,n} = \frac{\partial \vec{v}_{n+1}}{\partial \vec{v}_n} = \begin{bmatrix} \frac{\partial \phi_{n+1}}{\partial \phi_n} & \frac{\partial \phi_{n+1}}{\partial \phi'_n} & \frac{\partial \phi_{n+1}}{\partial z_n} & \frac{\partial \phi_{n+1}}{\partial z'_n} & \frac{\partial \phi_{n+1}}{\partial \lambda} \\ \frac{\partial \phi'_{n+1}}{\partial \phi_n} & \frac{\partial \phi'_{n+1}}{\partial \phi'_n} & \frac{\partial \phi'_{n+1}}{\partial z_n} & \frac{\partial \phi'_{n+1}}{\partial z'_n} & \frac{\partial \phi'_{n+1}}{\partial \lambda} \\ \frac{\partial z_{n+1}}{\partial \phi_n} & \frac{\partial z_{n+1}}{\partial \phi'_n} & \frac{\partial z_{n+1}}{\partial z_n} & \frac{\partial z_{n+1}}{\partial z'_n} & \frac{\partial z_{n+1}}{\partial \lambda} \\ \frac{\partial z'_{n+1}}{\partial \phi_n} & \frac{\partial z'_{n+1}}{\partial \phi'_n} & \frac{\partial z'_{n+1}}{\partial z_n} & \frac{\partial z'_{n+1}}{\partial z'_n} & \frac{\partial z'_{n+1}}{\partial \lambda} \\ \frac{\partial \lambda}{\partial \phi_n} & \frac{\partial \lambda}{\partial \phi'_n} & \frac{\partial \lambda}{\partial z_n} & \frac{\partial \lambda}{\partial z'_n} & \frac{\partial \lambda}{\partial \lambda} \end{bmatrix}. \tag{A.3.12}$$

Explicitly, the components of $\mathbf{M}$ are

$$\begin{array}{lllll} \mathbf{M}_{00} = 1 & \mathbf{M}_{01} = h + \frac{h^2 \phi''^{\phi'}}{2} & \mathbf{M}_{02} = \frac{h^2 \phi''^{z}}{2} & \mathbf{M}_{03} = \frac{h^2 \phi''^{z'}}{2} & \mathbf{M}_{04} = \frac{h^2 \phi''^{\lambda}}{2} \\ \mathbf{M}_{10} = 0 & \mathbf{M}_{11} = 1 + h\phi''^{\phi'} & \mathbf{M}_{12} = h\phi''^{z} & \mathbf{M}_{13} = h\phi''^{z'} & \mathbf{M}_{14} = h\phi''^{\lambda} \\ \mathbf{M}_{20} = 0 & \mathbf{M}_{21} = \frac{h^2 z''^{\phi'}}{2} & \mathbf{M}_{22} = 1 + \frac{h^2 z''^{z}}{2} & \mathbf{M}_{23} = h + \frac{h^2 z''^{z'}}{2} & \mathbf{M}_{24} = \frac{h^2 z''^{\lambda}}{2} \\ \mathbf{M}_{30} = 0 & \mathbf{M}_{31} = hz''^{\phi'} & \mathbf{M}_{32} = hz''^{z} & \mathbf{M}_{33} = 1 + hz''^{z'} & \mathbf{M}_{34} = hz''^{\lambda} \\ \mathbf{M}_{40} = 0 & \mathbf{M}_{41} = 0 & \mathbf{M}_{42} = 0 & \mathbf{M}_{43} = 0 & \mathbf{M}_{44} = 1 \end{array}$$

where superscripts on ϕ'' and z'' as ϕ''^{x}, z''^{x} denote differentiating with respect to the superscripted variable according to

$$\phi''^{x} = \frac{1}{2}\left(\frac{d\phi''_{n+1}}{dx} + \frac{d\phi''_{n}}{dx}\right) \tag{A.3.13}$$

$$z''^{x} = \frac{1}{2}\left(\frac{dz''_{n+1}}{dx} + \frac{dz''_{n}}{dx}\right). \tag{A.3.14}$$

The derivatives of the unprimed components ϕ_{n+1} and z_{n+1} in rows 1 and 3 of the matrix $\mathbf{M}^{n+1,n}$ are calculated by differentiating equations 5.14 and 5.16 respectively. In practice better estimates of these derivatives are obtained by substituting ϕ''_n with $\frac{1}{2}(\phi''_n + \phi''_{n+1})$ in equation 5.14, and substituting z''_n with $\frac{1}{2}(z''_n + z''_{n+1})$ in equation 5.16. Rows 2 and 4 of $\mathbf{M}^{n+1,n}$ are calculated by taking derivatives of equations 5.19 and 5.21 respectively.

The derivatives of ϕ'' and z'' are given as follows:

$$
\begin{aligned}
\frac{d\phi''}{dz} &= \frac{Q}{r}\lambda\left[z'\frac{dB_r}{dz} - \left(1+r^2\phi'^2\right)\frac{dB_z}{dz}\right] \\
\frac{dz''}{dz} &= Q\lambda\left(-r\phi'\frac{dB_r}{dz} - r\phi' z'\frac{dB_z}{dz}\right) \\
\frac{d\phi''}{dz'} &= \frac{Q}{r}\lambda B_r + z'\lambda\frac{1}{rQ}\left[B_r z' - B_z\left(r^2\phi'^2+1\right)\right] \\
\frac{dz''}{dz'} &= -Qr\lambda\phi' B_z - \lambda\left(r\phi' B_r + r\phi' z' B_z\right)\frac{z'}{Q} - r\phi'^2 \\
\frac{d\phi''}{d\phi'} &= -2B_z\phi' rQ\lambda + \lambda\phi'\frac{r}{Q}\left[B_r z' - B_z\left(\phi'^2 r^2+1\right)\right] \\
\frac{dz''}{d\phi'} &= Q\lambda\left(-B_z r z' - rB_r\right) + \lambda\phi' r^2\left(-B_z\phi' r z' - B_r\phi' r\right)\frac{1}{Q} - 2\phi' r z' \\
\frac{d\phi''}{d\lambda} &= \frac{Q}{r}\left(z' B_r - \left[1+r^2\phi'^2\right]B_z\right) \\
\frac{dz''}{d\lambda} &= Q\left(-r\phi' B_r - r\phi' z' B_z\right)
\end{aligned}
$$

where the derivatives of B_r and B_z are obtained numerically from the magnetic field map.

Appendix B

ρ^0-Analysis

B.1 Background Distributions for Hydrogen

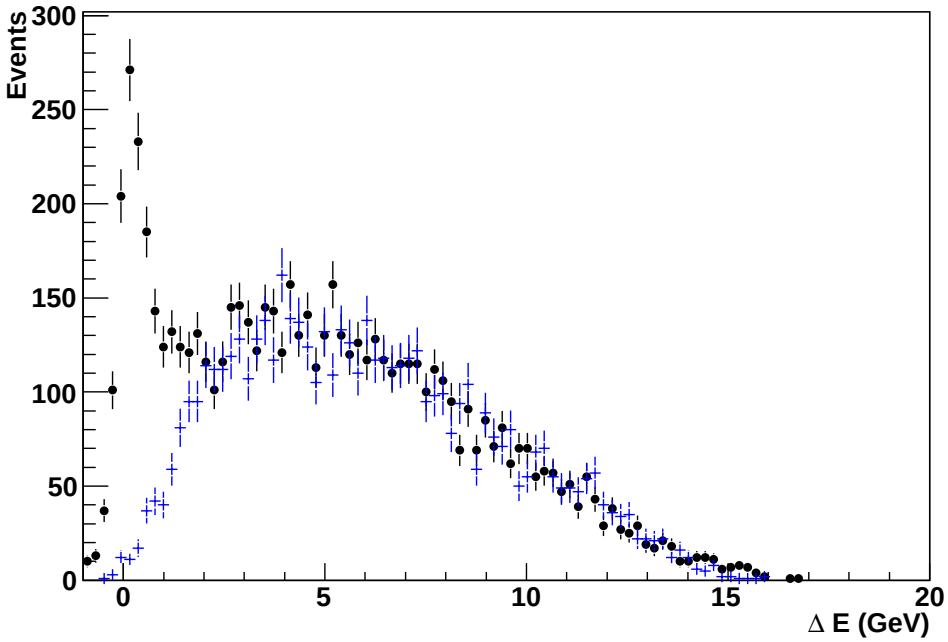

Figure B.1: ΔE distribution in 1996-2000 data (black circles) and Monte Carlo (blue crosses) for $0.08 < x_{Bj} < 0.102$ using a hydrogen target.

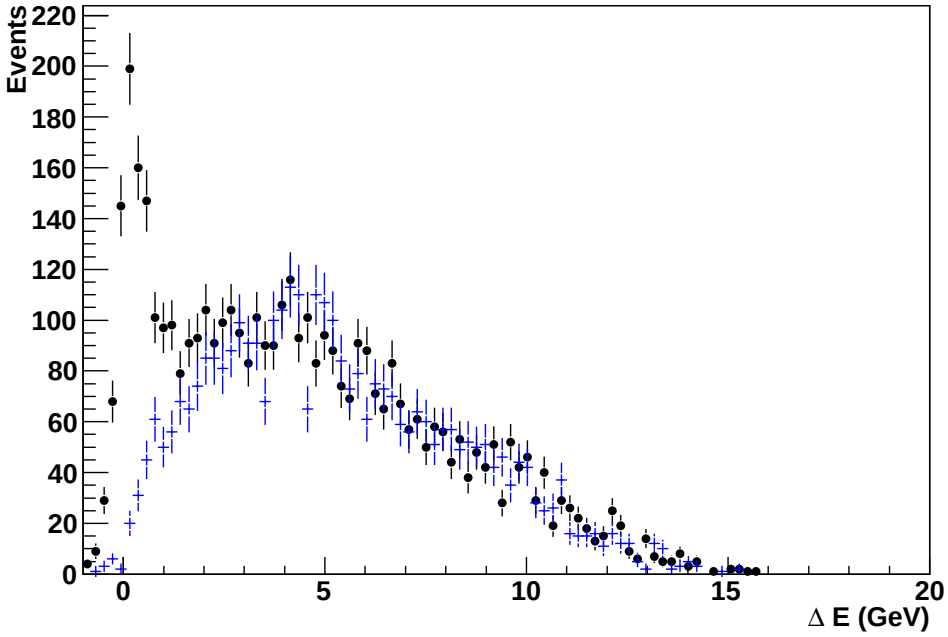

Figure B.2: ΔE distribution in 1996-2000 data (black circles) and Monte Carlo (blue crosses) for $0.102 < x_{Bj} < 0.124$ using a hydrogen target.

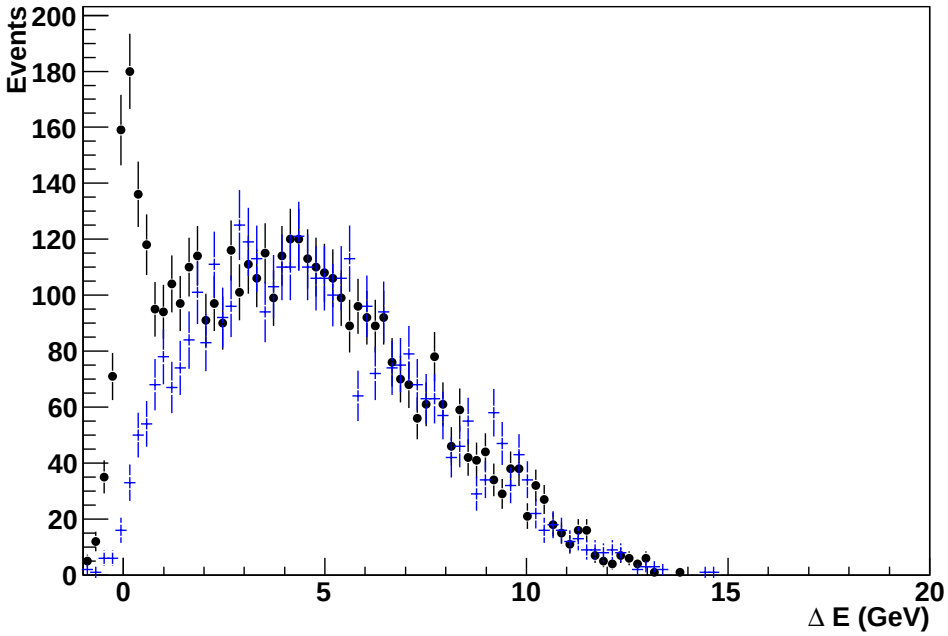

Figure B.3: ΔE distribution in 1996-2000 data (black circles) and Monte Carlo (blue crosses) for $0.124 < x_{Bj} < 0.168$ using a hydrogen target.

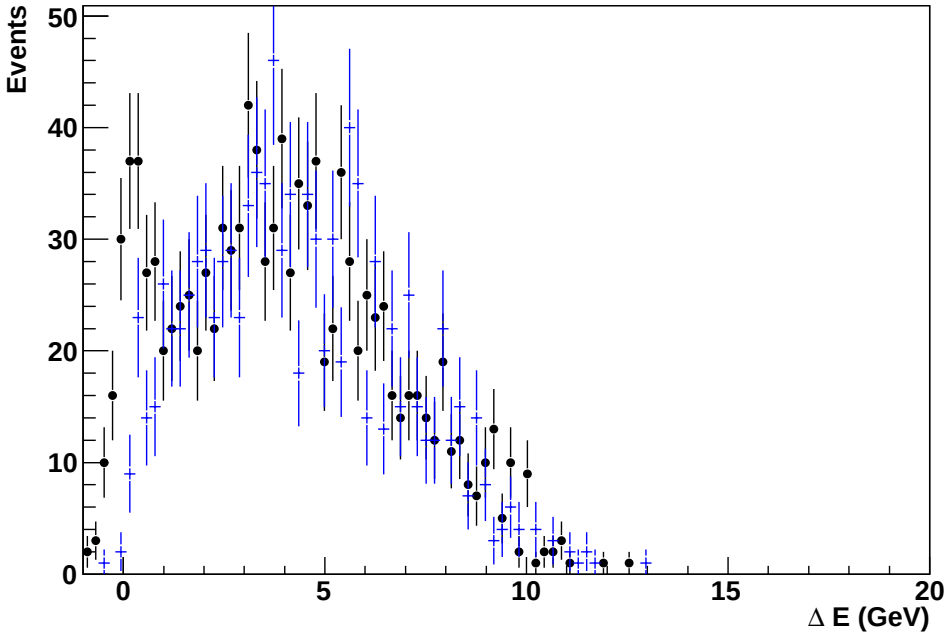

Figure B.4: ΔE distribution in 1996-2000 data (black circles) and Monte Carlo (blue crosses) for $0.168 < x_{Bj} < 0.19$ using a hydrogen target.

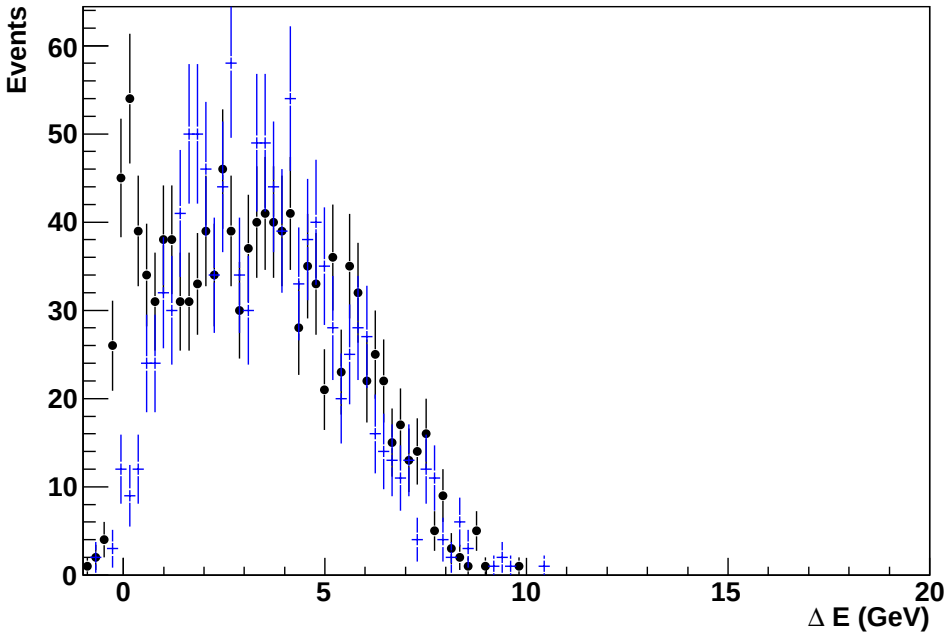

Figure B.5: ΔE distribution in 1996-2000 data (black circles) and Monte Carlo (blue crosses) for $0.19 < x_{Bj} < 0.25$ using a hydrogen target.

B.2 Background Distributions for Deuterium

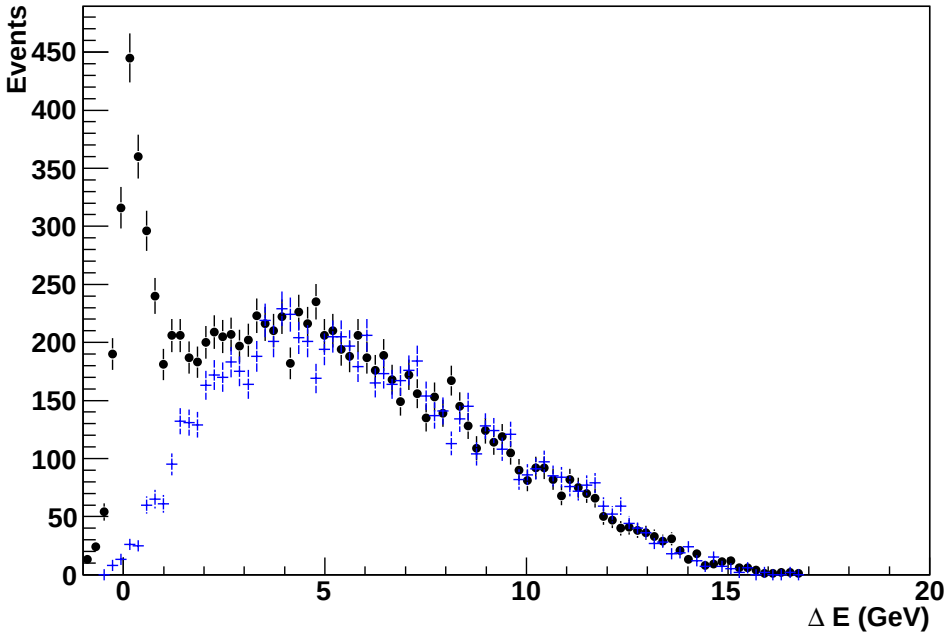

Figure B.6: ΔE distribution in 1996-2000 data (black circles) and Monte Carlo (blue crosses) for $0.08 < x_{Bj} < 0.102$ using a deuterium target.

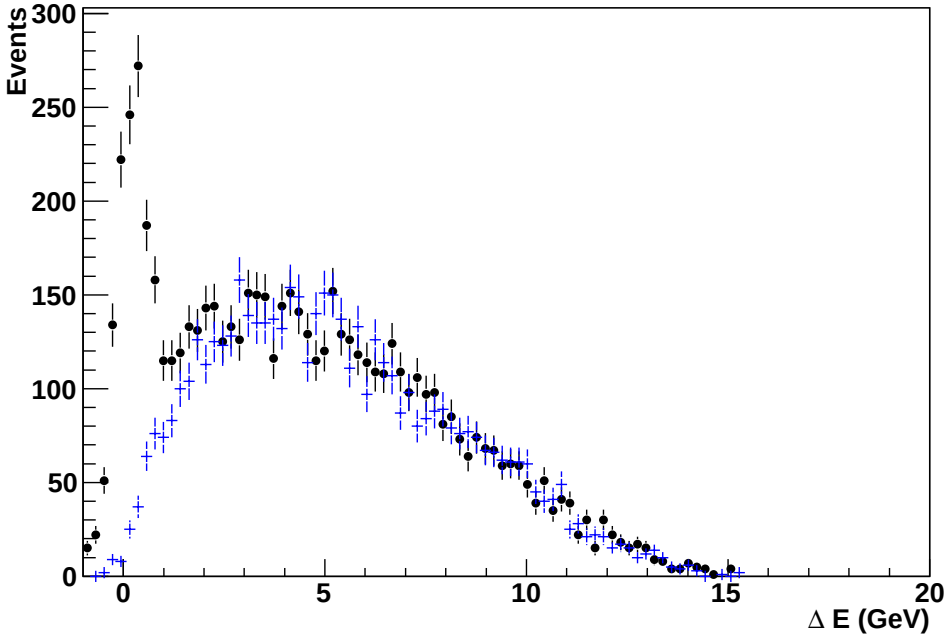

Figure B.7: ΔE distribution in 1996-2000 data (black circles) and Monte Carlo (blue crosses) for $0.102 < x_{Bj} < 0.124$ using a deuterium target.

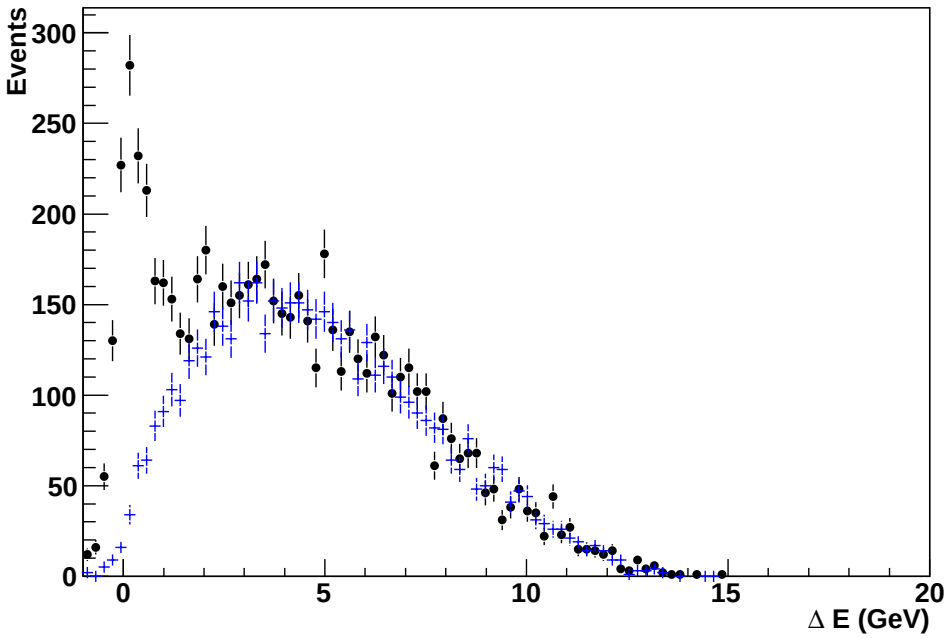

Figure B.8: ΔE distribution in 1996-2000 data (black circles) and Monte Carlo (blue crosses) for $0.124 < x_{Bj} < 0.168$ using a deuterium target.

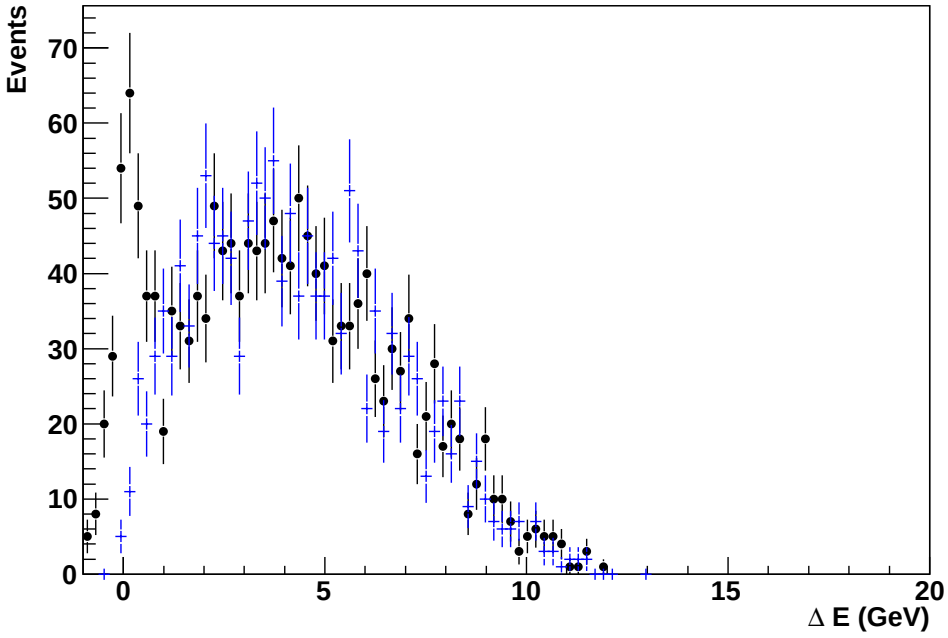

Figure B.9: ΔE distribution in 1996-2000 data (black circles) and Monte Carlo (blue crosses) for $0.168 < x_{Bj} < 0.19$ using a deuterium target.

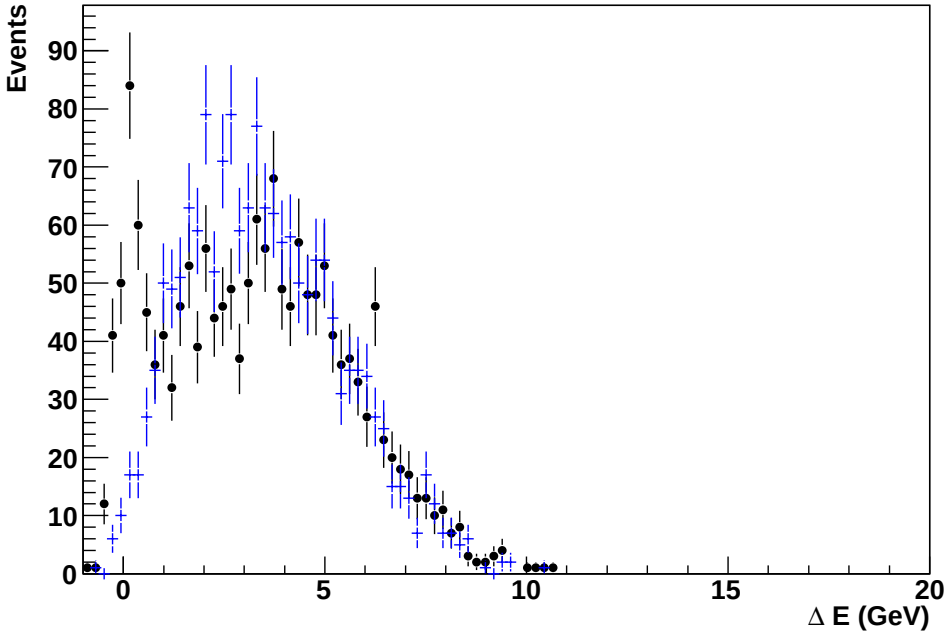

Figure B.10: ΔE distribution in 1996-2000 data (black circles) and Monte Carlo (blue crosses) for $0.19 < x_{Bj} < 0.25$ using a deuterium target.

Bibliography

[1] K. Abe et al. for E143 Collaboration (1998), Phys. Rev. **D58**, 112003.

[2] K. Ackerstaff et al. (1997), *Measurement of the Neutron Spin Structure Function G1(N) With a Polarized HE-3 Internal Target*, Phys.Lett **B404**, pp 383, hep-ex/9703005.

[3] K. Ackerstaff et al. (1997), *Flavor Decomposition of the Polarized Quark Distributions in the Nucleon From Inclusive and Semi-Inclusive Deep Inelastic Scattering*, Phys.Lett **B464**, pp 123, hep-ex/9906035.

[4] X. Ji (1996), *Gauge-Invariant Decomposition of Nucleon Spin and its Spin-Off*, Phys.Rev.Lett.**78**, pp 610, hep-ph/9603249.

[5] R. Hofstadter and R.W. McAllister (1955), *Electron Scattering From the Proton*, Phys.Rev. **98**:217-218.

[6] J.W. Rohlf (1994), *Modern Physics From a to Z0*, Wiley.

[7] A.W. Thomas and W. Weise (2001), *The Structure of the Nucleon*, Wiley-VCH.

[8] M.N. Rosenbluth (1950), *High Energy Elastic Scattering of Electrons on Protons*, Phys.Rev. **79**:615-619.

[9] D.J. Hamilton (2005), *Polarisation Transfer in Proton Compton Scattering at High Momentum Transfer*, Ph.D. Thesis.

[10] F. Halzen and A.D. Martin (1984), *Quarks and Leptons: An Introductory Course in Modern Particle Physics*, John Wiley & Sons, Inc.

[11] J.D. Bjørken and E.A. Paschos (SLAC) (1969), *Inelastic Electron Proton and Gamma Proton Scattering, and the Structure of the Nucleon*, Phys.Rev.**185**:1975-1982.

[12] R.P. Feynman (1969), *Very High-Energy Collisions of Hadrons*, Phys.Rev.Lett.**23**:1415-1417.

[13] B.R. Martin and G. Shaw (1997), *Particle Physics Second Edition*, John Wiley & Sons.

[14] S. Eidelman et al. (2004), Phys.Lett.**B592**:1 and 2005 partial update for the 2006 edition available on the PDG WWW pages (URL: http://pdg.lbl.gov/).

[15] G. Altarelli and G. Parisi (1977), Nucl.Phys.**B126**:298, V.N. Gribov and L.N. Lipatov (1972), Sov.J.Nucl.Phys.**15**:438,675, Yu.L.Dokshitzer (1977), Sov.Phys.JETP **46**:641.

[16] F.L. Pedrotti and L.S. Pedrotti (1993), *Introduction to Optics*, Prentice-Hall International.

[17] K.A. Fuka (2002), *The History of Adaptive Optics*, http://www.fuka.com/ kent/THAadaptiveoptics.htm.

[18] G. Alberi and G. Goggi (1981), Phys.Rep.**74**:1.

[19] J.B. Bellicard et al (1967), Phys.Rev.Lett.**19**:527.

[20] M.L. Perl (1974), *High Energy Hadron Physics*, Wiley & Sons.

[21] J.J. Sakurai and D. Schildknecht (1972), Phys.Lett.**B40**:121.

[22] T.H. Bauer, R.D. Spital, D.R. Yennie and F.M. Pipkin (1978), Rev.Mod.Phys.**50**:261.

[23] D.R. Yennie (1975), Rev.Mod.Phys.**47**:311.

[24] J.J. Sakurai (1969), Phys.Rev.Lett.**22**:981.

[25] C.del Papa et al (1979), Phys.Rev.**D19**:1303.

[26] D. Schildknecht, G.A. Schuler and B. Surrow (1999), Phys.Lett.**B449**:328.

[27] P.D.B. Collins (1977), *An Introduction to Regge Theory and High Energy Physics*, Cambridge University Press.

[28] V.N. Bolotov et al (1974), Nucl.Phys.**B73**:365.

[29] A. Donnachie and P.V. Landshoff (1992), Phys.Lett.**B296**:227.

[30] J. Grosse-Knetter (1997), *Measurement of Elastic ω Photoproduction at HERA*, Ph.D. Thesis, University of Hamburg.

[31] M. Diehl (2003), *Generalised Parton Distributions*, DESY-THESIS-2003-018.

[32] G.P. Lepage and S.J. Brodsky (1980), *Exclusive Processes in Perturbative Quantum Chromodynamics*, Phys.Rev.**D22**:2157.

[33] K. Goeke, M.V. Polyakov and M. Vanderhaegen (2001), *Hard Exclusive Reactions and the Structure of Hadrons*, Prog.Part.Nucl.Phys.**47**:401-515, hep-ph/0106012.

[34] X. Ji (1997), Phys.Rev.**D55**:7114.

[35] J.C. Collins, L. Frankfurt and M. Strikman (1997), Phys.Rev.**D56**:2982, hep-ph/9611433.

[36] W. Kugler, Private communication (May 2006).

[37] M. Diehl, A.V. Vinnikov (2004), hep-ph/0412162.

[38] J. Pumplin et. al. (2002), hep-ph/0201195

[39] M. Glueck, E. Reya and A. Vogt (1998), hep-ph/9806404

[40] A.D. Martin et al (2002), hep-ph/0201127

[41] S. Alekhin (2005), hep-ph/0508248

[42] M. Diehl, W. Kugler (DESY), A. Schafer (Regensburg U.), C. Weiss (Jefferson Lab), *Exclusive Channels in Semi-Inclusive Production of Pions and Kaons*. By . DESY-05-094, JLAB-THY-05-375, Jun 2005. 33pp. Published in Phys.Rev.D72:034034,2005, Erratum-ibid.D72:059902,2005 e-Print Archive: hep-ph/0506171

[43] S.I. Manayenkov (2004), Eur.Phys.J**C33**:397.

[44] S.V. Goloskokov and P. Kroll (2005), hep-ph/0501242.

[45] A.A. Sokolov and I.M. Ternov (1964), Sov. Phys. Dokladi **8**, pp 1203.

[46] D.P. Barber et al. (1993), *The HERA Polarimeter and the First Observation of Electron Spin Polarisation at HERA*, Nuclear Instruments and Methods in Physics Research **A329**, pp 79.

[47] J. Stewart et al. (1995), *Aspects of the Design of the Polarized H/D Internal Gas Target Storage Cell For the HERMES Experiment at HERA*, June 6-9 1995, International Workshop on Polarized Beams and Polarized Gas Targets, Cologne, Germany.

[48] K. Ackerstaff et al. (1998), *The HERMES Spectrometer*, hep-ex/9806007, Nuclear Instruments and Methods in Physics Research **A417**, pp 230.

[49] B. Krauss (2005), *Deeply Virtual Compton Scattering and the HERMES Recoil Detector*, Ph.D Thesis.

[50] W. Wander (1996), *Reconstruction of High Energy Scattering Events in the HERMES Experiment*, Ph.D Thesis.

[51] C. Shearer (2005), *Spin Density Matrix Element Extraction for the ρ^0 Vector Meson on Hydrogen and Deuterium Targets at HERMES*, Ph.D Thesis.

[52] K. S. Krane (1988), *Introductory Nuclear Physics*, John Wiley & Sons, Inc.

[53] H. Avakian et al. (1996), *The HERMES Electromagnetic Calorimeter*, 6th International Conference on Calorimetry in High-Energy Physics (ICCHEP 96), Rome, Italy, Jun 8 - 14, 1996

[54] R. Kaiser (1997), *Measurement of the Spin Structure of the Neutron using Polarised Deep Inelastic Scattering*, Ph.D Thesis.

[55] D. H. Perkins (1987), *Introduction to High Energy Physics*, Addison Wesley.

[56] D. De Schepper et al. (2000), *The HERMES Čerenkov detector*, HERMES Internal Report.

[57] *ADAMO-Entity Relationship Programming System, Version 3.3*, Programming Techniques Group, ECP Division, CERN, Geneva, 1994.

[58] W. Wander (1995), *DAD-Distributed ADAMO Database System at HERMES*, CHEP 95 conference proceedings, Rio de Janeiro.

[59] K. Ackerstaff and M.A. Funk (1995), *PinK, a Tcl/Tk Based Database Interface to ADAMO and DAD*, CHEP 95 conference proceedings, Rio de Janeiro.

[60] M. Tytgat (2000), *Diffractive Production of ρ^0 and ω Vector Mesons at HERMES*, Ph.D Thesis.

[61] V. Mexner (2005), *Determination of the Gluon Polarization in the Nucleon*, Ph.D Thesis.

[62] J.J.M. Steijger (2000), *The Lambda Wheels, a Silicon Vertex Detector for HERMES*, Nuclear Instruments and Methods in Physics Research **A453**, pp 98.

[63] B. Krauss (2001), *Ein Silizium Detektor Fuer Das HERMES Experiment*, HERMES Internal Report 01-041

[64] R. Kaiser (2005), *Status of the SFT and its Light Guides*, HERMES Internal Report 05-040.

[65] The HERMES Collaboration (2002), *The HERMES Recoil Detector Technical Design Report*, HERMES Internal Report 02-003.

[66] M. Hoek, Private communication, April 2006.

[67] M. Tytgat (2003), *The Recoil Photon Counter*, HERMES Internal Review Meeting, 7th January 2003.

[68] R. Fruehwirth (1987), *Application of Kalman Filtering to Track and Vertex Fitting*, Nuclear Instruments and Methods in Physics Research **A262**, pp 444-450.

[69] R. Fruehwirth et al (2000), *Data Analysis Techniques for High Energy Physics*, Cambrige University Press, 2nd Edition.

[70] N.C.R. Makins, *HERMES Software Boot Camp*, HERMES internal documentation.

[71] S. Balashov et al (2005), *Energy Calibration of the Silicon Modules for the Recoil Detector with the Tandem Facility*, HERMES Internal Report 05-020.

[72] C. Vogel, Private communication, June 2005.

[73] M.J. Murray (2005), *HERMES Recoil Silicon Detector Calibration to MIPs at T22 Test Beam*, 2nd year Ph.D report, University of Glasgow.

[74] B. Seitz, private communication, April 2005.

[75] M. Tytgat, *Clustering Routines for the Photon Detector*, HERMES Technical Recoil Meeting, October 17th 2005.

[76] C. Shearer (2005), *Integration of the Recoil Detector into the HERMES Monte Carlo Simulation*,HERMES Internal Report 04-007.

[77] Eric W. Weisstein, *Point-Line Distance - 3-Dimensional*, MathWorld - A Wolfram Web Resource http://mathworld.wolfram.com/Point-LineDistance3-Dimensional.html.

[78] D. Eberly (1999), *Least Squares Fitting of Data*, http://www.geometrictools.com/, Geometric Tools, Inc.

[79] W.H. Press et al (1992), *Numerical Recipes in C: The Art of Scientific Computing*, Cambridge University Press, 2nd Edition.

[80] D. Protopopescu, private communication, April 2005.

[81] T. Sjostrand et al (2003), *PYTHIA 6.3 Physics and Manual*, hep-ph/0308153.

[82] B. Zihlmann, *Magnet Status*, Recoil Group Meeting, DESY Hamburg, October 2004.

[83] J.C. Hart and D.H. Saxon (1984), *Track and Vertex Fitting in an Inhomogeneous Magnetic Field*, Nuclear Instruments and Methods in Physics Research **220**, pp 309-326.

[84] L. Bugge and J. Myrheim (1981), *Tracking and Track Fitting*, Nuclear Instruments and Methods **179**, pp 365-381.

[85] D. Saxon, *Recent Developments in Tracking Detectors*, Graduate Lectures, Department of Physics and Astronomy, University of Glasgow (2002).

[86] J. Visser et al (2004), Nuclear Instruments and Methods **A521**, pp 430.

[87] H. Bischel and C. Tschalaer (1967), Nuclear Data **A 3**, pp 343.

[88] C. Shearer, private communication, January 2005.

[89] A. Borissov, B. Marianski, C. Shearer (2005) *Kinematic Dependences of Spin Density Matrix Elements of Exclusive Diffractive ρ^0 on Hydrogen and Deuterium Targets*, HERMES release report, 21 June 2005.

[90] HERMES g_1^n group (1995), *Determination of the 1995 Data Quality and the Extraction of the Spin Structure Function of the Neutron*, HERMES Internal Note 97-007.

[91] Particle Data Group, S. Eidelman et al (2004), Physics Letters **B 592**, 1.

[92] T.G. O'Neill (1995), HERMES Internal Report 95-046.

[93] A. Airapetian et al (1999), *Observation of a Coherence Length Effect in Exclusive ρ^0 Electroproduction*, Phys.Rev.Lett.82, 3025.

[94] B. Povh and J. Hufner (1987), *Geometric Interpretation of Hadron-Proton Total Cross Sections and a Determination of Hadronic Radii*, Phys.Rev.Lett. **58**, 1612.

[95] A. Borrissov, Private communications 2005-2006.

[96] J. Wendland (2001), *Particle Identification for HERMES Run I*, HERMES Internal Note 01-067.

[97] R. Kaiser (1997), *Particle Identification at HERMES*, HERMES Internal Note 97-025.

[98] Rene Brun and Fons Rademakers (1996), *ROOT - An Object Oriented Data Analysis Framework*, Proceedings AIHEN'96 Workshop, Lausanne, Sep 1996, Nuclear Instruments and Methods in Physics Research **A 389**, pp 81-86.

[99] PAW User's Guide and Reference Manual, CERN Program Library Long Writeup **Q121**.

[100] A. Airapetian et al., *Hard Exclusive Electroproduction of $\pi^+\pi^-$ Pairs*, Physics Letters B 599 (2004) 212; Eprint numbers: hep-ex/0406052 and DESY-04-097.

[101] R.Fabbri, *Hard Exclusive Electroproduction of Two Pions at HERMES* , DESY-Thesis 03-036.

[102] R.Fabbri, P. di Nezza, A.Borissov *Hard Exclusive Electroproduction of Two Pions at HERMES* , HERMES release report, 29 March 2002.

[103] U.Elschenbroich *Single Spin Azimuthal Asymmetry in Exclusive Electroproduction of ρ^0 Mesons*, HERMES release report, 28 January 2003.

[104] J.Dreschler, A.Rostomyan *Single Spin Azimuthal Asymmetry in Exclusive Electroproduction of ρ^0 Mesons on a Transversely Polarized Hydrogen Target*, HERMES release report, 14 February 2005.

[105] F. Meissner (2000), *Measurement of the J/ψ-Cross Section and Double-Spin Asymmetries in Vector Meson Production in Polarised Lepton-Nucleon Scattering at HERMES*, Ph.D Thesis.

[106] A. Airapetian et al (2005), *Double Hadron Leptoproduction in the Nuclear Medium*, hep-ex/0510030, submitted to Phys.Rev.Lett.

[107] A. Airapetian et al (2001), *Hadron Formation in Deep-Inelastic Positron Scattering in a Nuclear Environment*, Eur.Phys.J.C 20, 479-486.

[108] A. Airapetian et al (2003), Q^2 *Dependence of Nuclear Transparency for Exclusive* ρ^0 *Production*, Phys.Rev.Lett.90(5).

[109] A. Airapetian et al (2000), *Exclusive Leptoproduction of* ρ^0 *Mesons From Hydrogen at Intermediate Virtual Photon Energies*, Eur.Phys.J.C 17, 389-398.

[110] J. Stewart, *Detector Status and Running Strategy*, HERMES Collaboration meeting, March 2006.